



**MONASH** University

**Mathematical Modelling  
of the Geometric Control  
of Bone Tissue Growth**

Mohd Almie Alias

A thesis submitted for the degree of Doctor of Philosophy at

Monash University

School of Mathematical Sciences

November 2017



# Copyright notice

©Mohd Almie Alias (2017).

I certify that I have made all reasonable efforts to secure copyright permissions for third-party content included in this thesis and have not knowingly added copyright content to my work without the owner's permission.



# Abstract

Bone tissues are formed under strong geometric controls. These controls may occur through various geometrical variables such as the local bone curvature and porosity. Geometric controls provide a high level of coupling in the evolution of the tissue, since changes in tissue shape affect in turn the tissue's evolution, which changes the geometric control. The influence of geometry in biological tissue growth has been shown recently in several experimental studies. In in-vitro bioscaffold studies, the velocity of tissue growth was found to be proportional to the local curvature of the bioscaffolds. In in-vivo studies, the velocity of tissue growth exhibits an inverse proportionality with local curvature.

In this thesis, we aim to understand these seemingly contradicting observations by developing mathematical models of biological tissue growth at the cellular scale. We investigate how tissue-synthesising cells mediate the interaction between geometry and tissue growth. This leads us to the development of a continuum model consisting of two coupled PDEs that describe the co-evolution of the tissue interface and the density of cells that secrete the new tissue matrix.

This thesis contains three main parts. In the first part, the main mathematical model coupling cell density to curvature is developed, and is used to explore different patterns of tissue growth that arise depending on model parameters, particularly cell diffusion. This cellular-level model enables us to relate certain experimental observations in tissue-engineered bioscaffolds to individual and collective cell behaviours: Smoothing of the interface observed in bioscaffolds can be related to a combination of curvature-induced crowding of cells and cell diffusion on tissue surface. Tissue deposition slowdown at later stage of formation can be related to some degree of cell depletion. This mathematical model leads to a type of hyperbolic curvature flow for biological tissue growth. A theoretical analysis of this model is then performed in the low-diffusion limit to demonstrate the emergence of shock waves, manifested by cusps in the tissue interface in numerical simulations.

The second part applies the mathematical model to experimental data on the rate of new bone formation in secondary osteons to gain insights into the influence of geometry on individual cell behaviours. Numerical simulations of the model suggest that the secretory rate of bone-forming cells within an osteon is controlled geometrically not by the pore interface curvature, but by the porosity of the infilling cavity, while the cell

depletion rate is controlled either by porosity or curvature. The inclusion of geometrical dependences of individual cell behaviours in the model reconciles the discrepancy of the curvature effect on tissue growth seen in-vivo and in-vitro.

The third part of this thesis focuses on the development of a parameterisation-free level set method to capture complex topological changes of the tissue interface. Numerical simulations produced by this method and by explicit parameterisations result in a very good match. This method promises to allow a direct extension of our model of the geometrical control of bone tissue growth to three dimensions.

# Declaration

This thesis contains no material which has been accepted for the award of any other degree or diploma at any university or equivalent institution and that, to the best of my knowledge and belief, this thesis contains no material previously published or written by another person, except where due reference is made in the text of the thesis.

Signature: 

Name: Mohd Almie Alias

Date: 17th November 2017



# Publications during enrolment

ALIAS, M. A. & BUENZLI, P. R. 2017. Modelling the effect of curvature on the collective behavior of cells growing new tissue. *Biophysical Journal* **112**(1), 193–204.

ALIAS, M. A. & BUENZLI, P. R. 2017. Bone-forming cells infill irregular pores under curvature and porosity controls: A hypothesis-testing analysis of cell behaviours. *Submitted*.



# Thesis including published works declaration

I hereby declare that this thesis contains no material which has been accepted for the award of any other degree or diploma at any university or equivalent institution and that, to the best of my knowledge and belief, this thesis contains no material previously published or written by another person, except where due reference is made in the text of the thesis.

This thesis includes 1 original paper published in peer reviewed journals and 1 manuscript in preparation for journal submission (not submitted). The core theme of the thesis is mathematical modelling of bone formation dynamics. The ideas, development and writing up of all the papers in the thesis were the principal responsibility of myself, the student, working within the School of Mathematical Sciences at Monash University under the supervision of A/Prof Tianhai Tian and Dr Pascal Buenzli.

The inclusion of co-authors reflects the fact that the work came from active collaboration between researchers and acknowledges input into team-based research.

In the case of Chapters 3 and 5, my contribution to the work involved the following:

Thesis Chapter	Publication Title	Status	Nature and % of student contribution	Co-author name(s) Nature and % of Co-author's contribution*	Co-author(s), Monash student Y/N*
3	<i>Modelling the effect of curvature on the collective behaviour of cells growing new tissue</i>	<i>Published</i>	<i>50%. Conceived and designed the study, performed the numerical simulations, drafted and edited the article.</i>	<i>Pascal R. Buenzli, input into manuscript 50%.</i>	<i>No</i>
5	<i>Bone-forming cells infill irregular pores under curvature and porosity controls: A hypothesis-testing analysis of cell behaviours</i>	<i>Submitted</i>	<i>50%. Conceived and designed the study, performed the numerical simulations, drafted and edited the article.</i>	<i>Pascal R. Buenzli, input into manuscript 50%.</i>	<i>No</i>

I have not renumbered sections of submitted or published papers in order to generate a consistent presentation within the thesis.

Signature:



Date: 17th November 2017

The undersigned hereby certify that the above declaration correctly reflects the nature and extent of the students and co-authors contributions to this work. In instances where I am not the responsible author I have consulted with the responsible author to agree on the respective contributions of the authors.

Main Supervisor signature:



Date: 17th November 2017

# Acknowledgements

This thesis would not have been possible without the presence of my wife, Fatien Adibah Wan Muhammad, my supervisors, Dr Pascal Buenzli and Assoc Prof. Dr Tianhai Tian, and my family members. I am grateful to have received your supports and definitely I can't thank you enough.

I would also like to thank everyone who have assisted me along this journey especially my PhD advisory committee panels, Prof. Kate Smith-Miles, Dr Simon Clarke and Dr Mark Flegg, and other people from the School of Mathematical Sciences at Monash University, especially Gertrude Nayak, Linda Mayer and John Chan, office mates especially Chloe Lerebours, my sponsors, teachers, and friends.



# Contents

<b>1</b>	<b>Introduction</b>	<b>1</b>
1.1	Bone remodelling . . . . .	1
1.2	Factors affecting remodelling . . . . .	2
1.2.1	Biochemical regulation . . . . .	3
1.2.2	Mechanical regulation . . . . .	3
1.2.3	Geometrical regulation . . . . .	3
1.3	Motivation . . . . .	4
1.4	Research aims . . . . .	5
1.5	Thesis outline . . . . .	6
<b>2</b>	<b>Mathematical models</b>	<b>9</b>
2.1	Introduction to the explicit parameterisation model . . . . .	10
2.1.1	Interface velocity . . . . .	10
2.1.2	Interface evolution . . . . .	11
2.1.3	Cell surface density evolution . . . . .	11
2.1.4	Specialisation to two-dimensional study . . . . .	12
2.2	Derivation of the implicit parameterisation (level set) method . . . . .	14
2.2.1	Evolution equation of the interface . . . . .	15
2.2.2	Evolution equation of velocity . . . . .	15
2.3	Numerical methods . . . . .	16
<b>3</b>	<b>Paper 1: Modelling the effect of curvature on the collective behaviour of cells growing new tissue</b>	<b>17</b>
3.1	Overview . . . . .	17
3.2	PDF of paper . . . . .	17
3.3	Numerical methods . . . . .	33
3.3.1	Finite difference scheme . . . . .	33
3.3.2	Finite volume scheme . . . . .	35
3.3.3	CFL condition . . . . .	36
<b>4</b>	<b>Zero-diffusion limit: hyperbolic conservation laws</b>	<b>39</b>
4.1	Overview . . . . .	39

4.2	Introduction . . . . .	39
4.2.1	Eigenstructure of $f'(u)$ . . . . .	42
4.2.2	Riemann invariants and integral curves . . . . .	43
4.3	Finite time blow up of smooth solution . . . . .	46
4.4	Wave structure in the Riemann problem . . . . .	48
4.4.1	Determination of the middle state $u_m$ . . . . .	49
4.4.2	Rarefaction waves . . . . .	50
4.4.3	Shock waves . . . . .	51
4.4.4	Results . . . . .	52
4.4.4.1	All-rarefaction problem . . . . .	53
4.4.4.2	All-shock problem . . . . .	56
4.5	Conclusions . . . . .	59
<b>5</b>	<b>Paper 2: Bone-forming cells infill irregular pores under curvature and porosity controls: A hypothesis-testing analysis of cell behaviours</b>	<b>61</b>
5.1	Overview . . . . .	61
5.2	PDF of paper . . . . .	61
<b>6</b>	<b>Modelling curvature-controlled tissue growth in complex interface geometries</b>	<b>75</b>
6.1	Overview . . . . .	75
6.2	Introduction . . . . .	76
6.3	Mathematical methods . . . . .	77
6.3.1	Implicit parameterisation of interface . . . . .	77
6.3.2	Numerical schemes . . . . .	78
6.3.2.1	Step 1: Initialisation of functions $\phi(x, y, t^0)$ and $V(x, y, t^0)$	79
6.3.2.2	Step 2: Solving for $\phi(x, y, t^0)$ . . . . .	79
6.3.2.3	Step 3: Reinitialisation of $\phi(x, y, t^0)$ . . . . .	80
6.3.2.4	Step 4: Solving for $V(x, y, t^0)$ . . . . .	82
6.4	Results . . . . .	85
6.4.1	Circular interface . . . . .	86
6.4.2	Hexagonal and square interfaces . . . . .	87
6.4.3	Fusion of two circular interfaces . . . . .	88
6.4.4	Curvature-controlled tissue growth in bioscaffold . . . . .	91
6.4.5	Fusion and elimination of trabecular struts . . . . .	94
6.5	Discussion and conclusions . . . . .	94
<b>7</b>	<b>Conclusions and outlook</b>	<b>97</b>

<b>Appendix</b>	<b>107</b>
A.1 The rarefaction conditions . . . . .	107
A.2 The rarefaction waves . . . . .	108
A.2.1 Determining the 1-rarefaction wave . . . . .	108
A.2.2 Determining the 2-rarefaction wave . . . . .	109
A.3 The Hugoniot loci and the shock speeds . . . . .	111
A.3.1 Nonlinearised problem . . . . .	111
A.3.2 Linearised problem . . . . .	112
A.4 The entropy conditions . . . . .	113
A.4.1 The entropy condition of 1-shock . . . . .	113
A.4.1.1 First inequality . . . . .	114
A.4.1.2 Second inequality . . . . .	115
A.4.1.3 Combining first and second inequalities . . . . .	115
A.4.2 The entropy condition of 2-shock . . . . .	116
A.4.2.1 First inequality . . . . .	117
A.4.2.2 Second inequality . . . . .	118
A.4.2.3 Combining first and second inequalities . . . . .	119

# Chapter 1

## Introduction

Bone is the main component of the skeletal system. It is a light, but strong porous material that provides structure to the body and levers for locomotion. It also provides shelter to important organs such as the brain, heart and lungs, and to the production of blood cells. Bones also store vital minerals such as calcium and phosphorus [1].

### 1.1 Bone remodelling

These properties of bone are enabled in part by a continuous self-renewal process, known as ‘remodelling’. Bone remodelling is essential to maintain the integrity of bone material properties that would otherwise deteriorate with time due to fatigue loading. Remodelling repairs bone microcracks and can occur in response to changes in the ambient mechanical state of bone.

Two main phases of bone remodelling are the resorption of old bones by (active) osteoclasts and the formation of new bone by (active) osteoblasts. Bone remodelling is operated by temporary cellular structures composed of both osteoclasts and osteoblasts referred to as basic multicellular units (BMUs) [2]. Osteoclasts arise from hematopoietic stem cells (HSCs) while osteoblasts arise from mesenchymal stem cells (MCSs) [3]. The coupling between bone resorption and formation, which is believed to be administered by another cell type called osteocytes, enables the replacement of bone without change in volume [1, 4]. While osteoclasts and osteoblasts reside on the surface of bones, osteocytes instead occupy the lacunae within the bone matrix. Osteocytes communicate with themselves and with other cells through elongated cytoplasmic processes connected via gap junctions [4] (refer to Fig. 1.1).

The macroscopic structure of bone involves two main types of bone tissues: cortical bone, and trabecular bone. These tissues differ in many aspects for example porosity,

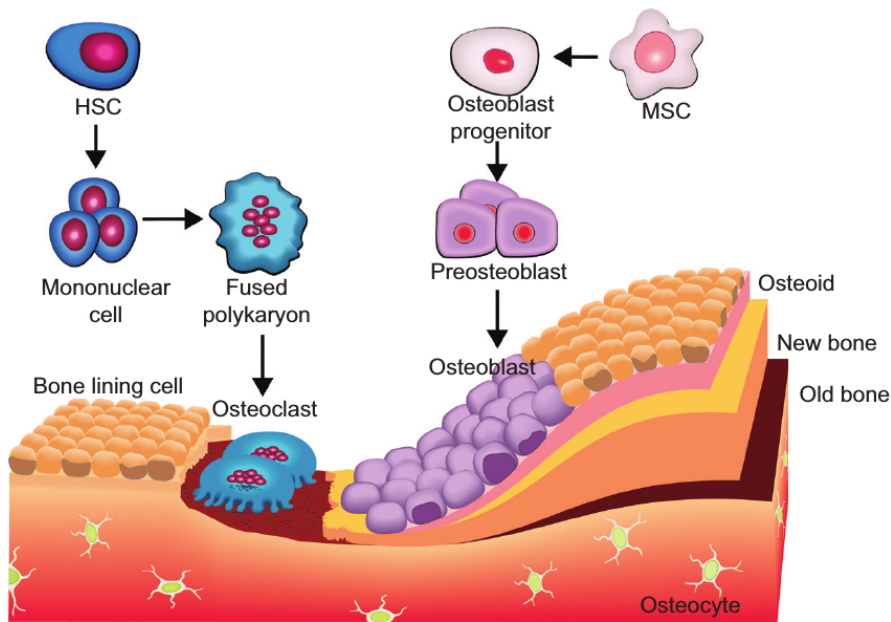


FIGURE 1.1: Development of osteoclasts and osteoblasts in BMU from hematopoietic stem cells (HSCs) and mesenchymal stem cells (MSCs), respectively (reproduced with permission from Rahman *et al.* [6]).

function, rapidity of turnover and proximity to the bone marrow [1]. Cortical bone is also called compact bone due to its low porosity. This type of bone tissue carries most of the uniaxial mechanical loads exerted on bones. Trabecular bone has a porous microarchitecture made of a meshwork of plates and struts called trabeculae. This type of bone tissue is usually encountered near articulations and often experiences changing loads coming from different directions. Both bone types undergo remodelling. In trabecular bone BMUs, osteoclasts dig a trench on the trabecular surface followed by matrix refilling by osteoblasts. In cortical bone BMUs, osteoclasts create new pores through the bone, followed by a refilling process [2, 5].

## 1.2 Factors affecting remodelling

The coordination of bone resorption and formation, which guarantees a proper balance between bone gain and loss, is known as ‘coupling’ [7]. It is affected by various factors, which can be classified as biochemical, mechanical and geometrical [8] (see flow chart in Fig. 1.2).

### 1.2.1 Biochemical regulation

Bone remodelling has long been thought to involve only the sequential roles of osteoclasts and osteoblasts. Present knowledge, however, has shown that remodelling is more complex due to multiscale involvements of systemic factors and local factors secreted by bone marrow cells and bone cells called osteocytes [9]. The systemic hormones involvement are based on global conditions of the body, while the local factors (growth factors and cytokines) act based on BMUs conditions [9]. Several computational models have been developed to incorporate the biochemical regulation of bone remodelling [3, 10–12], for example by integrating the RANK-RANKL-OPG signalling pathway into the models [13].

### 1.2.2 Mechanical regulation

One of the earliest idea of bone adaptation to mechanical loads was suggested by Roux and Wolff and is now known as Wolff’s law [14, 15]. Wolff’s law originates from the observation of arrangement of trabeculae in proximal femur and other bone parts according to the directions of principal stresses [16].

A refined theory called ‘mechanostat’ was later formalised by Frost [17]. This theory suggests that bone adapts to mechanical load (e.g. strain) through a feedback loop, operating based on the reference of the resulting stress to two setpoints or threshold values that bound the physiological window [18]. Bone subjected to loads that generate strains above the upper setpoint is classified as overused, and will receive a net bone gain. Conversely, bone subjected to loads that generate strains below the lower setpoint is called underused. This will stimulate bone loss. Loads that generate strain between these two upper and lower bounds will not create significant effect in terms of bone gain or loss [16].

There are numerous experimental works supporting the effect of mechanical loading on bone [18] for example inhibition of bone formation during space flight [19] and increase in bone mass due to exercise [20]. Several computational studies have been developed to model the mechanical regulation of bone for example in Refs. [21, 22].

### 1.2.3 Geometrical regulation

The biochemical and mechanical regulations of bone remodelling are well-established experimentally. However, studies on the geometrical regulation of bone remodelling

have been scarce, due to the experimental difficulty in disentangling the geometrical components [8]. Common geometric variables thought to regulate bone growth and remodelling are bone porosity (the volume fraction of bone not occupied by bone tissue), pore density (the number of pores per  $\text{mm}^2$ ) and the availability of bone surface to osteoclasts and osteoblasts [8, 23, 24] (see Fig. 1.2). Recent in-vitro tissue growth experiments in bioscaffolds have shown that the local curvature of a tissue substrate is also an important geometric variable controlling tissue growth, including bone formation during bone remodelling [25–39].

### 1.3 Motivation

In the in-vitro bioscaffolds experiments of Refs. [32–34, 36], it was shown that the velocity of tissue growth is proportional to the local curvature of the bioscaffolds, except at the end of the formation. This observation differs from in-vivo tetracycline double labelling experiments in which the velocity of bone growth (also called matrix apposition rate (MAR)) is inversely proportional to the mean curvature of the bone interface [40–42].

The discrepancy of the role of curvature in in-vivo and in-vitro experiments raises the question of what are the underlying mechanisms of the geometric control of bone (or tissue) growth. At the cellular/tissue scale, important geometrical variables suspected to control bone tissue growth are the local curvature of the bone surface, and bone porosity. The local curvature may influence tissue growth through the cells’ surface tension, as suggested by the patterns of alignment of stained cytoskeletal stress fibres in the in-vitro bioscaffold experiments of Refs. [32–34, 36]. The systematic influence of curvature on cell surface density and hence on tissue formation has never been quantified by past studies. This systematic curvature effect occurs due to the contraction or expansion of the local surface area during the evolution of tissue interface. Consequently, tissue formation on the concave portions of the interface causes cells and tissue crowding, resulting in the increase in cell surface density. The opposite occurs if tissue formation takes place on convex portions of the interface. Porosity may influence bone tissue growth via its effect on the extracellular fluid flow running in bone’s vascular pores and via the mechanical stimulus sensed by cells [43]. Indeed, bone porosity accounts for large proportion of the apparent stiffness of bone [44].

It is also unclear how cells sense geometrical features (curvature and porosity) that

involves spatial scales much larger than their cell bodies. Does the sensing occur individually or does it involve collective cell communication? Another interesting question is how does curvature affect the embedment of osteoblasts during their transition to osteocytes? Understanding the geometric control of the 3D distribution of osteocytes in bone is important for the regulation of remodelling and the mechanical adaptation of bone. With mathematical models, we can test the consequences of several hypotheses on the underlying mechanisms of the role of geometry during bone tissue growth to gain more insights into cellular behaviours.

## 1.4 Research aims

Bone mineralisation produces patchy bone tissues of different strength and quality depending on the frequency of bone matrix renewal. A mathematical model of mineral heterogeneity in bone depending on renewal rate was developed in Ref. [45]. In another work [46], osteocytes, which are known as the orchestrators of the bone tissue remodelling, were suggested to undergo rapid desensitisation, and replacement during remodelling. While these two studies tried to model the evolutions of bone material properties, the evolution of the bone interface, however, was assumed to be given. The main aim of this PhD is to build a comprehensive model which is able to describe the evolution of biological tissue interface at the cellular level under collective and individual geometrical controls. This model is used to investigate the following research questions:

1. What is the collective impact of the local curvature of bone (or of other tissues) on the cell surface density and hence on the rate of tissue growth? Can we reconcile the conflicting results of the in-vivo and in-vitro experiments in terms of how curvature correlates with the velocity of bone (or tissue) formation in-vivo and in-vitro?
2. What patterns of tissue deposition may result from curvature-controlled tissue growth?
3. Can we single out the collective effects of curvature to gain more insights into the control of geometry on individual cell behaviours during tissue growth, such as matrix secretory rate and cell death rate?

4. Can we develop a method to evolve curvature-controlled tissues of complex interface geometries?

## 1.5 Thesis outline

The work presented in this thesis is interdisciplinary. It combines biology, theoretical mathematics and numerical simulations. It comprises four related projects (one published, one in preparation, and two regular chapters).

The derivation of the main model equations used throughout the thesis is presented in Chapter 2. This main model is used in the other chapters, with slight modifications to suit their respective objectives. The numerical methods used to solve the equations are presented in the second half of Chapter 2.

Chapter 3 reproduces the article “Curvature effect on the collective behaviour of cells growing new tissue”, published in the *Biophysical Journal*. This work investigates the research question 1, and is marked as ① in Fig. 1.2. In Chapter 4, cell surface diffusion is assumed to be negligible, so that the equations developed in Chapter 2 form a system of hyperbolic conservation laws that is amenable to rigorous results. A theoretical analysis of this system is presented to show that shocks (or cusps) in the interface develop in finite time. This topic investigates the research question 2 and is marked as ② in Fig. 1.2. This will be followed in Chapter 5 by the study of the geometric control of individual cell behaviours on tissue growth, in particular, the interplay between curvature and porosity on cell secretory rate and cell death rate. This topic investigates the research question 3, and is marked as ③ in Fig. 1.2. In Chapter 6, the equations developed in Chapter 2 are adapted to the level set method’s viewpoint. The discretisation method and the comparison between the results obtained from this method and the ones produced in Chapter 3 are presented. Examples with topological changes in the bone geometry, which are common during bone loss and bone gain, are also shown. These examples manifest the advantage of the level set method in these situations. This topic investigates the research question 4, and is marked as ④ in Fig. 1.2.

Finally, Chapter 7 contains a general discussion, conclusions, and outlook on future works arising from the projects conducted in this PhD.

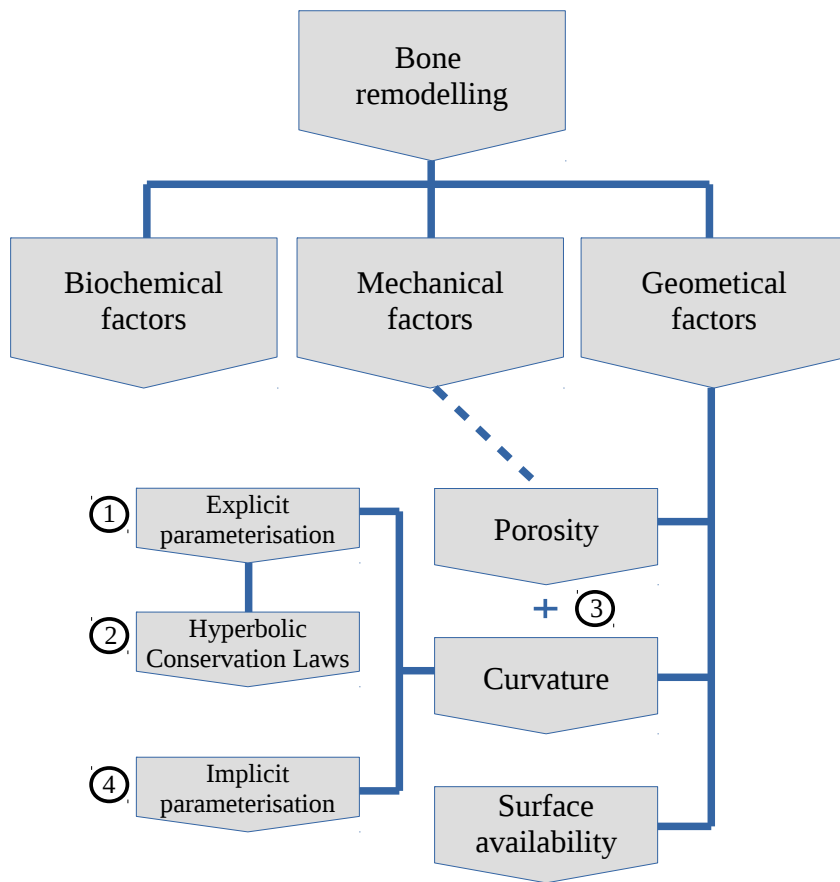


FIGURE 1.2: Biochemical, mechanical and geometrical regulations of bone remodelling. The four specific projects of this thesis are marked ① to ④. The dashed line represents the fact that mechanical feedback on bone formation occurs mainly via porosity. Bone porosity, to a large extent, explains the average strains in cortical bone [44].



## Chapter 2

# Mathematical models

This chapter provides an overview of the general approach employed by the specific mathematical models developed in more detail in the subsequent chapters. It contains two main parts, that specify two different representations of the mathematical models developed in this thesis. The first part presents the two model equations obtained when the tissue interface is parameterised explicitly and the influence of curvature and cell diffusion are included. One equation governs the evolution of the interface and the other governs the evolution of the population of bone-forming cells (osteoblasts) that secrete new tissue matrix. These equations can be specialised, for example, to Cartesian and polar coordinate systems for some interface geometries (see Sect. 3). Besides, these equations are rewritten in their equivalent conservative forms, which will later be shown to be beneficial to ensure cell conservation in the numerical methods. However, it is important to note that the derivation of these equations can be found in Chapter 3.

The second part presents the evolution equations of interface and density when the interface is described implicitly with a level set function. The advantage of this method is that it allows modelling for complex evolutions of the surface tissue topology, such as merging and splitting. Due to the coupling between the evolutions of the interface and of cell density, a level-set-like function must also be introduced for cell density. We will refer to this representation of the mathematical model as the ‘level set method’.

The models developed in this thesis are restricted to two dimensions, since they will be compared to experimental data obtained from cross-sectional slices. However, it is anticipated that a generalisation of the models to three dimensions would be straightforward to formulate using the level set method.

It is important to note that Sect. 2.1 only introduces briefly the explicit parameterisation model used in the thesis. Complete derivation of the model is presented in

Chap. 3 (reproduced from the published paper [47]). It is followed by Sect. 2.2 which presents how the explicit parameterisation model can be reformulated to derive the level set method. A detail derivation of this level set method is presented in Chap. 6.

## 2.1 Introduction to the explicit parameterisation model

We consider a biological tissue that grows from the deposition of new matrix by cells that reside at the tissue interface. This situation corresponds to new bone formation by osteoblasts in-vivo, in-vitro neo-tissue growth in bioengineering scaffolds, the growth of spheroid tumors that have proliferative outer rims, and wound healing [47]. The important elements in this derivation are the velocity of the interface, the interface's curvature, and the surface density of cells.

### 2.1.1 Interface velocity

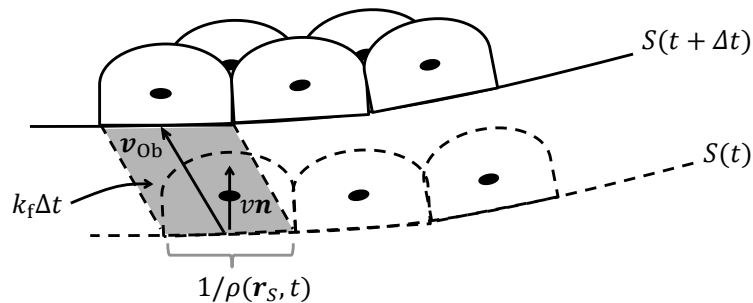


FIGURE 2.1: Derivation of the normal velocity of interface  $v = v(\mathbf{r}_S, t)$ .

The deposition of new tissue defines an evolving tissue interface  $S(t)$ . Let us denote a point on this surface by  $\mathbf{r}_S$ , and the surface density of the cells at  $\mathbf{r}_S$  by  $\rho(\mathbf{r}_S, t)$ . As depicted in Fig. 2.1, the volume of tissue matrix secreted per cell within a small time interval  $\Delta t$  is

$$k_f(\mathbf{r}_S, t)\Delta t \quad (2.1)$$

where  $k_f$  is the matrix secretory rate of a cell, i.e. the volume of new tissue secreted per cell per unit time. Since  $\rho(\mathbf{r}_S, t)$  is the cell surface density, the area occupied by a single cell is  $1/\rho(\mathbf{r}_S, t)$ . The volume of the region swept by this cell along its trajectory (shown by the darker grey shaded region) is

$$\frac{1}{\rho(\mathbf{r}_S, t)} \mathbf{v}_{\text{Ob}} \cdot \mathbf{n} \Delta t = \frac{1}{\rho(\mathbf{r}_S, t)} v \Delta t \quad (2.2)$$

where  $v = \mathbf{v}_{\text{Ob}} \cdot \mathbf{n}$  is the normal velocity of the interface. In bone biology,  $v$  is referred to as the matrix apposition rate (MAR). Here  $\mathbf{v}_{\text{Ob}}$  is the velocity of the cell, and  $\mathbf{n}$  is the outward unit normal vector of the tissue interface (see Fig. 2.1). The relationship between the normal velocity of the interface  $v$  and the cell velocity  $\mathbf{v}_{\text{Ob}}$  is due to the fact that the deposition of the new tissue matrix defines the evolving interface, and cells that secrete the tissue always reside on the interface. Equating (2.1) and (2.2) gives the normal velocity of the interface as:

$$v(\mathbf{r}_S, t) = k_f(\mathbf{r}_S, t) \rho(\mathbf{r}_S, t) \quad (2.3)$$

at any position  $\mathbf{r}_S$  of the interface  $S(t)$ . In 2D, the position  $\mathbf{r}_S$  on the interface can be parameterised by a single parameter  $s$ .

### 2.1.2 Interface evolution

The evolution of the interface parameterised by a general parameterisation  $\gamma(s, t) \in S(t)$  is constrained to evolve in such a way that the normal component of  $\gamma_t$  matches  $v$ , i.e.,

$$\gamma_t(s, t) \cdot \mathbf{n}(s, t) = v(s, t) \quad (2.4)$$

Partial derivatives are indicated by subscripts of the corresponding (italicised) variables. For example, the subscript  $t$  in Eq. (2.3) indicates the partial derivative of  $\gamma$  with respect to time  $t$ . Note that ‘f’ in  $k_f(\mathbf{r}_S, t)$  is not italicised variable, it stands for ‘formation’.

### 2.1.3 Cell surface density evolution

A number of surface-bound phenomena may occur during the evolution of bone tissue growth, such as the transport of cells along the interface and non-conservative changes in surface cell density due to cell creation or attachment to the surface, and cell depletion. These phenomena affect the surface density of cells (osteoblasts) denoted as  $\rho(\mathbf{r}_S, t)$ ,

such that the change in the density can be described, in general, by the material-balance equation [48–50]:

$$\frac{\partial}{\partial t}\rho(\mathbf{r}_S, t) = \sigma(\mathbf{r}_S, t) - \nabla \cdot \mathbf{J}(\mathbf{r}_S, t) \quad (2.5)$$

In this equation  $\sigma(\mathbf{r}_S, t)$  denotes source or sink terms that account for non-conservative mechanisms, for example cell depletion due to apoptosis and conversion to other cell types. In bone, it is known that osteoblasts are destined to be either buried to become osteocytes, to stay alive and become lining cells, or to undergo death [4]. The term  $\mathbf{J}(\mathbf{r}_S, t)$  represents the flux that corresponds to cell transport, such as advection and diffusion. Biochemical effects of hormones, growth factors and cytokines, may affect bone growth and remodelling by modifying  $\sigma$  and  $\mathbf{J}$ . Such effects will not be considered explicitly in this thesis.

#### 2.1.4 Specialisation to two-dimensional study

Since the model developed in this study is restricted to two dimensions, the interface  $S(t)$  can be tracked by a single parameter  $s$  in a general parameterisation  $\gamma(s, t)$  such that  $s \mapsto \gamma(s, t) \in S(t)$ . In this regard, the equations for the normal velocity of the interface in Eq. (2.3) and the evolution equation of the interface in Eq. (2.4) are adapted to 2D setup, giving  $v = v(s, t)$  as the normal velocity measured in mm/day,  $k_f = k_f(s, t)$  is the cell vigor measured in mm<sup>2</sup>/day,  $\rho = \rho(s, t)$  is the cell surface density measured in mm<sup>-1</sup>, and  $\mathbf{n} = \mathbf{n}(s, t)$  is the normal vector to the interface.

The derivation of the two-dimensional material-balance equation similar to Eq. (2.5) to represent the evolution of cell surface density  $\rho(s, t)$  can be found in the Section ‘Materials and Methods’ of Chapter 3. Among others, this evolution equation of cell density contains the systematic influence of curvature on the cell surface density, such that tissue formation on the concave portions of the interface causes cells and tissue crowding, resulting in the increase in cell surface density. The opposite is expected to happen when tissue formation takes place on the convex portions of the interface. Along with the evolution equation of the interface, we obtain two coupled equations:

$$\gamma_t \cdot \mathbf{n} = v \quad (2.6)$$

$$\rho_t = \frac{\gamma_t \cdot \boldsymbol{\tau}}{g} \rho_s - \rho v \kappa + D \rho_{\ell\ell} - A \rho \quad (2.7)$$

where the velocity  $v = k_f \rho$  as given in Eq. (2.3),  $g = |\gamma_s|$  is the metric associated with the parameterisation  $\gamma$ ,  $\mathbf{n}$  is the outward unit vector perpendicular to the tangential vector  $\boldsymbol{\tau} = \gamma_s/|\gamma_s|$ ,  $D$  is the diffusivity of cells along the tissue interface and  $A$  is the cell depletion rate. The operator  $\partial/\partial\ell = (1/g)\partial/\partial s$  is the partial derivative with respect to the arc length  $\ell$  which gives the one-dimensional Laplace-Beltrami operator as  $\partial^2/\partial\ell^2 = g^{-2}\partial^2/\partial s^2 - g^{-3}\boldsymbol{\tau} \cdot \gamma_{ss}\partial/\partial s$ . The RHS of Eq. (2.7) contains several elements: the transport of cells normal to the interface measured with respect to the coordinate  $s$ , the systematic dilution or concentration of cell density induced by the (signed) curvature of the interface, the diffusion of cells parallel to the interface, and the cell depletion.

The derivation of evolution equations similar to Eq. (2.7) in higher dimension was done in Stone [51] such that the evolution equation of so called ‘surfactant density’  $\Gamma$  under the influence of arbitrary velocity  $\mathbf{u}$  on a deforming interface can be written as:

$$\Gamma_t = -\nabla_\ell \cdot (\Gamma \mathbf{u}_\ell) - \Gamma(\nabla_\ell \cdot \mathbf{n})(\mathbf{u} \cdot \mathbf{n}) + D\nabla_\ell^2 \Gamma \quad (2.8)$$

where  $\mathbf{u}_\ell = (\mathbb{1} - \mathbf{n}\mathbf{n}^\top)\mathbf{u}$  and  $\nabla_\ell = (\mathbb{1} - \mathbf{n}\mathbf{n}^\top)\nabla$  are the velocity and gradient projected onto the interface  $S(t)$ , respectively. Note that  $(\mathbb{1} - \mathbf{n}\mathbf{n}^\top)$  is a projection operator perpendicular to the normal vector  $\mathbf{n}$ . In two dimensions,  $(\mathbb{1} - \mathbf{n}\mathbf{n}^\top)$  corresponds to taking the scalar product with the unit tangent vector to the interface  $\boldsymbol{\tau}$ , so that  $\nabla_\ell = (\boldsymbol{\tau} \cdot \nabla)\boldsymbol{\tau} = \boldsymbol{\tau} \frac{\partial}{\partial\ell}$ . This makes the first term in the RHS of Eq. (2.8) to become  $\nabla_\ell \cdot (\Gamma \mathbf{u}_\ell) = \boldsymbol{\tau} \frac{\partial}{\partial\ell} \cdot (\Gamma \frac{\partial \mathbf{u}}{\partial\ell}) = \frac{\boldsymbol{\tau} \cdot \gamma_t}{g} \Gamma_s$ . The second term in the RHS of Eq. (2.8) is the same as the second term in the RHS of Eq. (2.7) since  $\nabla_\ell \cdot \mathbf{n}$  is equal to the (mean) curvature  $\kappa$  in the two-dimensional interface, and  $\mathbf{u} \cdot \mathbf{n}$  is equal to the normal velocity  $v$ . The third term in both equations corresponds to each other since  $\nabla_\ell^2 \Gamma = (\boldsymbol{\tau} \frac{\partial}{\partial\ell} \cdot \boldsymbol{\tau} \frac{\partial}{\partial\ell}) \Gamma = (\frac{\partial}{\partial\ell} \frac{\partial}{\partial\ell} (\boldsymbol{\tau} \cdot \boldsymbol{\tau})) \Gamma = \Gamma_{\ell\ell}$ .

Depending on the surface geometry of bone or of an other tissue substrate, the model equations can be applied to two common types of parameterisation, the Cartesian and polar coordinate systems. This is done by taking  $\gamma(x, t) = (x, h(x, t))$  for the former and  $\gamma(\theta, t) = (R(\theta, t) \cos \theta, R(\theta, t) \sin \theta)$  for the latter. Tissue deposition in trench-like cavities of zero average curvature is represented by an evolving height  $y = h(x, t)$  in the Cartesian system, while tissue deposition in porous channels is represented by an evolving radius  $r = R(\theta, t)$  in the polar system.

Our simulations show that using finite difference method to numerically solve these equations results in significant amount of numerical loss of cells when cell diffusion is low. To minimise this issue, we rewrite the equations in their equivalent conservative form, and solve the equations using a finite volume scheme (see Chapter 3).

## 2.2 Derivation of the implicit parameterisation (level set) method

Abrupt topological changes in bone are common, for example, during enlargement and fusion of trabecular struts during bone gain, and trabecularisation of cortical bone or loss of connectivity of trabecular bone during age-related osteoporosis [52–55] (refer to Fig. 2.2). These topological changes require ad-hoc treatment of numerical simulations of the evolution of the bone interface, as the interface can no longer be continuously parameterised by a single function  $\gamma$  in the previous section [56].

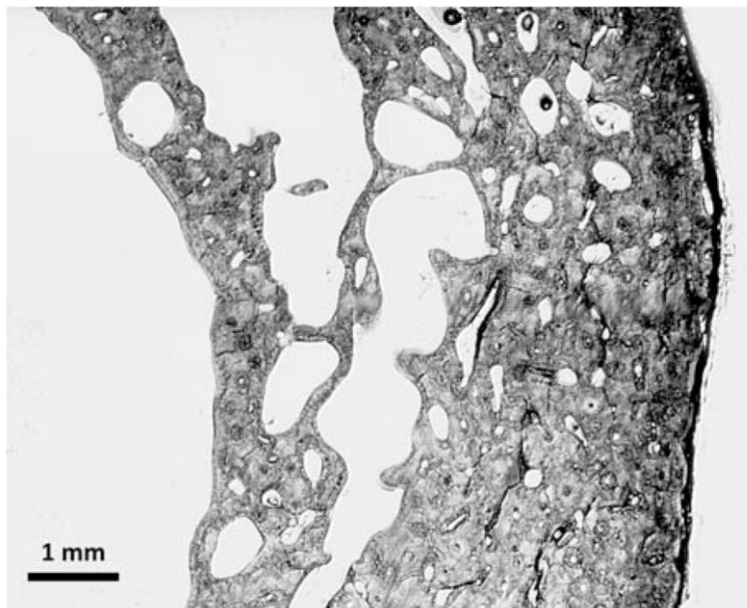


FIGURE 2.2: Structure of cortical bone during trabecularisation due to osteoporosis (reproduced with permission from Osterhoff *et al.* [52]).

---

A well-known method to alleviate this problem is the level set method introduced in Ref. [57]. In this method, the interface is positioned at the zero level set (or contour) of an evolving function, called the level set function  $\phi$ . This does not require the interface to be parameterised explicitly since the interface moves by the temporal changes of the level set function. It is anticipated that this method will provide an easier generalisation

to three dimensions, where the explicit interface parameterisation is more difficult to implement.

We show in this section the derivation of the evolution equations for the implicit parameterisation (level set) method. While the explicit parameterisation equations are used in Chapters 3, 4 and 5, the equations from this section are used only in Chapter 6 of this thesis.

### 2.2.1 Evolution equation of the interface

In the level set method, the 2D tissue interface  $S(t)$  previously parameterised as  $s \mapsto \gamma(s, t)$  can be described as the zero level set (or contour) of a function  $\phi$  in the 3D Cartesian coordinate system such that:

$$S(t) = \{(x, y) | \phi(x, y, t) = 0\} \quad (2.9)$$

Since  $\gamma(s, t) \in S(t)$  and  $\phi(\gamma(s, t)) = 0$ , differentiating  $\phi$  with respect to time  $t$  gives  $\phi_t + \nabla\phi \cdot \gamma_t = 0$ . Using the fact that the normal vector of a level set function is  $\mathbf{n} = \nabla\phi/|\nabla\phi|$  and utilising  $\gamma_t \cdot \mathbf{n} = v$  from Eq. (2.6), we obtain the standard level set equation [58]:

$$\phi_t + V|\nabla\phi| = 0 \quad (2.10)$$

where  $V$  is the normal velocity of the level set function  $\phi$  that coincides with  $v(s, t)$  at the interface point  $\gamma(s, t)$ .

### 2.2.2 Evolution equation of velocity

Now that the interface is described implicitly, an alternative description of cell surface density that does not refer to the explicit parameter  $s$  is also required. To this purpose, the cell surface density  $\rho(s, t)$  in Eq. (2.7) is extended to the whole computational domain where  $\phi$  is defined, rather than being only defined on the interface. In this regard, we define a velocity function  $V$ , such that its value at point  $\gamma(s, t)$  of the interface is  $v(s, t) = k_f\rho(s, t)$ , i.e.:

$$V(\gamma(s, t), t) = v(s, t) \quad (2.11)$$

Similarly to the case of  $\phi$ , differentiating Eq. (2.11) with respect to  $t$  gives  $V_t + \nabla V \cdot \boldsymbol{\gamma}_t = v_t$ , while from (2.3), the time derivative of the velocity is  $v_t = k_f \rho_t$ . Here cell vigor  $k_f$  is assumed to not depend on  $t$  for simplicity, whereas  $\rho_t$  is a known quantity governed by Eq. (2.7). Since the interface moves with the normal velocity only (i.e. the tangential component is irrelevant for the interface evolution), we take  $\boldsymbol{\gamma}_t = v \mathbf{n}$ , and by rewriting  $V = v$ , we obtain

$$V_t + \nabla V \cdot V \mathbf{n} = v_t = -\kappa V^2 + D \nabla_\ell^2 V - AV \quad (2.12)$$

Here, cell diffusion is assumed to be isotropic along  $S(t)$  and the surface Laplacian (also called ‘Laplace-Beltrami’) term is defined as  $\nabla_\ell^2 V = \nabla^2 V - \kappa \partial_n V - \partial_{nn} V$ , where  $\partial_n V = \partial V / \partial n = \mathbf{n} \cdot \nabla V$  and  $\partial_{nn} V = \partial^2 V / \partial n^2 = \mathbf{n} \cdot \mathbf{H}(V) \cdot \mathbf{n}$  [59]. Eqs. (2.10) and (2.12) are a coupled, nonlinear system of PDEs which govern the evolutions of the interface and its velocity (or density, since  $V = k_f \rho$  in (2.3)). Note the similarity between Eq. (2.12) and Eq. (2.8).

## 2.3 Numerical methods

The explicit parameterisation equations in Sect. 2.1 are discretised using finite difference and finite volume methods. These two methods are used to ensure conservation of cell number, while at the same time avoiding restrictive CFL conditions. Details on the numerical schemes for the explicit parameterisation equations are given in Sect. 3.3.

The implicit parameterisation (level set) equations are solved using a finite difference method. The sequence of steps to implement the numerical schemes are given in Sect. 6.3.2. There are other studies, for example in Ref. [60], which utilise finite element schemes to solve these kinds of implicit parameterisation equations.

## Chapter 3

# Paper 1: Modelling the effect of curvature on the collective behaviour of cells growing new tissue

### 3.1 Overview

The systematic influence of curvature on cell surface density occurs due to the contraction or expansion of the local surface area during the evolution of tissue interface. Tissue formation on the concave portions of the interface causes cells and tissue crowding, resulting in the increase in cell surface density. The opposite occurs if tissue formation takes place on convex portions of the interface.

In this chapter, we include this systematic influence of curvature on cell density and compare numerical simulations with results from bioscaffolds experiments conducted in Refs. [32, 33] which show tissue deposition slowdown and regularisation (or smoothing) of tissue interface regardless of the initial shape of the bioscaffolds.

A good match with experimental evolutions of tissue growth can be obtained when cell surface diffusion and cell depletion are accounted for. We thereby produce estimates of two parameters: cell surface diffusivity  $D$  and cell depletion rate  $A$ .

This work covers research question 1, marked as ① in Fig. 1.2. It has been published in Biophysical Journal and is reproduced below. The supplementary material of the paper is also enclosed in this chapter. The final section of this chapter contains detailed numerical techniques used to produce the results of the paper.

### 3.2 PDF of paper

# Modeling the Effect of Curvature on the Collective Behavior of Cells Growing New Tissue

Mohd Almie Alias<sup>1,2,\*</sup> and Pascal R. Buenzli<sup>1</sup>

<sup>1</sup>School of Mathematical Sciences, Monash University, Clayton VIC, Australia; and <sup>2</sup>School of Mathematical Sciences, National University of Malaysia, Bangi, Selangor D. Ehsan, Malaysia

**ABSTRACT** The growth of several biological tissues is known to be controlled in part by local geometrical features, such as the curvature of the tissue interface. This control leads to changes in tissue shape that in turn can affect the tissue's evolution. Understanding the cellular basis of this control is highly significant for bioscaffold tissue engineering, the evolution of bone microarchitecture, wound healing, and tumor growth. Although previous models have proposed geometrical relationships between tissue growth and curvature, the role of cell density and cell vigor remains poorly understood. We propose a cell-based mathematical model of tissue growth to investigate the systematic influence of curvature on the collective crowding or spreading of tissue-synthesizing cells induced by changes in local tissue surface area during the motion of the interface. Depending on the strength of diffusive damping, the model exhibits complex growth patterns such as undulating motion, efficient smoothing of irregularities, and the generation of cusps. We compare this model with *in vitro* experiments of tissue deposition in bioscaffolds of different geometries. By including the depletion of active cells, the model is able to capture both smoothing of initial substrate geometry and tissue deposition slowdown as observed experimentally.

## INTRODUCTION

Substrate geometry is an influential variable for new tissue growth with high significance for bioscaffold tissue engineering (1). Surface curvature (2,3) and roughness (4,5) have important effects on cell behavior in addition to the surface's chemical composition (6–9) and rigidity (10,11). At a single cell scale, tissue geometry affects the formation of focal adhesions on the cell membrane, resulting in differences in cell orientation, motility, shape, phenotype, and apoptosis due to biochemical and mechanical effects (12–18).

Larger geometrical features of substrates, that span multiple cell sizes, also influence tissue growth because they affect the collective behavior of cell populations. Direct and indirect (e.g., mechanics-mediated) effects of tissue geometry on tissue growth are expected to play an important role in bone, tissue engineering, wound healing (19,20) and in tumor growth (21). Neotissue secreted by preosteoblasts cultured on porous scaffolds of various shapes grows at a rate that correlates with the local mean curvature (22–31). Such mean curvature flow leads to smoothing of the initial substrate geometry (32,33). New bone deposition

*in vivo* occurs at different rates in compact cortical bone and porous trabecular bone, suggested to be due to the different substrate geometries in these tissues (34). In contrast to *in vitro* tissue growth, cylindrical cavities in cortical bone infill at rates that correlate with the inverse mean curvature, i.e., tissue deposition slows down as infilling proceeds (35–38). At the same time, irregularities of the initial substrate smooth out with tissue deposition: Haversian canals are more regular than osteon boundaries (39).

These conflicting observations on the role of geometry in tissue growth may be reconciled if one takes into consideration the cellular basis of new tissue deposition, in particular cell density and cell vigor (new tissue synthesis rate) (40), and the various biological and geometrical influences that these variables are subjected to. A decrease in active cell number, due for example to quiescence, cell death, or detachment from the tissue surface (41), could explain tissue deposition slowdown. At the same time, local inhomogeneities in cell density and in cell vigor could explain smoothing of corners and irregularities.

Previous mathematical models of the evolution of the tissue interface have proposed to capture the smoothing dynamics of *in vitro* tissue growth through a simple mathematical relation between interface velocity and mean curvature by comparing cell tension with surface tension problems in physics (23,25–27,30,31). However, these geometric models

Submitted September 23, 2016, and accepted for publication November 28, 2016.

\*Correspondence: [REDACTED]

Editor: Leah Edelstein-Keshet.

<http://dx.doi.org/10.1016/j.bpj.2016.11.3203>

© 2017 Biophysical Society.



do not account for cell numbers, which limits the interpretation of underlying biological processes. Part of the tissue growth slowdown observed in vitro in two-dimensional cross sections has been tentatively explained by scaffold boundary effects leading to a catenoid tissue surface of smaller mean curvature than a cylindrical surface (26,27). The influence of cellular processes (such as a reduction in active cells or in cell vigor) cannot be factored in easily into these geometric models. In cortical bone formation in vivo, tissue surface is mostly cylindrical or conical and has moving boundaries (42,43). A slowdown of tissue deposition due to cellular processes rather than three-dimensional geometrical effects is more likely. Both surface cell density and cell vigor decrease during cortical infilling (40,44,45).

In this article, we develop a mathematical model of the effect of local curvature on the collective behavior of cells synthesizing new tissue at the tissue interface. We compare numerical simulations of the model with tissue growth dynamics in bioscaffolds of different pores shapes obtained in Bidan et al. (25,26). This comparison suggests that a reduction in the number of active cells is a likely explanation for tissue deposition slowdown observed in these experiments.

The main purpose of the mathematical model is to determine the systematic influence of curvature on cell density due to the contraction or expansion of the local surface area during the evolution of the tissue interface. This influence is an inevitable geometrical pull: the deposition of new tissue on concave regions of the substrate reduces the local surface area, and so tends to increase surface cell density and to crowd tissue; the deposition of new tissue on convex regions of the substrate increases the local surface area, and so tends to decrease surface cell density and to spread tissue (Fig. 1 a). This systematic influence of curvature is important to elucidate and to single out, so that other geometrical influences on tissue growth can be determined, such as influences on individual cell vigor.

## MATERIALS AND METHODS

We consider a biological tissue that grows by deposition of new matrix secreted by cells at the tissue surface (Fig. 1 a). This situation corresponds

to new bone formation by osteoblasts in vivo, but also models in vitro neo-tissue growth in bioengineering scaffolds (23,25–27,30,31) where new tissue is predominantly produced near the tissue surface (46). It may also describe the growth of spheroid tumors that have proliferative outer rims (21), and wound healing (19). The normal velocity of the tissue surface is given by

$$v = k_t \rho, \quad (1)$$

where  $\rho$  is the surface density of tissue-synthesizing cells (number of cells per unit surface), and  $k_t$  is the cells' secretory rate (volume of new tissue formed per cell per unit time) (47). We assume here that tissue secretion is such that it displaces the cells perpendicularly to the surface at all times, i.e., cells are advected with velocity  $\mathbf{v} = v\mathbf{n}$ , where  $\mathbf{n}$  is the outward unit normal vector of the tissue surface.

We restrict in this article to two spatial dimensions as we will compare our model to experimental data obtained from cross-sectional slices. We track the evolution of the tissue interface  $S(t)$  by an explicit one-dimensional parameterization  $s \mapsto \boldsymbol{\gamma}(s, t)$  of  $S(t)$ . Because the normal velocity of the tissue interface is given by  $v$  in Eq. 1,  $\boldsymbol{\gamma}$  must be such that the normal component of  $\boldsymbol{\gamma}_t$  matches  $v$ , i.e.,

$$\boldsymbol{\gamma}_t \cdot \mathbf{n} = v, \quad (2)$$

where  $\mathbf{n}$  is the outward unit vector perpendicular to the tangential vector  $\boldsymbol{\tau} = \boldsymbol{\gamma}_s / |\boldsymbol{\gamma}_s|$  (Fig. 1 b). (Partial derivatives are denoted by subscripts throughout the article.) Because tissue geometry is unaffected by tangential components of interface velocity, Eq. 2 is the only constraint that  $\boldsymbol{\gamma}$  must satisfy. In particular, we do not assume that the paths  $t \mapsto \boldsymbol{\gamma}(s, t)$  follow cell trajectories normal to  $S(t)$  at each time. Later,  $\boldsymbol{\gamma}$  will be represented by tissue thickness functions in Cartesian and polar coordinates for which the tangential component  $\boldsymbol{\gamma}_t \cdot \boldsymbol{\tau} \neq 0$ .

On concave portions of the tissue substrate, new tissue deposition reduces the local surface area and thereby tends to increase cell density. By Eq. 1, this leads to crowding of new tissue produced. On convex portions of the tissue substrate, new tissue deposition increases the local surface area and thereby tends to decrease cell density (Fig. 1 a). This leads to dispersion of new tissue produced. To describe this influence of local curvature on the evolution of cell density and tissue growth rate, we write  $\rho$  at coordinate  $s$  of the surface and time  $t$  as

$$\rho(s, t) = \frac{\delta N(s, t)}{\delta \ell(s, t)}, \quad (3)$$

where  $\delta N$  is the number of cells residing on an infinitesimal length element  $\delta \ell = g ds$  centered at  $s$ , and  $g = |\boldsymbol{\gamma}_s|$  is the metric associated with  $\boldsymbol{\gamma}$  (48).

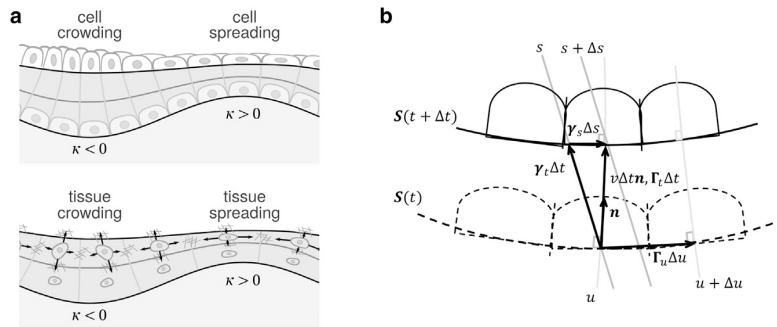


FIGURE 1 (a) Cells lining a tissue surface such as bone-forming osteoblasts will concentrate or spread during the evolution of the interface depending on whether the initial substrate is concave ( $\kappa < 0$ ) or convex ( $\kappa > 0$ ) (top). In a similar way, cellular and extracellular tissue volume produced near the tissue surface will crowd or spread depending on the substrate curvature (bottom). In both cases, this influences the local tissue growth rate. (b) Schematic diagram depicting the representation of the tissue surface  $S(t)$  by an arbitrary parameterization  $\boldsymbol{\gamma}(s, t)$  and by an orthogonal parameterization  $\boldsymbol{\Gamma}(u, t)$ . Timelines of  $\boldsymbol{\Gamma}(u, t)$  follow the cell's trajectories assumed normal to  $S(t)$  at all times.

We then determine changes in cell density along the normal trajectories taken by the cells. The rate of change in  $\rho$  in the normal direction is given by

$$D_t^\perp \rho \equiv \lim_{\Delta t \rightarrow 0} \frac{1}{\Delta t} [\rho(s + \Delta s, t + \Delta t) - \rho(s, t)] \\ = \rho_t - \frac{\boldsymbol{\gamma}_t \cdot \boldsymbol{\tau}}{g} \rho_s, \quad (4)$$

where the  $s$ -coordinate offset  $\Delta s$  is due to the fact that timelines  $t \rightarrow \boldsymbol{\gamma}(s, t)$  at fixed  $s$  are not normal to  $S(t)$  in general. This offset is defined such that  $v \Delta \mathbf{m} = \boldsymbol{\gamma}_t \Delta t + \boldsymbol{\gamma}_s \Delta s$  as  $\Delta t \rightarrow 0$  (Fig. 1 *b*). Projecting onto the tangential vector  $\boldsymbol{\tau}$  shows that  $\lim_{\Delta t \rightarrow 0} \Delta s / \Delta t = -(\boldsymbol{\gamma}_t \cdot \boldsymbol{\tau}) / g$ , which is used for the second equality in Eq. 4. The differential operator  $D_t^\perp$  corresponds here to the substantial derivative that follows the advective velocity  $v\mathbf{n}$ . This operator obeys standard differentiation rules such that with Eq. 3, one has

$$D_t^\perp \rho = \frac{D_t^\perp \delta N}{\delta \ell} - \rho \frac{D_t^\perp \delta \ell}{\delta \ell}. \quad (5)$$

The second term in the right-hand side of Eq. 5 represents a geometric contribution to density changes due to changes in the local length of the surface  $\delta \ell$  induced by the surface's evolution. This contribution is related to the tissue substrate curvature  $\kappa(s, t)$  by

$$\frac{D_t^\perp \delta \ell}{\delta \ell} = v\kappa \quad (6)$$

(see [Evolution of the Local Surface Stretch](#), Appendix A). We use the convention that  $\kappa < 0$  on concave portions of the substrate and  $\kappa > 0$  on convex portions of the substrate. The first term in the right-hand side of Eq. 5 represents a contribution to density changes due to changes in the number of cells  $\delta N$  populating the length element  $\delta \ell$ . These changes may occur by nonconservative and conservative processes, such as cell creation, cell elimination, and cell transport along the surface. We assume here that  $\delta N$  changes due to cells being eliminated from the active pool at rate  $A$  (probability per unit time) and diffusing along the bone surface with constant diffusivity  $D$ , giving

$$\frac{D_t^\perp \delta N}{\delta \ell} = D \rho_{\ell\ell} - A \rho, \quad (7)$$

where  $\partial / \partial \ell = (1/g) \partial / \partial s$  is the partial derivative with respect to the arc length  $\ell$ , and  $(\partial^2 / \partial \ell^2) = g^{-2} (\partial^2 / \partial s^2) - g^{-3} \boldsymbol{\tau} \cdot \boldsymbol{\gamma}_{ss} (\partial / \partial s)$  is the one-dimensional Laplace-Beltrami operator (49). Combining Eqs. 4–7, the evolution of cell density is governed by

$$\rho_t = \frac{\boldsymbol{\gamma}_t \cdot \boldsymbol{\tau}}{g} \rho_s - \rho v \kappa + D \rho_{\ell\ell} - A \rho. \quad (8)$$

The first term in the right-hand side of Eq. 8 depends on the choice of parameterization  $\boldsymbol{\gamma}$ . It describes the transport of cells normal to the interface measured with respect to the coordinate  $s$ . It is absent if  $\boldsymbol{\gamma}$  is chosen to be an orthogonal parameterization, defined such that  $\boldsymbol{\gamma}_t \cdot \boldsymbol{\gamma}_s = 0$ . The second term represents the systematic dilution or concentration of cell density induced by the (signed) curvature of the interface. The third and fourth terms describe the diffusion of cells parallel to the interface, and the cell depletion rate, respectively.

Equation 8 is coupled to the evolution of the tissue surface  $S(t)$  via Eqs. 1 and 2. Notice that because  $\rho$  is proportional to the normal velocity of  $S(t)$ , the contribution  $-\rho v \kappa = -k_t \rho^2 \kappa$  to  $\rho_t$  in Eq. 8 implies that the normal acceleration of the surface depends linearly on curvature, which constitutes a type of hyperbolic curvature flow (50). This is to be contrasted with mean curvature flow in which the normal velocity depends linearly on curvature

(32,51). The nonlinearity of the equations and their hyperbolic character suggest that shocks may develop, e.g., as cusps in the interface  $S(t)$ . This situation requires to seek weak solutions, such as entropic solutions found by adding infinitesimal diffusion of the interface, or equivalently, by devising diffusive (e.g., upwind) numerical schemes (33,52–54). In our case, a physiologically relevant weak solution additionally requires that cell densities remain finite at developing cusps of the interface. This is ensured by the explicit inclusion of cell diffusion along the interface. We note here that radii of curvature  $1/\kappa$  of the order of a single cell size ( $\approx 20$ – $30 \mu\text{m}$ ) may be considered cusps already within the continuum model. However, weak, entropic solutions provide a physically consistent extension of the continuum model below such radii of curvature.

In summary, the systematic effect of curvature onto cell density is expected to help smooth substrate irregularities by generating a curvature-dependent normal acceleration, while active cell depletion is expected to capture tissue deposition slowdown.

## Scaling analysis and choice of units

The mathematical model involves five generic parameters: a characteristic length scale of the initial substrate geometry  $\boldsymbol{\gamma}(s, 0)$  (e.g., a radius of curvature  $R_0$ ); a characteristic value  $\rho_0$  of the initial cell density  $\rho(s, 0)$ ; a characteristic value  $k_t^0$  of the secretory rate  $k_t(s, t)$ ; the diffusivity  $D$ ; and the cell depletion rate  $A$ . Through a scaling analysis in which cell density, space, and time are rescaled, it is possible to show that only two of these five parameters are independent. We choose these parameters to be the diffusivity  $D$  and the cell elimination rate  $A$  without restriction of generality. We can thus fix arbitrarily the length scale of the initial substrate, the parameter  $\rho_0$ , and the parameter  $k_t^0$ , and explore the qualitative behaviors of the solutions by modifying only  $A$  and  $D$ .

In [Application to Bioscaffold Tissue Growth](#), the length scale will be set to match the physical size of the experimental initial substrates (in millimeters), and the product  $v_0 = k_t^0 \rho_0$  will be set to match the experimental initial normal velocity (in mm/day). This ensures that  $D$  (in  $\text{mm}^2/\text{day}$ ) and  $A$  (in  $\text{day}^{-1}$ ) have proper physical dimensions. While the normal velocity is easily deduced experimentally, cell density (in  $\text{mm}^{-2}$ ) and secretory rate (in  $\text{mm}^3/\text{day}$ ) are difficult to estimate, and they are usually not measured. In bone in vivo, the density of osteoblasts ranges from  $\sim 2000$ – $10,000 \text{ mm}^{-2}$  (see Buenzli et al. (40) and references cited therein). In the in vitro bioscaffold tissue growth experiments of Rumpel et al. (23) and Bidan et al. (25,26), the seeding density is  $800$ – $1000 \text{ mm}^{-2}$ , but the initial confluent density at the onset of formation is not known. The evolution of the tissue interface does not actually depend on the relative proportion of cell density and secretory rate in  $v$  in Eq. 1. For ease of interpretation, we will thus choose in the remainder of the article units in which  $k_t^0 = 1$  is dimensionless, so that  $\rho$  corresponds to  $v$  (in mm/day) by Eq. 1. This is equivalent to first considering the scaled density  $\bar{\rho} \equiv k_t^0 \rho$  and scaled secretory rate  $\bar{k}_t^0 \equiv k_t^0 / k_t^0$ , where  $k_t^0$  has units, and then dropping the bars from the notation. This scaling only affects the units of  $\rho$  and  $k_t$ .

## Conservative form and total cell number

Numerical simulations of direct discretizations of Eq. 8 using finite difference upwind schemes were found to induce significant numerical nonconservation of the total number of cells at low diffusivities  $D$ , due to developing cusps in the interface. For these situations, the equations were first rewritten in conservative form, and then discretized using finite volume conservative numerical schemes (see below).

The conservative form of Eq. 8 is found for a general parameterization  $\boldsymbol{\gamma}$  by considering the projected density of cells on the  $s$  coordinate,  $\eta(s, t)$ , defined such that  $\delta N = \eta ds$  is the number of cells on the interface between the coordinates  $s$  and  $s + ds$ . Because  $\delta N = \rho \delta \ell = \rho g ds$ , one has  $\eta(s, t) = \rho(s, t) g(s, t)$ . It is shown in [Conservative Form of the Governing Equations](#) (see Appendix A) that

$$\eta_t + \left[ -\frac{\eta}{g}(\boldsymbol{\gamma}_t \cdot \boldsymbol{\tau}) - \frac{D}{g} \left( \frac{\eta}{g} \right)_{s,s} \right] = -A\eta. \quad (9)$$

Equation 9 is a conservation law that expresses the balance of cells between  $s$  and  $s + ds$  during the evolution. For periodic or no-flux boundary conditions, the total number of cells on the whole interface  $N(t) \equiv \int_a^b ds \eta(s,t)$  evolves as

$$\frac{dN}{dt} = \int_a^b ds \eta_t = - \int_a^b ds A\eta, \quad (10)$$

because the contribution to the integral of the flux term of Eq. 9 is zero. If the cell elimination rate  $A$  is homogeneous,  $N(t) = N_0 \exp(-\int_0^t dt A)$ , as expected.

### Numerical discretization

At high cell diffusivity, we used a straightforward semi-implicit finite difference discretization of the equations for  $\rho$  and  $\gamma$ . First-order and second-order spatial derivatives were discretized using upwind and central differencing, respectively. Advective and reaction terms were solved explicitly with forward Euler discretization in time, while diffusive terms were solved implicitly with backward discretization.

At low cell diffusivity, this finite difference scheme led to numerical nonconservation of cells requiring finer space grid resolution. To prevent the numerical nonconservation of cells, we discretized the conservative form of the equations with the finite volume method instead (53). We implemented the semidiscrete Kurganov-Tadmor scheme (55) with a fully explicit forward Euler discretization in time.

Both numerical schemes give indistinguishable results in a range of intermediate diffusivities. The maximum numerical error on cell number recorded in all our simulations was 3% (triangular pore,  $D = 0.005$ ). All other simulations had <1% cell number error. More details on these numerical schemes can be found in the [Supporting Material](#).

## RESULTS

During bone remodeling, new bone formation occurs on various types of bone interface topologies. In porous, meshed trabecular bone, new bone tissue is deposited on the floor of trenchlike cavities of zero average curvature

carved out of single struts. In dense cortical bone, new bone tissue is deposited on the walls of porous channels (34). Neotissue deposition in porous bioscaffolds has also been investigated on trenchlike cavities or within channels of various cross-sectional shapes (23,25–27).

We apply our mathematical model to these two classes of surface topologies by parameterizing  $S(t)$  with thickness functions in Cartesian or polar coordinates, respectively. Tissue deposition in trenchlike cavities of zero average curvature is represented by an evolving height  $y = h(x,t)$  with periodic boundary conditions. Tissue deposition in porous channels is represented by an evolving radius  $r = R(\theta,t)$ . Both  $h(x,t)$  and  $R(\theta,t)$  represent the local thickness of newly deposited tissue material at constant value of the parameter  $s = x$  in Cartesian coordinates,  $s = \theta$  in polar coordinates. The governing equations for  $\gamma$  and  $\rho$  (or  $\eta$ ) are specialized to these nonorthogonal parameterizations of  $S(t)$  ([Appendix A](#)), discretized, and solved numerically ([Supporting Material](#)).

### Influence of cell diffusion on interface smoothing

We start by investigating the smoothing of an initially rugged substrate due to the volumetric crowding of tissue modeled by the hyperbolic curvature flow proposed in this article. We first assume that cells are not eliminated, i.e.,  $A = 0$ , and that they produce new tissue at a constant rate  $k_f = k_f^0 = 1$  (dimensionless, so that  $\rho$  corresponds to  $v$  by Eq. 1; see [Materials and Methods](#)). Because interface smoothing can be expected to depend significantly on the amount of cell diffusion parallel to the interface (56), we performed simulations using a range of diffusivities  $D$  both in trenchlike cavities and in porous channels.

[Fig. 2](#) shows the evolution of a trenchlike initial interface with a rugosity modeled by cosine oscillations:

$$h(x,0) = 2 + \frac{1}{2} \cos(3x), \quad (11)$$

$$x \in [0, 2\pi).$$

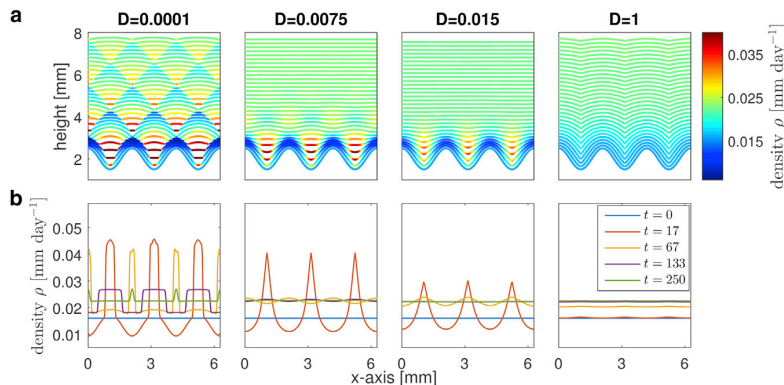


**FIGURE 2** Tissue deposition on a cosine initial substrate for a range of low to high diffusivities ( $D = 0.0001, 0.0075, 0.015, 1 \text{ mm}^2/\text{day}$ ). (a) Evolution of the tissue interface. Each line corresponds to the interface  $h(x,t)$  at regular time intervals  $\Delta t = 8.33$  days, and is colored according to cell density. (b) Cell density profiles at specific times. Simulations performed with  $A = 0$ ,  $k_f^0 = 1$ , and  $\rho_0 = 0.016 \text{ mm/day}$ . To see this figure in color, go online.

The surface is initially seeded with a homogenous cell density  $\rho(x, 0) = \rho_0 = 0.016$  mm/day (this value is calibrated from the pore scaffold tissue growth experiments of Bidan et al. (25); see [Application to Bioscaffold Tissue Growth](#)). The evolution is shown for different cell diffusivities  $D$ . Colored lines in [Fig. 2 a](#) represent the interface  $h(x, t)$  at regular time intervals  $\Delta t = 8.33$  days starting from  $t = 0$ . These interfaces are colored by the corresponding cell density  $\rho(x, t)$ . Plots of cell densities are also shown at specific times in [Fig. 2 b](#).

At low diffusivity ( $D = 0.0001$  mm<sup>2</sup>/day), concave portions of the interface rapidly concentrate cells (*red*), which increases the local propagation speed, while convex portions of the interface disperse cells (*dark blue*), which decreases the local propagation speed. The stark contrast in local propagation speed generates cusps in the interface, which propagate sideways as shock waves between the concave and convex regions. These shock waves collide and bounce off each other, resulting in an oscillatory spatio-temporal pattern whereby concave portions of the interface become convex, and convex regions of the interface become concave, repetitively. With increasing diffusivity, cusps in the interface smooth out and this oscillatory pattern dampens more rapidly ( $D = 0.0075$  mm<sup>2</sup>/day). At  $D = 0.015$  mm<sup>2</sup>/day, the interface smoothens to a flat interface without oscillatory pattern the quickest (see below). At large diffusivities ( $D \geq 1$  mm<sup>2</sup>/day), cell concentration and dispersion effects are entirely overridden by the diffusive redistribution of cells, resulting in nearly homogeneous cell densities throughout the simulation. The interface evolves by constant offsets in the normal directions. The size of these offsets increases with time because the total length of the interface decreases and therefore, the overall cell density increases. This kind of evolution by normal offsets is well known to create cusps in the interface within a finite range. For constant normal velocity, these cusps disappear at rate  $O(t^{-1})$  as  $t \rightarrow \infty$  (57). A faster rate of cusp disappearance occurs in our case as normal velocity is linked to total interface length.

It is clear from [Fig. 2](#) that the diffusivity  $D$  drives strong qualitative changes in the evolution of the interface, which influence in particular the rate of interface smoothing. The interface's total length  $L(t) = \int_0^{2\pi} dx g(x, t)$  in [Fig. 3](#) converges to the minimum length  $2\pi$  (flat interface) by transitioning from damped oscillation regimens at low diffusivity, to critically damped regimens at intermediate diffusivities, and to overdamped regimens at high diffusivity. The situation is similar to a damped harmonic oscillator except that two critical diffusivities can be distinguished: one for which the integral of the timelines  $t \rightarrow L(t)$  is minimal ( $D \approx 0.0075$  m<sup>2</sup>/day, *yellow curve*; see also *inset*); and one above which oscillating interface patterns do not occur ( $D \approx 0.015$  mm<sup>2</sup>/day, *purple*; see also [Fig. 2](#)). In a critically damped harmonic oscillator, these two critical behaviors coincide (58).

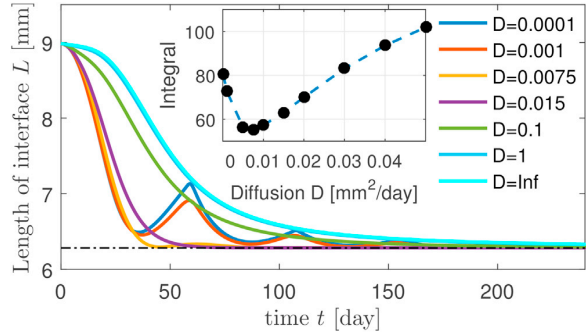


FIGURE 3 Influence of diffusivity on the rate and manner of smoothing of an initial cosine interface. The total length of the interface transitions from damped oscillation regimens at low diffusivities, to critically damped regimens at intermediate diffusivities, to overdamped regimens at high diffusivity. (*Inset*) The minimum integral of the timeline  $t \rightarrow L(t)$  is reached at a critical diffusivity  $D \approx 0.0075$  mm<sup>2</sup>/day smaller than the critical diffusivity  $D \approx 0.015$  mm<sup>2</sup>/day at which oscillating patterns are lost. To see this figure in color, go online.

The strength of diffusivity  $D$  drives similar qualitative changes in the evolution of porous channels during tissue deposition ([Fig. 4](#)). At low diffusivity ( $D = 0.0001$  mm<sup>2</sup>/day), the curvature-induced increase in cell density and resulting tissue crowding at corners of the initial pore shape increases the local propagation speed of the interface (*red*). New cusps in the interface are created laterally due to the contrast in propagation speed. These cusps propagate sideways as shock waves and collide. At intermediate diffusivity ( $D = 0.005$  mm<sup>2</sup>/day), cusps smooth out and the interface develops into a circular shape (at a rate that depends on acuteness). At high diffusivity ( $D = 1$  mm<sup>2</sup>/day), cell density is homogeneous, but increases with time as the interface's total length decreases. Initial cusps in the interface are maintained throughout the evolution.

### Application to bioscaffold tissue growth

We now apply our mathematical model to the in vitro experiments of Rumpler et al. (23) and Bidan et al. (25–27) in which tissue was grown on bioscaffolds of various shapes. In these experiments, hydroxyapatite bioscaffolds were initially seeded with a uniform density of cells. However, no tissue was produced on convex portions of these substrates. This suggests that the secretory rate  $k_f$  in Eq. 1 is itself a function of curvature, such that no tissue matrix is secreted by the cells when  $\kappa \geq 0$ . We take this function to be:

$$k_f(\kappa) = \begin{cases} k_f^0, & \text{if } \kappa < 0, \\ 0, & \text{if } \kappa \geq 0, \end{cases} \quad (12)$$

where  $k_f^0$  is a constant. With Eq. 12, the normal velocity of the interface is zero on convex portions of the interface, and it accelerates in proportion to curvature on concave portions of

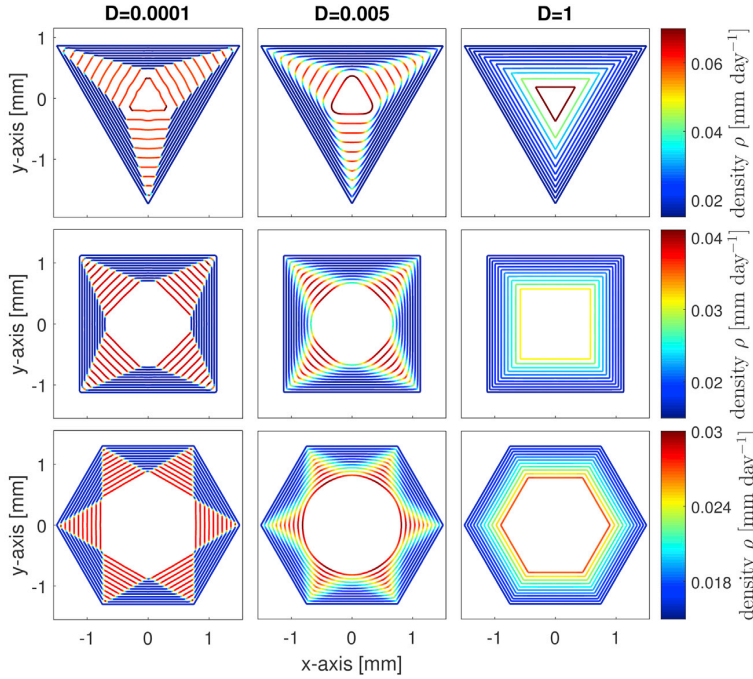


FIGURE 4 Tissue deposition within triangular, square, and hexagonal pores (each with initial perimeter 9 mm) for low ( $D = 0.0001$  mm<sup>2</sup>/day), intermediate ( $D = 0.005$  mm<sup>2</sup>/day), and high ( $D = 1$  mm<sup>2</sup>/day) diffusivities. The tissue interface is shown at regular time intervals  $\Delta t = 2.6$  days until  $t = 26$  days and colored according to cell density. Simulations performed with  $A = 0$ ,  $k_f^0 = 1$ , and  $\rho_0 = 0.016$  mm/day. To see this figure in color, go online.

the interface as per Eq. 8. In Rumpler et al. (23) and Bidan et al. (25–27), the authors suggested the phenomenological model of tissue growth given by  $v = -\lambda\kappa$  if  $\kappa < 0$ , and  $v = 0$  if  $\kappa \geq 0$ . With this phenomenological model the total cross-sectional area  $A_T(t)$  of new tissue produced up to time  $t$  increases at constant rate on pore substrates that are concave everywhere. Indeed,  $A_T'(t) \equiv \int_0^{P(t)} d\ell v(\ell, t) = 2\pi\lambda$  by the total absolute curvature theorem, where  $\ell$  is the arc length and  $P(t)$  is the pore's perimeter (48). This was used with experimental determinations of  $A_T(t)$  in circular pore shapes (25) and square pore shapes (26) to calibrate  $\lambda$ . Because rates of tissue growth  $A_T'(t)$  decreased at large times in the experiments (indicating tissue formation slowdown), this calibration was performed at the onset of tissue growth, assumed here to be  $t = 0$ , by setting  $\lambda = A_T'(0)/(2\pi)$ .

Our cell-based model is equivalent to this phenomenological model when tissue is deposited within perfectly circular pores and cells are not eliminated ( $A = 0$ ). Indeed, in this instance, by Eqs. 1 and 12:

$$v = k_f \rho = -\frac{k_f^0 N_0}{2\pi} \kappa \equiv -\lambda \kappa, \quad (13)$$

because  $\rho = N_0/(2\pi R)$  and  $\kappa = -1/R$ , where  $R$  is the pore radius, and  $N_0$  is the initial number of cells lining the circle's circumference. If active cells are depleted at constant rate  $A$ , the total number of active cells in our model decreases as  $N(t) = N_0 e^{-At}$  and the proportionality coefficient  $\lambda$  between velocity and curvature simply becomes time-dependent:

$$\lambda(t) = \frac{k_f^0 N_0 e^{-At}}{2\pi} = k_f^0 \rho_0 R_0 e^{-At}, \quad (14)$$

where  $\rho_0 = N_0/(2\pi R_0)$  is the initial cell density and  $R_0$  is the initial pore radius. In noncircular pore geometries, our cell-based model does not reduce to mean curvature flow. However, under the assumption that  $k_f^0$  and the initial seeding density  $\rho_0$  are independent of initial pore shape, Eq. 14, valid in the circular pore geometry, enables us to calibrate  $v_0 = k_f^0 \rho_0$ , the positive part of the initial normal velocity, in all pore geometries. From the experimental data  $A_T(t)/(\pi R_0^2)$  in Fig. 4B of Bidan et al. (25) ( $R_0 \approx 0.5$  mm), we estimated the slope at the onset of tissue growth by quadratic interpolation of the first five experimental points, giving an estimate of the initial tissue production rate measured in circular pore scaffolds to be  $A_T'(0) \approx 0.051$  mm<sup>2</sup>/day. We thus get from Eq. 14:

$$v_0 = k_f^0 \rho_0 = \frac{\lambda(0)}{R_0} = \frac{A_T'(0)}{2\pi R_0} \approx 16 \mu\text{m}/\text{day}. \quad (15)$$

As in [Influence of Cell Diffusion on Interface Smoothing](#), for ease of interpretation, we choose units in which  $k_f^0 = 1$  is dimensionless, so that  $\rho$  corresponds to  $v$  where  $\kappa < 0$ . We set the initial (scaled) density  $\rho_0 = v_0 = 0.016$  mm/day in all the numerical simulations.

Fig. 5 shows the growth of new tissue predicted by our cell-based model with Eqs. 12 and 15 in the circular, semicircular,

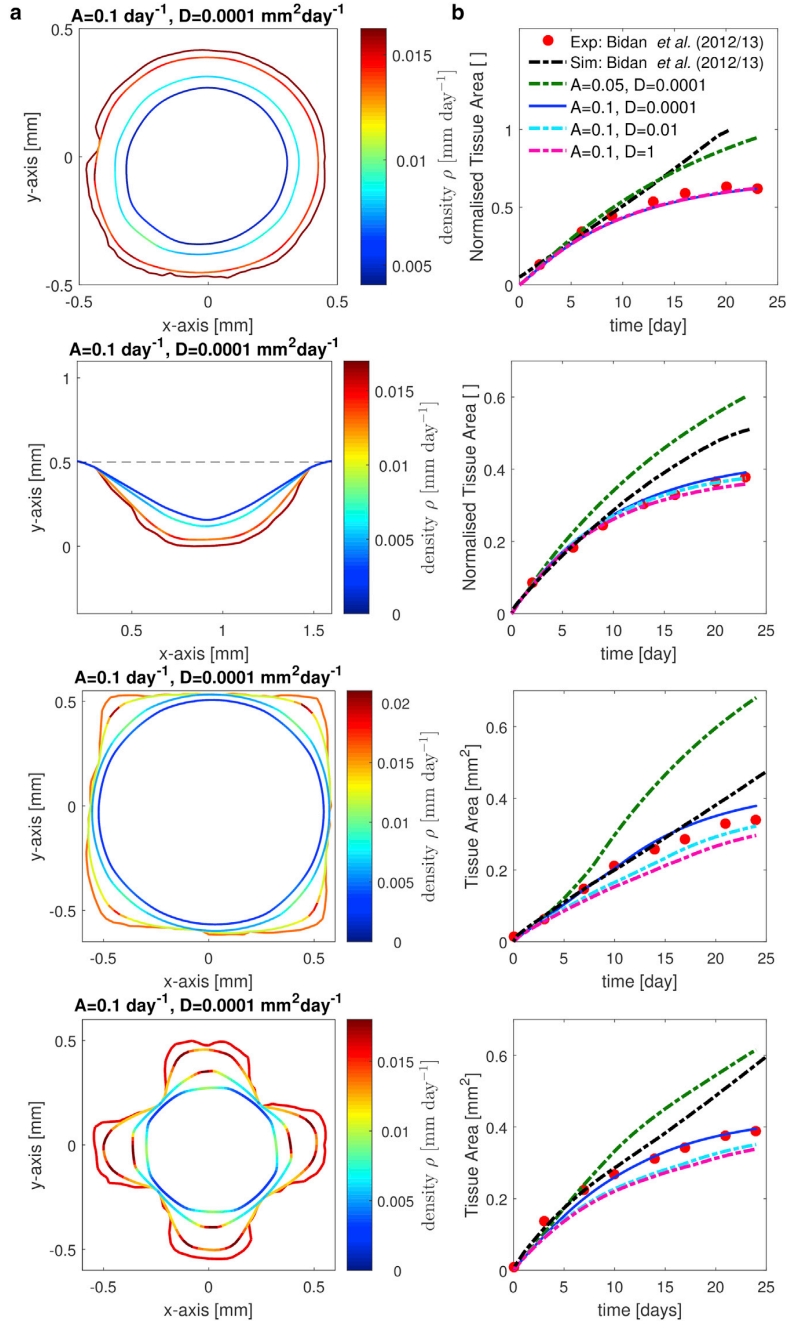


FIGURE 5 Tissue deposition predicted by our cell-based model with Eq. 12 in the bioscaffold pore shapes of Bidan et al. (25) (circular and semi-circular pore shapes) and Bidan et al. (26) (square and cross pore shapes). (a) The tissue interface is shown at days 4, 7, 14, and 21 and colored according to cell density. (b) The time evolution of the total tissue area produced  $A_T(t)$  (normalized by the initial pore area in the circular and semicircular cases) is shown for various values of diffusivity  $D$  and cell elimination rate  $A$ . These time evolutions are compared with the experimental results and simulations of the phenomenological model of Bidan et al. (25,26). To see this figure in color, go online.

square, and cross-shaped bioscaffold pores of Bidan et al. (25,26). The initial rate of tissue growth  $A'_T(0)$  depends on  $v_0$  and on the geometry of the initial substrate. While  $v_0$  is calibrated from measurements of  $A'_T(0)$  in the circular pore geometry, the rates  $A'_T(0)$  obtained with the same value of  $v_0$  in the other geometries (initial slope of the curves in Fig. 5 b) closely match the experimental initial growth rates.

Remarkably, our cell-based model reproduces the experimental tissue growth curves  $A_T(t)$  accurately—including tissue deposition slowdown—in all pore geometries for a single combination of diffusivity and cell depletion rate,  $D = 0.0001 \text{ mm}^2/\text{day}$  and  $A = 0.1/\text{day}$ . At these values, the interface rounds off efficiently regardless of initial pore shape, as observed experimentally (23,25,26) (see Fig. 5 a).

Clearly, the depletion rate of active cells  $A$  strongly influences tissue deposition slowdown (Fig. 5 b). While diffusivity  $D$  has only a weak influence on  $A_T(t)$ , it drives important qualitative changes in the shape of the tissue interface and in the distribution of cells on the interface, as in the simulations presented in Influence of Cell Diffusion on Interface Smoothing. Fig. 6 compares the experimental evolution of the tissue surface in the semicircular and cross-shaped pores with that predicted by the cell-based model with some of the combinations of  $A$  and  $D$  used in Fig. 5 b. While both combinations  $A = 0.1/\text{day}$ ,  $D = 0.0001 \text{ mm}^2/\text{day}$  (blue) and  $A = 0.1/\text{day}$ ,  $D = 0.01 \text{ mm}^2/\text{day}$  (cyan) give similar growth curves  $A_T(t)$  in Fig. 5 b, the evolution of the tissue interface obtained with  $D = 0.0001 \text{ mm}^2/\text{day}$  is much closer to the experimental tissue surface in Fig. 6. The values  $A = 0.1/\text{day}$ ,  $D = 0.0001 \text{ mm}^2/\text{day}$  are shown in the Supporting Material to minimize an error function that combines discrepancies both in tissue produced and in shape of the interface.

## DISCUSSION

The explicit consideration of the cellular origin of new tissue growth enables us to model a systematic influence of local curvature on cell density and growth rate. During the evolution of bone tissue in vivo, this influence represents the inevitable geometrical pull of the local expansion or contraction of curved bone surfaces. This effect is important to assess to understand the emergence of various formation patterns seen in bone histology in anthropological studies (59,60) and to correctly quantify the influence of other processes on tissue growth. During osteonal infilling for example, surface area shrinks to  $\sim 20\%$  of its initial extent, yet the density of active osteoblasts depositing new bone decreases. Area shrinkage is strongly overpowered by depletion pathways from the pool of active osteoblasts (40,44,61). Mathematical models of multistage osteoblast

development have modeled these different contributions in previous works (40,62), but they were restricted to perfectly cylindrical infilling cavities.

Here, we show that such cell-based models can explain both smoothing of irregular initial substrates and tissue deposition slowdown. The coevolution of tissue interface and cell density exhibits rich behaviors depending on the strength of cell diffusion along the interface (63) and on the depletion rate of active cells. This is due in part because cells diffusing on stretching domains may or may not colonize them depending on the ratio of diffusivity and domain growth (56). Here, cell density inhomogeneities induced by stretch additionally drive the evolution of domain stretch. Mathematically, our equations form a class of hyperbolic curvature flow (51) rather than mean-curvature flow (32,33). As a result, cusps may emerge in finite-time in the zero-diffusion limit. Curvature and cell density behave similarly to the conjugate variables of a harmonic oscillator (such as position and velocity). Shock waves and inertial effects leading to oscillatory interface motion occur for low enough diffusive damping (Figs. 2–4). These shocks and oscillatory motions involve strong inhomogeneities in cell density (Fig. 2 b). They could represent some patterns of stepwise lamellar sheet bone formation at a large scale (59), though it is also possible that these lamellar sheets are formed discontinuously in time. At a smaller scale, it is likely that cell density does not develop long-lasting inhomogeneities in space. Records of the forming bone surface provided by lamellae in cortical osteons (64), primary bone, and between curved trabecular structures in corticalized bone (59,60,65) display efficient smoothing and the absence of centered cusps in concavities, as in our simulations with intermediate cell diffusivity.

The density of osteoblasts on active bone surfaces is not often measured (45), making it difficult to disentangle the contributions of cell density and cell vigor to the normal

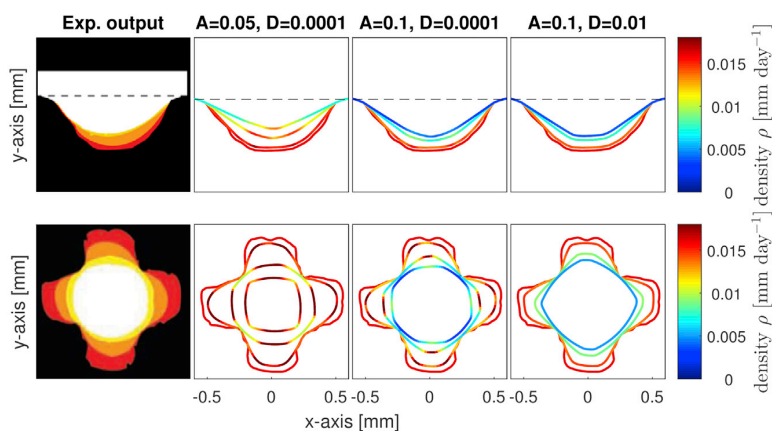


FIGURE 6 Evolution of the tissue interface of the cell-based model in the semicircular (top) and cross (bottom) interfaces with some of the combinations of  $A$  and  $D$  that were used in Fig. 5 b. The tissue interface is shown at days 7, 14, and 21 and colored according to cell density. Left column: experimental bioscaffold tissue growth showing the extent of new tissue at days 7 (red), 14 (orange), and 21 (yellow). Semi-circular pore image: reproduced with permission from Bidan et al. (25). Cross pore image: Copyright Wiley-VCH Verlag GmbH & Co. KGaA. Reproduced with permission from Bidan et al. (26). To see this figure in color, go online.

velocity of the interface, called the “matrix apposition rate” in Biology (39,40). Osteoblast density is influenced by the transition to nonsynthesizing, tissue-embedded cells called osteocytes. The sink term that describes the depletion of the pool of active cells at rate  $A$  in Eq. 8 also models the transition to such tissue-embedded cells (47). In Buenzli (47), it is shown that osteocyte density does not depend explicitly on osteoblast density, only on the ratio of the rate of osteoblast burial and secretory rate. One should therefore not regard a homogenous distribution of embedded osteocytes as a sign that osteoblast density was homogeneous. In fact, some degree of inhomogeneous osteoblast density is likely. Osteoblasts are believed not to move significantly with respect to the bone surface as they have several cellular projections linking with osteocytes through the bone tissue matrix (44,66).

Tissue growth in bioscaffolds is less polarized than bone apposition *in vivo*. Cells proliferate and may produce extracellular matrix in random directions to create new tissue. However, fibronectin labeling used recently by Bidan et al. (46) suggests that bulk tissue does not swell or compress during its maturation. Deep fibronectin labels are stationary and the density of embedded cells is homogeneous, showing that new tissue production is concentrated near the tissue surface, possibly as a result of increased tissue tension there (46) that could promote cell proliferation (22). The geometrical influence of curvature captured by our equations also holds in this situation. New cellular and extracellular tissue produced near concave portions of the surface will accelerate the velocity of the local interface in proportion to curvature (Fig. 1 *a*). Our numerical simulations show that this influence leads to a very good match with experimental tissue growth patterns and slowing rates (Figs. 5 and 6). In these simulations, the increased crowding of tissue produced in concavities leads to smoothing, while the depletion of active cells leads to tissue deposition slowdown. Depleting the pool of active cells corresponds to the hypothesis that cells slow down, and eventually stop, the production of new tissue as they find themselves deeper within the tissue and mature (25). It should also be noted here that cell proliferation was assumed in the simulations to be balanced out by the transition to quiescent tissue-embedded cells, with an overall net depletion of active cells as described by the negative first-order reaction rate in Eq. 8.

Tissue surface tension has been considered to play a role in bioscaffold tissue growth (22–28). Surface tension accounts for the relaxation of membranes toward minimal surfaces by curvature-controlled flow. In the thermodynamically consistent mechanical model of tissue growth of Gamsjäger et al. (28), surface tension was added to explain that new tissue could not be produced on convex substrates unless the chemical growth force dominated the surface stress, which works in the opposite direction at convexities. While surface tension due to the dense actin network near

the tissue surface may play a mechanical role in the tissue’s growth rate at concavities (25,28), we did not consider this effect here, and focused on how new tissue volume is created and fills available space. Our approach is similar to the (compressive) stress-dependent Eigenstrain tissue growth model of Dunlop et al. (24) and Gamsjäger et al. (28) except that we directly consider the volumetric crowding of tissue rather than the mechanics-induced movement of tissue created by its volumetric growth rate. Doing so enables us to exhibit an explicit dependence of the tissue interface motion upon local curvature (without surface tension). This dependence occurs via the normal acceleration of the tissue interface and leads to oscillatory behavior at low damping. While the model developed by Dunlop et al. (24) and Gamsjäger et al. (28) has been applied to circular pore shapes with rotation symmetric solutions only, it is also possible that the thermodynamic dissipation assumed in their model would disallow oscillatory motions.

Complex growth patterns also occur in problems of interfacial thermodynamics and in diffusion-limited aggregation. In these systems, growth is mostly determined by diffusive fluxes external to the growing substrate and by surface tension (e.g., via the Gibbs–Thomson relation) (67). External nutrient fluxes, surface tension, and mechanical loading (30,31) may of course add further dependences of tissue growth on curvature, in particular via cell vigor. The curvature influence on density exhibited by our model must be singled out to assess the true impact of these effects.

In summary, the shrinking or expanding available space near concavities or convexities of growing tissues provides an unavoidable geometric influence in a number of situations in which tissue production occurs near the interface, such as in tumor growth, wound healing, bone formation, and bioscaffold tissue growth. We showed that this influence is captured as a curvature-dependent acceleration of tissue growth. In bioscaffold tissue growth, contractile tension may further help even out cell densities and extracellular matrix, enhancing the smoothing dynamics. During bone formation *in vivo*, cellular tissue tension is likely to play a more minor role. Bone matrix quickly mineralizes and osteoblasts have been shown not to proliferate after becoming active (39,44).

Finally, we suggest that local changes in surface area during the evolution of the interface play a wider role than physically concentrating or spreading local cell densities. We hypothesize that dynamic surface area changes may be a mechanism by which cells on a substrate can perceive geometrical features that are much larger than the cells. Cells may not sense these geometrical features directly, but they may sense them dynamically when the interface contracts or expands, because of either changes in cell-cell contact pressure with neighboring cells or of stretching of focal adhesion sites.

## APPENDIX A: GOVERNING EQUATIONS

### Evolution of the local surface stretch

The local surface stretch in the normal direction  $D_t^\perp \delta \ell$  can be calculated using an orthogonal parameterization  $\Gamma(u, t)$  of  $S(t)$ , defined such that  $\Gamma_t = v\mathbf{n}$  and  $\Gamma_t \cdot \Gamma_u = 0$  at all times (see Fig. 1 b). Because trajectories  $t \mapsto \Gamma(u, t)$  (at  $u$  constant) are normal to  $S(t)$  at all times,  $D_t^\perp \equiv \partial/\partial t|_{u=\text{const}}$ . With  $\delta \ell = Gdu$ , where  $G = |\Gamma_u|$  is the metric associated with  $\Gamma(u, t)$ , one thus has  $D_t^\perp \delta \ell = G_t du$ . Differentiating the definition of  $G$  and using the unit tangent vector  $\boldsymbol{\tau} = \Gamma_u/|\Gamma_u|$  gives  $G_t = \boldsymbol{\tau} \cdot \Gamma_{ut} = \boldsymbol{\tau} \cdot (\Gamma_t)_u = \boldsymbol{\tau} \cdot (v\mathbf{n})_u = v\boldsymbol{\tau} \cdot \mathbf{n}_u$ , where the last equality uses the fact that  $\boldsymbol{\tau} \cdot \mathbf{n} = 0$ . By definition of the signed curvature,  $\kappa = -\boldsymbol{\tau}_t \cdot \mathbf{n} = \boldsymbol{\tau} \cdot \mathbf{n}_t$ , where  $\partial/\partial \ell = (1/G)(\partial/\partial u)$  (68). Therefore,  $G_t = vG\kappa$  and

$$\frac{D_t^\perp \delta \ell}{\delta \ell} = \frac{G_t}{G} = v\kappa. \quad (16)$$

### Conservative form of the governing equations

Equation 2 only specifies the normal component of  $\boldsymbol{\gamma}_t$ . The tangential component  $\boldsymbol{\tau} \cdot \boldsymbol{\gamma}_t$  can be chosen arbitrarily without modifying the evolution of  $S(t)$ . Once this choice is made,  $\boldsymbol{\gamma}$  satisfies

$$\boldsymbol{\gamma}_t = v\mathbf{n} + (\boldsymbol{\tau} \cdot \boldsymbol{\gamma}_t)\boldsymbol{\tau}, \quad (17)$$

where  $\boldsymbol{\tau} = \boldsymbol{\gamma}_s/|\boldsymbol{\gamma}_s|$ . For choices of  $\boldsymbol{\tau} \cdot \boldsymbol{\gamma}_t$  corresponding to thickness functions in Cartesian and polar coordinates, a conservative equation can be derived by differentiating Eq. 17 with respect to  $s$  (see [Cartesian Coordinates](#), and [Polar Coordinates](#), below).

To obtain the general conservative form of the evolution equation of cell density, it is necessary to consider the density of cells projected onto the  $s$  coordinate,  $\eta(s, t) = \rho(s, t)g(s, t)$  (see [Materials and Methods](#)). We first derive the evolution equation of the local stretch  $g$ . Differentiating the definition of  $g = |\boldsymbol{\gamma}_s|$  with respect to  $t$  as given above in Evolution of the Local Surface Stretch, using Eq. 17 and the fact that  $\boldsymbol{\tau} \cdot \mathbf{n} = 0$ ,  $\boldsymbol{\tau} \cdot \boldsymbol{\tau}_s = 0$ , and  $\kappa = \boldsymbol{\tau} \cdot \mathbf{n}_s/g$ :

$$g_t = \boldsymbol{\tau} \cdot (\boldsymbol{\gamma}_t)_s = v\boldsymbol{\tau} \cdot \mathbf{n}_s + (\boldsymbol{\tau} \cdot \boldsymbol{\gamma}_t)_s = g v \kappa + (\boldsymbol{\tau} \cdot \boldsymbol{\gamma}_t)_s. \quad (18)$$

Equation 18 generalizes the second equality in Eq. 16 to nonorthogonal parameterizations. Now differentiating  $\eta = \rho g$  with respect to  $t$ , and using Eqs. 8 and 18 gives Eq. 9:

$$\eta_t + \left( -\frac{\eta}{g} (\boldsymbol{\gamma}_t \cdot \boldsymbol{\tau}) - \frac{D}{g} \left( \frac{\eta}{g} \right)_s \right) = -A\eta. \quad (19)$$

This equation expresses the balance of cells on the interface element lying between the coordinates  $s$  and  $s+ds$ . It is of the form  $\eta_t + (f[\eta, \boldsymbol{\gamma}])_s = -A\eta$ , with total flux

$$f[\eta, \boldsymbol{\gamma}] = -\frac{\eta}{g} (\boldsymbol{\gamma}_t \cdot \boldsymbol{\tau}) - \frac{D}{g} \left( \frac{\eta}{g} \right)_s. \quad (20)$$

The first term in the flux represents the advection of cells with respect to the  $s$  coordinate. Curvature-induced changes in cell density are partly included in this term, and partly included in the evolution of the local stretch  $g$  in Eq. 18, which must be used to reconstruct the physical cell density  $\rho = \eta/g$ . For an orthogonal parameterization of  $S(t)$ , the first term in the flux is absent, in which case all the curvature-induced changes in  $\rho$  come from the evolution of the local stretch  $G$  in Eq. 16. The second term in the flux corresponds to the diffusion of cells along the interface. The factors

$g$  account for the fact that this diffusion is measured for the projected cell density along the  $s$  coordinate.

### Cartesian coordinates

Parameterizing  $S(t)$  by a height function  $y = h(x, t)$  in Cartesian coordinates corresponds to taking  $s = x$  and  $\boldsymbol{\gamma}(x, t) = (x, h(x, t))$ . In this case,  $\boldsymbol{\tau} \cdot \boldsymbol{\gamma}_t = v h_x$  and Eqs. 2 and 8 become

$$h_t = v\sqrt{1 + h_x^2}, \quad (21)$$

$$\rho_t = -\rho v \kappa - \rho_x v \cos \alpha + D \left( \frac{\rho_{xx}}{g^2} - \rho_x \kappa \cos \alpha \right) - A\rho, \quad (22)$$

where  $v = k_f \rho$ ,  $g = \sqrt{1 + h_x^2}$ ,  $\cos \alpha = \mathbf{n} \cdot \hat{\mathbf{x}} = -h_x/g$ , and  $\kappa = -h_{xx}/g^3$ . To write this system of coupled equations in conservative form, we define  $\sigma = h_x$  and  $\eta = \rho g$ , so that  $\sigma_t = h_{xt} = (h_x)_x = (k_f \eta)_x$ . With Eq. 19 rewritten with these definitions, one obtains the system of equations:

$$h_t = k_f \eta, \quad (23)$$

$$\sigma_t + [-k_f \eta]_x = 0, \quad (24)$$

$$\eta_t + \left[ -\frac{k_f \sigma \eta^2}{1 + \sigma^2} + D \left( \frac{\sigma \sigma_x \eta}{(1 + \sigma^2)^2} - \frac{\eta_x}{1 + \sigma^2} \right) \right]_x = -A\eta. \quad (25)$$

Note that Eq. 23 is decoupled from Eqs. 24 and 25.

### Polar coordinates

Parameterizing  $S(t)$  by the radius function  $r = R(\theta, t)$  in polar coordinates corresponds to taking  $s = \theta$  and  $\boldsymbol{\gamma}(\theta, t) = R(\theta, t)(\cos \theta, \sin \theta)$ . In this case,  $\boldsymbol{\tau} \cdot \boldsymbol{\gamma}_t = -vR_\theta/R$  and Eqs. 2 and 8 become

$$R_t = -v\sqrt{1 + (R_\theta/R)^2}, \quad (26)$$

$$\rho_t = -\rho v \kappa - \frac{\rho_\theta}{R} v \cos \alpha + D \left( \frac{\rho_{\theta\theta}}{g^2} - \frac{\rho_\theta}{R} \left[ \frac{2}{g} - \kappa \right] \cos \alpha \right) - A\rho, \quad (27)$$

where  $v = k_f \rho$ ,  $g = R\sqrt{1 + (R_\theta/R)^2}$ ,  $\cos \alpha = \mathbf{n} \cdot \hat{\boldsymbol{\theta}} = R_\theta/g$ , and  $\kappa = (R^2 - RR_{\theta\theta} + 2R_\theta^2)/g^3$ . Note that  $(2/g - \kappa)\cos(\alpha)/R = R_\theta(R + R_{\theta\theta})/g^4$ . To write this system of coupled equations in conservative form, we define  $\sigma = R_\theta$  and  $\eta = \rho g$ , so that  $\sigma_t = R_{\theta t} = (R_t)_\theta = (-k_f \eta/R)_\theta$ . With Eq. 19 rewritten with these definitions, one obtains the system of equations

$$R_t = -\frac{k_f \eta}{R}, \quad (28)$$

$$\sigma_t + \left[ \frac{k_f \eta}{R} \right]_\theta = 0, \quad (29)$$

$$\eta_r + \left[ \frac{k_t \sigma \eta^2}{R(R^2 + \sigma^2)} + D \left( \frac{\sigma(R + \sigma_\theta) \eta}{(R^2 + \sigma^2)^2} - \frac{\eta_\theta}{R^2 + \sigma^2} \right) \right]_\theta = -A\eta. \quad (30)$$

In contrast to the Cartesian case, Eq. 28 is not decoupled from Eqs. 29 and 30.

## SUPPORTING MATERIAL

Supporting Materials and Methods and two figures are available at [http://www.biophysj.org/biophysj/supplemental/S0006-3495\(16\)34272-2](http://www.biophysj.org/biophysj/supplemental/S0006-3495(16)34272-2).

## AUTHOR CONTRIBUTIONS

A.A. and P.R.B. conceived and designed the study; A.A. performed the numerical simulations; A.A. and P.R.B. analyzed the data; A.A. drafted the article; and both authors edited the article and gave final approval for publication.

## ACKNOWLEDGMENTS

We thank John Dunlop, Jérôme Droniou, Julie Clutterbuck, Isabel Maggiano, and Corey Maggiano for fruitful discussions. We are thankful to the anonymous reviewers whose comments helped improve and clarify the article.

P.R.B. gratefully acknowledges the Australian Research Council for Discovery Early Career Researcher Fellowship (project No. DE130101191).

## REFERENCES

- Ripamonti, U., and L. Roden. 2010. Biomimetics for the induction of bone formation. *Expert Rev. Med. Devices*. 7:469–479.
- Dunn, G. A., and J. P. Heath. 1976. A new hypothesis of contact guidance in tissue cells. *Exp. Cell Res.* 101:1–14.
- Curtis, A. S., and M. Varde. 1964. Control of cell behavior: topological factors. *J. Natl. Cancer Inst.* 33:15–26.
- Martin, J. Y., Z. Schwartz, ..., B. D. Boyan. 1995. Effect of titanium surface roughness on proliferation, differentiation, and protein synthesis of human osteoblast-like cells (MG63). *J. Biomed. Mater. Res.* 29:389–401.
- Deligianni, D. D., N. D. Katsala, ..., Y. F. Missirlis. 2001. Effect of surface roughness of hydroxyapatite on human bone marrow cell adhesion, proliferation, differentiation and detachment strength. *Biomaterials*. 22:87–96.
- Boyan, B. D., T. W. Hummert, ..., Z. Schwartz. 1996. Role of material surfaces in regulating bone and cartilage cell response. *Biomaterials*. 17:137–146.
- Gaudet, C., W. A. Marganski, ..., J. Y. Wong. 2003. Influence of type I collagen surface density on fibroblast spreading, motility, and contractility. *Biophys. J.* 85:3329–3335.
- Cavalcanti-Adam, E. A., T. Volberg, ..., J. P. Spatz. 2007. Cell spreading and focal adhesion dynamics are regulated by spacing of integrin ligands. *Biophys. J.* 92:2964–2974.
- Arnold, M., M. Schwieder, ..., J. P. Spatz. 2009. Cell interactions with hierarchically structured nano-patterned adhesive surfaces. *Soft Matter*. 5:72–77.
- Lo, C. M., H. B. Wang, ..., Y. L. Wang. 2000. Cell movement is guided by the rigidity of the substrate. *Biophys. J.* 79:144–152.
- Pelham, R. J., Jr., and Y. L. Wang. 1997. Cell locomotion and focal adhesions are regulated by substrate flexibility. *Proc. Natl. Acad. Sci. USA*. 94:13661–13665.
- Clark, P., P. Connolly, ..., C. D. Wilkinson. 1990. Topographical control of cell behaviour: II. Multiple grooved substrata. *Development*. 108:635–644.
- Curtis, A. S., and C. D. Wilkinson. 1998. Reactions of cells to topography. *J. Biomater. Sci. Polym. Ed.* 9:1313–1329.
- Vogel, V., and M. Sheetz. 2006. Local force and geometry sensing regulate cell functions. *Nat. Rev. Mol. Cell Biol.* 7:265–275.
- Parker, K. K., A. L. Brock, ..., D. E. Ingber. 2002. Directional control of lamellipodia extension by constraining cell shape and orienting cell tractional forces. *FASEB J.* 16:1195–1204.
- Théry, M., A. Pépin, ..., M. Bornens. 2006. Cell distribution of stress fibres in response to the geometry of the adhesive environment. *Cell Motil. Cytoskeleton*. 63:341–355.
- Chen, C. S., M. Mrksich, ..., D. E. Ingber. 1997. Geometric control of cell life and death. *Science*. 276:1425–1428.
- Yim, E. K. F., E. M. Darling, ..., K. W. Leong. 2010. Nanotopography-induced changes in focal adhesions, cytoskeletal organization, and mechanical properties of human mesenchymal stem cells. *Biomaterials*. 31:1299–1306.
- Rolli, C. G., H. Nakayama, ..., J. Nakanishi. 2012. Switchable adhesive substrates: revealing geometry dependence in collective cell behavior. *Biomaterials*. 33:2409–2418.
- Poujade, M., E. Grasland-Mongrain, ..., P. Silberzan. 2007. Collective migration of an epithelial monolayer in response to a model wound. *Proc. Natl. Acad. Sci. USA*. 104:15988–15993.
- Lowengrub, J. S., H. B. Frieboes, ..., V. Cristini. 2010. Nonlinear modelling of cancer: bridging the gap between cells and tumours. *Nonlinearity*. 23:R1–R9.
- Nelson, C. M., R. P. Jean, ..., C. S. Chen. 2005. Emergent patterns of growth controlled by multicellular form and mechanics. *Proc. Natl. Acad. Sci. USA*. 102:11594–11599.
- Rumpler, M., A. Woesz, ..., P. Fratzl. 2008. The effect of geometry on three-dimensional tissue growth. *J. R. Soc. Interface*. 5:1173–1180.
- Dunlop, J. W. C., F. D. Fischer, ..., P. Fratzl. 2010. A theoretical model for tissue growth in confined geometries. *J. Mech. Phys. Solids*. 58:1073–1087.
- Bidan, C. M., K. P. Kommareddy, ..., J. W. C. Dunlop. 2012. How linear tension converts to curvature: geometric control of bone tissue growth. *PLoS One*. 7:e36336.
- Bidan, C. M., K. P. Kommareddy, ..., J. W. C. Dunlop. 2013. Geometry as a factor for tissue growth: towards shape optimization of tissue engineering scaffolds. *Adv. Healthc. Mater.* 2:186–194.
- Bidan, C. M., F. M. Wang, and J. W. C. Dunlop. 2013. A three-dimensional model for tissue deposition on complex surfaces. *Comput. Methods Biomech. Biomed. Engin.* 16:1056–1070.
- Gamsjäger, E., C. M. Bidan, ..., J. W. C. Dunlop. 2013. Modelling the role of surface stress on the kinetics of tissue growth in confined geometries. *Acta Biomater.* 9:5531–5543.
- Knychala, J., N. Bouropoulos, ..., B. G. Sengers. 2013. Pore geometry regulates early stage human bone marrow cell tissue formation and organisation. *Ann. Biomed. Eng.* 41:917–930.
- Guyot, Y., I. Papantoniou, ..., L. Geris. 2014. A computational model for cell/ECM growth on 3D surfaces using the level set method: a bone tissue engineering case study. *Biomech. Model. Mechanobiol.* 13:1361–1371.
- Guyot, Y., F. P. Luyten, ..., L. Geris. 2015. A three-dimensional computational fluid dynamics model of shear stress distribution during neotissue growth in a perfusion bioreactor. *Biotechnol. Bioeng.* 112:2591–2600.
- Grayson, M. A. 1987. The heat equation shrinks embedded plane curves to round points. *J. Differ. Geom.* 26:285–314.

33. Crandall, M. G., and P. L. Lions. 1983. Viscosity solutions of Hamilton-Jacobi equations. *Trans. Am. Math. Soc.* 277:1–42.
34. Martin, R. B. 2000. Does osteocyte formation cause the nonlinear refilling of osteons? *Bone*. 26:71–78.
35. Lee, W. R. 1964. Appositional bone formation in canine bone: a quantitative microscopic study using tetracycline markers. *J. Anat.* 98: 665–677.
36. Manson, J. D., and N. E. Waters. 1965. Observations on the rate of maturation of the cat osteon. *J. Anat.* 99:539–549.
37. Frost, H. M. 1969. Tetracycline-based histological analysis of bone remodeling. *Calcif. Tissue Res.* 3:211–237.
38. Metz, L. N., R. B. Martin, and A. S. Turner. 2003. Histomorphometric analysis of the effects of osteocyte density on osteonal morphology and remodeling. *Bone*. 33:753–759.
39. Parfitt, A. M. 1983. The physiologic and clinical significance of bone histomorphometric data. In *Bone Histomorphometry: Techniques and Interpretation*. R. R. Recker, editor. CRC Press, Boca Raton, FL, pp. 143–224.
40. Buenzli, P. R., P. Pivonka, and D. W. Smith. 2014. Bone refilling in cortical basic multicellular units: insights into tetracycline double labelling from a computational model. *Biomech. Model. Mechanobiol.* 13:185–203.
41. Jilka, R. L., R. S. Weinstein, ..., S. C. Manolagas. 1999. Increased bone formation by prevention of osteoblast apoptosis with parathyroid hormone. *J. Clin. Invest.* 104:439–446.
42. Pazzaglia, U. E., G. Zarattini, ..., G. Feltrin. 2010. Morphometric analysis of the canal system of cortical bone: an experimental study in the rabbit femur carried out with standard histology and micro-CT. *Anat. Histol. Embryol.* 39:17–26.
43. Martin, R. B., D. B. Burr, and N. A. Sharkey. 1998. *Skeletal Tissue Mechanics*. Springer, New York.
44. Parfitt, A. M. 1994. Osteonal and hemi-osteonal remodeling: the spatial and temporal framework for signal traffic in adult human bone. *J. Cell. Biochem.* 55:273–286.
45. Marotti, G., A. Z. Zallone, and M. Ledda. 1976. Number, size and arrangement of osteoblasts in osteons at different stages of formation. *Calcif. Tissue Res.* 21 (Suppl):96–101.
46. Bidan, C. M., P. Kollmannsberger, ..., J. W. Dunlop. 2016. Gradual conversion of cellular stress patterns into pre-stressed matrix architecture during in vitro tissue growth. *J. R. Soc. Interface.* 13:20160136.
47. Buenzli, P. R. 2015. Osteocytes as a record of bone formation dynamics: a mathematical model of osteocyte generation in bone matrix. *J. Theor. Biol.* 364:418–427.
48. Kühnel, W. 2006. *Differential Geometry: Curves—Surfaces—Manifolds*, 2nd Ed. American Mathematical Society, Providence, RI.
49. Berger, M. 2003. *A Panoramic View of Riemannian Geometry*. Springer, Berlin, Germany.
50. LeFloch, P. G., and K. Smoczyk. 2008. The hyperbolic mean curvature flow. *J. Math. Pures Appl.* 90:591–614.
51. Sethian, J. A. 1999. *Level Set Methods and Fast Marching Methods: Evolving Interfaces in Computational Geometry, Fluid Mechanics, Computer Vision, and Materials Science*. Cambridge University Press, Cambridge, UK.
52. Lax, P. 1973. *Hyperbolic systems of conservation laws and the mathematical theory of shock waves*. SIAM, Philadelphia, PA.
53. LeVeque, R. J. 2004. *Finite Volume Methods for Hyperbolic Problems*. Cambridge University Press, Cambridge, UK.
54. Harten, A., P. D. Lax, and B. van Leer. 1983. On upstream differencing and Godunov-type schemes for hyperbolic conservation laws. *SIAM Rev.* 25:35–61.
55. Kurganov, A., and E. Tadmor. 2000. New high-resolution central schemes for nonlinear conservation laws and convection-diffusion equations. *J. Comput. Phys.* 160:241–282.
56. Simpson, M. J., K. A. Landman, and D. F. Newgreen. 2006. Chemotactic and diffusive migration on a nonuniformly growing domain: numerical algorithm development and applications. *J. Comput. Appl. Math.* 192:282–300.
57. Kardar, M., G. Parisi, and Y. C. Zhang. 1986. Dynamic scaling of growing interfaces. *Phys. Rev. Lett.* 56:889–892.
58. Serway, R., and J. Jewett. 2007. *Physics for Scientists and Engineers, Chapters 1–39*. In Available 2010 Titles Enhanced Web Assign Series. Cengage Learning, Boston, MA.
59. Maggiano, C. M. 2011. Making the mold. A microstructural perspective on bone modeling during growth and mechanical adaptation. In *Bone Histology. An Anthropological Perspective*. C. Crowder and S. Stout, editors. CRC Press, Boca Raton, FL, pp. 45–90.
60. Maggiano, C. M., I. S. Maggiano, ..., S. D. Stout. 2016. Methods and theory in bone modeling drift: comparing spatial analyses of primary bone distributions in the human humerus. *J. Anat.* 228:190–202.
61. Pazzaglia, U. E., T. Congiu, ..., D. Quacci. 2011. The fibrillar organization of the osteon and cellular aspects of its development : a morphological study using the SEM fractured cortex technique. *Anat. Sci. Int.* 86:128–134.
62. Polig, E., and W. S. S. Jee. 1990. A model of osteon closure in cortical bone. *Calcif. Tissue Int.* 47:261–269.
63. Crank, J. 1975. *The Mathematics of Diffusion*. Oxford University Press, Oxford, UK.
64. Pazzaglia, U. E., T. Congiu, ..., D. Quacci. 2012. Morphometry and patterns of lamellar bone in human Haversian systems. *Anat. Rec. (Hoboken)*. 295:1421–1429.
65. Streeter, M. 2011. Histological age-at-death estimation. In *Bone Histology. An Anthropological Perspective*. C. Crowder and S. Stout, editors. CRC Press, Boca Raton, FL, pp. 135–152.
66. Pazzaglia, U. E., T. Congiu, ..., D. Quacci. 2014. Osteoblast-osteocyte transformation. A SEM densitometric analysis of endosteal apposition in rabbit femur. *J. Anat.* 224:132–141.
67. Langer, J. S. 1980. Instabilities and pattern formation in crystal growth. *Rev. Mod. Phys.* 52:1–28.
68. Dineen, S. 2014. *Multivariate Calculus and Geometry*, 3rd Ed. Springer, London, UK.

**Biophysical Journal, Volume 112**

**Supplemental Information**

**Modeling the Effect of Curvature on the Collective Behavior of Cells  
Growing New Tissue**

**Mohd Almie Alias and Pascal R. Buenzli**

# Modelling the effect of curvature on the collective behaviour of cells growing new tissue – Supporting material

## 1 Numerical discretisation

Some aspects of the numerical schemes presented in Section 2 are detailed here.

At high diffusivity  $D$ , we used a semi-implicit finite difference scheme on Eqs (21)-(22) (Cartesian coordinates) or Eqs (26)-(27) (polar coordinates). Upwinding for all first-order derivatives was based on the sign of  $h_x$  (Cartesian) or  $R_\theta$  (polar). In Cartesian coordinates for example:

$$\frac{\partial f}{\partial x}(x_i) \approx \begin{cases} \frac{1}{\Delta x} [f(x_i) - f(x_{i-1})], & \text{if } h(x_{i-1}) > h(x_{i+1}), \\ \frac{1}{\Delta x} [f(x_{i+1}) - f(x_i)], & \text{otherwise.} \end{cases} \quad (\text{S1})$$

We used explicit forward Euler discretisation in time for advective and reaction terms and implicit backward discretisation for diffusive terms to avoid restrictive Courant–Friedrichs–Lewy (CFL) conditions at high diffusivities [1].

At low diffusivity  $D$ , we used a semi-discrete Kurganov–Tadmor (KT) finite volume method with fully explicit forward Euler time discretisation on Eqs (23)-(25) (Cartesian coordinates), or Eqs (28)-(30) (polar coordinates). These systems of equations were recast in the form

$$\mathbf{u}_t + [\mathbf{g}(\mathbf{u})]_x = [\mathbf{Q}(\mathbf{u}, \mathbf{u}_x)]_x + \mathbf{R} \quad (\text{S2})$$

for  $\mathbf{u} = (h, \sigma, \eta)$  (Cartesian) or  $\mathbf{u} = (R, \sigma, \eta)$  (polar), where  $\mathbf{R} = (0, 0, -A\eta)$ . The flux  $\mathbf{g}$  is hyperbolic and contains the part of the total flux that is independent of  $\eta_x$ . The flux  $\mathbf{Q}$  is parabolic and contains the part that depends on  $\eta_x$ . The semi-discrete KT form of Eq. (S2) at point  $x_i$  is

$$\frac{d}{dt} \mathbf{u}_i(t) = - \frac{\mathbf{H}_{i+1/2}(t) - \mathbf{H}_{i-1/2}(t)}{\Delta t} + \frac{\mathbf{P}_{i+1/2}(t) - \mathbf{P}_{i-1/2}(t)}{\Delta t} + \mathbf{R}_i(t), \quad (\text{S3})$$

where  $\mathbf{H}$  is the Rusanov numerical flux approximating the hyperbolic flux, and  $\mathbf{P}$  is a second order central difference approximation to the parabolic flux (see Eqs (4.13), (4.14), and (4.4) of Ref. [2]). The Rusanov fluxes involve left and right values of  $\mathbf{u}_{i\pm 1/2}$  interpolated using a minmod limiter componentwise. The only information on characteristics required in  $\mathbf{H}$  is the maximum absolute value of the eigenvalues of  $\mathbf{g}'(\mathbf{u})$  for the Riemann problem at a Riemann fan [2], which was determined numerically. Equation (S3) was discretised in time using a simple forward Euler scheme.

Space and time discretisation steps were reduced within constraints imposed by the Courant number [1] until numerical convergence. Hyperbolic problems of interface propagation are known to give good results even for low order time discretisations. They are more sensitive to spatial discretisation [3]. Note that the Kurganov–Tadmor scheme is a high-resolution central scheme in space. Both numerical schemes

were checked against each other for a range of intermediate diffusivities. They were also checked against the analytic solution of the rotation-symmetric infilling circular cavity found from Eqs (13)-(14):

$$R(t) = R_0 \sqrt{1 - 2 \frac{u_0}{R_0} \frac{1 - \exp(-At)}{A}}. \quad (\text{S4})$$

Figure 1 shows the case where  $A = 0$ , in which  $R \rightarrow 0$  and  $\rho \rightarrow \infty$  when  $t \rightarrow t_c = \frac{1}{2} \frac{R_0}{u_0} \approx 31$  days. Due to symmetry, the solution is independent of cell diffusion and all the numerical solutions are indistinguishable.

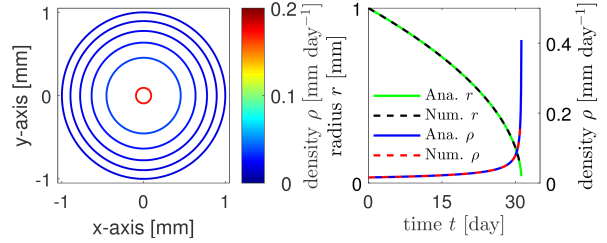


**Figure 1** – Evolution of circular interface and osteoblast surface density with any cell diffusion value (left). There is excellent agreement between the numerical and analytic evolutions of radius and cell density (right).

## 2 Error function for parameter estimation

Two types of errors were combined to estimate the cell depletion rate  $A$  and cell diffusivity  $D$  that minimise the discrepancy between numerical simulations and experimental data in Section 3.2. The first error corresponds to the discrepancy in total tissue produced  $A_T(p, t)$  summed over the data time points of Fig 5b, and over the four different bioscaffold pore shapes considered, i.e., circular, semi-circular, square, and cross ( $p = 1, \dots, 4$ ):

$$\epsilon_{\text{PTA}}(A, D) = \sum_{p=1}^4 \sum_t |A_T^{\text{model}}(p, t) - A_T^{\text{data}}(p, t)|. \quad (\text{S5})$$

Minimising this error ensures a good fit between simulations and data points in Fig. 5b, but this error is only weakly sensitive to values of  $D$ . In particular, this error does not measure discrepancies in the shape of the interface. To penalise such discrepancies, we considered in addition the least square error of the local curvature  $\kappa$  of the last interface

available ( $t = 21$  days):

$$\epsilon_{\kappa}(A, D) = \sum_{p=1}^4 \sum_i |\kappa^{\text{model}}(p, i) - \kappa^{\text{data}}(p, i)|^2 \Delta \ell_{p,i}, \quad (\text{S6})$$

where  $i$  runs over all the discretisation points of the interface, and  $\Delta \ell_{p,i}$  is the segmental length between points  $i$  and  $i + 1$ . Both error measures are combined into the total error function

$$\epsilon(A, D) = \alpha \epsilon_{\text{PTA}}(A, D) + \epsilon_{\kappa}(A, D), \quad (\text{S7})$$

where the weight  $\alpha \approx 549.6 \text{ mm}^{-3}$  accounts for the difference in unit and order of magnitude of  $\epsilon_{\text{PTA}}$  and  $\epsilon_{\kappa}$ , and was set as the ratio between the mean values of  $\epsilon_{\kappa}$  and  $\epsilon_{\text{PTA}}$ . A plot of this error surface in the  $(D, A)$  parameter space is shown in Figure 2. The minimum error is obtained for  $A \approx 0.1$  and  $D \approx \exp(-9.2) \approx 0.0001$ . We note here that an objective error function to penalise discrepancies in interface shape is difficult to define. We chose the least square error of local curvature rather than the least square error of interface height or radius because the latter was not very sensitive to  $D$  and similar to  $\epsilon_{\text{PTA}}$ . Other variations are possible, and may lead to slightly different optimal values of  $A$  and  $D$ .

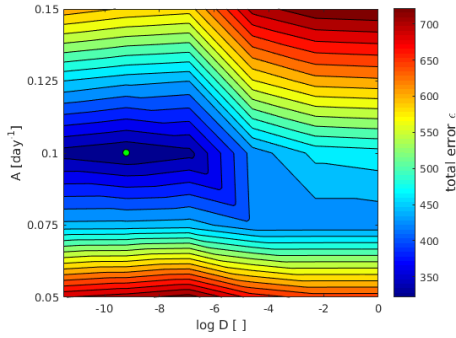


**Figure 2** – The map of total error  $\epsilon$  where  $\epsilon = \alpha \epsilon_{\text{PTA}} + \epsilon_{\kappa}$  and  $\alpha \approx 549.6$ . The minimum error, marked by the green dot corresponds to  $A = 0.1$  and  $D = \exp(-9,2) \approx 0.0001$ .

## Supporting References

- [1] LeVeque, R. J., 2004. Finite Volume Methods for Hyperbolic Problems. Cambridge University Press. Cambridge Books Online.
- [2] Kurganov, A., and E. Tadmor, 2000. New High-Resolution Central Schemes for Nonlinear Conservation Laws and Convection–Diffusion Equations. *Journal of Computational Physics* 160:241 – 282.
- [3] Sethian, J. A., 1999. Level Set Methods and Fast Marching Methods: Evolving Interfaces in Computational Geometry, Fluid Mechanics, Computer Vision, and Materials Science. Cambridge University Press.

### 3.3 Numerical methods

The published paper and its supplementary material, which have been reproduced in the previous section present several different forms of model equations developed using explicit parameterisation, namely:

(i) Non-conservative form

- Cartesian system in Eqs. (21) and (22)
- polar system in Eqs. (26) and (27)

(ii) Conservative form

- Cartesian system in Eqs. (23) to (25)
- polar system in Eqs. (28) to (30)

Each form of model equations is utilised uniquely according to the problem encountered. Specifically, the non-conservative equations are used for medium and high cell diffusivity  $D$ , while the conservative equations are intended for the case of low cell diffusivity  $D$ . The non-conservative form of the model equations are solved using a straightforward semi-implicit upwind finite difference scheme, while the conservative form equations are discretised by a finite volume Kurganov-Tadmor scheme [58, 61]. As shown in the paper, utilising different schemes for different levels of cell diffusivity  $D$  results in insignificant numerical loss of cell number while it also ensures low numerical calculation cost constrained by the CFL condition.

In the following, a more detail account on the numerical schemes used in the simulations is presented.

#### 3.3.1 Finite difference scheme

We exemplify this scheme on the polar system equations, Eqs. (26) and (27). A similar discretisation was used for the Cartesian system of equations.

We begin by defining a grid of points in the  $(t, \theta)$  space. Let  $\Delta t$  be the time step and  $\Delta \theta$  be the space step. The points in the grid becomes  $(t^n, \theta_i) = (n\Delta t, i\Delta \theta)$  for  $n = 0, 1, \dots, N$  and  $i = 0, 1, \dots, I$  where  $R_i^n$  and  $\rho_i^n$  approximate the solutions  $R(t, \theta)$  and  $\rho(t, \theta)$  at any grid point  $(t^n, \theta_i)$ . Here, the first-order and second-order spatial derivatives are discretised using upwind and central differences, respectively, such that:

$$(R_\theta)_i^n = \frac{a_{i,+}^n (R_i^n - R_{i-1}^n) + a_{i,-}^n (R_{i+1}^n - R_i^n)}{\Delta\theta}, \quad (\rho_\theta)_i^n = \frac{a_{i,+}^n (\rho_i^n - \rho_{i-1}^n) + a_{i,-}^n (\rho_{i+1}^n - \rho_i^n)}{\Delta\theta} \quad (3.1)$$

where

$$a_{i,+}^n = \begin{cases} 1 & \text{if } R_{i+1}^n > R_{i-1}^n \\ 0 & \text{if } R_{i+1}^n \leq R_{i-1}^n \end{cases}, \quad a_{i,-}^n = \begin{cases} 0 & \text{if } R_{i+1}^n > R_{i-1}^n \\ 1 & \text{if } R_{i+1}^n \leq R_{i-1}^n \end{cases} \quad (3.2)$$

and

$$(R_{\theta\theta})_i^n = \frac{R_{i+1}^n - 2R_i^n + R_{i-1}^n}{\Delta\theta^2}, \quad (\rho_{\theta\theta})_i^n = \frac{\rho_{i+1}^n - 2\rho_i^n + \rho_{i-1}^n}{\Delta\theta^2} \quad (3.3)$$

The advective and reaction terms are solved explicitly with forward Euler discretisation in time, while the diffusive terms are solved implicitly with backward Euler discretisation. Using periodic boundary conditions, we then obtain the discretised version of Eqs. (26) and (27) of the paper as:

$$R_i^{n+1} = R_i^n - \Delta t (k_f)_i^n \rho_i^n \sqrt{1 + \frac{((R_\theta)_i^n)^2}{(R_i^n)^2}} \quad (3.4)$$

$$\Psi^n \boldsymbol{\rho}^{n+1} = \boldsymbol{\phi}^n \quad (3.5)$$

where  $R_i^{n+1}$  for  $i = 0, 1, \dots, I-1$  and  $\boldsymbol{\rho}^{n+1} = [\rho_0^{n+1} \rho_1^{n+1} \dots \rho_{I-2}^{n+1} \rho_{I-1}^{n+1}]^T$  are the unknowns that we want to determine. The quantity  $\boldsymbol{\phi}^n = [\phi_0^n \phi_1^n \dots \phi_{I-2}^n \phi_{I-1}^n]^T$  is known from the previous time step  $n$ , such that, by using  $\cos \alpha = \mathbf{n} \cdot \hat{\boldsymbol{\theta}} = R_\theta/g$  where  $g = R\sqrt{1 + (R_\theta/R)^2} = \sqrt{R^2 + R_\theta^2}$ , we obtain:

$$\phi_i^n = \rho_i^n - \kappa_i^n (k_f)_i^n (\rho_i^n)^2 \Delta t - \frac{(k_f)_i^n \Delta t \rho_i^n (R_\theta)_i^n (\rho_\theta)_i^n}{R_i^n \sqrt{(R_i^n)^2 + ((R_\theta)_i^n)^2}} - A \Delta t \rho_i^n. \quad (3.6)$$

The matrix  $\Psi^n$  is an  $I \times I$  cyclic tridiagonal matrix written as

$$\Psi^n = \begin{bmatrix} \lambda_0^n & \gamma_0^n & \dots & 0 & \beta_0^n \\ \beta_1^n & \lambda_1^n & \dots & 0 & 0 \\ \vdots & \vdots & \ddots & \vdots & \vdots \\ 0 & 0 & \dots & \lambda_{I-2}^n & \gamma_{I-2}^n \\ \gamma_{I-1}^n & 0 & \dots & \beta_{I-1}^n & \lambda_{I-1}^n \end{bmatrix} \quad (3.7)$$

where

$$\lambda_i^n = 1 + 2 \frac{D\Delta t / \Delta \theta^2}{(R_i^n)^2 + ((R_\theta)_i^n)^2} + \frac{D\Delta t (R_\theta)_i^n (R_i^n + (R_{\theta\theta})_i^n)}{\Delta \theta [(R_i^n)^2 + ((R_\theta)_i^n)^2]^2} (a_{i,+}^n - a_{i,-}^n) \quad (3.8)$$

$$\beta_i^n = -\frac{D\Delta t / \Delta \theta^2}{(R_i^n)^2 + ((R_\theta)_i^n)^2} - \frac{D\Delta t (R_\theta)_i^n (R_i^n + (R_{\theta\theta})_i^n)}{\Delta \theta [(R_i^n)^2 + ((R_\theta)_i^n)^2]^2} a_{i,+}^n \quad (3.9)$$

$$\gamma_i^n = -\frac{D\Delta t / \Delta \theta^2}{(R_i^n)^2 + ((R_\theta)_i^n)^2} + \frac{D\Delta t (R_\theta)_i^n (R_i^n + (R_{\theta\theta})_i^n)}{\Delta \theta [(R_i^n)^2 + ((R_\theta)_i^n)^2]^2} a_{i,-}^n \quad (3.10)$$

The cyclic tridiagonal matrix  $\Psi^n$  is generally produced by implicit or semi-implicit finite difference scheme with periodic boundary conditions. Eq. (3.5) can be solved by explicitly finding the product of  $\Psi^{-1}$  and  $\phi^n$  or by using the Sherman-Morrison formula [62]. In MATLAB, there is a function capable of finding the solution  $\rho^{n+1}$  from Eq. (3.5) named ‘mldivide’. This function is implemented by a simple ‘backslash’ command  $\Psi^n \backslash \phi^n$ . Different calculation methods are used by this function when calculating the solution, determined according to how dense or sparse the input arrays are [63, page 7463].

### 3.3.2 Finite volume scheme

At low cell diffusivity  $D$ , the finite difference scheme can lead to numerical non-conservation of cells requiring finer grid resolution in space. To prevent the numerical non-conservation of cells without compromising computational speed, we discretise the conservative form of the equations in Eqs. (23) to (25) for the Cartesian system and Eqs. (28) to (30) for the polar system with the finite volume method instead [64]. We implement the semi-discrete Kurganov-Tadmor scheme [61] with a fully explicit forward Euler discretisation in time. Both finite difference and finite volume schemes give indistinguishable results in a range of intermediate diffusivities (refer Fig. 3.1).

In the finite volume method, the spatial domain is divided into “finite volumes” or “grid cells” denoted by  $\mathcal{C}_i = (\theta_{i-1/2}, \theta_{i+1/2})$  for polar coordinate system. Here, we keep track of an estimation to the average value of  $\mathbf{u}$ , in  $\mathcal{C}_i$  [64]. We define  $\Delta t = t^{n+1} - t^n$  to be the time step and  $\Delta \theta = \theta_{i+1/2} - \theta_{i-1/2}$  to be the space step or the length of the cell  $\mathcal{C}_i$  for  $n = 0, 1, \dots, N$  and  $i = 0, 1, \dots, I$ . To implement the Kurganov-Tadmor scheme, we recast the conservative model in polar system of Eqs. (28) to (30) (note that the model in the Cartesian system in Eqs. (23) to (25) uses similar approaches) as

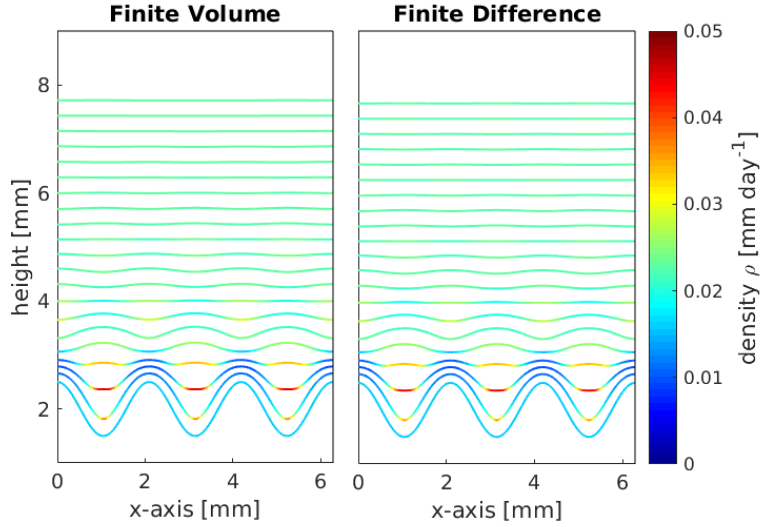


FIGURE 3.1: Comparison between the output of finite volume method and finite difference method for intermediate diffusion  $D = 0.005$ . Both graphs are indistinguishable.

$$\mathbf{u}_t + [\mathbf{g}(\mathbf{u})]_\theta = [\mathbf{Q}(\mathbf{u}, \mathbf{u}_\theta)]_\theta + \mathbf{R} \quad (3.11)$$

for  $\mathbf{u} = (R, \sigma, \eta)$ , where  $\mathbf{R} = (0, 0, -A\eta)$ . The flux  $\mathbf{g}$  is hyperbolic and contains the part of the total flux that is independent of  $\mathbf{u}_\theta$ . The flux  $\mathbf{Q}$  is parabolic and contains the part that depends on  $\mathbf{u}_\theta$ . The semi-discrete Kurganov-Tadmor scheme form of Eq. (3.11) at point  $\theta_i$  is

$$\frac{d}{dt} \mathbf{u}_i(t) = - \frac{\mathbf{H}_{i+1/2}(t) - \mathbf{H}_{i-1/2}(t)}{\Delta\theta} + \frac{\mathbf{P}_{i+1/2}(t) - \mathbf{P}_{i-1/2}(t)}{\Delta\theta} + \mathbf{R}_i(t), \quad (3.12)$$

where  $\mathbf{H}$  is the Rusanov numerical flux approximating the hyperbolic flux, and  $\mathbf{P}$  is a second order central difference approximation to the parabolic flux (see Eqs. (4.13), (4.14), and (4.4) of Ref. [61]). The Rusanov fluxes involve left and right values of  $\mathbf{u}_{i\pm 1/2}$  interpolated using a minmod limiter componentwise. The only information on characteristics required in  $\mathbf{H}$  is the maximum absolute value of the eigenvalues of  $\mathbf{g}'(\mathbf{u})$  for the Riemann problem at a Riemann fan [61], which can be determined numerically. Equation (3.12) is discretised in time using a simple forward Euler scheme.

### 3.3.3 CFL condition

The CFL condition states that a numerical scheme (finite difference or finite volume) can only be convergent if its numerical domain of dependence includes the domain

of dependence of the PDE. However, this CFL condition is a necessary condition to check for stability of a numerical scheme. CFL conditions may be derived using a von Neumann stability analysis. This will not be covered in this thesis, see e.g. Ref. [65].

In the case of low diffusion  $D \rightarrow 0$ , the CFL condition for the Kurganov-Tadmor scheme is  $\max_i(a_{i+1/2}^n)\Delta t/\Delta x \leq 1$ . Genuinely nonlinear and linearly degenerate cases define the local maximal speed  $a_{i+1/2}^n$  as:

$$a_{i+1/2}^n = \max \left\{ \max \left( \lambda(\mathbf{g}'(\mathbf{u}_{i+1/2}^-)) \right), \max \left( \lambda(\mathbf{g}'(\mathbf{u}_{i+1/2}^+)) \right) \right\} \quad (3.13)$$

where  $\mathbf{u}_{i+1/2}^- = \mathbf{u}_{i+1} - \frac{\Delta x}{2}(\mathbf{u}_x)_{i+1}^n$  and  $\mathbf{u}_{i+1/2}^+ = \mathbf{u}_{i+1} + \frac{\Delta x}{2}(\mathbf{u}_x)_{i+1}^n$  are the left and right intermediate values associated to the piecewise linear approximation  $\tilde{\mathbf{u}}(x, t^n)$  at the point  $x_{i+1/2}$  [61].

In the case of intermediate and high diffusivity, the use of the semi-implicit finite difference scheme to find  $\rho_i^{n+1}$  and the explicit scheme finite difference to find  $R_i^{n+1}$  causes the choice of space and time steps to be less confined, even when diffusivity is very high. This is because the semi-implicit scheme is stable for large values of time step  $\Delta t$ , and hence the whole calculation depends on the already less restrictive CFL condition of the discretised hyperbolic equation governing  $R_i^{n+1}$ .



## Chapter 4

# Zero-diffusion limit: hyperbolic conservation laws

### 4.1 Overview

In Chapter 3, it was shown numerically that without cell depletion (i.e.  $A = 0$ ), the evolution equations (23) to (25) in the Cartesian system led to the emergence of shock waves. In the present chapter, we investigate the shock structures in the zero diffusion limit ( $D \approx 0$ ), where we can take advantage of the theory of hyperbolic conservation laws. The first topic of this chapter shows the generation of shocks (or cusps) in the interface in finite time using a theorem by Lax [66, 67]. The second topic investigates the propagation of the cusps and the rarefaction waves in the interface once they have formed.

Both topics cover the focus of research question 3, marked as ③ in Fig. 1.2. Here, the normal acceleration of the interface depends linearly on curvature, which constitutes a type of hyperbolic curvature flow [68] (see Section ‘Materials and Methods’ in Chapter 3).

### 4.2 Introduction

In the zero diffusion limit and without cell depletion ( $D = 0$ ,  $A = 0$ ), Eqs. (23)–(25) of Chapter 3 become:

$$h_t = k_f \eta \tag{4.1}$$

$$\sigma_t + (-k_f \eta)_x = 0 \tag{4.2}$$

$$\eta_t + \left( -\frac{k_f \sigma \eta^2}{1 + \sigma^2} \right)_x = 0. \tag{4.3}$$

The variable  $h = h(x, t)$  in this Cartesian system represents the height of the graph which outlines the tissue interface. As described in Chapter 3, the other variables are  $\sigma = h_x$  and  $\eta = \rho g$  where  $\rho$  is the cell surface density and  $g = \sqrt{1 + h_x^2}$  is the metric associated with the parameterisation. Eq. (4.1) has no flux term and is decoupled from Eqs. (4.2) and (4.3), which enables Eqs. (4.2) and (4.3) to be solved independently. Since  $h$  is the height describing the interface, both  $h, \sigma \in \mathbb{R}$ . By definition,  $\eta$  is the projection of cell surface density onto the  $x$ -coordinate, so  $\eta \geq 0$ . In this study, we look at an evolving portion of the interface and will thereby assume nonzero cell density, so that  $\eta > 0$ .

Eqs. (4.2) and (4.3) can be rewritten as a system of two coupled conservation laws [67]:

$$\mathbf{u}_t + \mathbf{f}(\mathbf{u})_x = \mathbf{0} \quad (4.4)$$

where

$$\mathbf{u} = \begin{pmatrix} u_1 \\ u_2 \end{pmatrix} = \begin{pmatrix} \sigma \\ \eta \end{pmatrix} \quad (4.5)$$

and where

$$\mathbf{f}(\mathbf{u}) = \begin{pmatrix} -k_f \eta \\ \frac{k_f \sigma \eta^2}{1 + \sigma^2} \end{pmatrix} = \begin{pmatrix} -k_f u_2 \\ \frac{k_f u_1 u_2^2}{1 + u_1^2} \end{pmatrix} \quad (4.6)$$

is the hyperbolic flux term. Differentiating with respect to  $x$  gives  $\mathbf{f}(\mathbf{u})_x = \mathbf{f}'(\mathbf{u})\mathbf{u}_x$ . The aim is to find a solution of the nonlinear system in (4.4), given an initial condition:

$$\mathbf{u}(x, 0) = \mathbf{u}_0(x). \quad (4.7)$$

This is called the ‘Cauchy problem’. An important element in hyperbolic conservation laws is the concept of characteristic curve, or can simply be called as characteristic. A characteristic may be defined as a curve  $x = x(t)$  in the  $t$ - $x$  plane along which initial or boundary conditions of the PDEs are transported. However, it is common to use the  $x$ - $t$  plane to draw the characteristic [69].

There are infinitely many characteristics, all of which transport a different portion of the initial or boundary condition. For a single scalar linear conservation law  $u_t + cu_x = 0$  (here we write  $u$  instead of  $\mathbf{u}$  to indicate a scalar quantity), characteristics can be written as:

$$\frac{dx}{dt} = c \Rightarrow x = x_0 + ct \quad (4.8)$$

where  $x_0 = x(0)$ . In this case, the characteristics are parallel with slope  $1/c$  in the  $x$ - $t$  plane and the solution  $u(x, t)$  is constant along these curves, equal to the initial condition  $u_0(x-ct)$  (see, for example, Ref. [69, page 49] on how the solution is obtained). For a nonlinear problem, the characteristics are still lines in the  $x$ - $t$  plane, but these lines are no longer parallel to each other, since  $c = c(u)$ .

In a nonlinear system of conservation laws like in Eq. (4.4), characteristics are no longer straight lines and information from the initial and boundary conditions propagate along several waves related to the eigenvalues of the Jacobian matrix  $\mathbf{f}'(\mathbf{u})$ . For a system of two conservation laws, the 1-characteristics and 2-characteristics are defined by the eigenvalues  $\lambda_1$  and  $\lambda_2$  of  $\mathbf{f}'(\mathbf{u})$  as follows

$$\frac{dx}{dt} = \lambda_1(\mathbf{u}) \quad , \quad \frac{dx}{dt} = \lambda_2(\mathbf{u}). \quad (4.9)$$

In this case, there are two families of characteristics, each corresponds either to the 1-characteristics or 2-characteristics. It is usually difficult to obtain explicit expressions for the characteristics in Eq. (4.9). However, for systems of two conservation laws, the characteristics can be obtained implicitly as contour lines of two functions, the system's ‘‘Riemann invariants’’ (see Sect. 4.2.2).

In general, a smooth solution  $\mathbf{u}(x, t)$  does not exist for all times, as evidenced numerically in Chapter 3 [64, 70]. This is due to the collisions of characteristics, which might occur after a certain time  $t_0$ . Beyond  $t_0$ , solutions containing discontinuities (also called ‘shocks’) are possible. These discontinuous solutions are not differentiable and hence do not satisfy the system of conservation laws in differential form. However, they are solutions of the system of conservation laws in integral form, i.e., they satisfy the integral of Eq. (4.4), in which the derivative of  $\mathbf{f}$  with respect to  $x$  does not need to be evaluated [64].

The integral form of the conservation laws in Eq. (4.4) can be written slightly differently by first multiplying Eq. (4.4) with smooth functions  $\phi = [\phi_1 \ \phi_2]$  which have compact support, before integrating. This gives [64, 70, 71]:

$$\int_0^\infty \int_{-\infty}^\infty (\phi_t \circ \mathbf{u} + \phi_x \circ \mathbf{f}(\mathbf{u})) \, dx dt + \int_{-\infty}^\infty \phi(x, 0) \circ \mathbf{u}(x, 0) \, dx = \mathbf{0} \quad (4.10)$$

where the symbol  $\circ$  indicates component-wise vector multiplication. Note that in Eq. (4.10), the derivative with respect to  $x$  has been transferred onto the smooth functions  $\phi = [\phi_1 \ \phi_2]$  instead of  $\mathbf{u}$  or  $\mathbf{f}(\mathbf{u})$  by integration by parts. This means Eq. (4.10) will still be satisfied even if  $\mathbf{u}$  is not continuous. Any value of  $\mathbf{u}$  that satisfies Eq. (4.10) for all functions  $\phi$  is called a ‘weak solution’ [64]. This consequently implies that any smooth solution of the system of conservation laws in Eq. (4.4) is also a weak solution, but the opposite is not necessarily true.

#### 4.2.1 Eigenstructure of $\mathbf{f}'(\mathbf{u})$

Partially differentiating the hyperbolic flux  $\mathbf{f}(\mathbf{u})$  gives the Jacobian matrix

$$\mathbf{f}'(\mathbf{u}) = \begin{bmatrix} 0 & -k_f \\ -k_f \eta^2 \frac{1 - \sigma^2}{(1 + \sigma^2)^2} & -\frac{2k_f \sigma \eta}{1 + \sigma^2} \end{bmatrix}. \quad (4.11)$$

By solving the eigenvalue problem  $\mathbf{f}'(\mathbf{u})\mathbf{r} = \lambda\mathbf{r}$ , we obtain the eigenvalues  $\lambda_1$  and  $\lambda_2$  such that:

$$\lambda_1 = -\frac{k_f \eta (\sigma + 1)}{1 + \sigma^2}, \quad \lambda_2 = -\frac{k_f \eta (\sigma - 1)}{1 + \sigma^2}. \quad (4.12)$$

If  $\eta = 0$ , the eigenvalues  $\lambda_{1,2} = 0$ . This implies that the system is weakly hyperbolic. If  $\eta > 0$ , the eigenvalues are such that  $\lambda_1 < \lambda_2$ . In this case  $\mathbf{f}'(\mathbf{u})$  is diagonalisable and the system is strictly hyperbolic. Physically,  $\eta > 0$  implies that the velocity  $v > 0$ , and the interface propagates, since the tissue-forming cells are active. Hence, new tissue is continuously produced by these cells. To focus our attention to the evolution of portions of the interface where there is tissue formation by cells, we disregard the case  $\eta = 0$  for now, and hence assume that  $\eta > 0$ .

The right eigenvectors of  $\mathbf{f}'(\mathbf{u})$  corresponding to  $\lambda_1$  and  $\lambda_2$  are:

$$\mathbf{r}_1 = \begin{bmatrix} 1 \\ -\frac{\lambda_1}{k_f} \end{bmatrix} = \begin{bmatrix} 1 \\ \frac{\eta(\sigma+1)}{1+\sigma^2} \end{bmatrix}, \quad \mathbf{r}_2 = \begin{bmatrix} 1 \\ -\frac{\lambda_2}{k_f} \end{bmatrix} = \begin{bmatrix} 1 \\ \frac{\eta(\sigma-1)}{1+\sigma^2} \end{bmatrix}. \quad (4.13)$$

Furthermore, we obtain

$$\nabla \lambda_1(\mathbf{u}) \cdot \mathbf{r}_1(\mathbf{u}) = -\frac{2k_f\eta}{(1+\sigma^2)^2}, \quad \nabla \lambda_2(\mathbf{u}) \cdot \mathbf{r}_2(\mathbf{u}) = -\frac{2k_f\eta}{(1+\sigma^2)^2} \quad (4.14)$$

so that both quantities in Eq. (4.14) are nonzero when  $\eta > 0$ . In this case, the first and second fields associated with the eigenvalues are said to be ‘genuinely nonlinear’ (see Lax [72]). This notion resembles the convexity condition for scalar conservation laws. It implies that the eigenvalues  $\lambda_i, i = 1, 2$  are each strictly monotone along integral curves of the corresponding eigenvectors  $\mathbf{r}_i(\mathbf{u})$  (see Sect. 4.2.2). This guarantees that in the  $x$ - $t$  plane, the characteristics are not parallel to each other, which is likely to give rise to the development of shock wave (when characteristics collide) or rarefaction wave (when characteristics spread). [64, 73].

#### 4.2.2 Riemann invariants and integral curves

To study the nonlinear characteristics in this 2D system and to demonstrate that corners develop, it is useful to find the system’s Riemann invariants, defined to be functions  $w_1(\mathbf{u}), w_2(\mathbf{u})$  such that

$$\nabla w_i \cdot \mathbf{r}_i = 0, \quad i = 1, 2 \quad (4.15)$$

where  $\mathbf{r}_i$  are any of the right eigenvectors defined in Eq. (4.13). From this definition it is clear that Riemann invariants are constant along integral curves of the eigenvectors,  $\mathbf{u}(\beta)$  and  $\mathbf{u}(\gamma)$ , defined as

$$\frac{d\mathbf{u}(\beta)}{d\beta} = \mathbf{r}_1(\mathbf{u}(\beta)), \quad \frac{d\mathbf{u}(\gamma)}{d\gamma} = \mathbf{r}_2(\mathbf{u}(\gamma)). \quad (4.16)$$

Indeed, substituting Eq. (4.16) into Eq. (4.15), we obtain

$$\frac{dw_1(\mathbf{u}(\beta))}{d\beta} = \nabla w_1 \cdot \frac{d\mathbf{u}(\beta)}{d\beta} = 0, \quad \frac{dw_2(\mathbf{u}(\gamma))}{d\gamma} = \nabla w_2 \cdot \frac{d\mathbf{u}(\gamma)}{d\gamma} = 0. \quad (4.17)$$

Riemann invariants are known to exist in general only for a system of two conservation laws. The Riemann invariants  $w_1, w_2$  can be found by integrating Eq. (4.15). A simpler method is to first find the integral curves  $\mathbf{u}(\beta)$  and  $\mathbf{u}(\gamma)$  from Eq. (4.16), before manipulating the integral curves to get the Riemann invariants  $w_i, i = 1, 2$  [64].

If we denote the integral curve as  $\mathbf{u}(\beta) = (\sigma(\beta), \eta(\beta))$ , then using the eigenvector  $\mathbf{r}_1$  from Eq. (4.13) into Eq. (4.16), we have two ODEs as follows:

$$\sigma'(\beta) = 1 \quad , \quad \eta'(\beta) = \frac{\eta(\sigma + 1)}{1 + \sigma^2}. \quad (4.18)$$

Similarly, using the eigenvector  $\mathbf{r}_2$  from Eq. (4.13) into the second equation in (4.16), we produce another system of ODEs as follows:

$$\sigma'(\gamma) = 1 \quad , \quad \eta'(\gamma) = \frac{\eta(\sigma - 1)}{1 + \sigma^2}. \quad (4.19)$$

Solving directly these systems of Eqs. (4.18) and (4.19), we obtain the integral curves of  $\mathbf{r}_1$  and  $\mathbf{r}_2$ , written in general as

$$\eta_1(\sigma) = \eta_* \frac{e^{\arctan(\sigma)} \sqrt{1 + \sigma^2}}{e^{\arctan(\sigma_*)} \sqrt{1 + \sigma_*^2}} \quad , \quad \eta_2(\sigma) = \eta_* \frac{e^{-\arctan(\sigma)} \sqrt{1 + \sigma^2}}{e^{-\arctan(\sigma_*)} \sqrt{1 + \sigma_*^2}} \quad (4.20)$$

where each curve goes through the fixed point  $(\sigma_*, \eta_*)$ . To obtain the Riemann invariants  $w_i, i = 1, 2$ , we rewrite Eqs. (4.20) as

$$\frac{e^{\arctan(\sigma)} \sqrt{1 + \sigma^2}}{\eta} = \frac{e^{\arctan(\sigma_*)} \sqrt{1 + \sigma_*^2}}{\eta_*} \quad , \quad \forall(\sigma, \eta) \quad (4.21)$$

and

$$\frac{e^{-\arctan(\sigma)} \sqrt{1 + \sigma^2}}{\eta} = \frac{e^{-\arctan(\sigma_*)} \sqrt{1 + \sigma_*^2}}{\eta_*} \quad , \quad \forall(\sigma, \eta). \quad (4.22)$$

It is clear from these expressions that the left hand sides of Eqs. (4.21) and (4.22) are constant for any point  $(\sigma, \eta)$  on the integral curves corresponding to  $\mathbf{r}_1$  and  $\mathbf{r}_2$ , respectively. The Riemann invariants can thus be defined as:

$$w_1(\sigma, \eta) = \frac{e^{\arctan(\sigma)} \sqrt{1 + \sigma^2}}{\eta} \quad , \quad w_2(\sigma, \eta) = \frac{e^{-\arctan(\sigma)} \sqrt{1 + \sigma^2}}{\eta}. \quad (4.23)$$

so that  $w_1(\sigma, \eta)$  is constant on any integral curve of  $\mathbf{r}_1$ , and  $w_2(\sigma, \eta)$  is constant on any integral curve of  $\mathbf{r}_2$ . Note that any function of a Riemann invariant is also a Riemann invariant [74]. Fig. 4.1 shows the contour lines of the Riemann invariants  $w_1(\sigma, \eta)$  and  $w_2(\sigma, \eta)$  calculated from Eqs. 4.23.

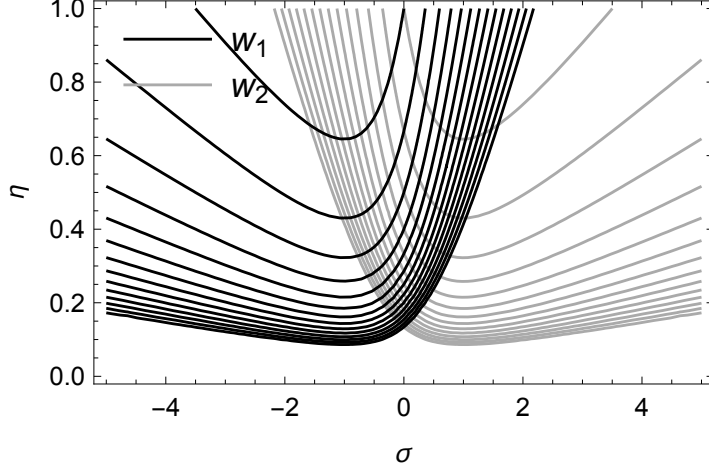


FIGURE 4.1: The contour lines of the Riemann invariants  $w_1(\sigma, \eta)$  and  $w_2(\sigma, \eta)$  calculated from Eqs. 4.23 for values 0.5 to 7.5 (from bottom to top), with an increment of 0.5.

Riemann invariants enable an alternative parameterisation of the phase space, i.e., the mapping between  $(\sigma, \eta)$  and  $(w_1, w_2)$  in Eqs. (4.23) is one-to-one. The inverse transformations are

$$\sigma(w_1, w_2) = \tan \left( \ln \left( \sqrt{\frac{w_1}{w_2}} \right) \right) \quad , \quad \eta(w_1, w_2) = \sqrt{\frac{1 + \sigma(w_1, w_2)^2}{w_1 w_2}}. \quad (4.24)$$

Since our system of two conservation laws is strictly hyperbolic, the right eigenvectors in (4.13) and left eigenvectors  $\mathbf{l}_{1,2}$  are biorthogonal, that is  $\mathbf{l}_1^T \cdot \mathbf{r}_2 = \mathbf{l}_2^T \cdot \mathbf{r}_1 = 0$  [67, 75]. The superscript T indicates matrix transposition. Due to the biorthogonality property and Eq. (4.15), we have  $\mathbf{l}_1^T \propto \nabla w_2$  and  $\mathbf{l}_2^T \propto \nabla w_1$ . Since both  $\mathbf{l}_{1,2}$  are left eigenvectors, then  $\nabla w_1^T \mathbf{f}'(\mathbf{u}) = \lambda_2 \nabla w_1^T$  and  $\nabla w_2^T \mathbf{f}'(\mathbf{u}) = \lambda_1 \nabla w_2^T$ . Left multiplying the system of conservation laws in Eq. (4.4) with  $\nabla w_1^T$ , we thus have  $\nabla w_1^T \mathbf{u}_t + \nabla w_1^T \mathbf{f}'(\mathbf{u}) \mathbf{u}_x = \nabla w_1^T \mathbf{u}_t + \lambda_2 \nabla w_1^T \mathbf{u}_x = \nabla w_1 \cdot \mathbf{u}_t + \lambda_2 \nabla w_1 \cdot \mathbf{u}_x = \mathbf{0}$ . Proceeding similarly with the other field, we obtain  $\nabla w_2 \cdot \mathbf{u}_t + \lambda_1 \nabla w_2 \cdot \mathbf{u}_x = \mathbf{0}$ . Both of these expressions can be written as:

$$(w_2)_t + \lambda_1 (w_2)_x = 0 \quad , \quad (w_1)_t + \lambda_2 (w_1)_x = 0 \quad (4.25)$$

Eqs. (4.25) show that Riemann invariant  $w_1$  is invariant (constant) along the 2-characteristics (defined by  $dx/dt = \lambda_2$ ) and  $w_2$  is invariant along the 1-characteristics (defined by  $dx/dt = \lambda_1$ ), i.e., contour lines of  $w_1$  in the  $x-t$  plane are the 2-characteristics, and contour lines of  $w_2$  in the  $x-t$  plane are the 1-characteristics.

Although  $w_1$  and  $w_2$  are constant along the 2- and 1-characteristics respectively, it is important to note that, in general, the characteristics are not straight lines since  $\lambda_1$  and  $\lambda_2$  depend on  $\mathbf{u} = (\sigma, \eta)$  [67, 74, 75]. It is also not usually possible to have a closed form for  $w_1(x, t)$  and  $w_2(x, t)$ , so we cannot visualise these characteristics (and their collisions) easily. This is where the theorem by Lax presented below (Sect. 4.3) is useful to show that our system of conservation laws in Eq. (4.4) does not permit smooth solutions for all times  $t$ . Here, the inexistence of smooth solutions for all time is shown by the blow-up of the derivative of smooth solutions at a finite time  $t_0$ , rather than by explicitly showing the collisions of characteristics as done usually in the case of single conservation laws.

### 4.3 Finite time blow up of smooth solution

The nonlinearity of the system of conservation laws in Eq. (4.4) with the hyperbolic flux term in Eq. (4.6) can cause a blow up of the derivative of solution  $\mathbf{u}_x$ , regardless of how smooth the initial data is. For a system of two conservation laws, the blow-up can be shown using the Riemann invariants  $w_1$  and  $w_2$  as shown by Lax [66, 67] (see also Refs. [75–77]). Here we enclose the theorem without its proof, and we show how it is applied to our system of equations.

**Theorem 1** (Lax’s finite time blow up). *Suppose  $\partial\lambda_j/\partial w_i > 0$  (or  $< 0$ ),  $i, j = 1, 2, i \neq j$ . Let  $\mathbf{u} = (\sigma, \eta)$  be a solution whose initial value is bounded; then if  $\partial w_i(x, 0)/\partial x < 0$  (or  $> 0$ ) at any point, the derivatives of the solution,  $\mathbf{u}_x = (\sigma_x, \eta_x)$ , become unbounded after a finite time.*

In our system of equations, curvature is equal to  $\kappa = -\sigma_x/(1 + \sigma^2)^{3/2}$ , so that a blow up of  $\sigma_x$  means a blow up of curvature  $\kappa$ , i.e. the development of a corner. In order to utilise Theorem 1, we first need to check the signs of  $\partial\lambda_2/\partial w_1$  and  $\partial\lambda_1/\partial w_2$ . Since the first and second fields associated to the eigenvalues have been shown to be genuinely linear (refer to Sect. 4.2.2), then  $\partial\lambda_2/\partial w_1 \neq 0$  and  $\partial\lambda_1/\partial w_2 \neq 0$ . Indeed, with the one-to-one mapping between  $(\sigma, \eta)$  and  $(w_1, w_2)$ :

$$\frac{\partial \lambda_1(\mathbf{u})}{\partial w_2} = \nabla \lambda_1 \cdot \frac{\partial \mathbf{u}}{\partial w_2} \quad , \quad \frac{\partial \lambda_2(\mathbf{u})}{\partial w_1} = \nabla \lambda_2 \cdot \frac{\partial \mathbf{u}}{\partial w_1}. \quad (4.26)$$

It is clear geometrically that  $\partial \mathbf{u} / \partial w_2$  ( $\partial \mathbf{u} / \partial w_1$ ) is parallel to  $\mathbf{r}_1$  ( $\mathbf{r}_2$ ). Indeed, maintaining  $w_1$  ( $w_2$ ) constant in the derivative  $\partial \mathbf{u} / \partial w_2$  ( $\partial \mathbf{u} / \partial w_1$ ) is equivalent to following a contour line of  $w_1$  ( $w_2$ ) in the  $u = (\sigma, \eta)$  phase space, and therefore considering an integral curve  $\mathbf{u}(\beta)$  ( $\mathbf{u}(\gamma)$ ) of the vector field  $\mathbf{r}_1$  ( $\mathbf{r}_2$ ). In this case we can change the coordinate  $\beta$  ( $\gamma$ ) for the coordinate  $w_2$  ( $w_1$ ). Using Eq. (4.16) we obtain

$$\frac{d\mathbf{u}(\beta(w_2))}{dw_2} = \mathbf{r}_1(\mathbf{u}(\beta)) \frac{d\beta}{dw_2} \quad , \quad \frac{d\mathbf{u}(\gamma(w_1))}{dw_1} = \mathbf{r}_2(\mathbf{u}(\gamma)) \frac{d\gamma}{dw_1}. \quad (4.27)$$

Plugging Eq. (4.27) into Eq. (4.26), we therefore obtain

$$\frac{\partial \lambda_1(\mathbf{u})}{\partial w_2} = \nabla \lambda_1 \cdot \mathbf{r}_1 \frac{d\beta}{dw_2} \quad , \quad \frac{\partial \lambda_2(\mathbf{u})}{\partial w_1} = \nabla \lambda_2 \cdot \mathbf{r}_2 \frac{d\gamma}{dw_1}. \quad (4.28)$$

An explicit calculation using Eqs. (4.24) shows that in our system, we have

$$\frac{\partial \mathbf{u}}{\partial w_1} = \frac{1 + \sigma^2}{2w_1} \mathbf{r}_2 \quad , \quad \frac{\partial \mathbf{u}}{\partial w_2} = -\frac{1 + \sigma^2}{2w_2} \mathbf{r}_1 \quad (4.29)$$

so that

$$\frac{\partial \lambda_1(\mathbf{u})}{\partial w_2} = -\frac{1 + \sigma^2}{2w_2} \nabla \lambda_1 \cdot \mathbf{r}_1 \quad , \quad \frac{\partial \lambda_2(\mathbf{u})}{\partial w_1} = \frac{1 + \sigma^2}{2w_1} \nabla \lambda_2 \cdot \mathbf{r}_2. \quad (4.30)$$

Eq. (4.30) can be simplified by using Eqs. (4.14) and (4.23). This gives

$$\frac{\partial \lambda_1(\mathbf{u})}{\partial w_2} = \frac{k_f \eta^2}{e^{-\arctan(\sigma)} (1 + \sigma^2)^{3/2}} > 0 \quad , \quad \frac{\partial \lambda_2(\mathbf{u})}{\partial w_1} = -\frac{k_f \eta^2}{e^{\arctan(\sigma)} (1 + \sigma^2)^{3/2}} < 0. \quad (4.31)$$

The hypotheses of Lax's theorem are thus satisfied, so that a finite time blow up will occur if  $\frac{\partial w_1(x,0)}{\partial x} > 0$  or  $\frac{\partial w_2(x,0)}{\partial x} < 0$  at any point  $x$ . We now calculate the initial derivatives  $\partial w_i(x,0) / \partial x$ ,  $i, j = 1, 2, i \neq j$ . Since the Riemann invariants  $w_i$ ,  $i = 1, 2$  are functions of the variables  $\sigma$  and  $\eta$ , then  $\frac{\partial w_i(x,0)}{\partial x} = \frac{\partial w_i}{\partial \sigma} \sigma'_0(x) + \frac{\partial w_i}{\partial \eta} \eta'_0(x)$ , where  $\sigma_0(x) = \sigma_0(x, t = 0)$  and  $\eta_0(x) = \eta(x, t = 0)$ . Using Eq. (4.23), the definition of curvature

$\kappa_0(x) = -\sigma'_0(x)/(1 + \sigma_0^2(x))^{3/2}$ , and of projected cell density  $\eta_0(x) = \rho_0(x)\sqrt{1 + \sigma_0^2(x)}$ , we have:

$$\frac{\partial w_{1,2}(x, 0)}{\partial x} = \frac{e^{\pm \arctan(\sigma_0(x))}(1 + \sigma_0^2(x))}{\eta_0^2(x)}(\mp \kappa_0(x)\eta_0(x) - \rho'_0(x)). \quad (4.32)$$

It is now clear that corners will develop in finite time whenever there is a portion of the initial interface with negative curvature, i.e.  $\kappa_0(x) < 0$ . If the initial surface density of cells is uniform, i.e.  $\rho_0(x) = \rho_0 = \text{const}$ , then both  $\frac{\partial w_1}{\partial x}(x, 0) > 0$  and  $\frac{\partial w_2}{\partial x}(x, 0) < 0$  where  $\kappa_0(x) < 0$  (only one of these inequalities is necessary for finite time blow up). For other initial surface cell densities  $\rho_0(x)$ , the subtraction by  $\rho'_0(x)$  in Eq. (4.32) may compensate and change the sign of either  $\partial w_1(x, 0)/\partial x$  or  $\partial w_2(x, 0)/\partial x$  but not of both simultaneously, so that corners also develop in finite time. If  $\kappa_0(x)$  is positive everywhere, then by Eq. (4.32), a blow up can only occur if the initial density of cell is not homogeneous, specifically when (i)  $\rho'_0(x) < -\kappa_0(x)\eta_0(x)$ ; or (ii)  $\rho'_0(x) > \kappa_0(x)\eta_0(x)$ .

In Sect. ‘Influence of cell diffusion on interface smoothing’ of Chapter 3, we use the initial interface described by the function  $h_0(x) = 2 + \frac{1}{2} \cos(3x)$  and homogeneous cell surface density  $\rho_0 = 0.016\text{mm/day}$  for  $x \in [0, 2\pi)$ . The curvature of the interface is  $\kappa_0(x) = \frac{(h_0)_{xx}}{[1+(h_0)_x^2]^{3/2}}$ . Since the denominator is always greater than zero, the sign of the initial curvature  $\kappa_0(x)$  is the same as the sign of the second derivative  $(h_0)_{xx}$ . In our equation, we have  $(h_0)_{xx} = -\frac{9}{2} \cos(3x)$  for  $x \in [0, 2\pi)$  which changes sign at every  $x = i\pi/3$  for  $i = 0, \dots, 6$ . This shows that the solution blows up in finite time by Theorem 1.

## 4.4 Wave structure in the Riemann problem

A Riemann problem is a Cauchy problem with initial data  $\mathbf{u}_0(x)$ , such that

$$\mathbf{u}_0(x) = \begin{cases} \mathbf{u}_l & \text{if } x < 0 \\ \mathbf{u}_r & \text{if } x > 0 \end{cases} \quad (4.33)$$

where  $\mathbf{u}_l$  and  $\mathbf{u}_r$  are constant states. In this section, we study the structure of waves that develop in the Riemann problem. Despite its simplicity, the Riemann problem is important in several aspects. First, Riemann problems enable us to understand how shocks propagate after their emergence. Indeed, after a shock is generated by the collision of characteristics, the solution becomes discontinuous there, and the future

evolution of the problem in a small neighbourhood around the shock is similar to a Riemann problem. Secondly, the solution of the Riemann problem has always been useful in formulating numerical methods and assessing their performance and accuracy, and hence becomes the ‘building block’ for these numerical methods (called ‘Riemann solvers’) [69]. Thirdly, Riemann problems generally give rise to three possible elementary waves in their solution which are a shock wave, a rarefaction wave, and a contact discontinuity [64, 67]. This helps ones to understand the wave structures.

In our system of two conservation laws, the solution to the Riemann problem consists of three states: the left state  $\mathbf{u}_l = (\sigma_l, \eta_l)$ , the middle state  $\mathbf{u}_m = (\sigma_m, \eta_m)$ , and the right state  $\mathbf{u}_r = (\sigma_r, \eta_r)$ . Since the system is genuinely nonlinear (see Eq. (4.14)), the middle state  $\mathbf{u}_m$  can be connected to the left and right states either by a shock wave or by a rarefaction wave [78] (see Sect. 4.4.2 and 4.4.3). The left state  $\mathbf{u}_l$  and right state  $\mathbf{u}_r$  are known from the initial data of the Riemann problem in Eq. (4.33), while the middle state  $\mathbf{u}_m$  is unknown and has to be determined.

#### 4.4.1 Determination of the middle state $\mathbf{u}_m$

As mentioned, our system of two conservation laws may generate a rarefaction wave and a shock wave in each 1- and 2-fields associated with  $\lambda_1$  and  $\lambda_2$ , respectively. This gives four possible wave combinations that can be used to determine the middle state  $\mathbf{u}_m$ , which are:

- (i) 1- and 2-rarefaction waves: The state  $\mathbf{u}_m$  can be determined from the intersection point of the 1-integral curve (of 1-field) and the 2-integral curve (of 2-field).
- (ii) 1-rarefaction wave and 2-shock wave: The state  $\mathbf{u}_m$  can be determined from the intersection point of the 1-integral curve (of 1-field) and 2-Hugoniot locus (of 2-field) (see Sect. 4.4.3 for the definition of a Hugoniot locus).
- (iii) 1-shock wave and 2-rarefaction wave: The state  $\mathbf{u}_m$  can be determined from the intersection point of the 1-Hugoniot locus (of 1-field) and the 2-integral curve (of 2-field).
- (iv) 1- and 2-shock waves: The state  $\mathbf{u}_m$  can be determined from the intersection point of the 1-Hugoniot locus (of 1-field) and 2-Hugoniot locus (of 2-field).

Details on these wave combinations are presented in the next sections.

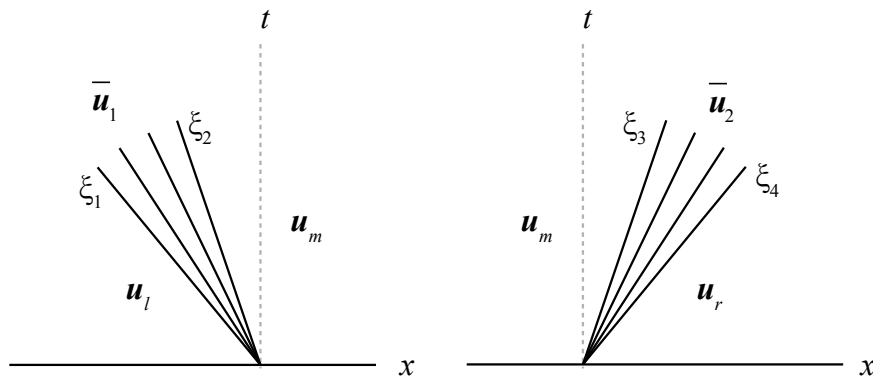


FIGURE 4.2: 1-rarefaction wave between the left state  $\mathbf{u}_l$  and the middle state  $\mathbf{u}_m$  in the 1-field (left); 2-rarefaction wave between the middle state  $\mathbf{u}_m$  and the right state  $\mathbf{u}_r$  in the 2-field (right). Note that in both cases the characteristics are spread out.

#### 4.4.2 Rarefaction waves

In a Riemann problem, a centered rarefaction wave is a continuous wave in the genuinely nonlinear field. Taking  $\xi = x/t$ , a solution with the 1-rarefaction wave can be written as (see Fig. 4.2 (left)):

$$\mathbf{u}(x, t) = \begin{cases} \mathbf{u}_l & \text{if } \xi \leq \xi_1 \\ \bar{\mathbf{u}}_1(\xi) & \text{if } \xi_1 \leq \xi \leq \xi_2 \\ \mathbf{u}_m & \text{if } \xi \geq \xi_2 \end{cases} \quad (4.34)$$

while a solution with the 2-rarefaction wave can be written as (see Fig. 4.2 (right))

$$\mathbf{u}(x, t) = \begin{cases} \mathbf{u}_m & \text{if } \xi \leq \xi_3 \\ \bar{\mathbf{u}}_2(\xi) & \text{if } \xi_3 \leq \xi \leq \xi_4 \\ \mathbf{u}_r & \text{if } \xi \geq \xi_4. \end{cases} \quad (4.35)$$

In the  $x$ - $t$  plane,  $\xi_1$  and  $\xi_3$  represent the left boundary of the rarefaction waves, while  $\xi_2$  and  $\xi_4$  represent the right boundary of the rarefaction waves. Each of these boundaries starts at the origin since the discontinuity of the initial data in the Riemann problem is assumed to take place at the origin. These boundaries and the solutions  $\bar{\mathbf{u}}_1$  and  $\bar{\mathbf{u}}_2$  for  $\xi$  between these two boundaries require first the determination of the middle state  $\mathbf{u}_m$ .

In both the 1- and 2-rarefaction waves, the possible middle states  $\mathbf{u}_m$  must lie on their corresponding integral curves only (see the integral curves in Eq. (4.20) obtained for our system). However, not all points on the integral curves are physically correct. A physically correct  $\mathbf{u}_m$  needs to satisfy a rarefaction condition. This condition ensures

that characteristics of the solution spread and hence do not collide with each other, which would otherwise correspond to a shock wave (refer to Figure 4.2). In our system, the 1-rarefaction condition is  $\sigma_l > \sigma_m$  while the 2-rarefaction condition is  $\sigma_m > \sigma_r$  (see Appendix A.1 for the calculations of the rarefaction conditions). Once the middle state  $\mathbf{u}_m$  has been obtained, the quantities  $\bar{\mathbf{u}}_1$ ,  $\bar{\mathbf{u}}_2$ , and the boundaries  $\xi_j$  (where  $j = 1, \dots, 4$ ) can be determined (see Appendix A.2 for the calculations).

#### 4.4.3 Shock waves

The second type of solution produced by a Riemann problem in a genuinely nonlinear field is called a shock wave. In contrast to the rarefaction wave, a shock wave is a discontinuous wave. A solution with the 1-shock wave can be written as (see Fig. 4.3 (left)):

$$\mathbf{u}(x, t) = \begin{cases} \mathbf{u}_l & \text{if } x/t < s_1 \\ \mathbf{u}_m & \text{if } x/t > s_1 \end{cases} \quad (4.36)$$

while for the 2-shock wave, the solution will be (see Fig. 4.3 (right))

$$\mathbf{u}(x, t) = \begin{cases} \mathbf{u}_m & \text{if } x/t < s_2 \\ \mathbf{u}_r & \text{if } x/t > s_2 \end{cases} \quad (4.37)$$

where  $s_1$  and  $s_2$  are the shock speeds. In the  $x$ - $t$  plane, the shocks start at the origin since the discontinuity of the initial data in the Riemann problem is assumed to take place at the origin.

In both the 1- and 2-shock waves, the possible middle state  $\mathbf{u}_m$  must lie on their corresponding Hugoniot loci only, known as 1-Hugoniot locus and 2-Hugoniot locus, respectively. The 1-Hugoniot locus represents the curve through the point  $\mathbf{u}_l$  consisting of all states that can be connected to  $\mathbf{u}_l$  by the 1-shock, and the 2-Hugoniot locus is the curve through the point  $\mathbf{u}_r$  consisting of all states that can be connected to  $\mathbf{u}_r$  by the 2-shock. The loci (and the shock speeds) are developed by utilising the Rankine-Hugoniot condition (see Appendix A.3 for the calculations of the Hugoniot loci and the formulae of the shock speeds for our problem).

However, not all points on the Hugoniot loci are physically correct. The use of entropy conditions helps determine admissible solutions among the numerous (weak) solutions. The entropy conditions state that a shock requires characteristics to run into the shock, as time advances (refer to Fig. 4.3), since a discontinuity with characteristics

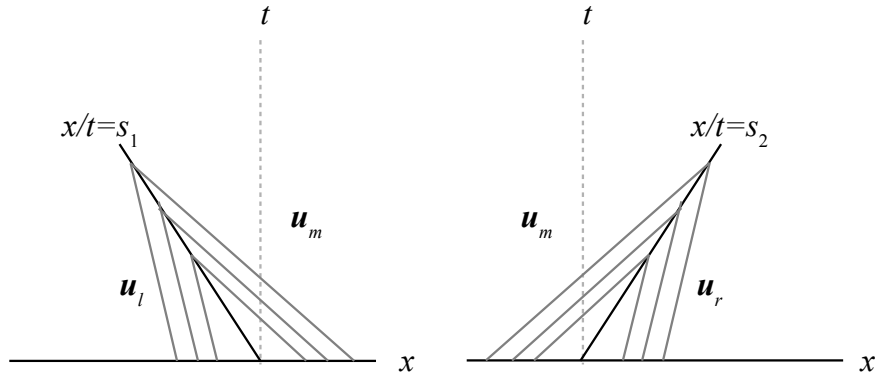


FIGURE 4.3: 1-shock connecting the left state  $\mathbf{u}_l$  and the middle state  $\mathbf{u}_m$  in the 1-field (left); 2-shock connecting the middle state  $\mathbf{u}_m$  and the right state  $\mathbf{u}_r$  in the 2-field (right). Note that in both cases the characteristics going into the shocks. The shock speeds are denoted as  $s_1$  and  $s_2$ .

emanating from it would be unstable to perturbations. Hence, in a genuinely nonlinear system, any Riemann problem will have a shock as its solution if an entropy condition is satisfied. Otherwise, the solution will be in the form of a rarefaction wave [64, 67]. Therefore, in our system, the 1-entropy condition is

$$\begin{aligned} \sigma_l < \sigma_m < -1/\sigma_l & \text{ if } \sigma_l < 0 \\ \sigma_m > \sigma_l & \text{ if } \sigma_l \geq 0. \end{aligned} \quad (4.38)$$

while the 2-entropy condition

$$\begin{aligned} \sigma_m < \sigma_r & \text{ if } \sigma_r \leq 0 \\ -1/\sigma_r < \sigma_m < \sigma_r & \text{ if } \sigma_r > 0. \end{aligned} \quad (4.39)$$

(see Appendix A.4 for how to find these entropy conditions). Once the middle state  $\mathbf{u}_m$  has been obtained, the shock speeds  $s_i, i = 1, 2$  can be determined.

#### 4.4.4 Results

The cosine function  $h(x, 0) = 2 + \frac{1}{2} \cos(3x), x \in [0, 2\pi]$  used in Chapter 3 contains portions that are concave and convex (see Section ‘Influence of cell diffusion on interface smoothing’ in Chapter 3). In Chapter 3 also, we have seen the development of shocks and centered rarefaction waves.

In this section, we test the model equations (in the zero diffusion limit) on two types of initial condition: a concave interface with a constant cell density and a convex

interface with a constant cell density. The concave interface is expected to produce an all-shock solution, while the convex interface is expected to produce an all-rarefaction solution. Investigating the mixture of the two waves (1-shock & 2-rarefaction or 1-rarefaction & 2-shock) is also possible, but it requires the consideration of both integral curves and Hugoniot loci simultaneously. These wave combinations will not be investigated further in this thesis.

For simplicity, we follow Chapter 3 (see Section ‘Scaling analysis and choice of units’) on the choice of units. In this regards, the length will be mentioned in ‘mm’, the cell secretary rate is dimensionless with  $k_f = 1$ , and the cell density corresponds to the velocity  $v$ , hence having a unit of ‘mm day<sup>-1</sup>’. Consequently,  $\sigma$  is dimensionless while  $\eta$  has the same unit as  $\rho$ .

#### 4.4.4.1 All-rarefaction problem

We consider a  $\Lambda$ -shaped interface with constant initial cell density, as shown by the red curves in the top plots of Fig 4.4. Specifically, we take the initial height  $h(x, t = 0) = 2x + 11$  for  $-5 \leq x \leq 0$  and  $h(x, t = 0) = -2x + 11$  for  $0 \leq x \leq 5$ , while the initial cell density is a constant  $\rho(x, t = 0) = 8.9443$  mm day<sup>-1</sup> for  $-5 \leq x \leq 5$ . From the change of variables in Sect. 4.2, that is  $\sigma = h_x$  and  $\eta = \rho\sqrt{1 + \sigma^2}$ , we obtain a Riemann problem centered at the origin for  $\mathbf{u} = (\sigma, \eta)$ , such that  $\sigma_l = 2$  and  $\sigma_r = -2$  and  $\eta_l = \eta_r = 20$ . We need to find the middle state  $\mathbf{u}_m = (\sigma_m, \eta_m)$ .

Due to the convexity of the initial interface, characteristics of the left portion of the interface (i.e. at  $-5 \leq x \leq 0$ ) propagate away from the characteristics of the right portion of the interface (i.e. at  $0 \leq x \leq 5$ ). Thus, we expect a solution that contains two rarefaction waves, as shown numerically in Chapter 3.

In this regard, the integral curves that correspond to the 1- and 2-rarefaction waves are (refer to Eq. (4.20)),

$$\eta_1 = \eta_l \frac{e^{\arctan(\sigma)} \sqrt{1 + \sigma^2}}{e^{\arctan(\sigma_l)} \sqrt{1 + \sigma_l^2}}, \quad \eta_2 = \eta_r \frac{e^{-\arctan(\sigma)} \sqrt{1 + \sigma^2}}{e^{-\arctan(\sigma_r)} \sqrt{1 + \sigma_r^2}}. \quad (4.40)$$

From Eq. (A.2), the range of  $\sigma_m$  which satisfies the 1-rarefaction condition is  $\sigma_m < \sigma_l$ , while from Eq. (A.4), the range of  $\sigma_m$  which satisfies the 2-rarefaction condition is  $\sigma_m > \sigma_r$ . Since the initial conditions i.e. the  $\Lambda$ -shaped interface and the initial density imply a symmetrical problem, the middle state for  $\sigma$  is  $\sigma_m = 0$ . Substituting  $\sigma_m = 0$

into any of the equations in (4.40), we then obtain  $\eta_m \approx 2.9561$ . Therefore, the pair  $\mathbf{u}_m \approx (0, 2.9561)$  is the middle state of the solution.

States connected by rarefaction waves must lie on integral curves (while states connected by shocks must lie on Hugoniot loci). The integral curves from Eq. (4.40) and the three states  $\mathbf{u}_l$ ,  $\mathbf{u}_m$  and  $\mathbf{u}_r$ , are shown in Fig. 4.6 (left). The red curve (denoted as  $R_1$ ) represents the 1-integral curve of the eigenvector  $\mathbf{r}_1$  through the point  $\mathbf{u}_l$ . This curve comprises all possible states that can be connected to  $\mathbf{u}_l$  by the 1-rarefaction wave. The blue curve (denoted as  $R_2$ ) is the 2-integral curve of the  $\mathbf{r}_2$  through the point  $\mathbf{u}_r$ . It consists of all possible states that can be connected to  $\mathbf{u}_l$  by the 2-rarefaction wave. The intersection of  $R_1$  and  $R_2$  is the middle state  $\mathbf{u}_m$ .

Note that in Fig. 4.6 (left) the dashed red and blue curves locate points that do not correspond to physically correct solutions connected to  $\mathbf{u}_l$  and  $\mathbf{u}_r$ , due to the violation of the rarefaction conditions in Eqs. (A.2) and (A.4). The point  $\mathbf{u}_m$  obtained falls onto the solid portions of the integral curves, and hence it is a correct middle state.

Any other types of wave combination (1-rarefaction & 2-shock, 1-shock & 2-rarefaction, and 1-shock and 2-shock) are not possible in this case. This is shown in Fig. 4.6 (right) where each of these non-feasible solutions would have a state  $\mathbf{u}_m$  lying at the intersection of at least one dashed curve. Specifically, 1-rarefaction & 2-shock would have state  $\mathbf{u}_m$  at intersection of  $R_1$  and  $S_2$ : there,  $S_2$  is dashed due to the violation of entropy condition. For 1-shock & 2-rarefaction, the intersection of the curves  $S_1$  and  $R_2$  occurs at the dashed portion of  $S_1$ , caused by the violation of the entropy condition. The case 1-shock & 2-shock is also not possible since the intersection occurs at the dashed portions of both  $S_1$  and  $S_2$  indicating the violation of the entropy conditions.

The solution is thus an all-rarefaction solution that has the form (see Sect. 4.4.2):

$$\mathbf{u}(x, t) = \begin{cases} \mathbf{u}_l & \text{if } x/t \leq \lambda_1(\mathbf{u}_l) \\ \bar{\mathbf{u}}_1\left(\frac{x}{t}\right) & \text{if } \lambda_1(\mathbf{u}_l) \leq x/t \leq \lambda_1(\mathbf{u}_m) \\ \mathbf{u}_m & \text{if } \lambda_1(\mathbf{u}_m) \leq x/t \leq \lambda_2(\mathbf{u}_m) \\ \bar{\mathbf{u}}_2\left(\frac{x}{t}\right) & \text{if } \lambda_2(\mathbf{u}_m) \leq x/t \leq \lambda_2(\mathbf{u}_r) \\ \mathbf{u}_r & \text{if } x/t \geq \lambda_2(\mathbf{u}_r) \end{cases} \quad (4.41)$$

where  $\bar{\mathbf{u}}_1\left(\frac{x}{t}\right) = (\bar{\sigma}_1, \bar{\eta}_1)$  is obtained from Eqs. (A.12) and (A.13). Similarly,  $\bar{\mathbf{u}}_2\left(\frac{x}{t}\right) = (\bar{\sigma}_2, \bar{\eta}_2)$  is obtained from Eqs. (A.18) and (A.19). Due to the complexity of these equations, both  $\bar{\mathbf{u}}_1$  and  $\bar{\mathbf{u}}_2$  need to be calculated numerically using the Newton's method or any other root-finding algorithm, making this whole method to be semi-analytic. The solution  $\mathbf{u} = (\sigma, \eta)$  at time  $t = 0.2$  is shown by the black curves in Fig 4.4 (bottom

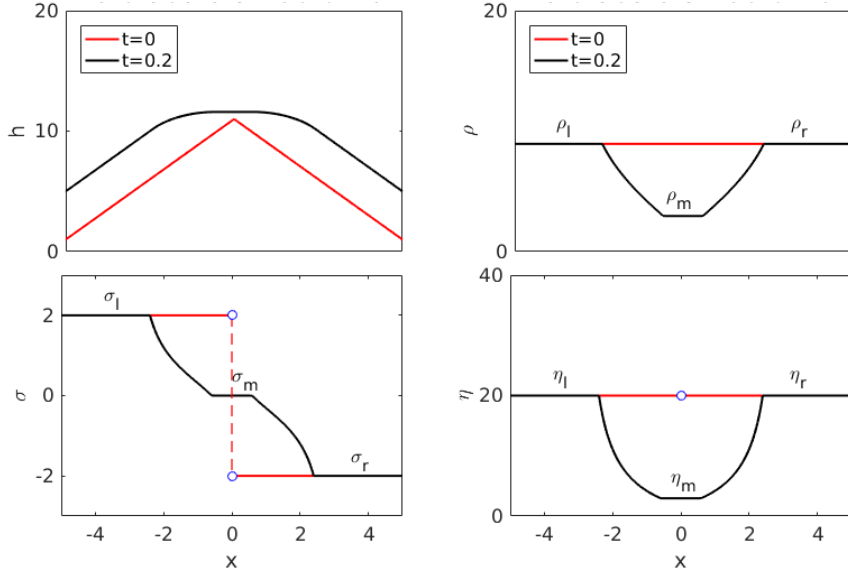


FIGURE 4.4: Semi-analytical method producing two rarefactions in  $\sigma$  and  $\eta$  (bottom plots), where these variables can be converted back to the original variables: the height  $h$  and density  $\rho$  (top plots). The initial states are indicated by the red curves while the evolved states at  $t = 0.2$  are coloured in black. The sequence of the change of the variables and their evolutions is  $(h_0, \rho_0) \rightarrow (\sigma_0, \eta_0) \rightarrow (\sigma_{0.2}, \eta_{0.2}) \rightarrow (h_{0.2}, \rho_{0.2})$ . Note that at  $x = 0$ ,  $\sigma_0 = (h_x)_0$  and hence  $\eta_0$  are undefined.

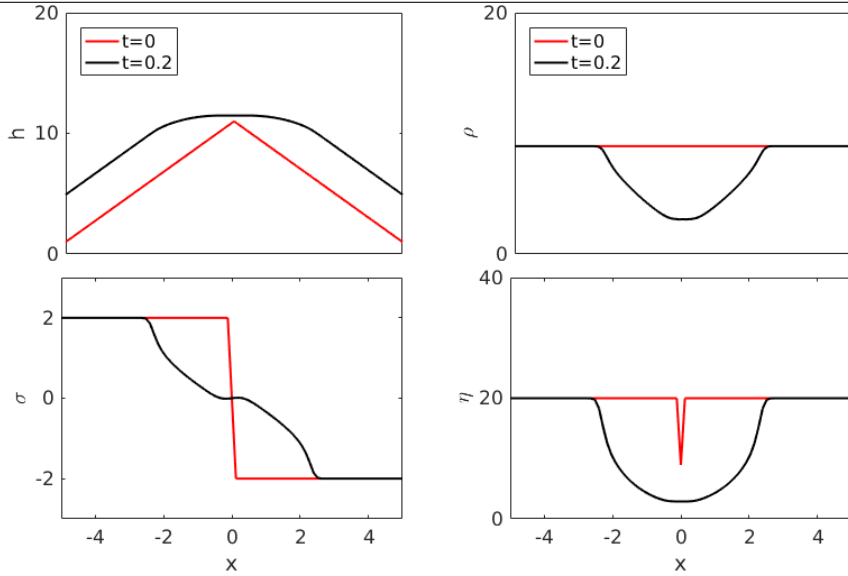


FIGURE 4.5: Numerical method (Kurganov-Tadmor scheme) producing two rarefactions in  $\sigma$  and  $\eta$  (bottom plots), where these variables can be converted back to the original variables: the height  $h$  and density  $\rho$  (top plots). The initial states are indicated by the red curves while the evolved states at  $t = 0.2$  are coloured in black. The sequence of the change of the variables and their evolutions is  $(h_0, \rho_0) \rightarrow (\sigma_0, \eta_0) \rightarrow (\sigma_{0.2}, \eta_{0.2}) \rightarrow (h_{0.2}, \rho_{0.2})$ . Since a centered difference was used to find  $\sigma_0$  from  $h_0$ , we obtained  $\sigma_0 = (h_x)_0 = 0$  at  $x = 0$ , and that consequently produced a spike in  $\eta_0$  at  $x = 0$ .

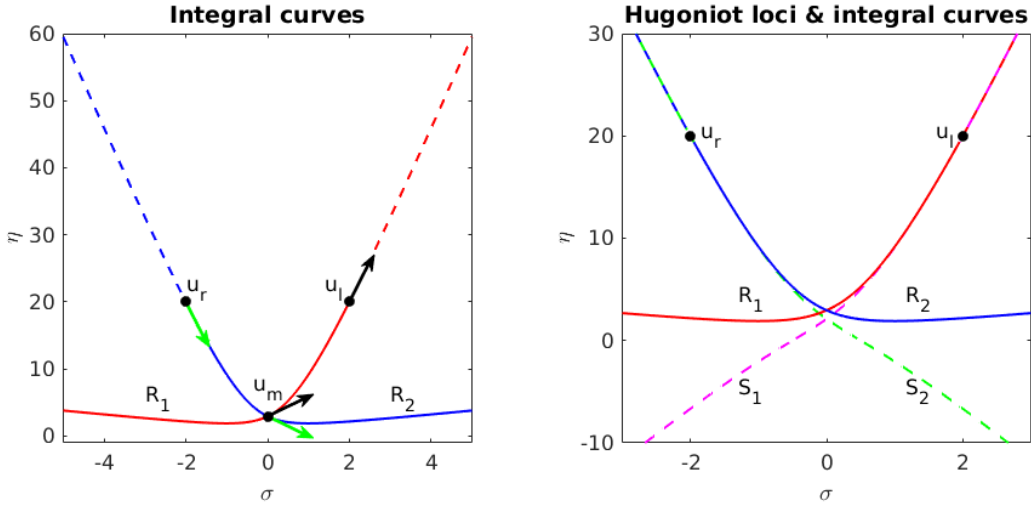


FIGURE 4.6: (Left) Integral curves for two rarefactions solution, denoted as  $R_1$  and  $R_2$ . Note that the eigenvectors  $\mathbf{r}_1$  (black) and  $\mathbf{r}_2$  (green) are always tangential to the curves  $R_1$  and  $R_2$ , respectively, at any points. (Right)  $S_1$ : 1-Hugoniot loci;  $R_1$ : 1-integral curve;  $S_2$ : 2-Hugoniot loci;  $R_2$ : 2-integral curve. Note that the dashed portions of the curves indicate violation of rarefaction/entropy condition.

plots). Fig. 4.4 (top plots) shows the solution in terms of the original variables, the height  $h$  and surface cell density  $\rho$ . Comparison with the output produced in Fig. 4.5 by numerical calculation using the finite volume scheme described in Chapter 3 shows a very good match, where the finite volume scheme causes smoothing of solution.

#### 4.4.4.2 All-shock problem

We consider now a V-shaped interface with constant initial cell density, as shown by the red curves in the top plots of Fig 4.7. In this regard, we take the initial height  $h(x, t = 0) = -2x + 1$  for  $-5 \leq x \leq 0$  and  $h(x, t = 0) = 2x + 1$  for  $0 \leq x \leq 5$ . The initial cell density is a constant  $\rho(x, t = 0) = 8.9443 \text{ mm day}^{-1}$  for  $-5 \leq x \leq 5$ . From the change of variables in Sect. 4.2, we obtain a Riemann problem centered at the origin such that  $\sigma_l = -2$  and  $\sigma_r = -\sigma_l = 2$ , and  $\eta_l = \eta_r = 20$ . Again, we need to find the middle state  $\mathbf{u}_m = (\sigma_m, \eta_m)$ .

Due to the concavity of the initial interface, characteristics of the left portion of the interface collide with the characteristics of the right portion of the interface. We thereby expect a solution that contains two shock waves, as shown numerically in Chapter 3.

In this regard, the Hugoniot loci for the 1-shock and 2- shock are (refer to Eqs. (A.27) and (A.28)):

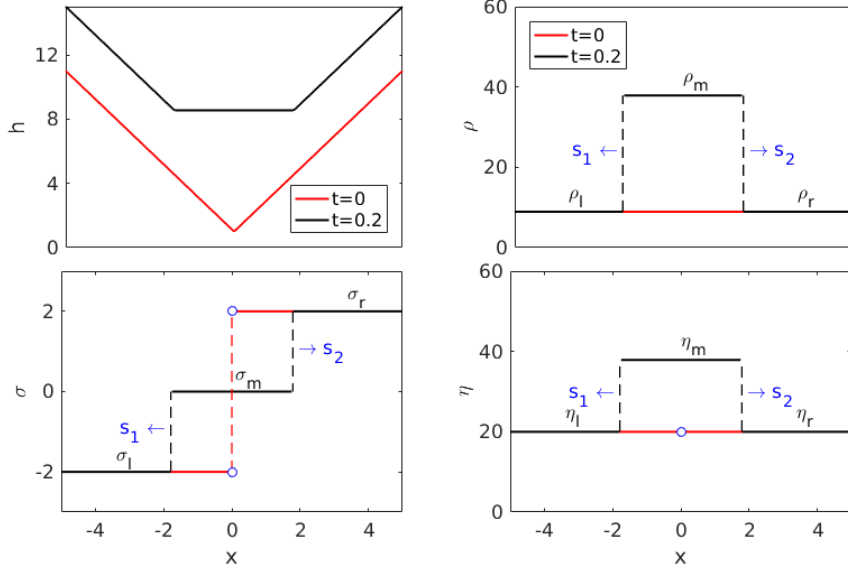


FIGURE 4.7: Analytical method producing two shocks in  $\sigma$  and  $\eta$  (bottom plots) where these variables can be converted back to the original variables: the height  $h$  and density  $\rho$  (top plots). The initial states are indicated by the red curves while the evolved states are coloured in black. The sequence of the change of the variables and their evolutions is  $(h_0, \rho_0) \rightarrow (\sigma_0, \eta_0) \rightarrow (\sigma_{0.2}, \eta_{0.2}) \rightarrow (h_{0.2}, \rho_{0.2})$ . Note that at  $x = 0$ ,  $\sigma_0 = (h_x)_0$  and hence  $\eta_0$  are undefined.

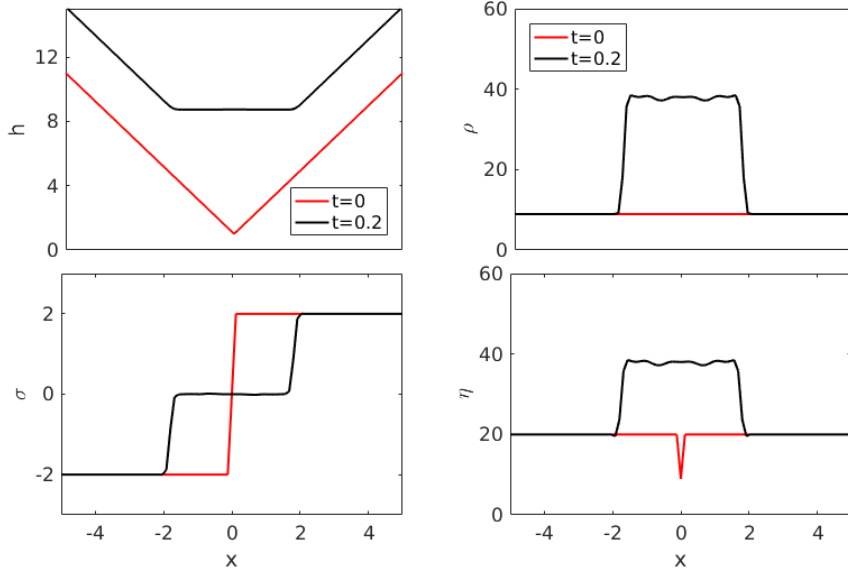


FIGURE 4.8: Numerical method (Kurganov-Tadmor scheme) producing two shocks in  $\sigma$  and  $\eta$  (bottom plots) where these variables can be converted back to the original variables: the height  $h$  and density  $\rho$  (top plots). The initial states are indicated by the red curves while the evolved states are coloured in black. The sequence of the change of the variables and their evolutions is  $(h_0, \rho_0) \rightarrow (\sigma_0, \eta_0) \rightarrow (\sigma_{0.2}, \eta_{0.2}) \rightarrow (h_{0.2}, \rho_{0.2})$ . Since a centered difference was used to find  $\sigma_0$  from  $h_0$ , we obtained  $\sigma_0 = (h_x)_0 = 0$  at  $x = 0$ , and that consequently produced a spike in  $\eta_0$  at  $x = 0$ .

$$\eta_1 = \frac{\eta_l}{1 + \sigma\sigma_l} \left[ (1 + \sigma^2) - (\sigma_l - \sigma) \sqrt{\frac{1 + \sigma^2}{1 + \sigma_l^2}} \right] \quad (4.42)$$

$$\eta_2 = \frac{\eta_r}{1 + \sigma\sigma_r} \left[ (1 + \sigma^2) + (\sigma_r - \sigma) \sqrt{\frac{1 + \sigma^2}{1 + \sigma_r^2}} \right]. \quad (4.43)$$

From Eq. (4.38), the range of  $\sigma_m$  which satisfies the entropy condition of 1-shock in Eq. (4.38) is  $\sigma_l < \sigma_m < -1/\sigma_l$ , while from Eq. (4.39), the range of  $\sigma_m$  which satisfies the entropy condition of 2-shock is  $-1/\sigma_r < \sigma_m < \sigma_r$ . Since the initial conditions, i.e. the V-shape interface and the initial density imply a symmetrical problem,  $\sigma_m = 0$  is again the middle state for  $\sigma$ . Substituting  $\sigma_m = 0$  into any of Eqs. (4.42) and (4.43), we then obtain  $\eta_m \approx 37.8885$ , and hence the set  $\mathbf{u}_m \approx (0, 37.8885)$  is the middle state of the solution.

States connected by shock waves must lie on Hugoniot loci. The Hugoniot loci (from Eqs. (4.42) and (4.43)) and the three states  $\mathbf{u}_l$ ,  $\mathbf{u}_m$  and  $\mathbf{u}_r$  are shown in Fig. 4.9 (left). The red curve (denoted as  $S_1$ ) represents the locus of 1-shock through the point  $\mathbf{u}_l$  consisting of all states that can be connected to  $\mathbf{u}_l$  by the 1-shock, and the blue curve (denoted as  $S_2$ ) is the locus of 2-shock through the point  $\mathbf{u}_r$  consisting of all states that can be connected to  $\mathbf{u}_r$  by the 2-shock. The intersection of  $S_1$  and  $S_2$  is the middle state  $\mathbf{u}_m$ . Note that the dashed red and blue curves locate the points that do not correspond to physically correct solutions connected to  $\mathbf{u}_l$  and  $\mathbf{u}_r$ , respectively, due to the violation of entropy conditions in Eqs. (4.38) and (4.39).

In this problem, any other type of wave combination (1-rarefaction & 2-shock, 1-shock & 2-rarefaction, and 1-rarefaction and 2-rarefaction) is not possible. This is shown in Fig. 4.9 (right) where each of these non-feasible solutions would have a state  $\mathbf{u}_m$  lying at the intersection of at least one dashed curve. Specifically, 1-rarefaction & 2-shock would have state  $\mathbf{u}_m$  at the intersection of  $R_1$  and  $S_2$ : there,  $S_2$  is dashed due to the violation of the entropy condition. For 1-shock & 2-rarefaction, the intersection of the curves  $S_1$  and  $R_2$  occurs at the dashed portion of  $S_1$ , caused by the violation of the entropy condition. The case 1-rarefaction and 2-rarefaction is also not possible since the intersection occurs at the dashed portions of both  $R_1$  and  $R_2$  indicating the violation of rarefaction conditions.

The solution is thus an all-shock solution that has the form (refer to Appendix A.2):

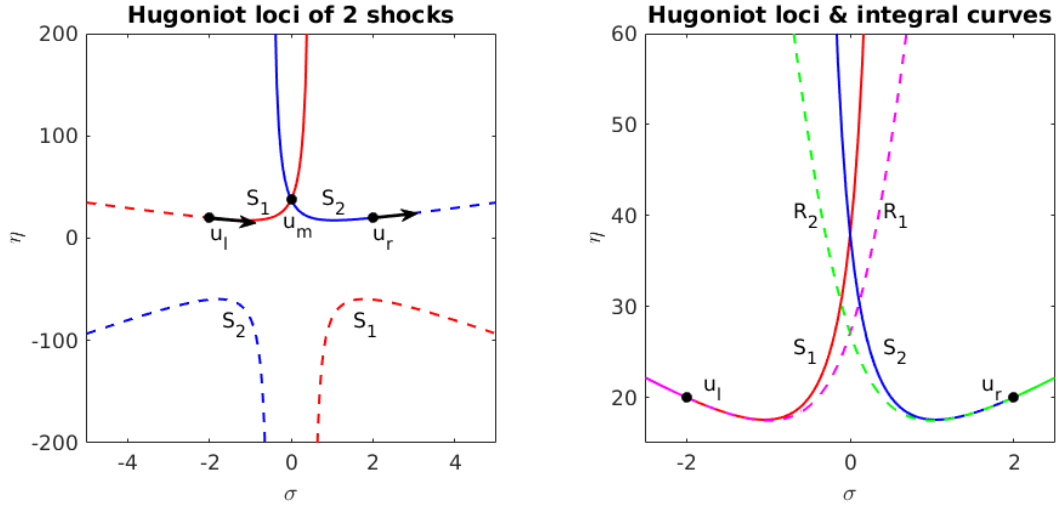


FIGURE 4.9: (Left) Hugoniot loci for two shocks solution, denoted as  $S_1$  and  $S_2$ . Note that the eigenvectors  $\mathbf{r}_1$  and  $\mathbf{r}_2$  are tangential to the locus at  $\mathbf{u}_l = (\sigma_l, \eta_l)$  and  $\mathbf{u}_r = (\sigma_r, \eta_r)$ , respectively. (Right)  $S_1$ : 1-Hugoniot loci;  $R_1$ : 1-integral curve;  $S_2$ : 2-Hugoniot loci;  $R_2$ : 2-integral curve. Note that the dashed portions of the curves indicate violation of rarefaction/entropy condition.

$$\mathbf{u}(x, t) = \begin{cases} \mathbf{u}_l & \text{if } x/t < s_1 \\ \mathbf{u}_m & \text{if } s_1 < x/t < s_2 \\ \mathbf{u}_r & \text{if } x/t > s_2 \end{cases} \quad (4.44)$$

where  $\mathbf{u}_l = (\sigma_l, \eta_l)$ ,  $\mathbf{u}_m = (\sigma_m, \eta_m)$  and  $\mathbf{u}_r = (\sigma_r, \eta_r)$  are all known quantities. From Eq. (A.24) the corresponding shock speeds are

$$s_1 = -\frac{k_f \eta_l}{\sqrt{1 + \sigma_l^2}} = -\frac{20}{\sqrt{5}}, \quad s_2 = \frac{k_f \eta_r}{\sqrt{1 + \sigma_r^2}} = \frac{20}{\sqrt{5}} \quad (4.45)$$

since cell secretion rate  $k_f = 1$  (refer to Sect. 4.4.4). The solution  $\mathbf{u} = (\sigma, \eta)$  at time  $t = 0.2$  is shown by the black curves in the bottom of Fig. 4.7. Figure 4.7 (top plots) shows the solution in terms of the original variables, the height  $h$  and surface cell density  $\rho$ . Comparison with the output produced in Fig. 4.8 by numerical calculation using the numerical scheme described in Chapter 3 shows a very good match. However, the numerical technique causes smoothing and oscillation of the solution.

## 4.5 Conclusions

In this chapter, we studied the evolution equations of the hyperbolic curvature flow defined in Chapter 3 in the zero diffusion limit. In this limit, these equations form a

system of hyperbolic conservation laws in which the emergence of shocks and rarefaction waves can be determined (semi-) analytically. The system was found to be genuinely nonlinear in the first and second fields associated with the two eigenvalues.

Two main parts of this chapter were a proof of the finite time blow up of the system, and the analysis of the waves structures formed by Riemann problems. In the first part, we used a theorem by Lax [66] to show that the existence of negative curvature in the initial interface would cause a blow up in the derivative of the solution. This explained the emergence of cusps in the tissue interface in finite time obtained numerically in Chapter 3 at low diffusivities.

The second part investigated the structure of shocks and rarefaction waves in the solution of Riemann problems. We showed that a convex interface seeded with a constant initial density would generate a rarefaction wave. On the other hand, a concave interface seeded with a constant initial density would induce a shock wave. These analytical output compared well with the results produced by the numerical simulations, except that there are some smoothing effects and/or oscillations in the solutions produced by the numerical simulations.

## Chapter 5

# Paper 2: Bone-forming cells infill irregular pores under curvature and porosity controls: A hypothesis-testing analysis of cell behaviours

### 5.1 Overview

An osteon is a bone structural unit that results from the renewal of a portion of bone matrix by bone-resorbing cells, followed by bone-forming cells. In cortical bone, osteons host a central porous canal (Haversian canal), which forms most of bone's porosity in compact bone. It is known that the flow of interstitial fluid within this porosity can trigger bone formation and prevent bone loss [43, 79].

In this chapter, the mathematical model developed previously is applied to experimental data on the rate of new bone formation in osteons to gain insights into the influence of geometry on individual cell behaviors, in particular, the interplay between curvature and porosity on cell secretory rate and cell death rate. This will also help reconcile the discrepancy of the role of curvature in the velocity of tissue formation seen in in-vivo and in-vitro experiments (see Sect. 1.3).

This is the focus of research question 3, marked as ③ in Fig. 1.2. The work is to be submitted to a peer-reviewed scientific journal, and is reproduced in this chapter.

### 5.2 PDF of paper

# Bone-forming cells infill irregular pores under curvature and porosity controls: A hypothesis-testing analysis of cell behaviours

Mohd Almie Alias<sup>a,b,\*</sup>; Pascal R Buenzli<sup>a,c</sup>

<sup>a</sup>School of Mathematical Sciences, Monash University, Clayton VIC 3800, Australia

<sup>b</sup>School of Mathematical Sciences, National University of Malaysia, 43600 Bangi, Selangor D. Ehsan, Malaysia

<sup>c</sup>School of Mathematical Sciences, Queensland University of Technology, Brisbane QLD 4001, Australia

February 21, 2018

**Abstract** – The geometric control of bone tissue growth plays a significant role in bone remodelling, age-related bone loss, and tissue engineering. However, how exactly geometry influences the behaviour of bone-forming cells remains elusive. Geometry acts collectively through the evolving space available to the population of cells, but it may also act on the individual behaviours of cells. To single out the collective influence of geometry and gain access to the geometric regulation of individual cell behaviours, we develop a mathematical model of the infilling of cortical bone pores and use it with available experimental data on cortical infilling rates. Testing different possible modes of geometric controls of individual cell behaviours consistent with the experimental data, we find that efficient smoothing of irregular pores only occurs when cell secretory rate is controlled by porosity rather than curvature. This porosity control suggests the convergence of a large scale of intercellular signalling to single bone-forming cells, consistent with that provided by the osteocyte network in response to mechanical stimulus. After validating the mathematical model with the histological record of a real cortical pore infilling, we explore the infilling of a population of randomly generated initial pore shapes. We find that amongst all the geometric regulations considered, the collective influence of curvature on cell crowding is a dominant factor for how fast cortical bone pores infill, and suggest that the irregularity of cement lines thereby explains some of the variability in double labelling data.

**Keywords:** Bone remodelling, tissue growth, osteoblast, tissue engineering, morphogenesis

## 1 Introduction

Bone tissues are remodelled throughout life to help remove micro-damage that accumulates by fatigue loading [1]. In compact bone, self-contained groups of bone-resorbing and bone-forming cells tunnel through old bone to replace it [2]. The bone-resorbing cells first hollow out a cylindrical pore. The bone-forming cells then attach to the walls of this cavity and infill the pore from outside in, leaving a residual channel for vascularisation (Haversian canals) [2, 3]. The new bone structure thus formed is called an osteon. During age-related bone loss and osteoporosis, it is known that bone porosity increases first as a result of these remodelling cavities not infilling completely, then as a result of increased resorption [4], but the detailed geometric and mechanical factors that control how bone pores infill remain poorly understood. By increasing their size, pores may coalesce and become more irregular [5, 6]. Because increased bone porosity leads to mechanically compromised bone and increased fracture risk [7–9], it is important to understand how bone-forming cells respond to the local geometric features of remodelling cavities.

In-vivo labelling experiments give some insights into the infilling rate of remodelling cavities. The sequential administration of fluorochrome substances in an organism, such as tetracycline, alizarin, and calcein, leaves a series of fluorescent labels within bone. These labels record the location of past bone surfaces that were forming at the time of administration. Such experimental data suggests that the velocity of bone-forming surfaces in cortical bone, called matrix apposition

rate (MAR) [10], is proportional to the average radius  $R$  of infilling cylindrical cavities [11–13]. However, it is unclear how the irregularity of infilling cavities may influence our interpretation of double labelling data. For perfectly symmetric pores (circular cross-section), the dependence upon  $R$  may correspond to an influence of the curvature of the bone surface  $1/R$ , or an influence of porosity  $\propto R^2$  indistinctively. For noncircular infilling pores, however, curvature and porosity are independent variables, so that their respective influence on bone-forming cells can be differentiated.

By seeding cells of osteoblastic (bone-forming) lineage onto bioscaffolds of different geometries, tissue engineering experiments have exhibited a specific influence of local curvature on the rate of tissue growth [14–20]. These studies have suggested that the velocity of the tissue surface at the onset of new tissue formation is described as a mean curvature flow, in which interface velocity is proportional to curvature where the tissue substrate is concave. In a previous work, we have developed a mathematical model of tissue-forming cells that captures a systematic influence of local curvature on cell density due to the shrinking or expanding surface area near concavities or convexities of the interface [21]. This model results in a type of hyperbolic curvature flow [22] in which the normal acceleration of the interface depends linearly on curvature. For circular pores, the model reduces to mean curvature flow with velocity proportional to curvature. Both the smoothing of highly curved regions of the interface and tissue deposition slowdown observed in the bioscaffold experiments in various pore shapes was explained by our model as a combination of (i) curvature-dependent changes in cell density; (ii) cell diffusion along the interface; and (iii)

\*Corresponding author. Email address: [almie.alias@monash.edu](mailto:almie.alias@monash.edu)

depletion of actively secreting cells.

In this paper, we apply this mathematical model of tissue-forming cells to cortical bone pore infilling in order to single out mathematically from double labelling data the unavoidable influence of curvature on cell crowding or spreading. By singling out this collective influence of curvature on cell density, we are able to examine how two individual cell behaviours, namely cell secretory rate (volume of bone formed per cell per unit time), and cell depletion rate (probability per unit time for the cell to become inactive, e.g. by undergoing apoptosis or anoikis) may depend upon curvature and porosity during the infilling of remodelling cavities. The underlying biological and physical processes involved in a curvature control of bone formation are likely to be fundamentally different from those involved in a porosity control of bone formation. This distinction could thus be important for understanding the evolution of age-related bone loss, and how to best counter it [23, 24]. To our knowledge, this is the first time that a mathematical model of cell population is used in combination with experimental data to gain insights into geometric influences at the level of individual cells.

Previous mathematical models of infilling bone pores have been developed [25–28]. These models all assumed perfectly cylindrical geometries in which no distinction is possible between curvature and porosity. The models in Refs [25, 27] included density concentration due to surface area shrinkage during pore infilling, and the generation of osteocytes by embedment of some of the bone-forming cells. The generation of osteocytes in arbitrary geometries was generalised in Refs [29, 30]. The novelty of the present mathematical model is to propose a comprehensive population model of bone-forming cells that includes osteocyte generation, and collective and individual geometric influences at the cell-tissue scale in arbitrary pore geometries.

## 2 Materials and methods

### 2.1 Mathematical model

Cortical bone pores form elongated cylindrical structures, so that most of the geometric regulation of pore infilling can be assumed to arise from their cross-sectional shape. We thus consider the infilling of a remodelling cavity viewed in a transverse cross section, with a pore interface  $S(t)$  described by an explicit parameterisation  $\theta \mapsto R(\theta, t)$  in polar coordinates. The interface evolves by the secretion of new bone matrix by osteoblasts (bone-forming cells) lining the interface with a surface density  $\rho$  (number of cells per unit surface). The normal velocity of the interface is

$$v = k_f \rho, \quad (1)$$

where  $k_f$  is the cell secretory rate (volume of new bone matrix secreted per cell per unit time) [29, 21]. In Ref. [21], we developed evolution equations for the crowding and spreading of cells induced by changes in the local surface area at concavities and convexities of the interface during its evolution. Here, we extend these equations by including explicitly the formation of osteocytes by embedment of some of the osteoblasts into the bone matrix [29, 30]. The evolution

equations governing the pore interface radius  $R(\theta, t)$  and surface density  $\rho(\theta, t)$  of osteoblasts are [21]:

$$\begin{aligned} R_t &= -v \sqrt{1 + \left(\frac{R_\theta}{R}\right)^2} \\ \rho_t &= -\rho v \kappa - \frac{\rho_\theta}{R} v \cos \alpha + D \left( \frac{\rho_{\theta\theta}}{g^2} - \frac{\rho_\theta}{R} \left[ \frac{2}{g} - \kappa \right] \cos \alpha \right) \\ &\quad - \text{O}_f v - A \rho, \end{aligned} \quad (2)$$

where  $g = R \sqrt{1 + (R_\theta/R)^2}$  is the metric, or local stretch of the parameterisation;  $\cos \alpha = \mathbf{n} \cdot \hat{\boldsymbol{\theta}} = R_\theta/g$  is the projection of the unit normal vector  $\mathbf{n}$  of the interface onto  $\hat{\boldsymbol{\theta}} = (-\sin \theta, \cos \theta)$ ; and

$$\kappa = -\frac{R^2 - RR_{\theta\theta} + 2R_\theta^2}{g^3} \quad (4)$$

is the local curvature in polar coordinates. Curvature is taken to be negative on concave portions of the bone substrate, and positive on convex portions of the bone substrate.

The first term in the right-hand side of Eq. (3) describes the systematic dilution or concentration of osteoblasts induced by the curvature of the interface. The second term represents the transport of osteoblasts perpendicularly to the interface but measured with respect to the coordinate  $\theta$ . The third term is proportional to the Laplace–Beltrami operator expressed in polar coordinates. It describes the diffusion of osteoblasts parallel to the interface with constant diffusivity  $D$ . The sink term  $-\text{O}_f v$  represents the decrease in cell density due to the embedment of osteoblasts in bone matrix, where  $\text{O}_f = \text{O}_f(R(\theta, t), \theta)$  is the instantaneous density of osteocytes (number of cells per unit volume) generated at the moving bone formation front [29]. The radial dependence of  $\text{O}_f$  denotes a possible spatial dependence of osteocyte density within the osteon, which could be provided from experimental measurements. It is known that the generation of this density does not depend explicitly on the curvature of the interface [29]. Here we assume for simplicity that osteocyte density is constant,  $\text{O}_f \approx 31,250 \text{ mm}^{-3}$  [10, 27, 29, 31–34]. Finally, the sink term  $-A\rho$  in Eq. (3) represent depletion from the pool of active osteoblasts other than by differentiation into osteocytes, occurring at rate  $A$  (in  $\text{day}^{-1}$ ). This depletion may represent cell death (such as apoptosis), or detachment from the bone surface. The shrinking of bone surface area during bone formation, which tends to increase osteoblast density and thereby also tends to increase interface velocity, contrasted with the observation of bone deposition slowdown, means that many cells are removed from the pool of active osteoblasts during bone formation by such a depletion mechanism [3, 27]. All the parameters and variables used in the model are listed in Table 2.

**Individual cell behaviours.** Individual cell behaviours are represented in Eqs (1)–(3) by the cell secretory rate  $k_f$ , cell depletion rate  $A$ , and cell diffusivity  $D$ . We will assume that secretory rate  $k_f$  and cell depletion rate  $A$  may depend on the local geometry of the interface, but will assume constant diffusivity  $D$ . Cell secretory rate is expected to scale with cell body volume [35], which is likely to depend on the local curvature of the bone substrate, e.g., via cell density. Geometry may also

control the reduction in cell secretory rate when osteoblasts become living, quiescent cells lining the bone surface at the end of bone formation, when the remaining pore is about  $40\mu\text{m}$  in diameter [3]. Similarly, curvature and its effect on cell density may influence osteoblast apoptosis or detachment from the bone surface. In contrast, osteoblast diffusion parallel to the bone surface is expected to be small and only weakly dependent on curvature. Indeed, active osteoblasts form a confluent layer of cells on the bone surface [3]. Their cellular protrusions link with bone-matrix-embedded osteocytes, but osteocytes density is generated independently of an explicit geometric regulation [29].

To gain insights into the geometric regulation of the individual cell behaviours  $k_f$  and  $A$ , we use the mathematical model in Eqs (1)–(3) in two steps:

1. **Circular pore geometry.** We first consider perfectly circular infilling remodelling cavities. In this case, cell diffusion is irrelevant, and both curvature and porosity are related to the infilling pore radius  $R(t)$ . Direct experimental data is available from the published literature on  $v(R)$ ,  $\rho(R)$ , and  $k_f(R)$  [36], see Section 2.2. The data  $k_f(R)$  is used as input to the model in Eqs (1) and (3), and we determine how cell depletion rate  $A(R)$  must depend on  $R$  for the model to match the experimental data on  $v(R)$  and  $\rho(R)$ .
2. **Noncircular pore geometry.** Knowing the dependence upon  $R$  of  $k_f(R)$  and  $A(R)$  in circular geometry, we then seek to extrapolate this geometric regulation in noncircular geometries, where curvature  $\kappa$  and porosity  $\phi$  are independent variables. To this end, we propose four models of geometric regulation of  $k_f$  and  $A$  that are consistent with their expression in circular geometry, and explore the infilling behaviour of irregular pores to test these models. The four models considered are:

**Model 1:**  $k_f(\kappa)$  and  $A(\kappa)$ ;

**Model 2:**  $k_f(\kappa)$  and  $A(\phi)$ ;

**Model 3:**  $k_f(\phi)$  and  $A(\kappa)$ ;

**Model 4:**  $k_f(\phi)$  and  $A(\phi)$ ;

The functional dependences of  $k_f$  and  $A$  upon the geometric variables  $\kappa$  or  $\phi$  in each model are determined by substituting  $R = -1/\kappa$  or  $R = L\sqrt{\phi/\pi}$  in the functions  $k_f(R)$  and  $A(R)$  determined in the first step, see Eqs (8),(9). All four models result in identical behaviour in circular pore geometries, but not in irregular pore geometries. A parametric study of cell diffusivity  $D$  is performed for each model.

In each model, pore infilling is assumed to stop once osteonal porosity

$$\phi(t) = \frac{\text{pore area}}{L^2} = \frac{1}{2L^2} \int_0^{2\pi} R(\theta, t)^2 d\theta$$

reaches the value  $\phi_H = \frac{\pi R_H^2}{L^2}$ , where  $R_H \approx 20\mu\text{m}$  is the average Haversian canal radius, and  $L \approx 300\mu\text{m}$  is chosen large enough to fit most typical cortical resorption cavities, which have an average diameter of about  $200\mu\text{m}$  [2, 10]. This porosity measure is similar to the ‘individual osteon porosity’

defined by the ratio of pore area and initial pore area [11], but it has the advantage of being able to compare the initial porosity of different resorption cavities, and of not being 1 initially, which helps regularise mechanical estimates (see Discussion).

To assess which model represents typical evolutions of irregular pores during their infilling, we define a discrepancy measure based on the circularity of the final interface shape  $R_{\text{end}}(\theta)$  when infilling has completed. Since Haversian canals are more regular and circular than initial resorption cavities [10, 11] we define the discrepancy

$$\epsilon = \frac{1}{N} \sum_{i=1}^N [R_{\text{end}}^i - R_H]^2 \quad (5)$$

where  $R_{\text{end}}^i = R_{\text{end}}(\theta_i)$  is the radius of the final interface at the angular discretisation point  $\theta_i$ , and  $N$  is the number of discretisation points along the pore interface. Since infilling continues in the model until the target porosity  $\phi_H$  is reached,  $\epsilon$  measures only deviations from circularity in the final shape, and not deviations in porosity.

### Three-dimensional vs two-dimensional parameter values.

To convert values of three-dimensional quantities to two-dimensional values in the cross-section, we use a nominative cross-section thickness of  $\Delta z = 20\mu\text{m}$ , corresponding roughly to the size of an osteoblast. For example, an osteocyte density of  $31,250/\text{mm}^3$  corresponds to the value  $31,250/\text{mm}^3 \times \Delta z = 625/\text{mm}^2$  in the cross section. Likewise, osteoblast surface density becomes  $\rho \Delta z$  in the cross-section, and cell secretory rate becomes  $k_f/\Delta z$ . In the following we will refer to values converted to two dimensions by this procedure.

**Numerical simulations.** Eqs (1)–(3) are solved numerically using the same techniques as in Ref. [21]. A straightforward finite difference upwind scheme is used at high diffusivities, but a high-resolution finite volume method (Kurganov–Tadmor scheme) is used at low diffusivities to prevent significant numerical loss of cells. We refer the reader to Ref. [21] for more detail on these numerical schemes.

The initial resorption cavity determines the initial cavity radius  $R(\theta, 0) = R_0(\theta)$ . The initial osteoblast density  $\rho(\theta, 0) = \rho_0 \approx 161/\text{mm}$  was assumed to be the same homogeneous value in all simulations, so that in circular pores of initial radius  $R_0 = 100\mu\text{m}$ , the initial normal velocity of the interface is  $v_0 = 1.9\mu\text{m}/\text{day}$ , consistently with experimental data (see Sect. 2.2).

## 2.2 Experimental data

Experimental data measuring osteon infilling dynamics comes mostly from double labelling experiments. These experiments enable the estimation of the speed of the bone interface  $v$  as a function of mean radius  $R$  (or mean area) [11]. There is little literature, however, on osteoblast density  $\rho$  in infilling remodelling cavities of different sizes. These two types of data ( $v$  and  $\rho$ ) determine  $k_f$  by Eq. (1). Due to the need to use different experimental methods to determine these quantities, they are not usually collected simultaneously on the same

**Table 1** – Scaled data on cell density, normal velocity (MAR), and cell secretory rate  $k_f$  at different radii of infilling remodelling cavities, based on measurements reported in dogs in Ref. [36] and the procedure outlined in Ref. [27] to rescale dog data onto human data. Conversions to two-dimensional values are based on an assumed cross-section thickness  $\Delta z = 20\mu\text{m}$ .

pore radius $R$	osteoblast density $\rho$		cell secretory rate $k_f$	
	3D	2D	3D	2D
$[\mu\text{m}]$	$[\text{mm}^{-2}]$	$[\text{mm}^{-1}]$	$[\text{mm}^3/\text{day}]$	$[\text{mm}^2/\text{day}]$
20	2300	46	0	0
22.9	3600	72	$112.5 \times 10^{-9}$	$5.63 \times 10^{-6}$
43.3	7016	140	$128.75 \times 10^{-9}$	$6.44 \times 10^{-6}$
92.7	8000	160	$225 \times 10^{-9}$	$11.25 \times 10^{-6}$

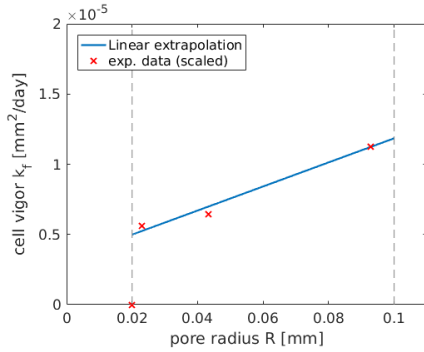


**Figure 1** – Scaled data on (nonzero) cell secretory rate  $k_f(R)$  from Table (1), and the linear interpolation in Eq. (6). The value of  $k_f$  at  $R_H = 0.02$  mm is excluded from the interpolation since the new matrix secretion terminates at  $R_H$ .

samples. Here, we gather data from experiments conducted on animal from different species, and rescale these data to typical dimensions seen in human bone samples according to known cross-species differences, as was done in Ref. [27].

**Cell density and secretory rate.** Marotti et al. have measured both  $v(R)$  and osteoblast density  $\rho(R)$  in infilling remodelling cavities of different radii  $R$  in dogs, which was used to deduce  $k_f(R)$  by Eq. (1) [36]. Following Ref. [27], we scaled dog pore radii to human values by a linear transformation. Cell secretory rate  $k_f^{\text{dog}}$  was scaled by a factor 1.25 to account for higher secretion rates in humans [25, 27], while osteoblast density was scaled by the inverse factor  $1/1.25$  [27]. Table 1 summarises the scaled experimental data on  $\rho(R)$  and  $k_f(R)$ . The first line of data in Table 1 corresponds to quiescent osteoblasts lining the bone surface after bone formation has completed [10].

We interpolate the data  $k_f(R)$  in Table 1 linearly in  $R$  between the average human Haversian canal  $R_H = 20\mu\text{m}$  (excl.) and the initial cavity radius (or cement line radius)  $R_c = 100\mu\text{m}$  [2] as

$$k_f(R) = a_{k_f} + b_{k_f}R, \quad (6)$$

where for  $k_f(R)$  in  $\text{mm}^2/\text{day}$ ,  $a_{k_f} = 3.2741 \times 10^{-6} \text{mm}^2/\text{day}$  and  $b_{k_f} = 8.5728 \times 10^{-5} \text{mm}^2/\text{day}$  (see Fig. 1).

**Interface velocity (matrix apposition rate).** Data on the velocity of the bone formation front is much more abundant. To take advantage of this abundance, we use a more extensive dataset collected on sheep by Metz et al. [11], whom report the

percentage of bone infilled versus cavity radius. We rescale this data onto human values by a similar linear transformation, such that a 100% unfilled cavity corresponds to the initial cavity radius  $R_c = 100\mu\text{m}$ , and a 0% unfilled cavity corresponds to the Haversian canal radius  $R_H = 20\mu\text{m}$ , as was also done in Ref. [27]. This scaled data is shown in Fig. 8 along with simulation results.

### 3 Results

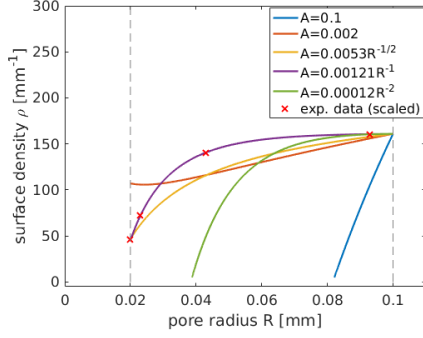
**Cell depletion rate in circular pore geometry.** The geometric regulation of cell depletion rate  $A(R)$  in a perfectly circular infilling pore is determined by comparing the osteoblast surface densities  $\rho(R)$  reached by the simulations at different radii with the data from Table 1. All the numerical simulations in this circular geometry assume that cell secretory rate  $k_f(R)$  is the function given in Eq. (6). In the circular geometry, cell diffusion is irrelevant so long as the initial confluence of osteoblasts is achieved with a uniform density before they become active, which is assumed here.

Figure 2 shows that a constant cell depletion rate does not lead to cell densities in the simulations that match the in-vivo cell density data from Table 1. The constant value  $A = 0.1 \text{mm}/\text{day}$  used in our previous analysis of bioscaffold tissue growth [21] leads to a rapid depletion of active cells and incomplete bone formation. The value  $A = 0.002 \text{mm}/\text{day}$  decreases density too fast initially (large  $R$ ), but too slowly towards the end of bone formation (small  $R$ ), where crowding of cells  $\propto 1/R$  induced by the shrinking pore surface area takes over. With this value of  $A$ , the density of quiescent cells lining the bone surface at completion of bone formation is twice larger than measured values.

To match the nonlinear decrease in cell surface density with decreasing cavity radius  $R$  despite the strong crowding of cells that occurs at small  $R$ , it is necessary to increase cell depletion as  $R$  decreases. Testing power-law dependences of  $A$  upon  $1/R$ , we find that an excellent fit of the simulation to the data is obtained by choosing

$$A(R) = \frac{A_0}{R} \quad (7)$$

with  $A_0 = 0.00121 \text{mm}/\text{day}$  (Fig. 2). Clearly, in this case, simulations also reproduce the dynamics of the interface  $v(R)$  measured in Ref. [36], by Eq. (1). When compared with the independent data  $v(R)$  measured in Ref. [11], there is only a slight deviation from the average behaviour that remains within the experimental variability (see Fig. 8). The bone



**Figure 2** – Comparison of cell surface density between model with various cell depletion rate  $A$  and the 2D-human-scaled experiment data from Ref. [10], along the infilling of a idealised circular osteon produced by the model  $k_f$  in Eq. (6).

formation period required to infill the circular pore with Eq. (7) is about 80 days, which is consistent with reported durations of 3 months mentioned in [3, 2].

These results suggest that in regular bone pores of circular cross-sections, the geometric regulation of the individual behaviours of osteoblasts is such that as cavity radius  $R$  decreases, cell secretory rate decreases linearly with  $R$  by Eq. (6), and cell depletion rate increases as  $1/R$  by Eq. (7). With these individual cell behaviours, the collective crowding of cells induced by the shrinking pore surface area, and with the generation of osteocytes, osteoblast density decreases nonlinearly as the pore infills (Fig. 2), while the velocity of the interface (matrix apposition rate) decreases roughly linearly with  $R$  (Fig. 8).

**Individual cell behaviours in non-circular pores.** Models 1–4 are proposed as possible generalisations of the behaviours of  $k_f$  and  $A$  in noncircular geometries (see Section 2.1). These models are obtained by interpreting  $R$  either by means of curvature  $\kappa$  or porosity  $\phi$  in Eqs (6) and (7). Doing so results in the following possible geometric regulations of cell secretory rate and cell depletion rate:

$$k_f(\phi) = a_{k_f} + \frac{b_{k_f} L}{\sqrt{\pi}} \sqrt{\phi}, \quad k_f(\kappa) = \begin{cases} a_{k_f} - \frac{b_{k_f}}{\kappa}, & \text{if } \kappa \leq \kappa_c < 0 \\ a_{k_f} - \frac{b_{k_f}}{\kappa_c}, & \text{if } \kappa_c < \kappa < 0 \\ 0, & \text{if } 0 \leq \kappa \end{cases} \quad (8)$$

$$A(\phi) = \frac{A_0 \sqrt{\pi}}{L \sqrt{\phi}}, \quad A(\kappa) = \begin{cases} -A_0 \kappa, & \text{if } \kappa < 0 \\ 0, & \text{if } 0 \leq \kappa \end{cases} \quad (9)$$

where  $\kappa_c = -1/R_c$  is the curvature of the cement line in the circular geometry. These expressions all recover Eqs (6) and (7) when  $\kappa = -1/R$  and  $\phi = \pi R^2/L^2$ , so long as  $R \leq R_c$ . Cell secretory rate has been bounded from above when controlled by curvature on portions of the bone substrate where  $\kappa_c < \kappa < 0$ , i.e., on portions that are flatter than the cement line in circular geometry, due to the limited capacity of cells to secrete new bone matrix. In convex regions of the bone substrate ( $\kappa \geq 0$ ), both  $k_f(\kappa)$  and  $A(\kappa)$  are extrapolated to be zero. It is assumed that when curvature controls these behaviours, osteoblasts in these regions become quiescent

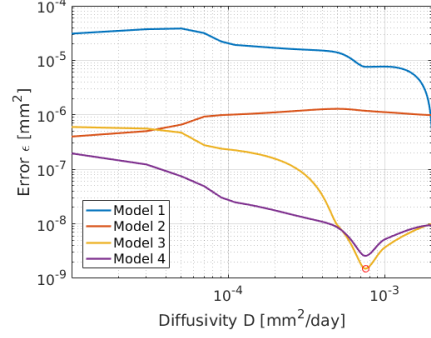


**Figure 3** – Errors calculated for Models 1, 2, 3 and 4 with different diffusivity  $D$ , plotted using the log-log scale. Minimum error is obtained when  $D \approx 0.00075$  and when using Model 3.

cells with  $k_f = 0$  and  $A = 0$ , as suggested by bioscaffold tissue growth experiments [14–16].

The extrapolation of the geometric regulations of individual cell behaviours to noncircular pore shapes in Eqs (8) and (9) now entirely defines Models 1–4 with the evolution equations Eqs (1)–(3). The only free parameter that remains in the four models is the cell diffusivity  $D$ .

**Influence of cell diffusivity.** In a circular pore with homogeneous initial osteoblast density, cell diffusion has no effect on the evolution, so that cell diffusivity  $D$  cannot be estimated. Our previous simulations of tissue growth in bioscaffold pores exhibited strong qualitative changes in growth patterns driven by diffusivity [21]. To assess the influence of cell diffusivity on the infilling of bone pores in noncircular geometries, we perform a parametric study of  $D$  on pores of square, hexagonal, and cosine shapes (the cosine initial pore shape is similar to a smoothed triangle) of identical perimeter 0.6 mm, so that there is the same number of osteoblasts at the onset of bone formation. Tissue growth within such pore shapes has been investigated in bioscaffold experiments. While these regular pore shapes are not realistic bone remodelling cavities, they enable us to understand the influence of the sharpness of a cusp in the initial interface without the confounding influence of other irregularities.

The measures of discrepancy from circularity calculated for each of these shapes at the end of bone formation by Eq. (5) are summed and plotted in Fig. 3 as a function of  $D$  for each model. The minimum total discrepancy  $\epsilon$  occurs for Model 3 when  $D \approx 0.00075$  mm<sup>2</sup>/day. However, the total discrepancies  $\epsilon$  in Model 3 and Model 4 are very similar and not significantly different from the minimum when  $D \gtrsim 0.0003$  mm<sup>2</sup>/day.

Figure 4 shows the evolution of the interface in each Model at the fixed value of diffusivity  $D = 0.00075$  mm<sup>2</sup>/day. It is clear from Figs 3 and 4 that Models 1 and 2, in which cell secretory rate is assumed to be controlled by curvature, do not lead to an efficient smoothing of the interface. In contrast, the final interfaces for Models 3 and 4 are all roughly circular and indifferentiable regardless of the initial corner angles. Note that Models 3 and 4 do not smooth out initial corners efficiently if diffusion is too low (Fig. 3). The influence of diffusivity on the evolution of the cosine pore interface is shown for Model 3 in Fig. 5.

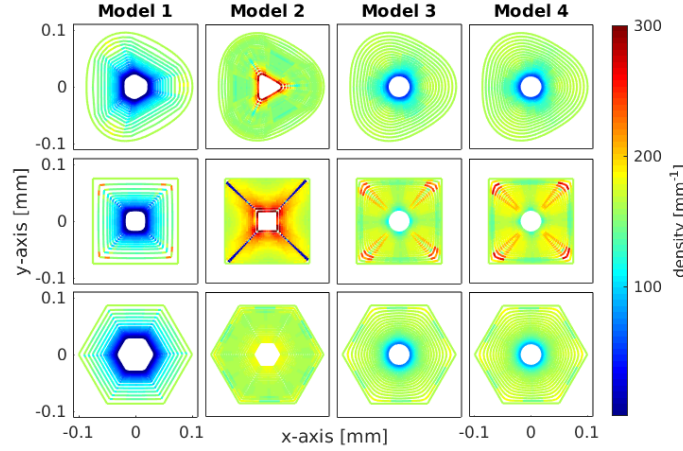


**Figure 4** – Infilling of various initial pore shapes (cosine, square, and hexagonal) simulated by Models 1–4 with  $D = 0.00075 \text{ mm}^2/\text{day}$ . The pore interface is colored according to cell density, shown at regular time intervals

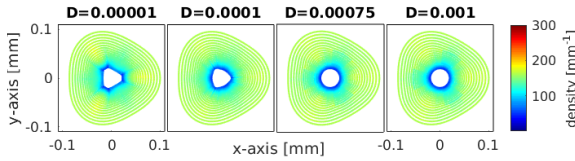


**Figure 5** – Influence of diffusivity  $D$  (in  $\text{mm}^2/\text{day}$ ) on the infilling of the cosine pore simulated by Model 3.

**Application to real osteonal geometry.** New bone formed during the infilling of cortical pores is lamellar. In this type of bone, past locations of the bone interface are recorded as lamellae boundaries visible experimentally in histological slices. These boundaries provide a point of comparison with simulations of our mathematical model.

Figure 6 compares simulations of cortical pore infilling starting from the cement line of a real osteon [37]. The initial pore cavity assumed in the simulations is the boundary between the light grey region at the edges of the histological image (old bone) and the darker grey region (lamellar bone formed by infilling). Lamellae boundaries in the new bone are seen as faint, thin dark lines. We have indicated the approximate boundary between two lamellae with arrowheads at about one third of the new bone wall thickness. The simulations shown in Fig. 6 were all performed with a cell diffusivity  $D = 0.00075 \text{ mm}^2/\text{day}$ , a uniform initial surface density of osteoblasts  $\rho_0 = 161/\text{mm}$ , and a uniform osteocyte density  $Ot_f = 625/\text{mm}^2$ . The simulations were stopped once the infilling pore reached the same porosity as that of the histological image in Fig. 6.

Pore interfaces simulated with Models 3 and 4 match the experimental lamellae boundary (arrowheads) very well, despite the irregularity of the initial interface and the lack of experimental information on the initial density of osteoblasts in the histological image. As time proceeds, the divergence between simulated interfaces and real lamellar boundaries increases. The final pore shape obtained by Models 3 and 4 is regular, but has some difference to the final pore shape in the experimental image. This can be expected from a dynamic system’s perspective as initial errors are likely to amplify without regulatory mechanisms. There is little qualitative

difference between Model 3 and Model 4. Model 3 leads to a slightly more homogeneous osteoblast density lining the final pore interface.

**Comparison with double labelling data.** To understand more thoroughly how efficiently variations in the initial pore interface are smoothed, and how these variations affect the speed of new bone formation, we generated 20 virtual initial pore interfaces by randomly perturbing the radius of the interface between the values  $R_{\min} = 0.06 \text{ mm}$  and  $R_{\max} = 0.12 \text{ mm}$  according to  $R_0(\theta) = R_{\min} + \zeta(\theta)(R_{\max} - R_{\min})$  with uniformly distributed random noise  $\zeta(\theta) \in (0, 1)$  smoothed by Matlab’s `loess` method using local regression based on the weighted linear least squares and a polynomial model to provide  $\zeta(\theta)$  [38].

The purpose of this population of initial pore shapes is to help understand the experimental variability seen in double labelling data [39]. Figure 7 shows simulations of the infilling of these random pore shapes using Model 3 with  $D = 0.00075 \text{ mm}^2/\text{day}$ . The final interfaces are all roughly circular with little inhomogeneity in cell surface density despite the varied initial pore shapes. The pores are organised and numbered according to how fast they refill.

In Figure 8, the average velocity of the interface in these simulations is shown versus average pore radius, and compared with double labelling experimental data. The average instantaneous velocity is estimated in the simulations as

$$\bar{v}(t) = \frac{|A'(t)|}{P(t)} \approx \frac{|\Delta A(t)|}{\Delta t P(t)}, \quad (10)$$

where  $A(t)$  is the pore area,  $\Delta A$  is the change in pore area during the time increment  $\Delta t$ , and  $P(t)$  is the pore perimeter. Simulation results are in good agreement with the linear regression line of the experimental data, particularly as the model has not been fitted to this experimental data. The average velocity of the interface is spread over a range of values around the regression line at an early stage of bone formation (large average radius). Irregular initial pores with highly curved interfaces tend to fill in quicker overall than more circular pores, as can be seen by identifying the highest

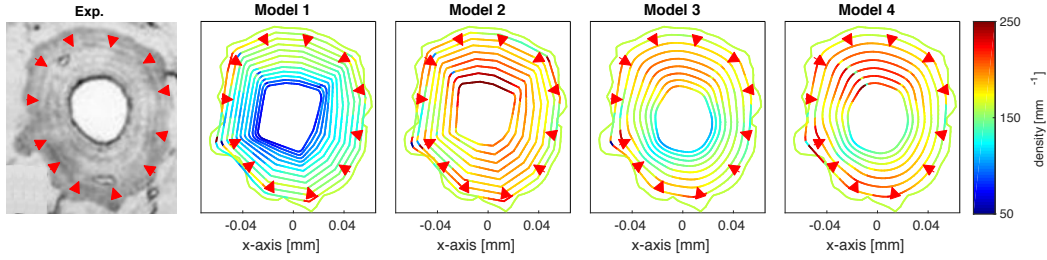


**Figure 6** – Image of a real osteon seen in a histological cross section of human cortical bone (reproduced with permission from Skedros *et al.* [37]) and corresponding simulations of pore infilling using Models 1–4. Arrowheads indicate the boundary between two lamellae in the histological image. Simulated interfaces are coloured according to osteoblast density and shown every 4.56 days.

and lowest average velocity curves with the initial shapes in Fig. 7.

This observation is corroborated by the infilling simulations of the regular pore shapes. The square initial pore (cyan dots in Fig. 8), which has the sharpest corners, infills the fastest, followed by the hexagonal, cosine, and circular pore shapes. In the square and hexagonal pore shapes, there are large sections of zero curvature where osteoblasts secrete new bone, but are not depleted in Model 3. However, when the infilling of these pore shapes is simulated with Model 4, where cell depletion rate occurs uninterruptedly as it depends on porosity rather than curvature, there is little difference in the average velocity curves (data not shown), which means that the mode of geometric control of cell depletion plays a subdominant role for the infilling rate compared to cell crowding.

## 4 Discussion

Bone remodelling is regulated at many scales by a variety of mechanisms of different nature, including biochemical, mechanical, and geometrical [10, 2, 40, 41]. At the tissue scale, the availability of bone surface area is an important factor that influences the propensity of bone renewal, and in particular, the rate and location of bone loss in osteoporosis [42–45, 41]. In this work, we have investigated the geometric regulation of bone remodelling cavities at a lower scale, the scale of cell–tissue interaction, using a comprehensive population model of osteoblasts and experimental data on cortical bone formation dynamics.

The geometric regulation of tissue-synthesising cells at the cell–tissue scale has been exhibited in many in-vitro experiments [14–16, 18–20, 46–50], but it remains difficult to understand the precise mechanisms by which geometry constrains tissue growth patterns. One difficulty is to disentangle the influence of geometry on the collective behaviour of cells and the influence of geometry on the individual behaviour of cells. Another difficulty is to determine what geometric variables are influencing cell behaviour, particularly as geometric features such as curvature and porosity involve length scales that are much larger than individual cell bodies. In this paper, we have addressed these two difficulties by a mathematical modelling approach.

A direct control of curvature onto single osteoblasts (e.g., via focal adhesions) may occur at the onset of new bone formation as osteoblasts may line a rough bone surface made of Howship’s lacunae eroded by bone-resorbing cells [2]. However, soon after Howship’s lacunae are filled and smoothed,

typical radii of curvature of infilling pores in cortical bone range from  $R_c \approx 100 \mu\text{m}$  at the start of bone formation to  $R_H \approx 20 \mu\text{m}$  at the end of bone formation, while osteoblasts have an approximate size of about  $20 \mu\text{m}$ . In Ref. [21], we have proposed that tissue-forming cells are still able to sense such large geometrical features of the tissue substrate dynamically, by the collective crowding or spreading influence of curvature onto cell density. Other curvature-dependent mechanisms have been proposed, such as the tissue surface tension of actin networks [46, 14, 15]. However, due to the fast primary mineralisation of bone [10, 2], it is unlikely that bone tissue surface tension plays a significant role during bone formation.

Interestingly, our simulations suggest that the pore infilling dynamics of Models 1 and 2, in which cell secretory rate  $k_f$  is influenced by curvature, is not smoothing irregularities of the interface very well (Figs 3, 4). Cortical pore infilling results in Haversian canals that are much smoother and regular than initial cement lines [10]. Our simulations thus suggest that cell secretory rate may be controlled not by curvature, but by the porosity of the infilling cavity as assumed in Models 3 and 4.

A porosity control of the individual behaviour of osteoblasts is harder to conceptualise than a curvature control, since it cannot be ascribed to osteoblasts sensing local density changes [21]. Curvature exerts a direct influence on local cell density changes, but not porosity (see Eq. (3)). The ability of osteoblasts to perceive porosity changes indicates a larger scale of intercellular signalling. It is well-known that bone formation is regulated mechanically by the network of osteocytes embedded within bone [51–57]. This network of cells is in direct contact with the layer of osteoblasts lining the bone surface [58, 33]. It is also known that microscopic mechanical strains of bone matrix are determined mostly by porosity [59–61]. A simple micromechanical model of stress concentration [57] shows indeed that the strain energy density of bone matrix  $\Psi$  is given by

$$\Psi = \frac{\frac{1}{2} C_{\text{bm}}^{\text{micro}^{-1}} (F/L^2)^2}{(1-\phi)^2},$$

where  $C_{\text{bm}}^{\text{micro}^{-1}} \approx 0.0482 \text{ GPa}^{-1}$  is the inverse longitudinal bone matrix stiffness, and  $F/L^2$  is the compressive stress exerting onto the osteonal region  $L^2$ . Our finding that cell secretory rate may depend on porosity rather than curvature may therefore indicate that during pore infilling, osteocytes respond to decreasing local mechanical strains by sending inhibitory signals to osteoblasts. This may occur e.g. via sclerostin inhibition of the Wnt pathway [58, 62–64]. This mechanics-

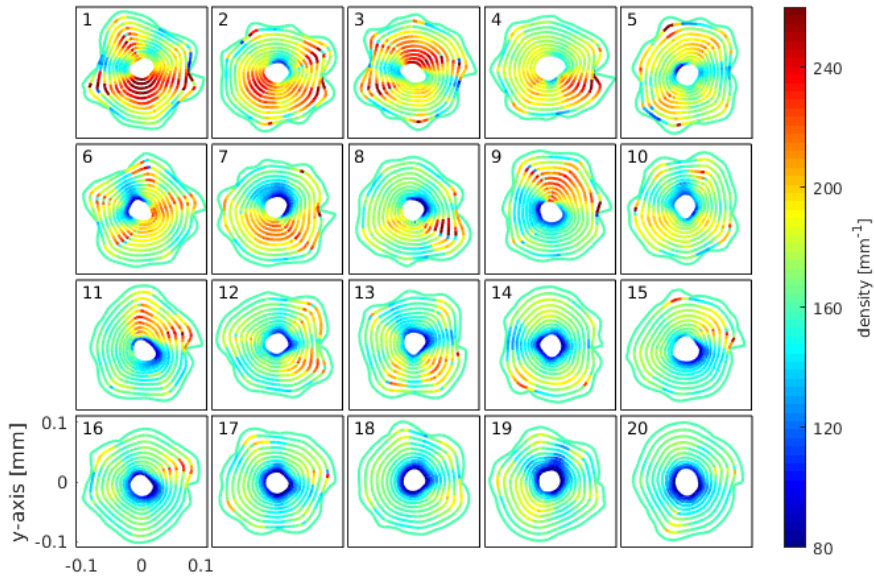


**Figure 7** – Infilling of random irregular pores resembling osteons using Model 3 and  $D = 0.00075$ . The pore interfaces are shown at regular time intervals and coloured according to cell density. The pores are organised by the time it requires to infill them to a porosity of 5%, and numbered accordingly from 1 (fastest infilling) to 20 (slowest infilling), see also Fig. 8.

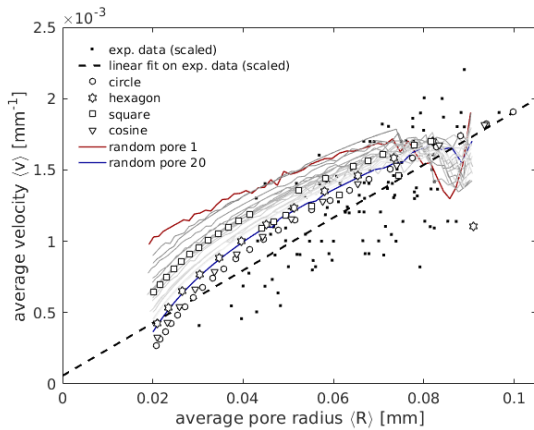


**Figure 8** – Comparison between experimental double labelling data on matrix apposition rate (black squares) and simulation data. Experimental data are based on measurements from Metz et al. [11], appropriately scaled to match human resorption cavity dimensions, see [27]. Simulation data are calculated as the average interface velocity versus the average pore radius during simulation runs of Model 3 with  $D = 0.00075 \text{ mm}^2/\text{day}$  starting from a variety of initial pore shapes: square pore (open squares), hexagonal pore (open stars), cosine pore (open triangles), circular pore (open circles), and the 20 random pores of Fig. 7 (solid red line for random pore 1, solid blue line for random pore 20, and solid grey lines for random pores 2–19).

induced inhibition is consistent with the mechanical control of bone adaptation [57], and may also act as a stopping mechanism for bone formation when local mechanical strains fall below a setpoint threshold.

Other porosity-dependent mechanisms than mechanical strains of bone matrix are possible. For example, fluid flow within Haversian pores has been shown to trigger bone formation and prohibit bone loss [65, 66], even without the presence of osteocytes [67, 68]. Martin et al. have suggested

that the decreasing space between osteoblasts and the blood vessel running within cortical pores might also signal osteoblasts to slow down, and perhaps stop, bone deposition during osteon infilling [2]. However, if so, one would expect to find differences in the activity of osteoblasts around the pore's perimeter in irregular pore shapes. Our finding that cell secretory rate depends on porosity thus excludes this model, because porosity has a uniform value in the cross section.

Our simulations do not enable us to clearly disentangle the nature of geometric regulation of cell depletion. Model 3 and Model 4, which assume curvature-dependent and porosity-dependent cell depletion rate respectively, result in similar pore infilling dynamics (Figs 3, 4, 6). Both models assume that the density of osteocytes generated at the bone deposition front is uniform. While radial dependences of osteocyte density within osteons have been reported [69, 31], it is unclear if there are also angular osteocyte density inhomogeneities in irregular osteons. High-resolution microCT scans of bone samples could be used to investigate such inhomogeneities [31, 70]. A dependence upon interface curvature of osteocyte density (e.g., induced by an implicit curvature dependence of cell burial rate [29]) would make the differentiation of osteoblasts into osteocytes curvature-dependent too in Eq. (3). This would affect the geometric regulation of cell depletion rate  $A$  determined in Fig. 2 and could thereby result in more pronounced differences between Model 3 and Model 4.

With a porosity control of cell secretory rate, one may understand the variability of double labelling data on average interface velocity (MAR) as being due to the level of irregularity of the initial resorption cavities and the strong influence of cell crowding in highly curved concavities of the bone interface. This is shown by our simulations where the fastest infilling pores shapes in Fig. 8 are those in which small

concavities of the initial interface concentrate cells strongly (e.g., random shapes no. 1 and 2 in Fig. 7). Conversely, the slowest infilling pore shapes in Fig. 8 are those that have a more circular initial interface (e.g., random shapes no. 19 and 20 in Fig. 7). All these random shapes have the same initial porosity. Despite porosity controlling secretory rate in Models 3 and 4, the overall porosity of the initial pore influences the average infilling rate less than the presence or absence of highly curved concavities. Figure S1 in the supplementary information shows simulations of random pore 8 scaled down by 70% and scaled up by 130%. While the smaller pore infills slower than the larger pore due to the porosity dependence of the secretory rate  $k_f$ , the difference in average interface velocity (MAR) (Fig. S2 in the supplementary information) is less than that induced by differences in the irregularity of the initial pores (Figs. 7-8). The nonlinearity of the curvature-induced cell crowding makes this influence dominant for the overall speed of pore infilling.

Cortical pore infilling is a complex biological process and some bone histomorphometric studies have shown that bone formation sometimes occurs with a different pattern than the usual regular infilling that we have assumed in this paper. For example, bone formation in some osteons may pause during refilling [2]. Other osteons may not infill, but drift sideways [71–73]. The lamellar structure of cortical bone seen in a cross-section may also be spiraling around the Haversian canal, or may not form a closed ring even on concave portions of the bone substrate [74]. These behaviours are not possible within our mathematical model. They are likely to require further regulatory mechanisms of active osteoblasts, such as local, inhomogeneous mechanical clues.

In summary, we have proposed a general mathematical model of pore infilling in cortical bone to investigate the geometric regulation of osteoblasts during bone formation. The novelties of this mathematical model are (i) to single out the collective influence of geometry on crowding and spreading of bone-forming cells in order to determine the influence of geometry on individual cell behaviours; and (ii) to use a population of initial pore shapes to understand variability in double labelling data. This approach to investigate cell behaviour and biological variability is a promising way to circumvent limitations of biological experiments. Our findings suggest that cell secretory rate is not regulated by the curvature of the bone surface, but by the porosity of the infilling cavity, for example by means of a mechanical response of the osteocytes generated during pore infilling. We also find that cell depletion rate is strongly regulated by the geometry of the infilling pore, but our model is unable to distinguish which geometrical variable is responsible for this regulation.

## Acknowledgments

PRB gratefully acknowledges the Australian Research Council for Discovery Early Career Research Fellowship (project No. DE130101191).

## References

- [1] R. B. Martin, "Fatigue damage, remodeling, and the minimization of skeletal weight," *Journal of Theoretical Biology*, vol. 220, no. 2, pp. 271 – 276, 2003.
- [2] R. Martin, D. Burr, and N. Sharkey, *Skeletal tissue mechanics*. New York: Springer, 1998.
- [3] A. M. Parfitt, "Osteonal and hemi-osteonal remodeling: The spatial and temporal framework for signal traffic in adult human bone," *J. Cell. Biochem*, vol. 55, pp. 273–286, 1994.
- [4] E. Seeman, "Chapter 1 - modeling and remodeling: The cellular machinery responsible for the gain and loss of bone's material and structural strength," in *Principles of Bone Biology (Third Edition)* (J. P. Bilezikian, L. G. Raisz, and T. J. Martin, eds.), pp. 1 – 28, San Diego: Academic Press, third edition ed., 2008.
- [5] K. L. Bell, N. Loveridge, J. Reeve, C. D. Thomas, S. A. Feik, and J. G. Clement, "Super-osteons (remodeling clusters) in the cortex of the femoral shaft: Influence of age and gender," *The Anatomical Record*, vol. 264, no. 4, pp. 378–386, 2001.
- [6] C. D. L. Thomas, S. A. Feik, and J. G. Clement, "Increase in pore area, and not pore density, is the main determinant in the development of porosity in human cortical bone," *Journal of Anatomy*, vol. 209, no. 2, pp. 219–230, 2006.
- [7] M. B. Schaffler and D. B. Burr, "Stiffness of compact bone: Effects of porosity and density," *Journal of Biomechanics*, vol. 21, no. 1, pp. 13 – 16, 1988.
- [8] J. Currey, "The effect of porosity and mineral content on the Young's modulus of elasticity of compact bone," *Journal of Biomechanics*, vol. 21, no. 2, pp. 131 – 139, 1988.
- [9] R. W. McCalden, J. A. McGeough, M. B. Barker, and C. M. Court-Brown, "Age-related changes in the tensile properties of cortical bone. the relative importance of changes in porosity, mineralization, and microstructure," *J Bone Joint Surg Am*, vol. 75, no. 8, pp. 1193–1205, 1993.
- [10] A. Parfitt, "The Physiologic and Clinical significance of Bone Histomorphometric Data," in *Bone histomorphometry: Techniques and Interpretation* (R. Recker, ed.), ch. 9, pp. 143–224, CRC Press, Boca Raton, 1983.
- [11] L. N. Metz, R. B. Martin, and A. S. Turner, "Histomorphometric analysis of the effects of osteocyte density on osteonal morphology and remodeling," *Bone*, vol. 33, no. 5, pp. 753–759, 2003.
- [12] W. R. Lee, "Appositional bone formation in canine bone: a quantitative microscopic study using tetracycline markers," *J Anat*, vol. 98, no. 4, pp. 665–677, 1964.
- [13] J. D. Manson and N. E. Waters, "Observations on the rate of maturation of the cat osteon," *J Anat*, vol. 99, no. 3, pp. 539–549, 1965.
- [14] M. Rumpler, A. Woesz, J. Dunlop, J. van Dongen, and P. Fratzl, "The effect of geometry on three-dimensional tissue growth," *Journal of the Royal Society Interface*, vol. 5, pp. 1173–1180, 2008.
- [15] C. M. Bidan, K. P. Kommareddy, M. Rumpler, P. Kollmannsberger, Y. J. M. Bréchet, P. Fratzl, and J. W. C. Dunlop, "How linear tension converts to curvature: geo-

**Table 2** – Model variables, parameters and estimations

Symbol	Description	Value/Formula	Sources/comments
$\theta$	angle from the positive $x$ -axis	$0, \dots, 2\pi$ rad	–
$t$	time	$\geq 0$ days	–
$R(\theta, t)$	pore radius	Solve Eq. (2)	–
$\rho(\theta, t)$	surface density of cells	Solve Eq. (3)	–
$R_0, R_c$	cement line radius	100 $\mu\text{m}$	Buenzli <i>et al.</i> [27]
$R_H$	Haversian canal radius	20 $\mu\text{m}$	Buenzli <i>et al.</i> [27]
$\rho_0 = \rho(\theta, 0)$	initial cell density	161/mm	extrapol. 2D data (Table 1)
$v$	pore interface velocity	(given function in Eq. (1))	–
$O_t$	osteocyte density within osteon	625/mm <sup>2</sup>	rescaled to 2D
$L$	side length of region of interest	300 $\mu\text{m}$	large enough to fit initial pores
$\phi(t)$	porosity	$\int_0^{2\pi} R(\theta, t)^2 d\theta / (2L^2)$	Lerebours <i>et al.</i> [41]
$\phi_H$	porosity at Haversian canal	$\pi R_H^2 / L^2$	special case of $\phi(t)$ at $R_H$
<b>Circular pore<sup>1</sup></b>			
$D$	surface diffusivity	0	not relevant for circular pore
$k_f(R(t)) = k_f(\theta, t)$	matrix secretion rate	(given function in Eq. (6))	–
$A(R(t)) = A(\theta, t)$	cell depletion rate	0.00121/ $R$	(see table footnote <sup>1</sup> )
<b>Noncircular pore<sup>2</sup></b>			
$\kappa_c$	cement line curvature in circular pore	$-1/R_c$	to bound matrix secretion rate
$D$	surface diffusivity	0.00075 mm <sup>2</sup> /day	(see table footnote <sup>2</sup> )
$k_f(\phi(t)) = k_f(\theta, t)$	matrix secretion rate	(given function in Eq. (8))	(see table footnote <sup>2</sup> )
$A(\kappa(\theta, t)) = A(\theta, t)$	cell depletion rate	(given function in Eq. (9))	(see table footnote <sup>2</sup> )

<sup>1</sup> The rate  $A$  of the circular pore is found by comparing  $\rho$  of the simulations with the scaled 2D data from Table 1.

<sup>2</sup> The optimum rates  $k_f(\phi)$  and  $A(\kappa)$  (from Model 3) and  $D = 0.00075$  for the noncircular pore are found by calculating the error  $\epsilon$ .

- metric control of bone tissue growth,” *PLoS One*, vol. 7, p. e36336, 2012.
- [16] C. M. Bidan, K. P. Kommareddy, M. Rumpfer, P. Kollmannsberger, P. Fratzl, and J. W. C. Dunlop, “Geometry as a factor for tissue growth: Towards shape optimization of tissue engineering scaffolds,” *Advanced Healthcare Materials*, vol. 2, no. 1, pp. 186–194, 2013.
- [17] C. M. Bidan, P. Kollmannsberger, V. Gering, S. Ehrig, P. Joly, A. Petersen, V. Vogel, P. Fratzl, and J. W. C. Dunlop, “Gradual conversion of cellular stress patterns into pre-stressed matrix architecture during in vitro tissue growth,” *J Roy Soc Interface*, vol. 13, p. 20160136, 2016.
- [18] Y. Guyot, I. Papantoniou, Y. Chai, S. Van Bael, J. Schrooten, and L. Geris, “A computational model for cell/ECM growth on 3D surfaces using the level set method: a bone tissue engineering case study,” *Biomechanics and Modeling in Mechanobiology*, vol. 13, no. 6, pp. 1361–1371, 2014.
- [19] Y. Guyot, F. Luyten, J. Schrooten, I. Papantoniou, and L. Geris, “A three-dimensional computational fluid dynamics model of shear stress distribution during neotissue growth in a perfusion bioreactor,” *Biotechnology and Bioengineering*, vol. 112, no. 12, pp. 2591–2600, 2015.
- [20] Y. Guyot, I. Papantoniou, F. P. Luyten, and L. Geris, “Coupling curvature-dependent and shear stress-stimulated neotissue growth in dynamic bioreactor cultures: a 3D computational model of a complete scaffold,” *Biomechanics and Modeling in Mechanobiology*, pp. 1–12, 2016.
- [21] M. A. Alias and P. R. Buenzli, “Modeling the effect of curvature on the collective behavior of cells growing new tissue,” *Biophysical Journal*, vol. 112, no. 1, pp. 193 – 204, 2017.
- [22] P. G. LeFloch and K. Smoczyk, “The hyperbolic mean curvature flow,” *Journal de Mathématiques Pures et Appliquées*, vol. 90, no. 6, pp. 591 – 614, 2008.
- [23] S. C. Cowin, “Bone poroelasticity,” *Journal of Biomechanics*, vol. 32, no. 3, pp. 217 – 238, 1999.
- [24] R. M. Daly, “Exercise and nutritional approaches to prevent frail bones, falls and fractures: an update,” *Climacteric*, vol. 20, no. 2, pp. 119–124, 2017. PMID: 28286988.
- [25] E. Polig and W. Jee, “A model of osteon closure in cortical bone,” *Calcified Tissue International*, vol. 47, no. 5, pp. 261–269, 1990.
- [26] P. R. Buenzli, P. Pivonka, and D. Smith, “Spatio-temporal structure of cell distribution in cortical bone multicellular units: a mathematical model,” *Bone [P]*, vol. 48, no. 4, pp. 918–926, 2011.
- [27] P. R. Buenzli., P. Pivonka, and D. Smith, “Bone refilling in cortical basic multicellular units: insights into tetracycline double labelling from a computational model,” *Biomechanics and Modeling in Mechanobiology [P]*, vol. 13, no. 1, pp. 185–203, 2014.
- [28] N. Petrov, S. Pollack, and R. Blagoeva, “A discrete model for streaming potentials in a single osteon,” *Journal of Biomechanics*, vol. 22, no. 6, pp. 517 – 521, 1989.

- [29] P. R. Buenzli, "Osteocytes as a record of bone formation dynamics: A mathematical model of osteocyte generation in bone matrix," *Journal of Theoretical Biology*, vol. 364, pp. 418–427, 2015.
- [30] P. R. Buenzli, "Governing equations of tissue modelling and remodelling: A unified generalised description of surface and bulk balance," *PLoS ONE*, vol. 11, pp. 1–25, 04 2016.
- [31] K. Hannah, C. Thomas, J. Clement, F. D. Carlo, and A. Peele, "Bimodal distribution of osteocyte lacunar size in the human femoral cortex as revealed by micro-CT," *Bone*, vol. 47, no. 5, pp. 866 – 871, 2010.
- [32] J. M. Graham, B. P. Ayati, S. A. Holstein, and J. A. Martin, "The role of osteocytes in targeted bone remodeling: A mathematical model," *PLoS ONE*, vol. 8, pp. 1–10, 05 2013.
- [33] T. A. Franz-Odenaal, B. K. Hall, and P. E. Witten, "Buried alive: How osteoblasts become osteocytes," *Dev. Dyn*, vol. 235, pp. 176–190, 2006.
- [34] S. L. Dallas and L. F. Bonewald, "Dynamics of the transition from osteoblast to osteocyte," *Annals of the New York Academy of Sciences*, vol. 1192, no. 1, pp. 437–443, 2010.
- [35] A. Z. Zallone, "Relationships between shape and size of the osteoblasts and the accretion rate of trabecular bone surfaces," *Anatomy and Embryology*, vol. 152, no. 1, pp. 65–72, 1977.
- [36] G. Marotti, A. Z. Zallone, and M. Ledda, "Number, size and arrangement of osteoblasts in osteons at different stages of formation," *Calcified Tissue Research*, vol. 21, pp. 96–101, 1976.
- [37] J. G. Skedros, J. L. Holmes, E. G. Vajda, and R. D. Bloebaum, "Cement lines of secondary osteons in human bone are not mineral-deficient: New data in a historical perspective," *The Anatomical Record Part A: Discoveries in Molecular, Cellular, and Evolutionary Biology*, vol. 286A, no. 1, pp. 781–803, 2005.
- [38] MATLAB, *version 9.1.0 (R2016b)*. Natick, Massachusetts: The MathWorks Inc., 2016.
- [39] E. Marder and A. L. Taylor, "Multiple models to capture the variability in biological neurons and networks," *Nature neuroscience*, vol. 14, pp. 133–8, 02 2011.
- [40] N. A. Sims and T. J. Martin, "Coupling the activities of bone formation and resorption: a multitude of signals within the basic multicellular unit," *BoneKEy Reports*, vol. 3, no. 481, 2014.
- [41] C. Lerebours, P. R. Buenzli, S. Scheiner, and P. Pivonka, "A multiscale mechanobiological model of bone remodelling predicts site-specific bone loss in the femur during osteoporosis and mechanical disuse," *Biomechanics and Modeling in Mechanobiology*, vol. 15, pp. 43–67, Feb 2016.
- [42] R. Martin, "The effects of geometric feedback in the development of osteoporosis," *Journal of Biomechanics*, vol. 5, no. 5, pp. 447 – 455, 1972.
- [43] R. B. Martin, "Porosity and specific surface of bone," *Crit Rev Biomed Eng*, vol. 10, no. 3, pp. 179–222, 1984.
- [44] P. R. Buenzli., P. Pivonka, C. Thomas, and J. Clement, "Endocortical bone loss in osteoporosis: the role of bone surface availability," *Int J Num Meth Biomed Eng*, vol. 29, pp. 1307–1322, 2013.
- [45] P. Pivonka, P. R. Buenzli, S. Scheiner, R. Hellmich, and C. Dunstan, "The influence of bone surface availability in bone remodelling—a mathematical model including coupled geometrical and biomechanical regulations of bone cells," *Eng Struct*, vol. 47, pp. 134–147, 2013.
- [46] C. M. Nelson, R. P. Jean, J. L. Tan, W. F. Liu, N. J. Sniadecki, A. A. Spector, C. S. Chen, and R. Langer, "Emergent patterns of growth controlled by multicellular form and mechanics," *Proceedings of the National Academy of Sciences of the United States of America*, vol. 102, no. 33, pp. 11594–11599, 2005.
- [47] J. Dunlop, F. Fischer, E. Gamsjäger, and P. Fratzl, "A theoretical model for tissue growth in confined geometries," *Journal of the Mechanics and Physics of Solids*, vol. 58, no. 8, pp. 1073 – 1087, 2010.
- [48] C. M. Bidan, F. M. Wang, and J. W. Dunlop, "A three-dimensional model for tissue deposition on complex surfaces," *Computer Methods in Biomechanics and Biomedical Engineering*, vol. 16, no. 10, pp. 1056–1070, 2013. PMID: 23528179.
- [49] E. Gamsjäger, C. Bidan, F. Fischer, P. Fratzl, and J. Dunlop, "Modelling the role of surface stress on the kinetics of tissue growth in confined geometries," *Acta Biomaterialia*, vol. 9, no. 3, pp. 5531 – 5543, 2013.
- [50] J. Knychala, N. Bouropoulos, C. Catt, O. Katsamenis, C. Please, and B. Sengers, "Pore geometry regulates early stage human bone marrow cell tissue formation and organisation," *Annals of Biomedical Engineering*, vol. 41, no. 5, pp. 917–930, 2013.
- [51] S. C. Cowin and S. Weinbaum, "Strain amplification in the bone mechanosensory system," *The American Journal of the Medical Sciences*, vol. 316, no. 3, pp. 184 – 188, 1998.
- [52] C. H. Turner, M. R. Forwood, and M. W. Otter, "Mechanotransduction in bone: do bone cells act as sensors of fluid flow?," *The FASEB Journal*, vol. 8, no. 11, pp. 875–8, 1994.
- [53] E. H. Burger and J. Klein-Nulend, "Mechanotransduction in bone—role of the lacuno-canalicular network," *The FASEB Journal*, vol. 13, no. 9001, pp. 101–112, 1999.
- [54] V. I. Sikavitsas, J. S. Temenoff, and A. G. Mikos, "Biomaterials and bone mechanotransduction," *Biomaterials*, vol. 22, no. 19, pp. 2581 – 2593, 2001.
- [55] L. F. Bonewald, "The amazing osteocyte," *Journal of Bone and Mineral Research*, vol. 26, no. 2, pp. 229–238, 2011.
- [56] P. R. Buenzli and N. A. Sims, "Quantifying the osteocyte network in the human skeleton," *Bone*, vol. 75, pp. 144 – 150, 2015.
- [57] C. Lerebours and P. R. Buenzli, "Towards a cell-based mechanostat theory of bone: the need to account for osteocyte desensitisation and osteocyte replacement," *Journal of Biomechanics*, vol. 49, no. 13, pp. 2600 – 2606, 2016.
- [58] G. Marotti, "The osteocyte as a wiring transmission system," *Journal of musculoskeletal & neuronal interactions*, vol. 1, no. 2, pp. 133–136, 2000.
- [59] Q. Grimal, K. Raum, A. Gerisch, and P. Laugier, "A de-

- termination of the minimum sizes of representative volume elements for the prediction of cortical bone elastic properties,” *Biomechanics and Modeling in Mechanobiology*, vol. 10, pp. 925–37, 12 2011.
- [60] M. Granke, O. Lopez, Q. Grimal, J.-M. Allain, A. Saied, J. Crépin, and P. Laugier, “Contribution of matrix heterogeneity and pores to local strains in human cortical bone,” *Journal of Biomechanics*, vol. 45, no. Supplement 1, p. S474, 2012. Proceedings of ESB2012 - 18th Congress of the European Society of Biomechanics.
- [61] D. Rohrbach, S. Lakshmanan, F. Peyrin, M. Langer, A. Gerisch, Q. Grimal, P. Laugier, and K. Raum, “Spatial distribution of tissue level properties in a human femoral cortical bone,” *Journal of Biomechanics*, vol. 45, no. 13, pp. 2264 – 2270, 2012.
- [62] R. Martin, “Does osteocyte formation cause the nonlinear refilling of osteons?,” *Bone*, vol. 26, pp. 71–78, 2000.
- [63] L. F. Bonewald and M. L. Johnson, “Osteocytes, mechanosensing and Wnt signaling,” *Bone*, vol. 42, no. 4, pp. 606 – 615, 2008.
- [64] P. R. Buenzli, P. Pivonka, B. S. Gardiner, and D. W. Smith, “Modelling the anabolic response of bone using a cell population model,” *Journal of Theoretical Biology*, vol. 307, no. Supplement C, pp. 42 – 52, 2012.
- [65] S. C. Cowin and L. Cardoso, “Blood and interstitial flow in the hierarchical pore space architecture of bone tissue,” *Journal of Biomechanics*, vol. 48, no. 5, pp. 842 – 854, 2015. In Memory of Rik Huiskes.
- [66] Y.-X. Qin, T. Kaplan, A. Saldanha, and C. Rubin, “Fluid pressure gradients, arising from oscillations in intramedullary pressure, is correlated with the formation of bone and inhibition of intracortical porosity,” *Journal of Biomechanics*, vol. 36, no. 10, pp. 1427 – 1437, 2003. Bone Cell and Tissue Mechanics.
- [67] R. Y. Kwon, D. R. Meays, W. J. Tang, and J. A. Frangos, “Microfluidic enhancement of intramedullary pressure increases interstitial fluid flow and inhibits bone loss in hindlimb suspended mice,” *Journal of Bone and Mineral Research*, vol. 25, no. 8, pp. 1798–1807, 2010.
- [68] R. Y. Kwon, D. R. Meays, A. S. Meilan, J. Jones, R. Miramontes, N. Kardos, J. Yeh, and J. A. Frangos, “Skeletal adaptation to intramedullary pressure-induced interstitial fluid flow is enhanced in mice subjected to targeted osteocyte ablation,” *PLoS One*, vol. 7, no. 3, p. e33336, 2012.
- [69] J. Power, K. E. Poole, R. van Bezooijen, M. Doube, A. M. Caballero-Alias, C. Lowik, S. Papapoulos, J. Reeve, and N. Loveridge, “Sclerostin and the regulation of bone formation: Effects in hip osteoarthritis and femoral neck fracture,” *Journal of Bone and Mineral Research*, vol. 25, no. 8, pp. 1867–1876, 2010.
- [70] P. Dong, S. Hauptert, B. Hesse, M. Langer, V. Goutenoire, Pierre-Jean Bousson, and F. Peyrin, “3D osteocyte lacunar morphometric properties and distributions in human femoral cortical bone using synchrotron radiation micro-CT images,” *Bone*, vol. 60, pp. 172 – 185, 2014.
- [71] A. G. Robling and S. D. Stout, “Morphology of the drifting osteon,” *Cells Tissues Organs*, vol. 164, no. 4, pp. 192–204, 1999. Copyright - Copyright (c) 1999 S. Karger AG, Basel; Last updated - 2013-01-25.
- [72] C. M. Maggiano, “Making the mold. A microstructural perspective on bone modeling during growth and mechanical adaptation,” in *Bone histology. An anthropological perspective* (C. Crowder and S. Stout, eds.), pp. 45–90, Boca Raton: CRC Press, 2011.
- [73] C. Crowder and S. Stout, eds., *Bone Histology: An Anthropological Perspective*. CRC Press, 2011.
- [74] U. E. Pazzaglia, T. Congiu, M. Marchese, R. Spagnuolo, and D. Quacci, “Morphometry and patterns of lamellar bone in human Haversian systems,” *Anat. Rec.*, vol. 295, pp. 1421–1429, 2012.

## Supporting material

### 1 Influence of initial porosity on average infilling rate

Figure S1 shows simulations of the infilling of random pore 8 of Fig. 7 scaled down by 70% and scaled up by 130%, performed with Model 3 and  $D = 0.00075\text{mm}^2/\text{day}$ . The corresponding plot of the average interface velocity versus the average pore radius are shown in Fig. S2.

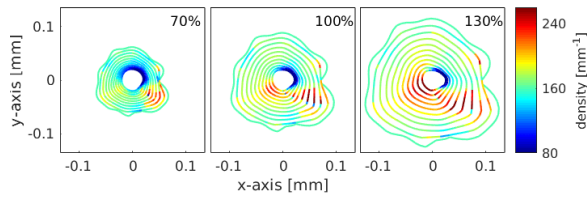


**Figure S1** – Infilling of random pore 8 using Model 3 and  $D = 0.00075$  at 70%, 100% and 130% of the size shown in Fig. 7.

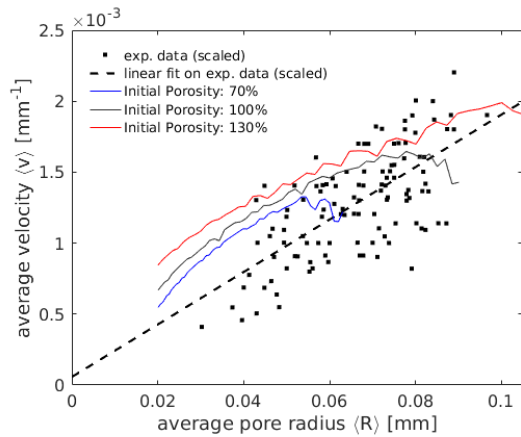


**Figure S2** – Comparison of the average interface velocity versus the average pore radius between different scales of random pore 8 (solid lines) and experimental data (black squares).

## Chapter 6

# Modelling curvature-controlled tissue growth in complex interface geometries

### 6.1 Overview

In all of the previous chapters, bone (or tissue) interfaces were parameterised explicitly. The evolution equations were specialised to specific coordinate systems depending on the overall geometry of the interface and were also converted into the conservative forms.

In this chapter, we present the situation when the evolving bone (or tissue) interface is captured implicitly. This is done by embedding the interface as the zero level set of an evolving function, avoiding the need to explicitly parameterise the interface.

One of the advantages of this method compared to the explicit parameterisation method, is its ability to undertake complex bone (or tissue) geometries. This method is anticipated to provide an easier generalisation to the evolution of tissues in three dimensions, where explicit parameterisations of interface are more difficult to implement. However, employing this method requires us to reformulate the explicit parameterisation equations, as presented in Sect. 2.2.

Future work on this topic includes to implement better conserving level set techniques and to find methods with better estimations of geometric quantities such as normal vector and curvature.

## 6.2 Introduction

Topological changes in bone occur, for example, due to enlargement and fusion of trabecular struts during bone growth, and trabecularisation of cortical bone or loss of connectivity of trabecular bone during age-related osteoporosis [52–55]. Figure 6.1 shows the cross-section of a femoral mid-shaft taken from Bell *et al.* [54]. In the figure, there are large cannals inhabiting giant osteons, in which the giant osteons were suggested to be formed by the merging of adjacent, clustered smaller osteons [80]. In terms of numerical simulations, these topological changes require ad-hoc treatment of the numerical techniques, as the interface can no longer be continuously parameterised by a single function, say  $\gamma(s, t)$ , used in the previous chapters [56].

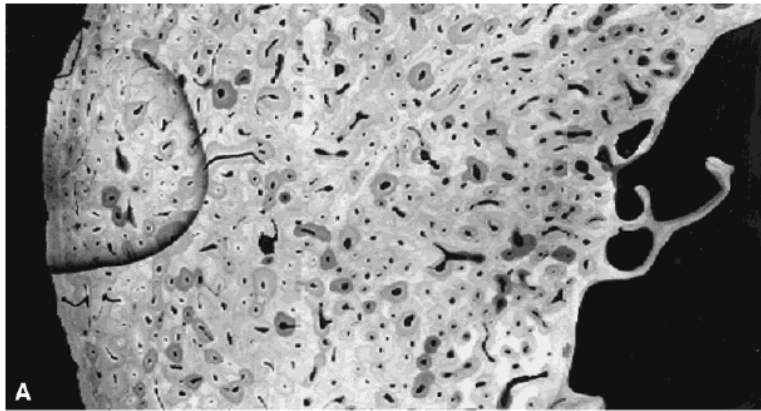


FIGURE 6.1: Structure of cortical bone during trabecularisation due to osteoporosis (reproduced with permission from Bell *et al.* [54]).

---

The level set method was created to overcome this problem [57]. In terms of the tissue growth dynamics, the level set method has been employed in Ref. [81] to study tumor growth. This has been followed by Ref. [82, 83] and also other studies focusing on this topic, each coming up with improved numerical techniques and more realistic model assumptions. The level set method has also been used to study epidermal wound healing in [84]. This model takes into account certain elements, for example, the wound edge (interface) dynamics, transport of nutrient, growth factors and cells, and cell mitosis. Recently, the level set method has been employed in Refs. [37–39] to model curvature-controlled neotissue growth in bioscaffolds.

In all these models, there was no consideration made on the density of cells residing on the interface, and how the local curvature of the interface co-evolves with the cell surface density. The inclusion of the cell surface density, so far, is similar to the case

of considering the distribution of surfactants on an impermeable deforming interface in Ref. [59]. However, in the case of biological tissue, there is a coupling between the evolutions of the interface and the cell surface density, which was not available for surfactants. Hence, the level set model in Ref. [59] assumed that the interface was advected by an external known velocity field.

The aim of this chapter is to develop a cell-based level set method, adapted from our previous model in Chapter 3. The advantages of the level set model are well-known [85]. They will enable us to model complex tissue topologies and abrupt changes that these tissues may be subjected to, such as splitting or merging of different tissue parts.

The coupled level-set-like equations have been derived in Sect. 2.2 by reformulating the explicit parameterisation equations. Chapter 6 is organised as follows. First, we recall the coupled level-set-like equations derived in Sect. 2.2. This will be followed by the numerical techniques implemented to discretise the level-set-like equations. To assist readers, we also outline the procedure of the numerical implementation chronologically. Finally, we present the results of the numerical simulations and how they compare to the output of the explicit model in [47]. We also implement the level set method for a few complex tissue interface geometries.

## 6.3 Mathematical methods

### 6.3.1 Implicit parameterisation of interface

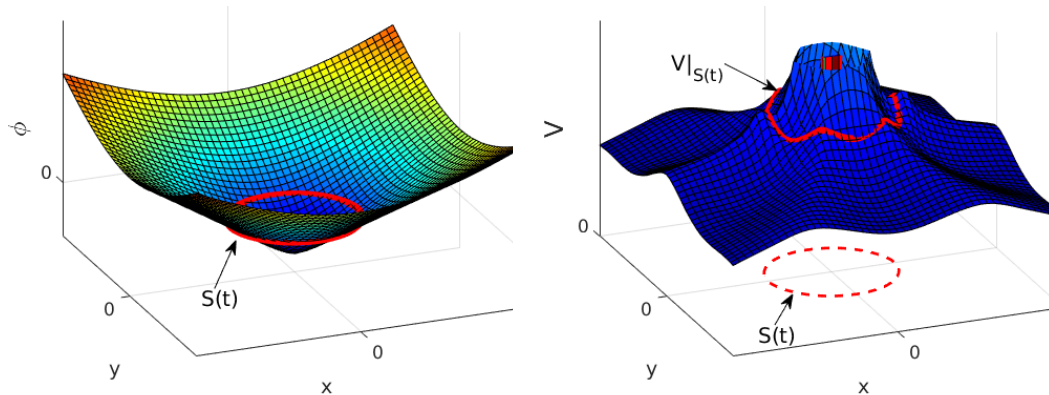


FIGURE 6.2: Level set function  $\phi$  with interface  $S(t)$  at its zero level set (left). The values of velocity function  $V$  at the interface points  $S(t)$  are the interface velocity

$$V|_{S(t)} = \{V(x, y, t) | (x, y) \in S(t)\} \text{ (right).}$$

The 1D interface  $S(t)$  of a two-dimensional tissue can be described by the zero contour level of a 2-parametric surface (as shown in Fig. 6.2). The 2D surface of a

real biological tissue in 3D space can similarly be described by the zero contour level of a 3-parametric hypersurface. Since the tissue interface  $S(t)$  grows by the deposition of new tissue matrix secreted by cells at the tissue surface, this results in two coupled level-set-like equations (see Sect. 2.2):

$$\phi_t + V|\nabla\phi| = 0 \quad (6.1)$$

$$V_t + \nabla V \cdot V\mathbf{n} = -\kappa V^2 + D\nabla_\ell^2 V - AV \quad (6.2)$$

where  $V|_{S(t)} = \{V(x, y, t) | (x, y) \in S(t)\}$ . The level set function  $\phi$  is usually initialised as a signed distance function such that the interface is always at its zero level set. Here, we will always assume that the initial surface density of cells and hence the initial velocity of the interface  $v(s, 0)$  is a uniform constant  $v^0$ . For simplicity, we assume that the initial velocity  $V(x, y, 0)$  is a plane with a height  $v^0$  on the  $z$ -axis. This provides a way to extrapolate the velocity  $V$  far from the interface.

Here, cell diffusion is assumed to be isotropic in space and the surface Laplacian operator is defined as  $\nabla_\ell^2 V = \nabla^2 V - \kappa\partial_n V - \partial_{nn} V$ , where  $\partial_n V = \partial V / \partial n = \mathbf{n} \cdot \nabla V$  and  $\partial_{nn} V = \partial^2 V / \partial n^2 = \mathbf{n} \cdot \mathbf{H}(V) \cdot \mathbf{n}$ , where  $\mathbf{H}(V)$  is the Hessian matrix of  $V$  [59]. Methodologically, to obtain  $v$  at  $S(t)$  for any time  $t$ , interpolation on  $V$  must be done since the obtained interface  $S(t)$  may not fall on the grid points defined during numerical simulation.

### 6.3.2 Numerical schemes

Since the interface  $S(t)$  is described by the zero level set of the function  $\phi$ , the level set method adds computational cost due to calculations made on the entire domain of  $\phi$  (and  $V$ ). Several methods have been developed to localise calculations within a band near the interface resulting in less computational effort [86]. This was not pursued here.

The following parts of this section explain the steps to solve the level set equations (6.1) and (6.2) from time  $t^0$  to  $t^1 = t^0 + \Delta t$ . These steps are based on those outlined in Ref. [87], with some modifications to account for the discretisation of the surface Laplacian operator  $\nabla_\ell^2$ . Here we use a finite difference method for calculations. We also consider reflective boundary condition, that is,  $\phi_x = \phi_y = 0$  at the boundaries of the level set domain at any time  $t$ . Using a periodic boundary condition does not change the results significantly.

*Step 1:* Initialise  $\phi(x, y, t^0) = \phi^0$  to be a signed normal distance function to the interface  $\gamma(s, t^0) \in S(t^0)$ . The velocity  $V(x, y, t^0)$  is initialised, in this study, as a constant  $v^0$  (see Sect. 6.3.2.1).

*Step 2:* Solve the level set equation of the interface  $\phi_t + V|\nabla\phi| = 0$  for one time step with initial condition  $\phi^0$  (see Sect. 6.3.2.2). Denote the updated  $\phi$  by  $\phi^{\frac{1}{2}}$ .

*Step 3:* The updated  $\phi^{\frac{1}{2}}$  is no longer a signed distance function. Construct a new distance function by reinitialisation, i.e., by solving  $\psi_\tau = -\mathbf{S}(\psi)(|\nabla\psi| - 1)$  to steady state with initial condition  $\psi^0 = \phi^{\frac{1}{2}}$ , where  $\mathbf{S}(\psi)$  is a smoothed sign function defined in Eq. (6.8) (see Sect. 6.3.2.3). The steady state solution  $\psi^\infty$  is then denoted by  $\phi^1$ .

*Step 4:* Use the Alternating Direction Implicit Method (ADI) to find  $V^{\frac{1}{2}}$  followed by  $V^1$ , with  $\kappa^0$  and  $\mathbf{n}^0$  (calculated from  $\phi^0$ ) are part of the algorithm's inputs (see Sect. 6.3.2.4).

*Step 5:* The zero level set of  $\phi^1$  gives the new interface position  $\gamma(s, t^1) \in S(t^1)$  while  $\phi^1$  is still a distance function. The value of the velocity function  $V^1$  at the interface point  $\gamma(s, t^1)$  corresponds to the interface velocity  $v(s, t^1)$  in the explicit parameterisation scheme. Repeat Steps 2 to 4 to progress from  $t^1$  to  $t^2 = t^1 + \Delta t$  and further.

### 6.3.2.1 Step 1: Initialisation of functions $\phi(x, y, t^0)$ and $V(x, y, t^0)$

The interface function and velocity function can be initialised using

$$\phi(x, y, t^0) = \phi^0 = d(x, y) \quad , \quad V(x, y, t^0) = v^0 \quad (6.3)$$

where  $d(x, y)$  is the signed distance from point  $\mathbf{x} = (x, y)$  to the interface  $\gamma(s, t^0)$  and  $v^0$  is assumed constant. Thus, the function  $V(x, y, t^0)$  can be thought of as a plane with a height  $v^0$  on the  $z$ -axis.

### 6.3.2.2 Step 2: Solving for $\phi(x, y, t^0)$

Once the function  $\phi$  has been initialised, the level set equation of the interface in (6.1) can be solved by the finite difference method with initial condition  $\phi^0$ . In this regard, the term  $V|\nabla\phi|$  in Eq. (6.1) can be discretised by an upwind scheme:

$$V|\nabla\phi| \approx \max(V, 0)\nabla^+ + \min(V, 0)\nabla^- \quad (6.4)$$

where

$$\begin{aligned} \nabla^+ &= \sqrt{\max(\phi_x^-, 0)^2 + \min(\phi_x^+, 0)^2 + \max(\phi_y^-, 0)^2 + \min(\phi_y^+, 0)^2} \\ \nabla^- &= \sqrt{\min(\phi_x^-, 0)^2 + \max(\phi_x^+, 0)^2 + \min(\phi_y^-, 0)^2 + \max(\phi_y^+, 0)^2} \end{aligned} \quad (6.5)$$

known as the Hamilton-Jacobi (also called Engquist-Osher-type) scheme [57, 58, 86].

Other schemes can also be used for example the Godunov-type scheme, which is given as follows [58, 86]:

$$\begin{aligned} \nabla^+ &= \sqrt{\max[\max(\phi_x^-, 0)^2, \min(\phi_x^+, 0)^2] + \max[\max(\phi_y^-, 0)^2, \min(\phi_y^+, 0)^2]} \\ \nabla^- &= \sqrt{\max[\min(\phi_x^-, 0)^2, \max(\phi_x^+, 0)^2] + \max[\min(\phi_y^-, 0)^2, \max(\phi_y^+, 0)^2]}. \end{aligned} \quad (6.6)$$

The results of both schemes (6.5) and (6.6) can be improved by using the high-order ENO or WENO approximations of the first derivatives  $\phi_x$  and  $\phi_y$  [88–90]. We use the fifth-order WENO scheme from the work of Ref. [91] to approximate the derivatives. Details of this scheme is also given in Ref. [92]. The output obtained in this step is denoted as  $\phi^{\frac{1}{2}}$ , which will then be used as an input in the next step.

### 6.3.2.3 Step 3: Reinitialisation of $\phi(x, y, t^0)$

When the interface moves, the function  $\phi$  initialised in *Step 1* usually stops from being a signed distance. Thus, the function  $\phi$  needs to be reinitialised as a signed distance without modifying the new interface position. The most direct method is to explicitly measure the distance of each grid points to the interface, as done in *Step 1* [93]. However, this approach is very costly especially if that is done at every time step. Another method to achieve this purpose is by using a reinitialisation equation:

$$\psi_\tau = -\mathbf{S}(\psi)(|\nabla\psi| - 1) \quad (6.7)$$

as suggested in [86]. Here, the time  $\tau$  is a virtual time that is not the same as the real time  $t$ . The function  $\mathbf{S}(\psi)$  is the smoothed sign function defined as:

$$\mathbf{S}(\psi) = \frac{\psi}{\sqrt{\psi^2 + |\nabla\psi|^2(\Delta x)^2}}. \quad (6.8)$$

There are other variations of the sign function  $\mathbf{S}(\psi)$  for example the one proposed in [87]. In this step, the initial condition of the problem in (6.7) is taken to be  $\psi^0 = \phi^{\frac{1}{2}}$  obtained from Step 2 while the produced steady-state output  $\psi^\infty$  is denoted as the evolved level set function at the next time step  $\phi^1$ . From Eq. (6.7), when the steady-state is achieved, i.e.  $\psi_\tau \approx 0$ , then  $|\nabla\psi| \approx 1$ , which indicates the resulting function  $\psi^\infty$  is approximately a signed distance function. The method ensures that the reinitialisation is done efficiently without changing significantly the interface position as the zero level set (or contour) of the level set function, since  $\mathbf{S}(0) = 0$ .

Similarly to the previous step, the RHS of Eq. (6.7) can be discretised by an upwind scheme:

$$\mathbf{S}(\psi)(|\nabla\psi| - 1) \approx \max(s, 0)(\nabla^+ - 1) + \min(s, 0)(\nabla^- - 1) \quad (6.9)$$

where  $\nabla^+$  and  $\nabla^-$  are as defined in Eq. (6.5) or Eq. (6.6) (except that  $\phi$  is changed to  $\psi$ ), and  $s$  is a finite difference approximation to  $\mathbf{S}(\psi)$  in Eq. (6.8). The reinitialisation condition is checked at every time step, such that the reinitialisation will only occur when the average slope of  $\phi$  for points within the band  $\beta$  of the interface deviates significantly from 1, i.e., when the level set function is no longer a good approximation of a distance function [86]. This is implemented mathematically by enforcing reinitialisation whenever

$$\frac{1}{M} \sum_{(i,j):|\phi_{ij}^{n'}|<\beta} \left| |\nabla\phi_{ij}^{n'}| - 1 \right| > \epsilon_{\text{reinit}} \Delta x \Delta y. \quad (6.10)$$

This is the same to the condition given in Ref. [87] in a way that the condition  $\left| |\nabla\phi_{ij}^{n'}| - 1 \right|$  in Eq. (6.10) is equivalent to the condition  $|\phi_{ij}^{n'+1} - \phi_{ij}^{n'}|$  in Ref. [87] at the steady state (see Eq. (6.7)). In Eq. (6.10),  $M$  is the number of the grid points within the band  $\beta$  of the interface, in which  $\beta = 5\Delta x = 5\Delta y$  is usually used in this study. The error tolerance  $\epsilon_{\text{reinit}}$  varies according to the type of problem, and is mentioned specifically for each problem in the results section. It is important to note from Eq. (6.10) that the space steps  $\Delta x$  and  $\Delta y$  of the problem affects the value of  $\epsilon_{\text{reinit}}$  selected. The

superscript  $n'$  implies the virtual timestep corresponds to  $\tau$  in Eq. (6.7) which differs from the real timestep  $n$ . The gradient  $\nabla\phi$  in this reinitialisation step is calculated using the central difference scheme.

#### 6.3.2.4 Step 4: Solving for $V(x, y, t^0)$

In the level set method, a normal vector  $\mathbf{n}$  and curvature  $\kappa$  can be calculated directly in the whole domain by using

$$\mathbf{n} = \frac{\nabla\phi}{|\nabla\phi|} \quad , \quad \kappa = \nabla \cdot \left( \frac{\nabla\phi}{|\nabla\phi|} \right). \quad (6.11)$$

These two quantities are important for the evolution of the velocity (and hence the cell surface density) in Eq. (6.2). Besides, it has been shown in Ref. [59] that  $\nabla_\ell^2 V = \nabla^2 V - \kappa \partial_n V - \partial_{nn} V$ , where  $\partial_n V = \partial V / \partial n = \mathbf{n} \cdot \nabla V$  and  $\partial_{nn} V = \partial^2 V / \partial n^2$ , which require us to calculate frequently the normal vector  $\mathbf{n}$  and curvature  $\kappa$ . Since the level set function  $\phi$  is taken to be a signed distance function, there is a possibility of producing a jump in the gradient of  $\phi$  which causes the normal vector to become ambiguous. This jump is produced at points that are equidistant from two or more of the interface points, for example the centre of circle (that also happens to fall on the grid points). To alleviate this issue, we use the technique proposed in Ref. [56] by taking the normal vector  $\mathbf{n} = (n_1, n_2)$  as the average of the four limiting normal vectors calculated by the backward and forward finite differences.

By writing the normal vector componentwise, and considering a two-dimensional domain in the  $xy$ -plane, we can write certain terms as follows:

$$\nabla V \cdot V \mathbf{n} = (n_1 V) V_x + (n_2 V) V_y \quad (6.12)$$

$$\nabla^2 V = \nabla \cdot (\nabla V) = \frac{\partial^2 V}{\partial x^2} + \frac{\partial^2 V}{\partial y^2} \quad (6.13)$$

$$\partial_n V = \frac{\partial V}{\partial n} = \mathbf{n} \cdot \nabla V = \begin{bmatrix} n_1 \\ n_2 \end{bmatrix} \cdot \begin{bmatrix} \partial V / \partial x \\ \partial V / \partial y \end{bmatrix} = n_1 V_x + n_2 V_y \quad (6.14)$$

$$\partial_{nn} V = \frac{\partial^2 V}{\partial n^2} = \mathbf{n} \cdot \mathbf{H}(V) \cdot \mathbf{n} = n_1^2 \frac{\partial^2 V}{\partial x^2} + 2n_1 n_2 \frac{\partial^2 V}{\partial y \partial x} + n_2^2 \frac{\partial^2 V}{\partial y^2} \quad (6.15)$$

where  $\mathbf{H}(V)$  is the Hessian matrix of  $V$ . This consequently recasts Eq. (6.2) as:

$$V_t = D \left( \frac{\partial^2 V}{\partial x^2} + \frac{\partial^2 V}{\partial y^2} \right) + \alpha(x, y, t) \quad (6.16)$$

where

$$\begin{aligned} \alpha(x, y, t) = & - [(n_1 V)V_x + (n_2 V)V_y] - \kappa V^2 - AV \\ & - D\kappa (n_1 V_x + n_2 V_y) - D \left( n_1^2 \frac{\partial^2 V}{\partial x^2} + 2n_1 n_2 \frac{\partial^2 V}{\partial y \partial x} + n_2^2 \frac{\partial^2 V}{\partial y^2} \right) \end{aligned} \quad (6.17)$$

### ***Space discretisations***

As done in Ref. [59], the advection terms  $(n_1 V)V_x + (n_2 V)V_y$  in Eq. (6.17) are discretised using the upwind scheme while the other terms in Eq. (6.17), including the Laplacian operator in Eq. (6.16), are discretised using the central difference schemes. The upwind approximation of the advection terms is done as follows:

$$\begin{aligned} (n_1 V)V_x + (n_2 V)V_y \approx & \max(n_1 V, 0)V_x^- + \min(n_1 V, 0)V_x^+ \\ & + \max(n_2 V, 0)V_y^- + \min(n_2 V, 0)V_y^+. \end{aligned} \quad (6.18)$$

Note that we only depend on the signs of  $Vn_1$  and  $Vn_2$  to correctly determine the upwind direction. While the derivatives  $V_x^-, V_x^+, V_y^-$  and  $V_y^+$  can be computed by the first order forward and backward differences, the high resolution fifth-order WENO schemes are used in this study [88–91]. On the other hand, the standard second-order central differences are used when discretising the other non-advective terms including the normal vector  $\mathbf{n}$  and curvature  $\kappa$ . These second-order central differences can also be replaced by the fourth-order central differences, whose formulae can be found for example in Ref. [94].

### ***Time discretisations***

Decomposing the surface Laplacian operator as  $\nabla_\ell^2 V = \nabla^2 V - \kappa \partial_n V - \partial_{nn} V$  allows us to lessen the stiffness caused by surface diffusion [59, 95]). Numerical stability is obtained by a semi-implicit scheme where the standard Laplacian operator is solved

implicitly, while the other terms are solved explicitly. Here we use the Alternating Direction Implicit Method (ADI) [96] to discretise the time derivative that rewrites the velocity evolution equation in Eq. (6.16) as:

$$\frac{V_{i,j}^{\frac{1}{2}} - V_{i,j}^0}{0.5\Delta t} = D \left( \frac{\partial^2 V^{\frac{1}{2}}}{\partial x^2} + \frac{\partial^2 V^0}{\partial y^2} \right)_{i,j} + \alpha_{i,j}^0 \quad (6.19)$$

$$\frac{V_{i,j}^1 - V_{i,j}^{\frac{1}{2}}}{0.5\Delta t} = D \left( \frac{\partial^2 V^{\frac{1}{2}}}{\partial x^2} + \frac{\partial^2 V^1}{\partial y^2} \right)_{i,j} + \alpha_{i,j}^0. \quad (6.20)$$

This allows us to avoid costly numerical calculations incurred by other methods, for example, the implicit iterative method, if both derivatives  $\partial^2 V / \partial x^2$  and  $\partial^2 V / \partial y^2$  in Eq. (6.16) are solved simultaneously. The step to determine  $V_{i,j}^{\frac{1}{2}}$  from Eq. (6.19) is known as the predictor step, while the step to find  $V_{i,j}^1$  from Eq. (6.20) is known as the corrector step. We keep on using  $\alpha_{i,j}^0$  in Eq. (6.20) rather than  $\alpha_{i,j}^{\frac{1}{2}}$ , which will otherwise add significant amount of calculations. By using the central difference schemes to discretise the second derivatives, and taking

$$r = \frac{0.5\Delta t D}{\Delta x^2} = \frac{0.5\Delta t D}{\Delta y^2} \quad (6.21)$$

(provided  $\Delta x = \Delta y$ ), we obtain a system of equations for a specific  $j$  (where  $j = 1, 2, \dots, Y + 1$ ):

$$\mathbf{A}_r \mathbf{V}_j^{\frac{1}{2}} = \boldsymbol{\gamma}_j^0 \quad (6.22)$$

where  $\mathbf{V}_j^{\frac{1}{2}} = [V_{1,j}^{\frac{1}{2}}, V_{2,j}^{\frac{1}{2}}, \dots, V_{X+1,j}^{\frac{1}{2}}]$  is the unknown vector. On the other hand, the vector  $\boldsymbol{\gamma}_j^0 = [\gamma_{1,j}^0, \gamma_{2,j}^0, \dots, \gamma_{X+1,j}^0]$  is a known  $\boldsymbol{\gamma}$  vector whose elements are computed at each time step by

$$\gamma_{i,j}^0 = V_{i,j}^0 + r (V_{i,j+1}^0 - 2V_{i,j}^0 + V_{i,j-1}^0) + 0.5\Delta t \alpha_{i,j}^0. \quad (6.23)$$

The  $(X + 1) \times (X + 1)$  matrix  $\mathbf{A}_r$  is represented by the tridiagonal matrix

$$\mathbf{A}_r = \begin{bmatrix} 1+2r & -2r & 0 & \cdots & 0 & 0 & 0 \\ -r & 1+2r & -r & \cdots & 0 & 0 & 0 \\ 0 & -r & 1+2r & \cdots & 0 & 0 & 0 \\ \vdots & \vdots & \vdots & \ddots & \vdots & \vdots & \vdots \\ 0 & 0 & 0 & \cdots & 1+2r & -r & 0 \\ 0 & 0 & 0 & \cdots & -r & 1+2r & -r \\ 0 & 0 & 0 & \cdots & 0 & -2r & 1+2r \end{bmatrix} \quad (6.24)$$

and  $\alpha_{ij}^0$  in Eq. (6.23) is obtained from Eq. (6.17). Solving Eq. (6.22) for  $j = 1, 2, \dots, Y+1$  gives a matrix  $[V_{i,j}^{\frac{1}{2}}]_{1 \leq i \leq X+1, 1 \leq j \leq Y+1}$ . Once  $V_{i,j}^{\frac{1}{2}}$  is obtained for all  $i$ 's and  $j$ 's, we need to implement the corrector step.

Similarly to the previous step, we obtain a system of equations for a specific  $i$  (where  $i = 1, 2, \dots, X+1$ ):

$$\mathbf{A}_r \mathbf{V}_i^1 = \boldsymbol{\mu}_i^{\frac{1}{2}} \quad (6.25)$$

with  $\mathbf{V}_i^1 = [V_{i,1}^1, V_{i,2}^1, \dots, V_{i,Y+1}^1]$  is the unknown vector, while the known vector  $\boldsymbol{\mu}_i^{\frac{1}{2}} = [\mu_{i,1}^{\frac{1}{2}}, \mu_{i,2}^{\frac{1}{2}}, \dots, \mu_{i,Y+1}^{\frac{1}{2}}]$  has elements computed by

$$\mu_{i,j}^{\frac{1}{2}} = V_{i,j}^{\frac{1}{2}} + r \left( V_{i+1,j}^{\frac{1}{2}} - 2V_{i,j}^{\frac{1}{2}} + V_{i-1,j}^{\frac{1}{2}} \right) + 0.5\Delta t \alpha_{i,j}^0. \quad (6.26)$$

Similarly, the matrix  $\mathbf{A}_r$  is the cyclic trigonometric matrix in Eq. (6.24), while  $\alpha_{ij}^0$  in Eq. (6.26) is obtained from Eq. (6.17). Solving Eq. (6.25) for  $i = 1, 2, \dots, X+1$  gives a matrix  $[V_{i,j}^1]_{1 \leq i \leq X+1, 1 \leq j \leq Y+1}$ , whose elements are the required solutions for  $t^1$ .

Performing the steps 2 to 4 (described in detail in Sects. 6.3.2.2 to 6.3.2.4), the solution for  $\phi$  and  $V$  has now advanced one time step. The zero level set of  $\phi^1$  gives the new interface position  $S(t^1)$  and  $\phi^1$  is still a distance function. The values of the velocity function  $V^1$  at the interface points are the interface velocity  $V|_{S(t^1)}$ . To progress from  $t^1$  to  $t^2 = t^1 + \Delta t$  and further, Steps 2 to 4 need to be repeated.

## 6.4 Results

In this section, we present some numerical examples implemented using the level set method presented in Sect. 6.3, and compare the results with those obtained analytically or by using the explicit interface parameterisation method in Chapter 3. We then

present the results when the level set method is applied to a situation of merging of two interfaces, something that is not straightforward to implement with the explicit interface parameterisation. We also test the level set method on a few complex tissue interface geometries of bioscaffolds and trabecular networks. These are a prototype for the design of more comprehensive model to undertake real tissue remodelling process, for example, within the complex interconnected trabecular and osteon networks [53, 54, 97].

In the figures of this section, the colour used in each interface represents the surface density of cells residing on the interface. We look at several aspects of the output, specifically, the shape of the interface, cell density on the interface and conservation of cell number. Cell number is calculated by integrating the product of the interface length and cell surface density, i.e.  $N(t) = \int_{S(t)} \rho dl$  throughout the interface. Here, unless otherwise stated, we set  $A = 0$  which means there is no cell depletion. Consequently, we expect the cell number to be constant throughout the interface motion, so that any recorded loss of cell number can then be attributed to numerical shortcomings.

#### 6.4.1 Circular interface

Starting with a radius  $R^0$  and a homogeneous cell surface density  $\rho^0$ , we can calculate (refer Eqs. (26)-(27) of Chapter 3) the analytical radius and cell surface density at any time  $t$ :

$$R(t) = \sqrt{R^0(-2k_f\rho^0t + R^0)} \quad , \quad \rho(t) = R^0\rho^0/R(t) \quad (6.27)$$

For a circular interface, changing cell diffusivity  $D$  gives no effect on the evolutions of interface and cell surface density. This is clearly seen in Eqs. (6.27) which do not depend on  $D$ .

Fig. 6.3 (left and middle) shows the output of the level set method and the analytical solution when the interface is moving inwards. Here, the cell secretion rate  $k_f$ , is scaled to 1, while  $R^0 = 9/(2\pi)$  mm and  $\rho^0 = 0.016$  mm/day (and hence  $v^0 = k_f\rho^0 = 0.016$  mm/day) initialise the interface radius and cell density, respectively. The choice  $v^0 = \rho^0 = 0.016$  mm/day is due to the calibration with in-vivo experimental output [47]. The interfaces in both of these plots match very well, showing the excellent performance of our level set method. The numerical cell number  $N(t)$  throughout the interface motion is constant indicating conservation of cell number (Fig. 6.3 (right)).

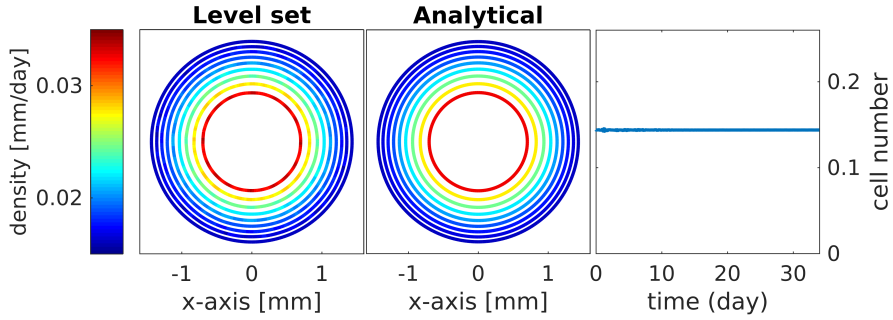


FIGURE 6.3: Temporal plots showing numerical and analytical output for inward motion of circular interface. The analytical solution is obtained from (6.27) while the numerical solution is calculated from the methods in Sect. 6.3.2. The numerical cell number is constant throughout the interface motion. The numerical scheme has details  $\epsilon_{\text{reinit}} = 5$ ,  $\beta = 5\Delta x = 5\Delta y$ ,  $x = -2.5 : \Delta x : 2.5$ ,  $y = -2.5 : \Delta y : 2.5$ ,  $t = 0 : \Delta t : 34$  days, where  $\Delta x = \Delta y = 0.0313$  and  $\Delta t = 0.0189$ .

#### 6.4.2 Hexagonal and square interfaces

Similarly to the hexagonal and square interfaces (both have the same perimeter), we take  $k_f = 1$  and  $\rho^0 = 0.016$  mm/day (and hence  $v^0 = k\rho^0 = 0.016$  mm/day). Here, cell diffusion is taken as  $D = 0.0001$ (low),  $0.0005$ ,  $0.001$ ,  $0.005$  (medium). The level set results are compared with the output produced by the explicit interface parameterisation method. Figs. 6.4 and 6.5 show the output of the hexagonal and square interfaces, respectively. In general, the output produced by the level set method exhibits the same behaviours as when using the explicit interface parameterisation: development of corners at low cell diffusion and regularisation (or smoothing) effect at medium diffusion, where the final interface for the latter becomes roughly circular. The case of high diffusion has considerably stricter CFL condition in the level set method (even after using ADI), and hence has not been studied extensively. While the output of the level set and explicit parameterisation for the hexagonal interface are much alike, the square interfaces in Fig. 6.5 seem to differ in terms of their velocities. This is caused by a numerical loss of cell number.

Fig. 6.6 shows the corresponding cell number throughout the inwards motion of the interfaces. The level set method records certain loss of cell number, as opposed to the case of explicit interface parameterisation that preserves cell number. This loss of cell number appears to be more severe in the case of the square interface, rather than its counterpart. Since  $N(t) = \int_{S(t)} \rho dl$  and the density  $\rho$  (or velocity  $V$ ) is coupled to the interface embedded in the level set function  $\phi$ , it is not surprising that the evolution of

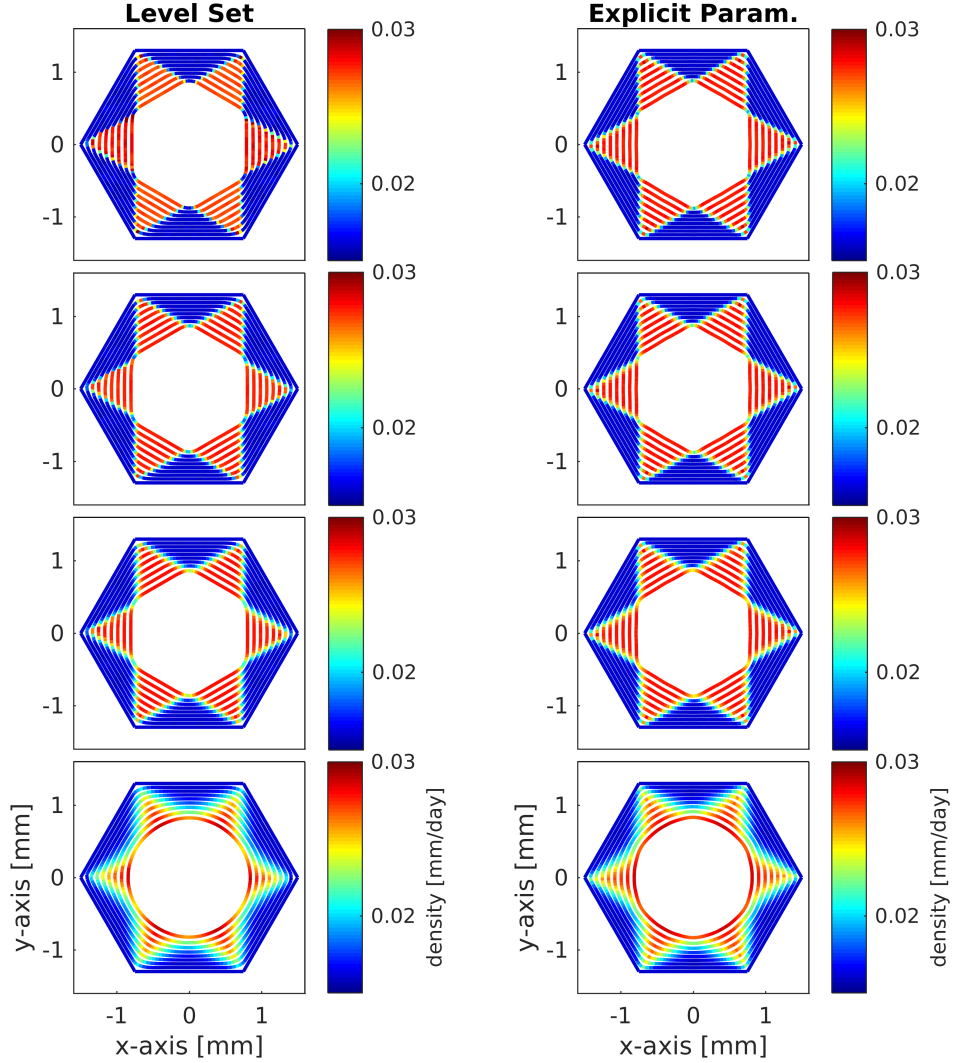


FIGURE 6.4: Evolutions of the hexagonal interface for  $D = 0.0001, 0.0005, 0.001, 0.005$  (from top to bottom) calculated using finite difference level set method (left column) and polar finite volume K-T scheme (right column). For the level set method,  $\epsilon_{\text{reinit}} = 5$ ,  $\beta = 5\Delta x = 5\Delta y$ ,  $x = -2.5 : \Delta x : 2.5$ ,  $y = -2.5 : \Delta y : 2.5$ ,  $t = 0 : \Delta t : 26$  days, where  $\Delta x = \Delta y = 0.0278$  and  $\Delta t = 0.0163$ . For the finite volume scheme, we use  $\theta = 0 : \Delta\theta : 2\pi$  and  $t = 0 : \Delta t : 26$  where  $\Delta\theta = 0.0349$  and  $\Delta t = 0.0163$ .

the square interface produced by the level set method (left column of Fig. 6.5) is not similar to that of the explicit interface parameterisation (right column of Fig. 6.5).

### 6.4.3 Fusion of two circular interfaces

We test the level set method on a hypothetical situation in trabecular struts where there is a topological change in the interface. We start with two nearby circular interfaces, each with a radius  $9/(4\pi)$  and with centres 1.9 mm apart, and assume that new tissue

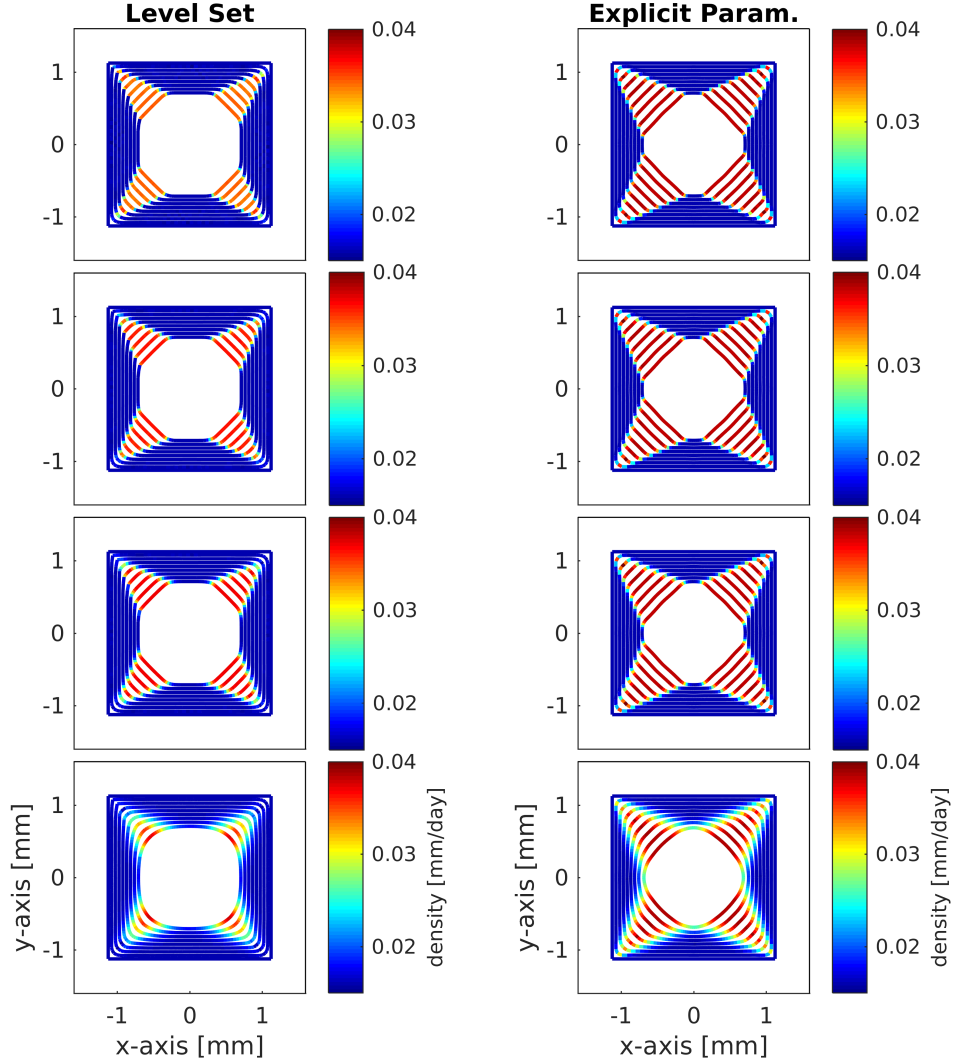


FIGURE 6.5: Evolutions of the square interface for  $D = 0.0001, 0.0005, 0.001, 0.005$  (from top to bottom) calculated using finite difference level set method (left column) and polar finite volume K-T scheme (right column). For the level set method,  $\epsilon_{\text{reinit}} = 5$ ,  $\beta = 5\Delta x = 5\Delta y$ ,  $x = -2.5 : \Delta x : 2.5$ ,  $y = -2.5 : \Delta y : 2.5$ ,  $t = 0 : \Delta t : 26$ , where  $\Delta x = \Delta y = 0.0313$  and  $\Delta t = 0.0163$ . For the finite volume scheme, we use  $\theta = 0 : \Delta\theta : 2\pi$  and  $t = 0 : \Delta t : 26$  days where  $\Delta\theta = 0.0393$  and  $\Delta t = 0.0163$ .

is grown outwards from their surfaces. These two interfaces and their fusion cannot easily be parameterised by a smooth explicit parameterisation, but it is possible to capture this evolution conveniently using the level set method. The moment when the two interfaces meet can directly be calculated using the analytical solution of  $R$  in Eq. (6.27). Here, we obtain  $t_{\text{fusion}} \approx 17$  days.

Fig. 6.7 (left) shows the merging of the two circular interfaces, with the first and final tissue geometries shown in Fig. 6.7 (right). This simulation represents the fusion

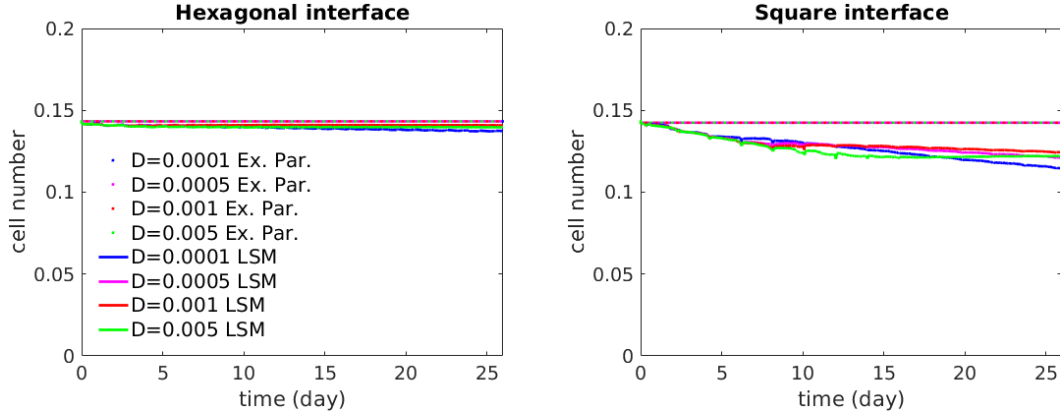


FIGURE 6.6: Evolution of cell number along the inward motion of hexagonal (left) and square (right) interfaces.

of two trabecular struts seen in cross section, due to bone gain induced for example by mechanical adaptation of bone. As for now, we only use  $D = 0.0001 \text{ mm}^2/\text{day}$ , which has been shown to give good match when comparing our model with the in-vitro experimental data [47]. The initial velocity is again chosen to be  $v^0 = 0.016 \text{ mm/day}$ .

The reverse process can be done by assuming the cells to be tissue-resorbing cells (osteoclasts), and hence the tissue secretion rate is changed to tissue resorption rate. Starting from the final interface of Fig. 6.7 as the new initial interface with  $v^0 = 0.016 \text{ mm/day}$ , the evolution shown in Fig. 6.8 does not recover the initial interface assumed for formation, i.e., two separate circles. In other words, bone resorption is not simply bone formation reversed in time. The reason for this time irreversibility is due to having to resort to weak solutions after the emergence of shocks which breaks time-reversal symmetry. One of the examples is the irreversibility of chemical reactions, for instance, when a fire line burns grass. Two fire fronts will not cross each other because once grass is burnt, it is not possible to ‘unburn it’. While our cell-based model also possesses irreversible reaction rates (cell death), the analogy with fire fronts is the fact that when two tissue interface fronts collide with each other, tissue-forming cells will not invade tissue already formed by the other front to continue adding new tissue within this existing tissue, but they will interact and reorganise themselves nonlinearly [58].

Fig. 6.9 shows the reduction in cell number calculated by the level set method, which starts earlier than the fusion time at  $t_{\text{fusion}} \approx 17$  days. The number continues to decrease at a slower rate and we expect that it will become fairly constant after some time. The loss of cells is due to the corners development during fusion, as will be

discussed in Sect. 6.5.

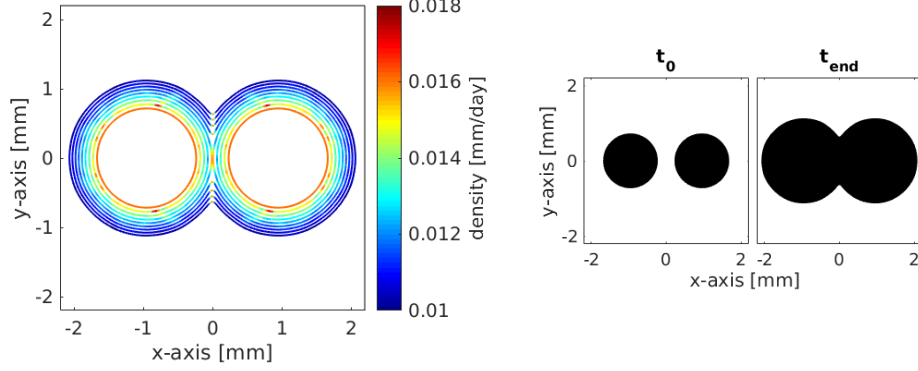


FIGURE 6.7: Outward motion of two circular interfaces at  $D = 0.0001$  calculated using the level set method (left). The initial and final interfaces (right). In this simulation,  $\epsilon_{\text{reinit}} = 5$ ,  $\beta = 5\Delta x = 5\Delta y$ ,  $x = -2.5 : \Delta x : 2.5$ ,  $y = -2.5 : \Delta y : 2.5$ ,  $t = 0 : \Delta t : 32$  days, where  $\Delta x = \Delta y = 0.0238$  and  $\Delta t = 0.0167$  and  $0.0133$ .

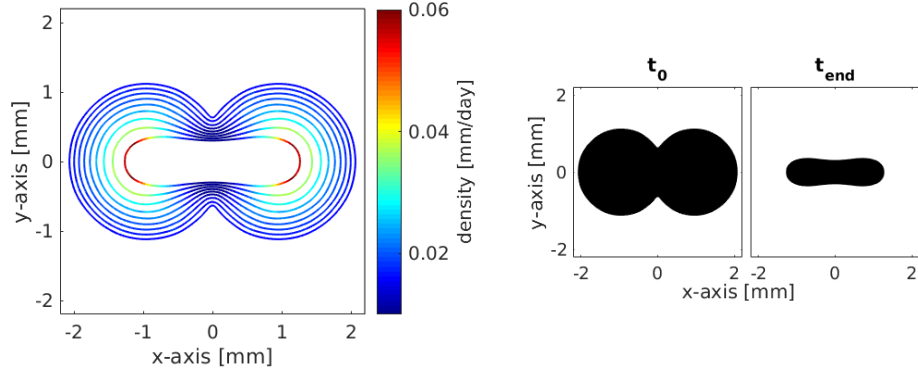


FIGURE 6.8: Inward motion of interface at  $D = 0.0001$  calculated using the level set method. The initial interface of this simulation is taken from the final interface of Fig. 6.7. Seeded with a constant density, the evolution does not recover the two separate circles. In this simulation,  $\epsilon_{\text{reinit}} = 5$ ,  $\beta = 5\Delta x = 5\Delta y$ ,  $x = -2.5 : \Delta x : 2.5$ ,  $y = -2.5 : \Delta y : 2.5$ ,  $t = 0 : \Delta t : 32$  days, where  $\Delta x = \Delta y = 0.0238$  and  $\Delta t = 0.0167$  and  $0.0133$ .

#### 6.4.4 Curvature-controlled tissue growth in bioscaffold

Bioscaffolds are important to allow cell attachment and to support tissue formation. In the bioscaffold experiments of Refs. [32–34, 36], it was shown that the velocity of tissue formation at concave areas of bioscaffolds is proportional to the local curvature, while at flat and convex areas, there is little tissue growth. To imitate this situation, we modify slightly the evolution equation of interface in Eq. (6.1) by adding a curvature-dependent Heaviside-like function producing

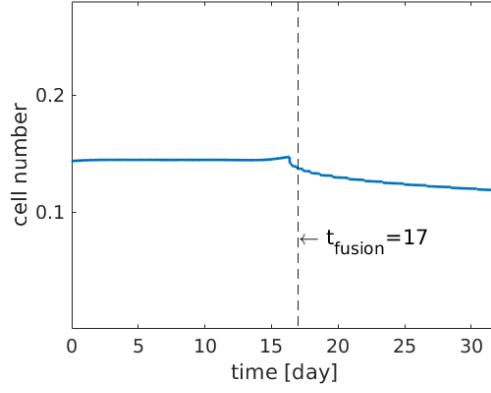


FIGURE 6.9: Evolution of numerical cell number for two circular interfaces that merge at time  $t_{\text{fusion}} \approx 17$  days, calculated using the level set method.

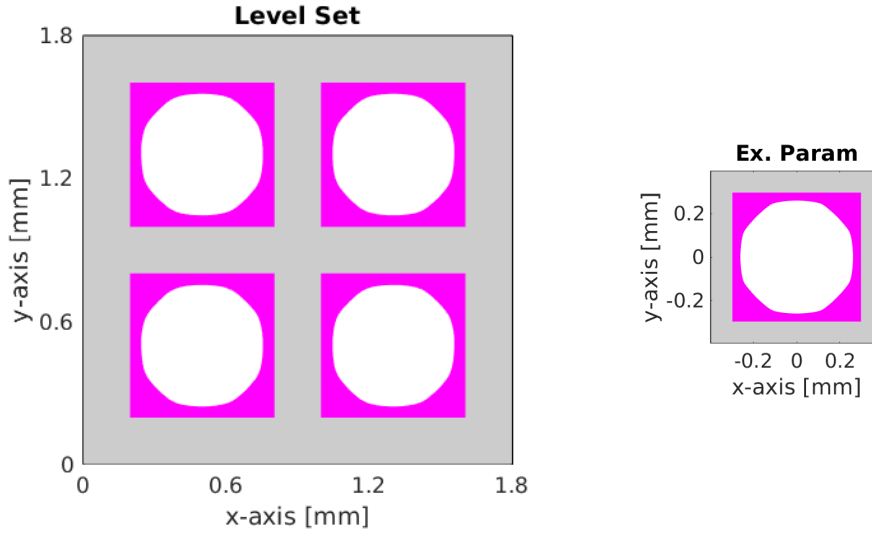


FIGURE 6.10: Evolutions of four square pores simultaneously in a bioscaffold calculated using the level set method, where the grey colour represents the bioscaffold, the magenta colour represents the new tissues, and the white colour represents the pore areas (left). A single pore produced by the explicit parameterisation model (right).

$$\phi_t + H(\kappa)V|\nabla\phi| = 0 \quad (6.28)$$

such that

$$H(\kappa) = \begin{cases} 1 & \text{for } \kappa < 0 & \text{(concave)} \\ 0 & \text{for } \kappa \geq 0 & \text{(flat and convex)} \end{cases} \quad (6.29)$$

Here we use cell secretion rate  $k_f = 1$ , diffusivity  $D = 0.0001 \text{ mm}^2/\text{day}$ , cell depletion rate  $A = 0.1/\text{day}$ , and initial cell density  $\rho^0 = 0.016 \text{ mm}/\text{day}$  (and hence initial velocity  $v^0 = 0.016 \text{ mm}/\text{day}$ ).

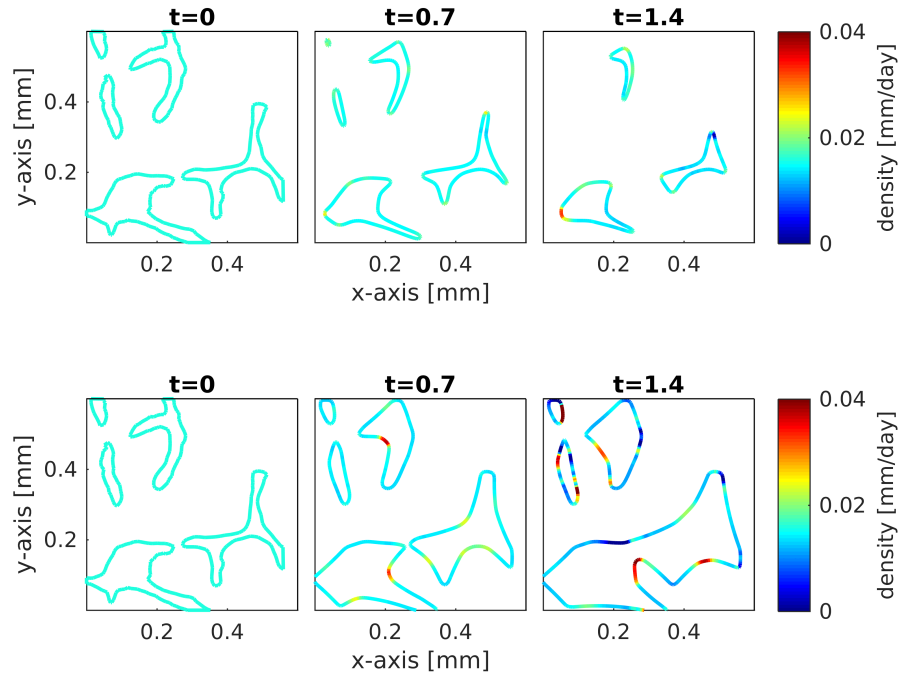


FIGURE 6.11: Evolution of trabecular bone calculated using the level set method, with the initial interface obtained from Ref. [97] is as shown at time  $t = 0$ . The resorption of bone causes inward motion of the bone interface and elimination of tissues (top). The formation of bone causes outward motion of the bone interface and fusion of tissue regions (bottom). Note that the time  $t$  is not representative to the real processes in bone tissues due to the arbitrary value  $\rho_0 = 0.016$  mm/day chosen for the initial surface density of cells.

Fig. 6.10 (left) shows the evolutions of four square pores in a virtual bioscaffold. Here, the grey colour represents the bioscaffold, the magenta colour represents the new tissues, and the white colour represents the pore areas. The level set method has the capability to evolve all these pores simultaneously. The explicit parameterisation model, while producing similar tissue growth pattern in Fig. 6.10 (right), can only conveniently deal with a single pore. Future works on this topic can involve simulating more pores with various pore shapes to imitate a real 3D bioscaffold. The level set method has been used to study the curvature-controlled tissue growth in bioscaffolds in Guyot *et al.* [37–39]. However, the model used in these studies does not take into account the presence of cells and their activities (for example the tissue secretion rate of cells, cell diffusion and cell depletion).

### 6.4.5 Fusion and elimination of trabecular struts

The level set method is now tested on a realistic complex bone geometry. The initial interface shown in Fig. 6.11 (left) is extracted from a histological section of trabecular bone from Ref. [97]. Here we use the same values of parameters as in Sect 6.4.4.

Temporal snapshots showing bone loss due to resorption are presented in Fig. 6.11 (top) and bone gain due to formation in Fig. 6.11 (bottom). These two events, which involve elimination and fusion of interfaces, are conveniently handled by the level set method.

## 6.5 Discussion and conclusions

In this study, the level set equation has been coupled to the evolution equation of velocity (or cell surface density, since  $v = k_f \rho$  in Eq. (2.3)). This allowed us to model any complex (e.g. disjoint) two-dimensional tissue interface by solving a single governing evolution law for the interface, which is something that is difficult to do with the explicit parameterisation model that we have developed in Ref. [47] (reproduced in Chapter 3). The method could also enrich the level set techniques readily available in tumor growth and wound healing models [81–84].

The ability of the level set method to handle topological changes of interfaces makes the method powerful [98]. The extension to three dimensions, although often mentioned in the literature to be ‘direct’, needs certain modifications. This includes considerations of how cell density should be modelled on a three-dimensional tissue interface, which might differ from the two-dimensional case due to the anisotropy of curvature. However, an advantage of the level set method is its simplicity in calculating geometric variables, particularly the normal vector and curvature (see Eq. (6.11)).

Our results showed that the loss of cell number for the circular interface is small and can be omitted. However, the loss becomes perceptible in the case of the hexagonal interface, and significant for the square interface, due to its sharper corners. This suggests that the loss of cell number incurred by the current level set model originates from mishandling the dynamics occurring at corners. This is also the case in the non-conservative form of the explicit parameterisation model (see Sect. ‘Conservative form and total cell number’ of Chapter 3).

At developing corners of the interface, the level set function  $\phi$  becomes nonsmooth, its derivatives become discontinuous, and most of the associated geometric quantities

such as the normal vector to the interface and curvature become ambiguous [92]. Since the velocity function defined in Eq. (6.2) is coupled to the level set function  $\phi$  through both the normal vector and curvature, we deduce that the loss of cell number is mainly due to the inaccurate estimation of these quantities. The reason why the numerical cell number decreases even before merging occurs during the fusion of two circular interfaces (Fig. 6.9) at  $t_m \approx 17$  days is that the estimations of the normal vector and curvature in a neighbourhood of the interface are ill-defined when interfaces are close to each other [99]. The issue of inaccurate numerical estimates of the normal vector and curvature in the solution including during fusion is also mentioned in Refs. [100–106] in their respective studies.

Several methods have been suggested to improve the estimation of the normal vector and curvature, such as the ‘advected normal method’ [101] and a similar method named the ‘gradient augmented level set method (GALS)’. The latter, which has been proposed in [107], is a semi-Lagrangian method based on bicubic Hermite interpolation with high order accuracy and small stencil. These two methods couple the level set function with separate evolution equations of the normal vector and gradient, respectively. Curvature is then calculated either from the normal vector using the relationship  $\kappa = \nabla \cdot \mathbf{n}$  or from the gradient using  $\kappa = \nabla \cdot (\nabla\phi/|\nabla\phi|)$ . A method generalising the GALS method to arbitrary order has been presented in Ref. [108], known as the ‘jet schemes’. Other methods can also be found in [99, 102–106, 109]. The availability of various methods presented above looks promising for better solution estimation. Another possible source for the numerical loss of cell number is the inaccuracy of the level set function reinitialisation particularly in highly curved regions of the interface [98]. This problem is known in the level set literature as mass or area conservation problem. A number of techniques have been developed to limit this problem, called mass-preserving level set method [60, 92, 110, 111].



## Chapter 7

# Conclusions and outlook

In this thesis, we investigated growth patterns of biological tissues that evolve under geometrical controls by developing a series of mathematical models. The motivation for this study emanated from contradicting observations on the role of tissue curvature in in-vitro bioscaffold tissue growth experiments, and in-vivo bone tissue growth dynamics.

To better understand the mechanistic role of tissue curvature in the evolution of biological tissues, we developed a cell-based mathematical model that includes a systematic influence of curvature on the population of cells synthesising new tissue. New tissue produced near concave areas of the tissue interface tends to crowd, resulting in faster tissue growth in these regions. In contrast, new tissue produced near convex areas of the tissue interface tends to spread, resulting in slower tissue growth in these regions. This curvature-induced crowding and spreading of tissue material was formalised mathematically as a geometric term in mass balance equations describing the evolutions of tissue interface and tissue-synthesising cells (Chapter 3). Previous mathematical models of the influence of curvature on tissue growth were purely geometrical and phenomenological (e.g., relating tissue interface velocity directly to curvature). These phenomenological models provided limited opportunities to investigate biological and physical mechanisms responsible for the geometric control of tissue growth. The importance of our mathematical description of the inevitable geometric pull induced by crowding and spreading effects lies in being able to single out this influence from experimental data, and thereby accessing finer influences of geometry on the behaviour of cells.

**Application to in-vitro and in-vivo biological tissue growth.** This mathematical model was first applied to in-vitro experiments of new tissue growth in porous

bioscaffolds (Chapter 3). We found that cell diffusion along the interface drives important qualitative changes in tissue growth patterns and in the distribution of tissue-synthesising cells at the interface, including: (i) oscillatory motion and the development of shocks propagating sideways at low diffusion; (ii) effective smoothing of the initial substrate geometry at intermediate diffusion; and (iii) centred shocks at high diffusion. At intermediate cell diffusivity, the model captures both smoothing of the initial substrate geometry and tissue deposition slowdown. Tissue deposition slowdown was observed in the in-vitro experiments in Refs. [32, 33], but not captured by previous geometric models of curvature control. Our model thus provides a novel mechanistic interpretation of the geometric control of tissue growth observed in these experiments, which was the first part of Research Question 1.

The mathematical model was also applied to the in-vivo situation of bone remodelling (Chapter 5), in which cortical pores created by bone-resorbing cells are closed in by bone-forming cells (osteoblasts) as part of a normal bone renewal process. By singling out the systematic influence of curvature on the collective crowding and spreading of osteoblasts, we were able to determine from experimental data on bone formation dynamics how the geometry of infilling bone pores influences the individual behaviour of osteoblasts (Research Question 3). We found that the secretory rate of osteoblasts is not controlled by curvature, but rather by the average porosity of the infilling cavity, and that osteoblast depletion increases significantly during osteon closure. These insights suggest a mechanical control of cell secretory rate via osteocyte signalling. Indeed, local mechanical stresses are known to be highly dependent on local porosity in bone and bioscaffolds [38, 43, 112, 113], and to have the capability to influence cell differentiation and tissue matrix secretion [38].

These two studies enable us to reconcile the apparent discrepancy between the curvature dependence of tissue growth in in-vitro bioscaffolds experiments and in-vitro bone formation dynamics. The dynamics of tissue growth can be captured by the mathematical model in both situations, provided the cells' individual behaviours are adjusted (second part of Research Question 1).

**Hyperbolic curvature flow: shock wave development, and shock wave structure.** The numerical simulations of the mathematical model in Chapter 3 suggested the emergence of shock waves in some regimes of diffusivity that we analysed theoretic-

cally in Chapter 4 (Research Question 2). The hyperbolic curvature flow of the model could be analysed by the theory of hyperbolic conservation laws in the zero-diffusion limit. Using Riemann invariants and a well-known theorem by Lax [67], we showed rigorously that the interface of the tissue develops cusps in finite time whenever the initial tissue substrate is concave in some region of the interface. A complete description of the propagation of the shock wave structure is possible and confirms the accuracy of the numerical schemes employed in Chapter 3.

Future work related to this topic includes the theoretical investigation of these behaviours at nonzero diffusion. It is unclear numerically whether the inclusion of diffusive damping necessarily prevents the emergence of cusps in the interface. Also, numerical simulations suggest the existence of two critical diffusive dampings. One at which the interfaces converges to a flat interface the quickest, and one at which oscillatory motion of the interface is entirely damped. These two critical behaviours are known to coincide in the motion of a damped harmonic oscillator, but they seem to be distinct here (see Sect. 3.2, Fig. 3). Clearly the addition of diffusion cause the equations to fall into a different class of PDEs and different analysis techniques will be required to investigate these questions, such as methods developed in the analysis of curvature flows.

The two-dimensional tissue growth considered in the thesis may be interpreted as the growth of a three-dimensional tissue that is homogeneous in the third dimension, and that would be seen in a transverse cross section. All the shock waves that may emerge in 2D can therefore be observed in 3D too. However, shocks in 3D would allow for new shock structures as well due to the tensorial aspect of the curvature of tissue surfaces. A shock may propagate along one direction jointly with a rarefaction wave in the perpendicular direction, because curvature in one direction of the tissue surface may have the opposite sign as curvature in the other direction.

In Chap. 3, it is shown by the model that shocks also develop when cell diffusion is strong: high cell diffusivity causes uniform distributions of cells, and hence a tissue interface that evolves by uniform offsets. This situation corresponds to the case of very low *interface* diffusion of the deterministic KPZ (Kardar-Parisi-Zhang) equation in Ref. [114]. In the context of biological tissues such as bone, simulations we performed with high and low cell diffusivities are not realistic, since the interface of the growing tissue would not exhibit smoothing. Smoothing of the interface occurs most efficiently at

intermediate cell diffusivities, where lateral cell diffusion counteracts the emergence of curvature-induced cell inhomogeneities but retains higher tissue growth rates in concavities of the tissue substrate [32, 33, 114]. Whether shock wave in tissue interface motion may occur in in-vitro setups or abnormal bone formation in vivo remains an open question.

While the theory of shock formation in high dimension is available [64], our explicit parameterisation model in Chap. 3 would first need to be extended to account for higher dimension setups. This is difficult to implement, and is the reason why we resorted to developing a level set method in Chap. 6.

**Extension to complex interface geometries and to three dimensions.** In Chapter 6, we developed a parameterisation-free method of the mathematical model based on the level set method in order to simulate curvature-controlled tissue growth in complex interface geometries. The results obtained by this method compared well with those obtained using explicit parameterisations. It enabled the simulation of important biological situations that arise during bone formation and bone resorption, in which bone structure undergoes abrupt topological changes due to fusion or fenestration of trabecular struts (Research Question 3). However, some of these simulations exhibited significant nonconservation of cell number. Numerical loss of cells occurs predominantly when the interface develops cusps, including during abrupt topological changes of the tissue interface.

Several numerical techniques exist to circumvent such nonconservation problems in level set methods (Section 6.5). These shall be investigated in future works to enable more accurate simulations of the evolution of complex trabecular structures. This is an important area as loss of trabecular connectivity by trabecular fenestration is particularly common during age-related bone loss and osteoporosis. Vertebral microfractures in the spine, for example, lead to kyphosis, i.e., the spine arches and people decrease their body height. Understanding the geometric control of trabecular loss might help us understand the evolution of such disorders, and predict the site-specific efficiency of anti-resorptive drug treatments.

Bones and other biological tissues, whether natural or synthetic, are inherently anisotropic 3D materials. As the gap between mathematical modelling and biomedical or clinical applications closes, it will be of prime importance to generalise the

two-dimensional hyperbolic curvature flow proposed in this thesis to three dimensions. Bioscaffold experiments have been shown to exhibit three-dimensional effects [34, 37–39]. Our determination of the influence of geometry on the collective and individual behaviours of cells might still be affected by irregularities of pores occurring in the third dimension, which were not included in the 2D models [39, 115].

The level set method developed in Chapter 6 provides a natural mathematical framework for the extension of the mathematical model to complex 3D interfaces and structures. The evolution equations of the level set functions involve vector differential operators and are similar to the evolution equations of surfactant density developed in arbitrary dimension by Stone in Ref. [51]. A level set method has been utilised in Refs. [37–39] to simulate the growth of new tissue in 3D bioscaffolds by a mean curvature flow. However, this type of curvature flow is a geometric model only. It does not represent a population of cells, and it is much easier to implement as it involves a single level set function only. Nevertheless, these studies include a dynamic microenvironment of cell culture, by considering fluid flow and the production of fluid-flow-induced shear stress. This kind of approach would enable the investigation of complex interactions between the geometry and mechanics in three-dimensional tissue structures, that would be challenging to conduct with explicit parameterisations of the tissue interface.

**Influence of mechanics on cell behaviour** The in-vitro experiments of Refs. [32, 33] did not involve mechanical loading nor the generation of osteocytes like in bone remodelling. The absence of mechanical stimulus onto tissue-synthesising cells in vitro is likely to affect their individual behaviour compared to in-vivo bone formation. Some bioscaffold experiments of tissue growth have been conducted under mechanical loading [37–39]. The application of our mathematical model to these situations could shed more light into the coupling between geometrical and mechanical regulations of the individual behaviour of cells growing new tissue.

The influence of local mechanical clues for tissue growth rates considered in Chap. 5 focuses on the single pore scale. This treatment is limited to the scale of a single bone remodelling unit as no consideration was made on the density of pores, nor on the three dimensional pore structure. Despite its simplicity, this treatment remains accurate in cortical bone, where pore structure is mostly cylindrical (homogeneity along the longitudinal axis) and single bone remodelling units represent standalone bone forming

events.

Guyot *et al.* have modelled links between tissue growth and mechanical shear stresses in bioreactors based on experimental data [37–39]. In these works, the level set method is used to evolve the tissue interface as a mean curvature flow, with an interface velocity coupled additionally to the shear stresses induced on tissue-forming cells by the perfusion of a physiological solution in the bioreactor. The shear stresses are calculated using the Brinkman equation (modified Stokes and Darcy equations).

The mathematical model and experimental setup in Ref. [37–39] are elegant, but the mathematical model has its own limitation as it does not include a description of the cell populations. Extensions of the models presented in this thesis could combine the cell-based model of curvature-induced crowding/spreading of cells with the Brinkman equation to determine shear stresses. However, to deal with the complex three-dimensional geometries of scaffolds in bioreactors, an important requirement is to first extend the model to three dimensions.

**Cell patterning and cell migration** Most studies of biological tissue growth focus on the quantity and shape of the new tissue produced. There is very little quantitative information on changes in cell density associated with tissue growth. Some information is available in bone histomorphometric studies, and we have used this information in Chap. 5 to calibrate the mathematical model of bone pore infilling. However, this data is not accurate enough to provide detailed experimental links between curvature and cell density in irregular geometries. Such links are important to investigate to develop a better understanding of how the systematic curvature-induced crowding and spreading of cells at concavities and convexities of the tissue substrate may be counteracted by other mechanisms. Tissue engineering constructs are a promising avenue for investigating quantitative links between curvature and cell density, due to the ease with which cells can be stained and tracked in such setups.

A major mechanism by which cells may counteract curvature-induced cell crowding or spreading is by modifying their own migration properties. In this thesis, cell migration was assumed to be uniformly diffusive only. However, it is possible, and quite likely, that migration properties of cells may depend themselves on substrate curvature. In Ref. [116], vortex-like patterns of cells were seen to form at the umbilical points of ellipsoid surfaces, due to the particles moving so as to minimising the “in-

teraction energy” between them, an energy that depends on the cell distribution. The proper identification of curvature-dependent migration properties requires the extraction, from measurements of cell distribution, of the systematic influence of curvature on cell crowding or spreading.

**Controls of the arrangement of the anisotropic extracellular matrix** In bioscaffold experiments, it was observed that actin stress fibres in cells located at the proximity of tissue interface were aligned parallel to the interface [32, 33, 35, 36]. This is to be contrasted to other location far from the tissue interface, where the actin stress fibres were found to be randomly oriented. In Bidan *et al.* [35], it was shown that bulk tissue produced in the bioscaffolds did not expand or compress when maturing, and neotissue production mainly occurred close to the tissue interface. Tissue fiber anisotropies also occur in bone tissues. Woven bone is made of poorly organised tissue where collagen fibers and mineral crystals are arranged randomly. In contrast, lamellar bone is a highly organised bone, made up of by parallel layers of collagen fibers and mineral crystals [4]. In these cases, the simple effect of curvature on tissue growth modelled by our equations still holds, but these equations do not model the anisotropic generation of fibres in the tissue. They model the overall shape (and quantity) of new tissue produced and the cell population.

The generation of anisotropic and inhomogeneous tissue material properties within the evolving new tissue boundaries requires the introduction of fields  $\eta(\underline{r}, t)$  within the tissue that represent fibre orientation or fibre arrangement. These fields evolve by means of generalised bulk and surface balance equations that depend in particular on the velocity of the tissue interface [45]. The purpose of this thesis was precisely to develop cell-based mathematical models of the tissue interface velocity, so that they can be coupled to detailed models of tissue material properties. Of particular interest will be the study of the influence of interface curvature for the generation of tissue anisotropies, e.g. due to inhomogeneities in cell density [117]

**Geometric control of tissue resorption.** The present thesis focused on the geometrical control of new tissue formation. Equally important is the geometric control of tissue resorption, particularly in bone where remodelling starts with bone resorption and may lead to irreversible bone loss. Curvature induces a similar collective crowding or spreading of bone-resorbing cells, except that it works in reverse. Osteoclasts tend

to crowd when resorption occurs on convex portion of the bone surface, and they tend to spread when they resorb concave portions of the bone surface. The curvature control of the collective behaviour of osteoclasts can be modelled much in the same way, except that the normal velocity of the interface changes sign. We can define the velocity of a resorbing interface as  $v = -v_r$ , where  $v_r > 0$  is given by

$$v_r(\mathbf{r}_S, t) = k_r(\mathbf{r}_S, t) \mu(\mathbf{r}_S, t) \quad (7.1)$$

where  $k_r$  is the rate of bone resorption of a single osteoclast (volume of bone resorbed per cell per unit time) and  $\mu$  is the cell surface density of osteoclasts.

Bone balance during remodelling is critical to the structural integrity of bones. Our results in Sect. 6.4.3 have shown that achieving bone balance during remodelling is not simply a matter of reversing time, i.e., of reversing interface velocity. The propagation of shock waves seen in tissue growth patterns (Sect. 4.3) and the satisfaction of an entropy condition by these shocks mean that information propagating along characteristics is gradually lost where characteristics collide, even in the absence of diffusion. The evolution of the interface is thereby irreversible. Substituting bone-resorbing cells for bone-forming cells instantly will not rewind the evolution of the interface (see Fig. 6.8). This lack of symmetry between bone resorption and bone formation could be a very important factor to analyse for the evolution of bone disorders such as osteoporosis, as well as in the mechanical adaptation of bone tissue. The symmetry breaking of the geometric control of tissue formation and resorption may provide a very fundamental reason why it is harder to gain bone than it is to lose it [46, 118].

Bone resorption has been difficult to investigate experimentally until recent years because resorption removes records in bone. It is not possible to label regions in bone tissues that keep track of where there has been bone resorption [119], in contrast to bone formation which can be tracked using tetracycline double labeling techniques [120]. However, recent developments in imaging technologies have enabled the use of time-lapse in-vivo micro-computed tomography (micro-CT) in longitudinal animal studies. This has enabled the evolution of bone resorbing surfaces to be tracked and quantified [119, 121–125]. As these techniques become more broadly available, mathematical models that investigate the geometric control of both bone resorption and bone formation will be able to shed new light into the geometric regulations of individual cell behaviours of osteoclasts and osteoblasts. It is possible to envision that in a not-so-distant future,

this kind of studies coupled with micro-finite-element analyses [119, 126, 127] will be able to address new challenging questions on the mechanoregulation of active bone cells.

**Other geometrical factors of tissue formation.** The mathematical model developed in this thesis focused on the microscopic scale of interaction between cells and tissue, ranging from about  $10\mu\text{m}$  to  $200\mu\text{m}$ . At this scale, the most important variables characterising the morphology of bone tissue are the surface curvature, the porosity, and the availability of bone surfaces that bone-resorbing cells and bone-forming cells attach to and operate on [8] (see Fig. 1.2). We did not investigate the influence of bone surface availability in this thesis. At the tissue scale ( $\sim 1\text{mm}$ ), bone surface availability is described by the density of surfaces in a region of interest (bone surface area per unit volume) [128, 129]. It has been shown by Martin (1984) (see [128]) that the density of surfaces correlates well with porosity. This is clearly the case for perfectly circular cylindrical pores in cortical bone, in which the density of surfaces ( $\sim R$ ) is proportional to  $\sqrt{\phi}$  (since  $\phi \sim R^2$ ). However, this relationship is modified in irregular pores, and it would be interesting to investigate whether different models of individual cell behaviours depending on porosity and surface density would lead to distinguishable tissue growth patterns.

The porous space of bone remodelling cavities is also a micro-environment containing several signalling molecules such as TGF- $\beta$ , RANKL, and OPG that couple bone-resorbing and bone-forming cells, leading to the establishment of cellular structures propagating as travelling waves within cortical bone whilst renewing it [2, 4, 48, 130]. It remains unclear how the communication between osteoclasts and osteoblasts mediated by the diffusion of these signalling molecules is affected by the confined and evolving pore space.

**Application to other tissues.** Finally, the model developed in this study could also be applied to similar problems in which geometry plays a regulatory role, such as tumor growth, wound healing and other problems of moving interfaces where velocity is proportional to the density of a population of particles residing near the interface. Geometry is known to be able to affect cancer cells. For example, the curvature of a tumour's periphery has been shown to regulate the spatial arrangement of cells due to interfacial energy created by cortical tension and intercellular adhesion [131]. Deposition and removal (etching) of particles to and from a surface may also suit this model

since these processes alter the surface profile as particles are deposited or removed [58]. In such other applications, the relationship between the normal velocity of the interface and the density of particles may no longer be linear. This could in turn lead to different classes of growth patterns.

# Appendix

## A.1 The rarefaction conditions

In Sect. 4.2.2, we showed that Riemann invariants can easily be found from the integral curves. The range of physically correct solutions of  $\mathbf{u}_m$  on the 1-integral curve is given by a rarefaction condition: across the 1-rarefaction wave, characteristics must increase i.e.  $\lambda_1(\sigma_l, \eta_l) < \lambda_1(\sigma_m, \eta_m)$  in order for the characteristics to spread and hence to not collide with each other (see Fig. 4.2 (left)). Using  $\lambda_1$  from Eq. (4.12), the 1-rarefaction condition  $\lambda_1(\sigma_l, \eta_l) < \lambda_1(\sigma_m, \eta_m)$  becomes

$$\frac{(1 + \sigma_l)e^{\arctan(\sigma_l)}}{\sqrt{1 + \sigma_l^2}} > \frac{(1 + \sigma_m)e^{\arctan(\sigma_m)}}{\sqrt{1 + \sigma_m^2}}. \quad (\text{A.1})$$

This inequality cannot easily be solved analytically for  $\sigma_m$ . However the function  $f(\sigma) = \frac{(1+\sigma)e^{\arctan(\sigma)}}{\sqrt{1+\sigma^2}}$  is monotone increasing. The derivative  $f'(\sigma) = \frac{2e^{\arctan(\sigma)}}{(1 + \sigma^2)^{3/2}}$  is positive for any  $\sigma$ . Therefore, the above inequality in Eq. (A.1) is satisfied when

$$\sigma_l > \sigma_m \quad (\text{A.2})$$

for any  $\sigma_l, \sigma_m \in \mathbb{R}$ .

Similarly, the range of physically correct state of  $\mathbf{u}_m$  on the 2-integral curve is given by the rarefaction condition: across the 2-rarefaction wave, characteristic must increase i.e.  $\lambda_2(\sigma_m, \eta_m) < \lambda_2(\sigma_r, \eta_r)$  (see Fig. 4.2 (right)). Using  $\lambda_2$  from Eq. (4.12), this condition implies that

$$\frac{(\sigma_m - 1)e^{-\arctan(\sigma_m)}}{\sqrt{1 + \sigma_m^2}} > \frac{(\sigma_r - 1)e^{-\arctan(\sigma_r)}}{\sqrt{1 + \sigma_r^2}}. \quad (\text{A.3})$$

The function  $f(\sigma) = \frac{(\sigma-1)e^{-\arctan(\sigma)}}{\sqrt{1+\sigma^2}}$  is monotone increasing. Its derivative with respect to  $\sigma$ ,  $f'(\sigma) = \frac{2e^{-\arctan(\sigma)}}{(1+\sigma^2)^{3/2}} \left[ \left(\sigma - \frac{1}{2}\right)^2 + \frac{3}{4} \right]$  is positive. The above inequality is satisfied when

$$\sigma_m > \sigma_r \quad (\text{A.4})$$

for any  $\sigma_r, \sigma_m \in \mathbb{R}$ .

## A.2 The rarefaction waves

In order to determine the rarefaction wave  $\bar{\mathbf{u}}(\xi) = (\bar{\sigma}(\xi), \bar{\eta}(\xi))$  that varies for example for  $\xi_a \leq \xi \leq \xi_b$ , we solve the system of ODEs [64]:

$$\bar{\mathbf{u}}'(\xi) = \frac{\mathbf{r}(\bar{\mathbf{u}}(\xi))}{\nabla \lambda(\bar{\mathbf{u}}(\xi)) \cdot \mathbf{r}(\bar{\mathbf{u}}(\xi))}. \quad (\text{A.5})$$

Here  $\xi = x/t$ . To find the boundaries, we set

$$\xi_a = \lambda_i(\mathbf{u}_l) \quad , \quad \xi_b = \lambda_i(\mathbf{u}_r). \quad (\text{A.6})$$

where  $\mathbf{u}_l$  and  $\mathbf{u}_r$  are any of the left and right states of a Riemann problem.

### A.2.1 Determining the 1-rarefaction wave

From Eq. (4.34), the solution with 1-rarefaction wave can be written as (see also Fig. 4.2 (left)):

$$\mathbf{u}(x, t) = \begin{cases} \mathbf{u}_l & \text{if } \xi \leq \xi_1 \\ \bar{\mathbf{u}}_1(\xi) & \text{if } \xi_1 \leq \xi \leq \xi_2 \\ \mathbf{u}_m & \text{if } \xi \geq \xi_2 \end{cases} \quad (\text{A.7})$$

where  $\xi = x/t$ . To find the left  $\xi_1$  and right  $\xi_2$  boundaries of the 1-rarefaction wave of our system, the first eigenvalue  $\lambda_1$  from Eq. (4.12) is used in Eq. (A.6). This produces the following rarefaction boundaries:

$$\xi_1 = \lambda_1(\mathbf{u}_l) = -\frac{k_f \eta_l}{1 + \sigma_l^2}(\sigma_l + 1) \quad , \quad \xi_2 = \lambda_1(\mathbf{u}_m) = -\frac{k_f \eta_m}{1 + \sigma_m^2}(\sigma_m + 1). \quad (\text{A.8})$$

To determine  $\bar{\mathbf{u}}_1(\xi)$  in Eq. (A.7), we substitute the eigenvalue  $\lambda_1$  from Eq. (4.12) into the system of ODEs in Eq. (A.5) producing:

$$\bar{\mathbf{u}}_1'(\xi) = -\frac{(1 + \bar{\sigma}^2)^2}{2k_f \bar{\eta}} \left[ \begin{array}{c} 1 \\ \bar{\eta}(\bar{\sigma} + 1) \\ 1 + \bar{\sigma}^2 \end{array} \right] \quad (\text{A.9})$$

where the right eigenvector  $\mathbf{r}_1$  is given by Eq. (4.13) and  $\nabla\lambda_1 \cdot \mathbf{r}_1$  by Eq. (4.14). Component-wise, the resulting ODEs are

$$\frac{d\bar{\sigma}}{d\xi} = -\frac{(1+\bar{\sigma}^2)^2}{2k_f\bar{\eta}}, \quad \frac{d\bar{\eta}}{d\xi} = -\frac{(1+\bar{\sigma})(1+\bar{\sigma}^2)}{2k_f}. \quad (\text{A.10})$$

This is a system of autonomous ODEs. The easiest way to solve this system of ODEs is by decoupling one of the equations followed by solving the resulting decoupled equation. Here, we utilise the 1-integral curve from Eq. (4.20) to achieve this purpose. This is because only the pairs of  $\bar{\sigma}$  and  $\bar{\eta}$  that reside on the integral curve are accepted as the solutions  $\bar{\mathbf{u}}_1 = (\bar{\sigma} \ \bar{\eta})$ . Thus, substituting  $\bar{\eta}$  from the 1-integral curve of Eq. (4.20) into the first equation in Eqs. (A.10) gives

$$\frac{e^{\arctan(\bar{\sigma})}}{(1+\bar{\sigma}^2)^{3/2}} \frac{d\bar{\sigma}}{d\xi} = -\frac{e^{\arctan(\sigma_l)}\sqrt{1+\sigma_l^2}}{2k_f\eta_l}. \quad (\text{A.11})$$

Integrating Eq. (A.11) with respect to  $\xi$  using integration by parts on the LHS, and direct integration on the RHS, and using the first rarefaction boundary condition  $\xi_1$  of Eq. (A.8), we obtain the solution  $\bar{\sigma}$  of the 1-rarefaction wave in implicit form as:

$$\frac{e^{\arctan(\bar{\sigma})}(1+\bar{\sigma})}{\sqrt{1+\bar{\sigma}^2}} = -\frac{\xi}{k_f}w_1(\sigma_l, \eta_l) = -\frac{\xi}{k_f}w_1(\sigma_m, \eta_m) \quad (\text{A.12})$$

where again  $\xi = x/t$  and the 1-Riemann invariant  $w_1$  is given by Eq. (4.23). Note that the Riemann invariant  $w_1(\sigma_l, \eta_l)$  is equal to  $w_1(\sigma_m, \eta_m)$  on the integral curve. Eq. (A.12) can be solved by an iterative method for nonlinear equations, such as Newton's method [64]. The corresponding 1-rarefaction wave solution for  $\bar{\eta}$  in (A.12) is

$$\bar{\eta} = \frac{e^{\arctan(\bar{\sigma})}\sqrt{1+\bar{\sigma}^2}}{w_1(\sigma_l, \eta_l)} = \frac{e^{\arctan(\bar{\sigma})}\sqrt{1+\bar{\sigma}^2}}{w_1(\sigma_m, \eta_m)} \quad (\text{A.13})$$

since  $(\bar{\sigma}, \bar{\eta})$  resides on the integral curve (4.20). Finally, the set  $(\bar{\sigma}, \bar{\eta})$  obtained from Eqs. (A.12) and (A.13) is the solution  $\bar{\mathbf{u}}_1$  for the 1-rarefaction wave in Eq. (4.34).

### A.2.2 Determining the 2-rarefaction wave

Similarly to the case of 1-rarefaction wave, the solution with 2-rarefaction wave can be written as (see Fig. 4.2 (right)):

$$\mathbf{u}(x, t) = \begin{cases} \mathbf{u}_m & \text{if } \xi \leq \xi_3 \\ \bar{\mathbf{u}}_2(\xi) & \text{if } \xi_3 \leq \xi \leq \xi_4 \\ \mathbf{u}_r & \text{if } \xi \geq \xi_4 \end{cases} \quad (\text{A.14})$$

where  $\xi = x/t$ . To find the left  $\xi_3$  and right  $\xi_4$  boundaries of the 2-rarefaction wave, the second eigenvalue  $\lambda_2$  from Eq. (4.12) need to be used in Eq. (A.6). This produces the following rarefaction boundaries:

$$\xi_3 = \lambda_2(\mathbf{u}_m) = -\frac{k_f \eta_m}{1 + \sigma_m^2}(\sigma_m - 1) \quad , \quad \xi_4 = \lambda_2(\mathbf{u}_r) = -\frac{k_f \eta_r}{1 + \sigma_r^2}(\sigma_r - 1). \quad (\text{A.15})$$

To determine  $\bar{\mathbf{u}}_2(\xi)$  in Eq. (A.14), we solve the system of ODEs in Eq. (A.5) which are given component-wise as (note that  $\mathbf{r}_2$  is given by Eq. (4.13) and  $\nabla \lambda_2 \cdot \mathbf{r}_2$  is given by Eq. (4.14)):

$$\frac{d\bar{\sigma}}{d\xi} = -\frac{(1 + \bar{\sigma}^2)^2}{2k_f \bar{\eta}} \quad , \quad \frac{d\bar{\eta}}{d\xi} = -\frac{(\bar{\sigma} - 1)(1 + \bar{\sigma}^2)}{2k_f}. \quad (\text{A.16})$$

As in the case of 1-rarefaction wave, this is also a system of autonomous ODEs. To solve this system, we follow the method used in the previous section, i.e. by decoupling one the equations in Eq. (A.16). Using the 2-integral curve from Eq. (4.20), the first equation in Eqs. (A.16) decouples as:

$$\frac{e^{-\arctan(\bar{\sigma})} d\bar{\sigma}}{(1 + \bar{\sigma}^2)^{3/2} d\xi} = -\frac{e^{-\arctan(\sigma_r)} \sqrt{1 + \sigma_r^2}}{2k_f \eta_r}. \quad (\text{A.17})$$

Integrating Eq. (A.17) with respect to  $\xi$  using integration by parts on the LHS, and direct integration on the RHS, and using the second rarefaction boundary condition  $\xi_4$  of Eq. (A.15), we obtain the solution  $\bar{\sigma}$  of the 2-rarefaction wave in implicit form as:

$$\frac{e^{-\arctan(\bar{\sigma})}(\bar{\sigma} - 1)}{\sqrt{1 + \bar{\sigma}^2}} = -\frac{\xi}{k_f} w_2(\sigma_r, \eta_r) = -\frac{\xi}{k_f} w_2(\sigma_m, \eta_m) \quad (\text{A.18})$$

where  $\xi = x/t$  and the 2-Riemann invariant can be found in Eq. (4.23). The corresponding rarefaction wave solution for  $\bar{\eta}$  in (A.18) obtained from the 2-integral curve is:

$$\bar{\eta} = \frac{e^{-\arctan(\bar{\sigma})} \sqrt{1 + \bar{\sigma}^2}}{w_2(\sigma_r, \eta_r)} = \frac{e^{-\arctan(\bar{\sigma})} \sqrt{1 + \bar{\sigma}^2}}{w_2(\sigma_m, \eta_m)} \quad (\text{A.19})$$

since  $(\bar{\sigma}, \bar{\eta})$  resides on the 2-integral curve in Eq. (4.20). The resulting set of  $(\bar{\sigma}, \bar{\eta})$  obtained from Eqs. (A.18) and (A.19) is the solution  $\bar{\mathbf{u}}_2$  for the 2-rarefaction wave in Eq. (4.35).

### A.3 The Hugoniot loci and the shock speeds

This section presents the method to determine the Hugoniot loci and the shock speeds of our model. We first consider the original nonlinearised problem, before linearising the equations to determine which loci and shock speed that correspond to each eigenvector.

#### A.3.1 Nonlinearised problem

Following LeVeque [64], we consider all states  $\mathbf{u} = (\sigma, \eta)$  that can be connected to a fixed state  $\mathbf{u}_* = (\sigma_*, \eta_*)$  by a shock. The state  $\mathbf{u}_*$  can represent the left state  $\mathbf{u}_l = (\sigma_l, \eta_l)$  or the right state  $\mathbf{u}_r = (\sigma_r, \eta_r)$ . Across a shock, the Rankine-Hugoniot condition holds, and it can be written as  $s[\mathbf{u}] = [\mathbf{f}(\mathbf{u})]$  for a system of conservation laws. Here  $[\mathbf{u}]$  and  $[\mathbf{f}(\mathbf{u})]$  represent the jumps in  $\mathbf{u}$  and  $\mathbf{f}(\mathbf{u})$ , respectively, across the shock. For example, in a single conservation law problem, the jumps become  $[u] = u_r - u_l$  and  $[f(u)] = f(u_r) - f(u_l)$ .

In our problem of two conservation laws, the Rankine-Hugoniot condition can be written as:

$$s(\sigma_* - \sigma) = -k_f(\eta_* - \eta) \quad (\text{A.20})$$

$$s(\eta_* - \eta) = -k_f \left( \frac{\sigma_* \eta_*^2}{1 + \sigma_*^2} - \frac{\sigma \eta^2}{1 + \sigma^2} \right). \quad (\text{A.21})$$

Here we use  $\mathbf{u}$  and  $\mathbf{f}(\mathbf{u})$  from Eqs. (4.5) and (4.6). We wish to find all states  $\mathbf{u} = (\sigma, \eta)$  and the corresponding speeds  $s$  (either  $s_1$  or  $s_2$ ) satisfying Eqs. (A.20) and (A.21). In the above system, there are two equations with three unknowns, so we expect to find a one-parameter family of solutions, where the parameter is chosen to be  $\sigma$ .

Manipulating Eq. (A.20) we have

$$s = -k_f \frac{\eta_* - \eta}{\sigma_* - \sigma}. \quad (\text{A.22})$$

Substituting  $s$  from Eq. (A.22) into Eq. (A.21), we obtain a quadratic equation in  $\eta$  which can be solved to give two Hugoniot loci for  $\eta$  which are:

$$\eta = \frac{\eta_*}{1 + \sigma\sigma_*} \left[ (1 + \sigma^2) \pm (\sigma_* - \sigma) \sqrt{\frac{1 + \sigma^2}{1 + \sigma_*^2}} \right] \quad (\text{A.23})$$

(note the ‘+’ and ‘-’ signs). All the points  $\mathbf{u} = (\sigma, \eta)$  which satisfy the loci in Eqs. (A.23) are the possible states that can be connected to the fixed state  $\mathbf{u}_*$  by a shock wave. The shock wave is a 1-shock wave if  $\mathbf{u}_* = \mathbf{u}_l$ , and a 2-shock wave if  $\mathbf{u}_* = \mathbf{u}_r$ .

Replacing  $\eta$  in Eq. (A.23) back into Eq. (A.22) we obtain the shock speeds

$$s = \frac{k_f \eta_*}{1 + \sigma\sigma_*} \left[ -\sigma \pm \sqrt{\frac{1 + \sigma^2}{1 + \sigma_*^2}} \right]. \quad (\text{A.24})$$

We do not know, however, which of the ‘+’ and ‘-’ signs in Eq. (A.23) and Eq. (A.24) correspond to the 1-shock wave and 2-shock wave. To resolve this issue, we need to consider the linearised problem.

### A.3.2 Linearised problem

To linearise the problem about  $\mathbf{u}_*$ , we take  $\sigma = \sigma_* + \mu$ , where  $\mu \ll 1$ . This implies that  $\sigma = \sigma_*$  when  $\mu = 0$ . Expanding in Taylor series to the first order, we obtain

$$\begin{aligned} \eta &= \eta_* \left[ 1 + \frac{\sigma_* \mu}{1 + \sigma_*^2} + \mathcal{O}(\mu^2) \mp \left( \frac{\mu}{1 + \sigma_*^2} + \mathcal{O}(\mu^2) \right) \sqrt{1 + \mathcal{O}(\mu)} \right] \\ &= \eta_* \left[ 1 + \frac{\mu}{1 + \sigma_*^2} (\sigma_* \mp 1) \right] + \mathcal{O}(\mu). \end{aligned} \quad (\text{A.25})$$

Therefore, the linearised version of Hugoniot loci is:

$$\mathbf{u} = \begin{bmatrix} \sigma \\ \eta \end{bmatrix} = \begin{bmatrix} \sigma_* \\ \eta_* \end{bmatrix} + \mu \begin{bmatrix} 1 \\ \frac{\eta_*(\sigma_* \mp 1)}{1 + \sigma_*^2} \end{bmatrix}. \quad (\text{A.26})$$

Comparing with the eigenvectors in Eqs. (4.13), these linearised loci in Eq. (A.26) are tangential to the vectors  $\mathbf{r}_2$  (when taking the ‘+’ sign in (A.23)) and  $\mathbf{r}_1$  (when taking the ‘-’ sign in (A.23)). From this it is clear that choosing the ‘+’ sign in (A.23) gives the locus of 2-shock, while the ‘-’ sign gives the locus of 1-shock.

Rewriting from Eqs. (A.23), the Hugoniot locus are

$$\eta_1 = \frac{\eta_l}{1 + \sigma\sigma_l} \left[ (1 + \sigma^2) - (\sigma_l - \sigma) \sqrt{\frac{1 + \sigma^2}{1 + \sigma_l^2}} \right] \quad (\text{A.27})$$

$$\eta_2 = \frac{\eta_r}{1 + \sigma\sigma_r} \left[ (1 + \sigma^2) + (\sigma_r - \sigma) \sqrt{\frac{1 + \sigma^2}{1 + \sigma_r^2}} \right] \quad (\text{A.28})$$

in which the subscripts 1 and 2 correspond to the 1- and 2-shocks.

## A.4 The entropy conditions

To effectively solve hyperbolic equations that develop shocks, an additional condition is needed to ensure the solution is unique and physically correct.

A common numerical method is the vanishing-viscosity method. This method is implemented by adding a small amount of viscosity or diffusion into the system of conservation laws. It has been shown that when the viscosity parameter  $\epsilon \rightarrow 0$ , a limiting solution is obtained, which captures the same discontinuity as the shock wave [58, 64].

This method can be hard to analyse within the theory of conservation laws. An alternative is to apply an entropy condition to select the physically correct weak solution. The use of the entropy condition discards the portions of possible states  $\mathbf{u}_m$  on the Hugoniot loci that are not physically correct. The entropy condition states that a shock requires characteristics to run into the shock as time advances [64, 67]. This is shown for example in Fig. 4.3. A discontinuity with characteristics emanating from it would be unstable to perturbations and lead to unphysical evolutions, such as a rarefaction shock [69]. To have the solution characteristics running into the 1-shock, the characteristic must decrease i.e.  $\lambda_1(\sigma_l, \eta_l) > s_1 > \lambda_1(\sigma_m, \eta_m)$ . Across the 2-shock, the characteristic must also decrease i.e.  $\lambda_2(\sigma_m, \eta_m) > s_2 > \lambda_2(\sigma_r, \eta_r)$ . The next two sections present the calculations made when adapting these entropy conditions into our system.

### A.4.1 The entropy condition of 1-shock

In this section, we find the entropy condition of 1-shock that connects the left state  $\mathbf{u}_l$  with the middle state  $\mathbf{u}_m$ , where the value of the vector state  $\mathbf{u}_l$  is given by the Riemann problem in Eq. (4.33). As shown in Fig. 4.3 (left), a shock should possess characteristics going into it. This implies that across 1-shock, characteristics must

decrease, i.e.,  $\lambda_1(\mathbf{u}_l) > s_1 > \lambda_1(\mathbf{u}_m)$ . From Eq. (4.12), the eigenvalues at the constant states are

$$\lambda_1(\mathbf{u}_l) = -\frac{k_f \eta_l}{1 + \sigma_l^2} (\sigma_l + 1) \quad , \quad \lambda_1(\mathbf{u}_m) = -\frac{k_f \eta_m}{1 + \sigma_m^2} (\sigma_m + 1). \quad (\text{A.29})$$

Since the 1-shock connects  $\mathbf{u}_l$  to  $\mathbf{u}_m$ , and (of course),  $\mathbf{u}_m$  to  $\mathbf{u}_l$ , then the speed of 1-shock from Eq. (A.24) can be written as:

$$s_1 = \frac{k_f \eta_l}{1 + \sigma_m \sigma_l} \left[ -\sigma_m - \sqrt{\frac{1 + \sigma_m^2}{1 + \sigma_l^2}} \right] \quad , \quad s_1 = \frac{k_f \eta_m}{1 + \sigma_l \sigma_m} \left[ -\sigma_l - \sqrt{\frac{1 + \sigma_l^2}{1 + \sigma_m^2}} \right] \quad (\text{A.30})$$

(note that we are using the negative part, as discussed in Sect. A.3.2). Then the condition  $\lambda_1(\mathbf{u}_l) > s_1 > \lambda_1(\mathbf{u}_m)$  becomes

$$\begin{aligned} -\frac{k_f \eta_l}{1 + \sigma_l^2} (\sigma_l + 1) &> \frac{k_f \eta_l}{1 + \sigma_m \sigma_l} \left[ -\sigma_m - \sqrt{\frac{1 + \sigma_m^2}{1 + \sigma_l^2}} \right] \\ &= \frac{k_f \eta_m}{1 + \sigma_l \sigma_m} \left[ -\sigma_l - \sqrt{\frac{1 + \sigma_l^2}{1 + \sigma_m^2}} \right] > -\frac{k_f \eta_m}{1 + \sigma_m^2} (\sigma_m + 1) \end{aligned} \quad (\text{A.31})$$

Here we need to find the range of  $\sigma_m$  that satisfies the first and second inequalities in (A.31).

#### A.4.1.1 First inequality

The first inequality in (A.31) above gives

$$-1 + \frac{\sigma_m - \sigma_l}{1 + \sigma_m \sigma_l} + \frac{1 + \sigma_l^2}{1 + \sigma_m \sigma_l} \sqrt{\frac{1 + \sigma_m^2}{1 + \sigma_l^2}} > 0 \quad (\text{A.32})$$

Manipulation of the inequality in (A.32) shows that it is satisfied when

$$\begin{aligned} \sigma_m > \sigma_l &\quad \text{if } \sigma_l \geq 0 \\ \sigma_l < \sigma_m < -1/\sigma_l &\quad \text{if } \sigma_l < 0 \end{aligned} \quad (\text{A.33})$$

If we take the expression on the LHS of (A.32) as the function  $f(\sigma_m) = f(\sigma_m|\sigma_l) = -1 + \frac{\sigma_m - \sigma_l}{1 + \sigma_m \sigma_l} + \frac{1 + \sigma_l^2}{1 + \sigma_m \sigma_l} \sqrt{\frac{1 + \sigma_m^2}{1 + \sigma_l^2}}$ , then the entropy condition in (A.33) can also be seen in the  $f(\sigma_m)$  plots in Fig. A.1 for various  $\sigma_l$ .

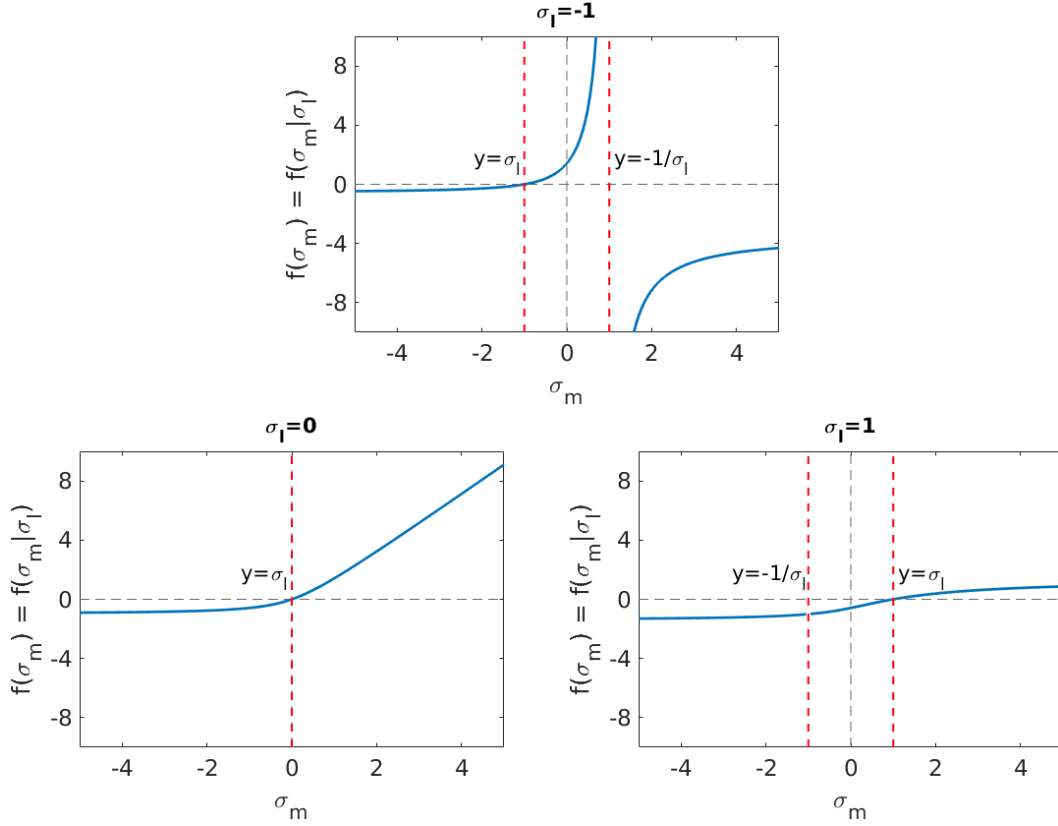


FIGURE A.1:  $f(\sigma_m)$  plots where  $f(\sigma_m)$  is given in Sect. A.4.1.1 for arbitrarily chosen  $\sigma_l = -1, 0, 1$

#### A.4.1.2 Second inequality

Similarly, the second inequality in (A.31) gives

$$-1 + \frac{\sigma_l - \sigma_m}{1 + \sigma_l \sigma_m} + \frac{1 + \sigma_m^2}{1 + \sigma_l \sigma_m} \sqrt{\frac{1 + \sigma_l^2}{1 + \sigma_m^2}} < 0 \quad (\text{A.34})$$

The inequality in (A.34) is satisfied when

$$\begin{aligned} \sigma_m > \sigma_l & \quad \text{if } \sigma_l \leq 0 \text{ and } \sigma_m \neq -1/\sigma_l \\ \sigma_m < -1/\sigma_l \text{ and } \sigma_m > \sigma_l & \quad \text{if } \sigma_l > 0 \end{aligned} \quad (\text{A.35})$$

This is also shown in the  $f(\sigma_m)$  plots in Fig. A.2 where  $f(\sigma_m) = -1 + \frac{\sigma_l - \sigma_m}{1 + \sigma_l \sigma_m} + \frac{1 + \sigma_m^2}{1 + \sigma_l \sigma_m} \sqrt{\frac{1 + \sigma_l^2}{1 + \sigma_m^2}}$ .

#### A.4.1.3 Combining first and second inequalities

The conditions in (A.33) and (A.35) can be combined to give the entropy condition of 1-shock which is:

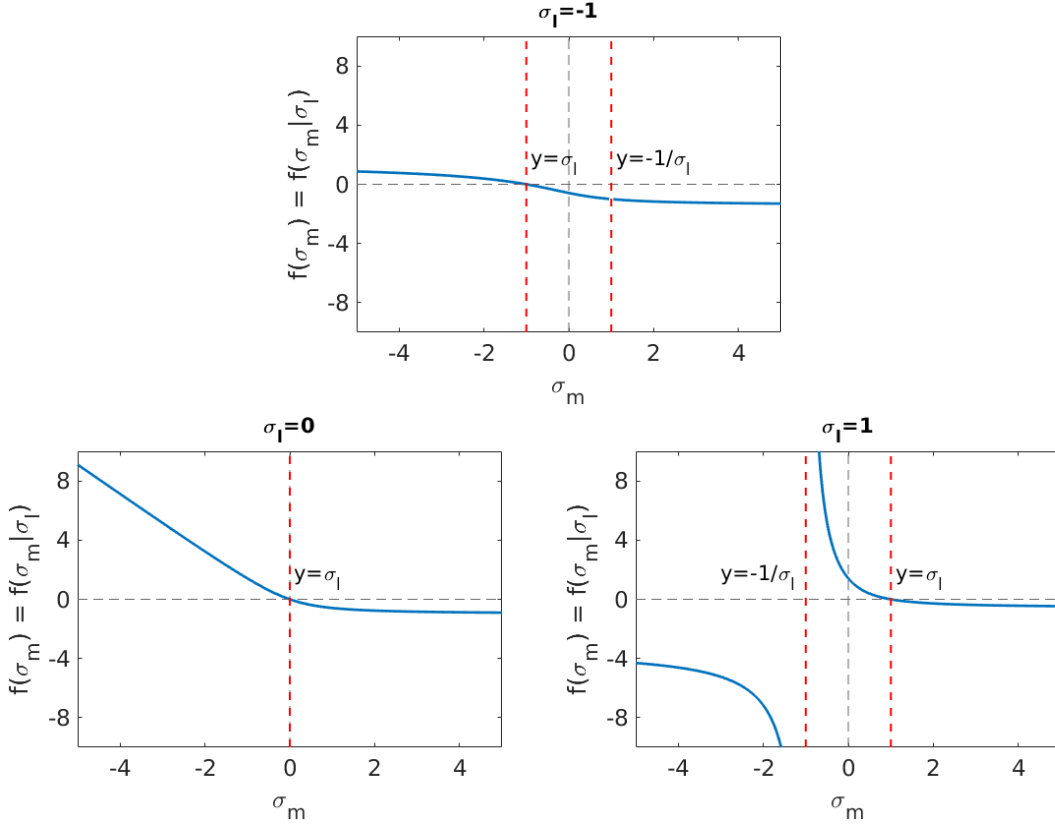


FIGURE A.2:  $f(\sigma_m)$  plots where  $f(\sigma_m)$  is given in Sect. A.4.1.2 for arbitrarily chosen  $\sigma_l = -1, 0, 1$

$$\begin{aligned}
 \sigma_m &> \sigma_l && \text{if } \sigma_l = 0 \\
 \sigma_l < \sigma_m < -1/\sigma_l && \text{if } \sigma_l < 0 \\
 \sigma_m > \sigma_l && \text{if } \sigma_l > 0
 \end{aligned} \tag{A.36}$$

or simply

$$\begin{aligned}
 \sigma_l < \sigma_m < -1/\sigma_l && \text{if } \sigma_l < 0 \\
 \sigma_m > \sigma_l && \text{if } \sigma_l \geq 0
 \end{aligned} \tag{A.37}$$

#### A.4.2 The entropy condition of 2-shock

In this section, we find the entropy condition of 2-shock that connects the middle state  $\mathbf{u}_m$  with the right state  $\mathbf{u}_r$ , where the value of the vector state  $\mathbf{u}_r$  is given by the Riemann problem in Eq. (4.33). As shown in Fig. 4.3 (right), characteristics must be going into the shock, and hence we have  $\lambda_2(\sigma_m, \eta_m) > s_2 > \lambda_2(\sigma_r, \eta_r)$ . From Eq. (4.12), the eigenvalues at the constant states are

$$\lambda_2(\sigma_m, \eta_m) = -\frac{k_f \eta_m}{1 + \sigma_m^2} (\sigma_m - 1) \quad , \quad \lambda_2(\sigma_r, \eta_r) = -\frac{k_f \eta_r}{1 + \sigma_r^2} (\sigma_r - 1). \quad (\text{A.38})$$

Since the 2-shock connects  $\mathbf{u}_m$  to  $\mathbf{u}_r$ , and of course,  $\mathbf{u}_r$  to  $\mathbf{u}_m$ , then the speed of 2-shock from Eq. (A.24) can be written as:

$$s_2 = \frac{k_f \eta_m}{1 + \sigma_r \sigma_m} \left[ -\sigma_r + \sqrt{\frac{1 + \sigma_r^2}{1 + \sigma_m^2}} \right] \quad , \quad s_2 = \frac{k_f \eta_r}{1 + \sigma_m \sigma_r} \left[ -\sigma_m + \sqrt{\frac{1 + \sigma_m^2}{1 + \sigma_r^2}} \right] \quad (\text{A.39})$$

(note that we are using the positive part, as discussed in Sect. A.3.2). Then the entropy condition becomes

$$\begin{aligned} -\frac{k_f \eta_m}{1 + \sigma_m^2} (\sigma_m - 1) &> \frac{k_f \eta_m}{1 + \sigma_r \sigma_m} \left[ -\sigma_r + \sqrt{\frac{1 + \sigma_r^2}{1 + \sigma_m^2}} \right] \\ &= \frac{k_f \eta_r}{1 + \sigma_m \sigma_r} \left[ -\sigma_m + \sqrt{\frac{1 + \sigma_m^2}{1 + \sigma_r^2}} \right] > -\frac{k_f \eta_r}{1 + \sigma_r^2} (\sigma_r - 1) \end{aligned} \quad (\text{A.40})$$

Here we need to find the range of  $\sigma_m$  that satisfies the first and second inequalities in (A.40).

#### A.4.2.1 First inequality

The first inequality in (A.40) gives

$$-1 + \frac{\sigma_m - \sigma_r}{1 + \sigma_m \sigma_r} + \frac{1 + \sigma_m^2}{1 + \sigma_m \sigma_r} \sqrt{\frac{1 + \sigma_r^2}{1 + \sigma_m^2}} < 0 \quad (\text{A.41})$$

This first inequality of 2-shock is similar to the first inequality of 1-shock in (A.32) except for the direction of the inequality, and  $\sigma_l$  now is being replaced by  $\sigma_r$ . This is also shown in the  $f(\sigma_m)$ -plots of Fig. A.3 for various  $\sigma_l$ , where  $f(\sigma_m) = f(\sigma_m|\sigma_r) = -1 + \frac{\sigma_m - \sigma_r}{1 + \sigma_m \sigma_r} + \frac{1 + \sigma_m^2}{1 + \sigma_m \sigma_r} \sqrt{\frac{1 + \sigma_r^2}{1 + \sigma_m^2}}$ . Therefore, by using the results of the first inequality of 1-shock in (A.33), the inequality in (A.41) is satisfied when

$$\begin{array}{ll} \sigma_m < \sigma_r & \text{if } \sigma_r \geq 0 \text{ and } \sigma_m \neq -1/\sigma_r \\ \sigma_m < \sigma_r \text{ and } \sigma_m > -1/\sigma_r & \text{if } \sigma_r < 0 \end{array} \quad (\text{A.42})$$

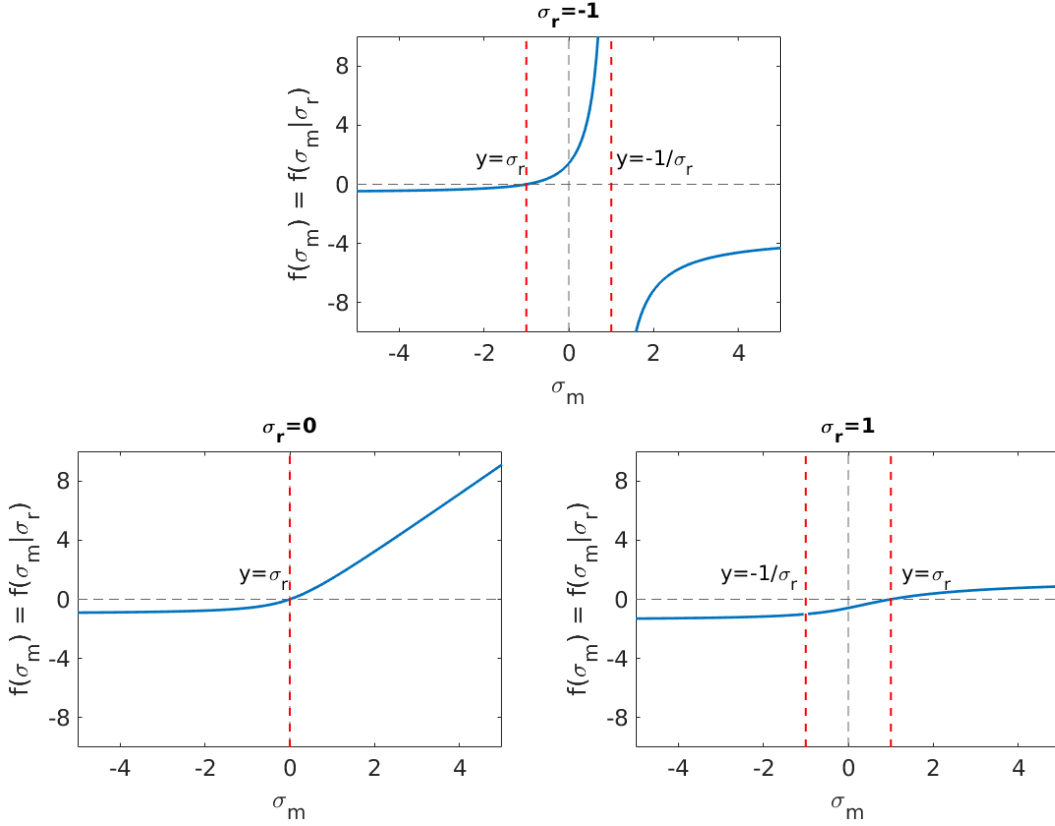


FIGURE A.3:  $f(\sigma_m)$  plots where  $f(\sigma_m)$  is given in Sect. A.4.2.1 for arbitrarily chosen  $\sigma_r = -1, 0, 1$

#### A.4.2.2 Second inequality

The second inequality in (A.40) gives

$$-1 + \frac{\sigma_r - \sigma_m}{1 + \sigma_m \sigma_r} + \frac{1 + \sigma_r^2}{1 + \sigma_m \sigma_r} \sqrt{\frac{1 + \sigma_m^2}{1 + \sigma_r^2}} > 0 \quad (\text{A.43})$$

This second inequality of 2-shock is similar to the second inequality of 1-shock in (A.34) except for the direction of the inequality, and  $\sigma_l$  now is being replaced by  $\sigma_r$ . This is also shown in the  $f(\sigma_m)$ -plots of Fig. A.4 for various  $\sigma_r$ , where  $f(\sigma_m) = f(\sigma_m | \sigma_r) = -1 + \frac{\sigma_r - \sigma_m}{1 + \sigma_m \sigma_r} + \frac{1 + \sigma_r^2}{1 + \sigma_m \sigma_r} \sqrt{\frac{1 + \sigma_m^2}{1 + \sigma_r^2}}$ . Therefore, by using the results of the second inequality of 1-shock in (A.35), the entropy condition for the second inequality of 2-shock is satisfied when

$$\begin{aligned} \sigma_m < \sigma_r & \quad \text{if } \sigma_r \leq 0 \\ -1/\sigma_r < \sigma_m < \sigma_r & \quad \text{if } \sigma_r > 0 \end{aligned} \quad (\text{A.44})$$

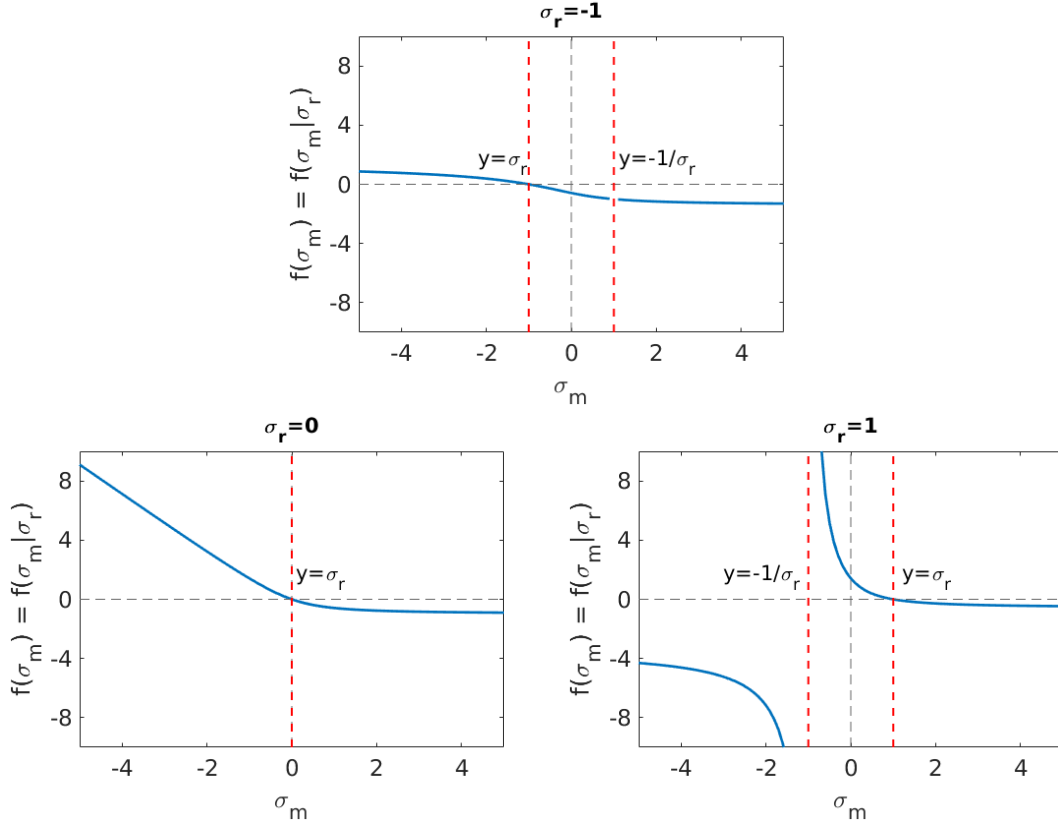


FIGURE A.4:  $f(\sigma_m)$  plots where  $f(\sigma_m)$  is given in Sect. A.4.2.2 for arbitrarily chosen  $\sigma_r = -1, 0, 1$

### A.4.2.3 Combining first and second inequalities

The conditions in (A.42) and (A.44) can be combined to give the range of  $\sigma_m$  where entropy condition of 2-shock is satisfied, which is:

$$\begin{aligned}
 \sigma_m < \sigma_r & \quad \text{if } \sigma_r = 0 \\
 \sigma_m < \sigma_r & \quad \text{if } \sigma_r < 0 \\
 -1/\sigma_r < \sigma_m < \sigma_r & \quad \text{if } \sigma_r > 0
 \end{aligned} \tag{A.45}$$

or simply

$$\begin{aligned}
 \sigma_m < \sigma_r & \quad \text{if } \sigma_r \leq 0 \\
 -1/\sigma_r < \sigma_m < \sigma_r & \quad \text{if } \sigma_r > 0
 \end{aligned} \tag{A.46}$$



# Bibliography

- [1] S. C. Cowin, ed., *Bone Mechanics Handbook*. CRC Press, 2nd ed., 2001.
- [2] A. M. Parfitt, “Osteonal and hemi-osteonal remodeling: The spatial and temporal framework for signal traffic in adult human bone,” *J. Cell. Biochem*, vol. 55, pp. 273–286, 1994.
- [3] V. Lemaire, F. L. Tobin, L. D. Greller, C. R. Cho, and L. J. Suva, “Modeling the interactions between osteoblast and osteoclast activities in bone remodeling,” *Journal of Theoretical Biology*, vol. 229, no. 3, pp. 293 – 309, 2004.
- [4] R. Martin, D. Burr, and N. Sharkey, *Skeletal tissue mechanics*. New York: Springer, 1998.
- [5] R. L. Jilka, “Biology of the basic multicellular unit and the pathophysiology of osteoporosis,” *Med Pediatr Oncol*, vol. 41, no. 3, pp. 182–185, 2003.
- [6] M. S. Rahman, N. Akhtar, H. M. Jamil, R. S. Banik, and S. M. Asaduzzaman, “TGF- $\beta$ /BMP signaling and other molecular events: regulation of osteoblastogenesis and bone formation,” *Bone Research*, vol. 3, no. 15005, pp. 1 – 20, 2015.
- [7] G. A. Rodan and T. J. Martin, “Role of osteoblasts in hormonal control of bone resorption—a hypothesis,” *Calcified Tissue International*, vol. 33, no. 1, pp. 349–351, 1981.
- [8] P. Pivonka, P. R. Buenzli, S. Scheiner, R. Hellmich, and C. Dunstan, “The influence of bone surface availability in bone remodelling—a mathematical model including coupled geometrical and biomechanical regulations of bone cells,” *Eng Struct*, vol. 47, pp. 134–147, 2013.
- [9] R. J. Majeska, “Cell biology of bone,” in *Bone Mechanics Handbook* (S. C. Cowin, ed.), ch. 2, pp. 2–1–2–24, CRC Press, second ed., 2001.
- [10] P. Pivonka, J. Zimak, D. W. Smith, B. S. Gardiner, C. R. Dunstan, N. A. Sims, T. J. Martin, and G. R. Mundy, “Model structure and control of bone remodeling: A theoretical study,” *Bone*, vol. 43, no. 2, pp. 249 – 263, 2008.

- [11] P. Pivonka, J. Zimak, D. W. Smith, B. S. Gardiner, C. R. Dunstan, N. A. Sims, T. J. Martin, and G. R. Mundy, “Theoretical investigation of the role of the RANK–RANKL–OPG system in bone remodeling,” *Journal of Theoretical Biology*, vol. 262, no. 2, pp. 306 – 316, 2010.
- [12] P. R. Buenzli, P. Pivonka, C. Thomas, and J. Clement, “Endocortical bone loss in osteoporosis: the role of bone surface availability,” *Int J Num Meth Biomed Eng*, vol. 29, pp. 1307–1322, 2013.
- [13] N. A. Sims and T. . Martin, “Coupling the activities of bone formation and resorption: a multitude of signals within the basic multicellular unit,” *BoneKEy Reports*, vol. 3, no. 481, 2014.
- [14] J. Wolff, P. Maquet, and R. Furlong, *The law of bone remodelling*. Springer-Verlag, 1986.
- [15] C. Turner, “Three rules for bone adaptation to mechanical stimuli,” *Bone*, vol. 23, no. 5, pp. 399 – 407, 1998.
- [16] O. M. Pearson and D. E. Lieberman, “The aging of Wolff’s law: Ontogeny and responses to mechanical loading in cortical bone,” *American Journal of Physical Anthropology*, vol. 125, no. S39, pp. 63–99, 2004.
- [17] H. M. Frost, “Bone “mass” and the “mechanostat”: A proposal,” *The Anatomical Record*, vol. 219, no. 1, pp. 1–9, 1987.
- [18] R. L. Duncan and C. H. Turner, “Mechanotransduction and the functional response of bone to mechanical strain,” *Calcified Tissue International*, vol. 57, no. 5, pp. 344–358, 1995.
- [19] E. R. Morey and D. J. Baylink, “Inhibition of bone formation during space flight,” *Science*, vol. 201, no. 4361, pp. 1138–1141, 1978.
- [20] I. Wolff, J. J. van Croonenborg, H. C. G. Kemper, P. J. Kostense, and J. W. R. Twisk, “The effect of exercise training programs on bone mass: A meta-analysis of published controlled trials in pre- and postmenopausal women,” *Osteoporosis International*, vol. 9, no. 1, pp. 1–12, 1999.
- [21] R. Huiskes, H. Weinans, H. Grootenboer, M. Dalstra, B. Fudala, and T. Slooff, “Adaptive bone-remodeling theory applied to prosthetic-design analysis,” *Journal of Biomechanics*, vol. 20, no. 11, pp. 1135 – 1150, 1987. F. Gaynor Evans Anniversary Issue on Bone Biomechanics.
- [22] R. Huiskes, R. Ruimerman, G. H. van Lenthe, and J. D. Janssen, “Effects of mechanical forces on maintenance and adaptation of form in trabecular bone,” *Nature*, vol. 405, pp. 704–706, 2000.

- [23] G. A. P. Renders, L. Mulder, L. J. Van Ruijven, and T. M. G. J. Van Eijden, “Porosity of human mandibular condylar bone,” *Journal of Anatomy*, vol. 210, no. 3, pp. 239–248, 2007.
- [24] C. D. L. Thomas, S. A. Feik, and J. G. Clement, “Increase in pore area, and not pore density, is the main determinant in the development of porosity in human cortical bone,” *Journal of Anatomy*, vol. 209, no. 2, pp. 219–230, 2006.
- [25] A. G. Mikos and J. S. Temenoff, “Formation of highly porous biodegradable scaffolds for tissue engineering,” *Electronic Journal of Biotechnology*, vol. 3, no. 2, 2000.
- [26] R. Nazarov, H.-J. Jin, and D. L. Kaplan, “Porous 3-D scaffolds from regenerated silk fibroin,” *Biomacromolecules*, vol. 5, no. 3, pp. 718–726, 2004. PMID: 15132652.
- [27] V. Karageorgiou and D. Kaplan, “Porosity of 3D biomaterial scaffolds and osteogenesis,” *Biomaterials*, vol. 26, no. 27, pp. 5474 – 5491, 2005.
- [28] P. Kasten, I. Beyen, P. Niemeyer, R. Luginbhl, M. Böhner, and W. Richter, “Porosity and pore size of  $\beta$ -tricalcium phosphate scaffold can influence protein production and osteogenic differentiation of human mesenchymal stem cells: An in vitro and in vivo study,” *Acta Biomaterialia*, vol. 4, no. 6, pp. 1904 – 1915, 2008.
- [29] S. J. Hollister, “Porous scaffold design for tissue engineering,” *Nat Mater.*, vol. 4, no. 7, pp. 518–524, 2005.
- [30] C. M. Murphy, M. G. Haugh, and F. J. O’Brien, “The effect of mean pore size on cell attachment, proliferation and migration in collagen-glycosaminoglycan scaffolds for bone tissue engineering,” *Biomaterials*, vol. 31, no. 3, pp. 461 – 466, 2010.
- [31] C. M. Murphy and F. J. O’Brien, “Understanding the effect of mean pore size on cell activity in collagen-glycosaminoglycan scaffolds,” *Cell Adhesion & Migration*, vol. 4, no. 3, pp. 377 – 381, 2010.
- [32] C. M. Bidan, K. P. Kommareddy, M. Rumpler, P. Kollmannsberger, Y. J. M. Bréchet, P. Fratzl, and J. W. C. Dunlop, “How linear tension converts to curvature: geometric control of bone tissue growth,” *PLoS One*, vol. 7, p. e36336, 2012.
- [33] C. M. Bidan, K. P. Kommareddy, M. Rumpler, P. Kollmannsberger, P. Fratzl, and J. W. C. Dunlop, “Geometry as a factor for tissue growth: Towards shape op-

- timization of tissue engineering scaffolds,” *Advanced Healthcare Materials*, vol. 2, no. 1, pp. 186–194, 2013.
- [34] C. M. Bidan, F. M. Wang, and J. W. Dunlop, “A three-dimensional model for tissue deposition on complex surfaces,” *Computer Methods in Biomechanics and Biomedical Engineering*, vol. 16, no. 10, pp. 1056–1070, 2013. PMID: 23528179.
- [35] C. M. Bidan, P. Kollmannsberger, V. Gering, S. Ehrig, P. Joly, A. Petersen, V. Vogel, P. Fratzl, and J. W. C. Dunlop, “Gradual conversion of cellular stress patterns into pre-stressed matrix architecture during in vitro tissue growth,” *J Roy Soc Interface*, vol. 13, p. 20160136, 2016.
- [36] M. Rumppler, A. Woesz, J. Dunlop, J. van Dongen, and P. Fratzl, “The effect of geometry on three-dimensional tissue growth,” *Journal of the Royal Society Interface*, vol. 5, pp. 1173–1180, 2008.
- [37] Y. Guyot, I. Papantoniou, Y. Chai, S. Van Bael, J. Schrooten, and L. Geris, “A computational model for cell/ECM growth on 3D surfaces using the level set method: a bone tissue engineering case study,” *Biomechanics and Modeling in Mechanobiology*, vol. 13, no. 6, pp. 1361–1371, 2014.
- [38] Y. Guyot, F. Luyten, J. Schrooten, I. Papantoniou, and L. Geris, “A three-dimensional computational fluid dynamics model of shear stress distribution during neotissue growth in a perfusion bioreactor,” *Biotechnology and Bioengineering*, vol. 112, no. 12, pp. 2591–2600, 2015.
- [39] Y. Guyot, I. Papantoniou, F. P. Luyten, and L. Geris, “Coupling curvature-dependent and shear stress-stimulated neotissue growth in dynamic bioreactor cultures: a 3D computational model of a complete scaffold,” *Biomechanics and Modeling in Mechanobiology*, pp. 1–12, 2016.
- [40] W. R. Lee, “Appositional bone formation in canine bone: a quantitative microscopic study using tetracycline markers,” *J Anat*, vol. 98, no. 4, pp. 665–677, 1964.
- [41] J. D. Manson and N. E. Waters, “Observations on the rate of maturation of the cat osteon,” *J Anat*, vol. 99, no. 3, pp. 539–549, 1965.
- [42] L. N. Metz, R. B. Martin, and A. S. Turner, “Histomorphometric analysis of the effects of osteocyte density on osteonal morphology and remodeling,” *Bone*, vol. 33, no. 5, pp. 753–759, 2003.
- [43] S. C. Cowin and L. Cardoso, “Blood and interstitial flow in the hierarchical pore space architecture of bone tissue,” *Journal of Biomechanics*, vol. 48, no. 5, pp. 842 – 854, 2015. In Memory of Rik Huiskes.

- [44] Q. Grimal, K. Raum, A. Gerisch, and P. Laugier, “A determination of the minimum sizes of representative volume elements for the prediction of cortical bone elastic properties,” *Biomechanics and Modeling in Mechanobiology*, vol. 10, pp. 925–937, Dec 2011.
- [45] P. R. Buenzli, “Governing equations of tissue modelling and remodelling: A unified generalised description of surface and bulk balance,” *PLoS ONE*, vol. 11, pp. 1–25, 04 2016.
- [46] C. Lerebours and P. R. Buenzli, “Towards a cell-based mechanostat theory of bone: the need to account for osteocyte desensitisation and osteocyte replacement,” *Journal of Biomechanics*, vol. 49, no. 13, pp. 2600 – 2606, 2016.
- [47] M. A. Alias and P. R. Buenzli, “Modeling the effect of curvature on the collective behavior of cells growing new tissue,” *Biophysical Journal*, vol. 112, no. 1, pp. 193 – 204, 2017.
- [48] P. R. Buenzli, P. Pivonka, and D. Smith, “Spatio-temporal structure of cell distribution in cortical bone multicellular units: a mathematical model,” *Bone [P]*, vol. . 48, no. 4, pp. 918–926, 2011.
- [49] C. Affane, S. Elnashaie, and F. Uhlig, *Numerical Techniques for Chemical and Biological Engineers Using MATLAB®: A Simple Bifurcation Approach*. Springer New York, 2007.
- [50] J. Logan, *Transport Modeling in Hydrogeochemical Systems*. Interdisciplinary Applied Mathematics, Springer New York, 2013.
- [51] H. A. Stone, “A simple derivation of the time-dependent convective–diffusion equation for surfactant transport along a deforming interface,” *Physics of Fluids A*, vol. 2, no. 1, pp. 111–112, 1990.
- [52] G. Osterhoff, E. F. Morgan, S. J. Shefelbine, L. Karim, L. M. McNamara, and P. Augat, “Bone mechanical properties and changes with osteoporosis,” *Injury*, vol. 47, pp. S11 – S20, 2016. Osteoporotic fracture fixation - a biomechanical perspective.
- [53] I. S. Maggiano, C. M. Maggiano, J. G. Clement, C. D. L. Thomas, Y. Carter, and D. M. L. Cooper, “Three-dimensional reconstruction of haversian systems in human cortical bone using synchrotron radiation-based micro-CT: morphology and quantification of branching and transverse connections across age,” *Journal of Anatomy*, vol. 228, no. 5, pp. 719–732, 2016.

- [54] K. L. Bell, N. Loveridge, J. Reeve, C. D. Thomas, S. A. Feik, and J. G. Clement, “Super-osteons (remodeling clusters) in the cortex of the femoral shaft: Influence of age and gender,” *The Anatomical Record*, vol. 264, no. 4, pp. 378–386, 2001.
- [55] J. H. Kinney and A. J. C. Ladd, “The relationship between three-dimensional connectivity and the elastic properties of trabecular bone,” *Journal of Bone and Mineral Research*, vol. 13, no. 5, pp. 839–845, 1998.
- [56] J. A. Sethian and J. Straint, “Crystal growth and dendritic solidification,” *Journal of Computational Physics*, vol. 98, no. 2, pp. 231 – 253, 1992.
- [57] S. Osher and J. Sethian, “Fronts propagating with curvature-dependent speed: algorithms based on Hamilton-Jacobi formulations,” *J. Comput. Phys*, vol. 79, no. 1, pp. 12–49, 1988.
- [58] J. A. Sethian, *Level Set Methods and Fast Marching Methods: Evolving Interfaces in Computational Geometry, Fluid Mechanics, Computer Vision, and Materials Science*. Cambridge University Press, 1999.
- [59] J.-J. Xu and H.-K. Zhao, “An Eulerian formulation for solving partial differential equations along a moving interface,” *Journal of Scientific Computing*, vol. 19, no. 1, pp. 573–594, 2003.
- [60] E. Olsson and G. Kreiss, “A conservative level set method for two phase flow,” *Journal of Computational Physics*, vol. 210, no. 1, pp. 225 – 246, 2005.
- [61] A. Kurganov and E. Tadmor, “New high-resolution central schemes for nonlinear conservation laws and convection–diffusion equations,” *Journal of Computational Physics*, vol. 160, no. 1, pp. 241 – 282, 2000.
- [62] W. Press, *Numerical Recipes 3rd Edition: The Art of Scientific Computing*. Cambridge University Press, 2007.
- [63] MathWorks, *MATLAB Function Reference*. MathWorks, 2017.
- [64] R. J. LeVeque, *Finite Volume Methods for Hyperbolic Problems*. Cambridge University Press, 2004. Cambridge Books Online.
- [65] R. LeVeque, *Numerical Methods for Conservation Laws*. Lectures in mathematics ETH Zürich, Birkhäuser Verlag, 1990.
- [66] P. D. Lax, “Development of singularities of solutions of nonlinear hyperbolic partial differential equations,” *Journal of Mathematical Physics*, vol. 5, no. 5, pp. 611–613, 1964.
- [67] P. Lax, *Hyperbolic systems of conservation laws and the mathematical theory of shock waves*. SIAM Philadelphia, 1973.

- [68] P. G. LeFloch and K. Smoczyk, “The hyperbolic mean curvature flow,” *Journal de Mathématiques Pures et Appliquées*, vol. 90, no. 6, pp. 591 – 614, 2008.
- [69] E. F. Toro, *Riemann Solvers and Numerical Methods for Fluid Dynamics: A Practical Introduction*. Berlin: Springer, 2nd ed., 1999.
- [70] P. Lax and B. Wendroff, “Systems of conservation laws,” *Communications on Pure and Applied Mathematics*, vol. 13, no. 2, pp. 217–237, 1960.
- [71] T. Nishida, “Global solution for an initial boundary value problem of a quasilinear hyperbolic system,” *Proc. Japan Acad.*, vol. 44, no. 7, pp. 642–646, 1968.
- [72] P. D. Lax, “Hyperbolic systems of conservation laws II,” *Communications on Pure and Applied Mathematics*, vol. 10, no. 4, pp. 537–566, 1957.
- [73] A. Bressan, *Hyperbolic Conservation Laws: An Illustrated Tutorial*, pp. 157–245. Berlin, Heidelberg: Springer Berlin Heidelberg, 2013.
- [74] E. Godlewski and P. Raviart, *Numerical Approximation of Hyperbolic Systems of Conservation Laws*. No. no. 118 in Applied Mathematical Sciences, Springer, 1996.
- [75] J. Smoller, *Shock waves and reaction-diffusion equations*. Grundlehren der mathematischen Wissenschaften, Springer-Verlag, 1983.
- [76] Y. Zheng, *Systems of Conservation Laws: Two-Dimensional Riemann Problems*. Progress in Nonlinear Differential Equations and Their Applications, Birkhäuser Boston, 2012.
- [77] L. Evans, *Partial Differential Equations*. Graduate studies in mathematics, American Mathematical Society, 1998.
- [78] R. J. DiPerna, “Global existence of solutions to nonlinear hyperbolic systems of conservation laws,” *Journal of Differential Equations*, vol. 20, no. 1, pp. 187 – 212, 1976.
- [79] Y.-X. Qin, T. Kaplan, A. Saldanha, and C. Rubin, “Fluid pressure gradients, arising from oscillations in intramedullary pressure, is correlated with the formation of bone and inhibition of intracortical porosity,” *Journal of Biomechanics*, vol. 36, no. 10, pp. 1427 – 1437, 2003. Bone Cell and Tissue Mechanics.
- [80] G. Jordan, N. Loveridge, K. Bell, J. Power, N. Rushton, and J. Reeve, “Spatial clustering of remodeling osteons in the femoral neck cortex: a cause of weakness in hip fracture?,” *Bone*, vol. 26, no. 3, pp. 305 – 313, 2000.
- [81] P. Macklin, “Numerical simulation of tumor growth and chemotherapy,” 2003.

- [82] P. Macklin and J. Lowengrub, “Evolving interfaces via gradients of geometry-dependent interior poisson problems: application to tumor growth,” *Journal of Computational Physics*, vol. 203, no. 1, pp. 191 – 220, 2005.
- [83] S. Wise, J. Lowengrub, H. Frieboes, and V. Cristini, “Three-dimensional multispecies nonlinear tumor growth: Model and numerical method,” *Journal of Theoretical Biology*, vol. 253, no. 3, pp. 524 – 543, 2008.
- [84] F. Vermolen, M. W. G. van Rossum, E. J. Perez, and J. Adam, *Modeling of Self Healing of Skin Tissue*, pp. 337–363. Dordrecht: Springer Netherlands, 2007.
- [85] S. Osher and R. P. Fedkiw, “Level set methods: An overview and some recent results,” *Journal of Computational Physics*, vol. 169, no. 2, pp. 463 – 502, 2001.
- [86] D. Peng, B. Merriman, S. Osher, H. Zhao, and M. Kang, “A PDE-based fast local level set method,” *Journal of Computational Physics*, vol. 155, no. 2, pp. 410 – 438, 1999.
- [87] M. Sussman, P. Smereka, and S. Osher, “A level set approach for computing solutions to incompressible two-phase flow,” *Journal of Computational Physics*, vol. 114, no. 1, pp. 146 – 159, 1994.
- [88] C.-W. Shu and S. Osher, “Efficient implementation of essentially non-oscillatory shock-capturing schemes,” *Journal of Computational Physics*, vol. 77, no. 2, pp. 439–471, 1988.
- [89] C.-W. Shu, “Essentially non-oscillatory and weighted essentially non-oscillatory schemes for hyperbolic conservation laws,” in *Advanced Numerical Approximation of Nonlinear Hyperbolic Equations* (A. Quarteroni, ed.), vol. 1697 of *Lecture Notes in Mathematics*, pp. 325–432, Springer Berlin Heidelberg, 1998.
- [90] G.-S. Jiang and C.-W. Shu, “Efficient implementation of weighted ENO schemes,” *Journal of Computational Physics*, vol. 126, no. 1, pp. 202–228, 1996.
- [91] G.-S. Jiang and D. Peng, “Weighted ENO schemes for hamilton–jacobi equations,” *SIAM Journal on Scientific Computing*, vol. 21, no. 6, pp. 2126–2143, 2000.
- [92] S. Osher and R. Fedkiw, *Level Set Methods and Dynamic Implicit Surfaces*. New York: Springer New York, 1 ed., 2003.
- [93] D. L. Chopp, “Computing minimal surfaces via level set curvature flow,” *Journal of Computational Physics*, vol. 106, no. 1, pp. 77 – 91, 1993.

- [94] B. Düring, M. Fournié, and A. Rigal, *High-Order ADI Schemes for Convection-Diffusion Equations with Mixed Derivative Terms*, pp. 217–226. Cham: Springer International Publishing, 2014.
- [95] H. D. Ceniceros and T. Y. Hou, “An efficient dynamically adaptive mesh for potentially singular solutions,” *Journal of Computational Physics*, vol. 172, no. 2, pp. 609 – 639, 2001.
- [96] D. W. Peaceman and J. H. H. Rachford, “The numerical solution of parabolic and elliptic differential equations,” *Journal of the Society for Industrial and Applied Mathematics*, vol. 3, no. 1, pp. 28–41, 1955.
- [97] Y. Shiga, S. Orita, G. Kubota, H. Kamoda, M. Yamashita, Y. Matsuura, K. Yamauchi, Y. Eguchi, M. Suzuki, K. Inage, T. Sainoh, K. Sato, J. Fujimoto, K. Abe, H. Kanamoto, M. Inoue, H. Kinoshita, Y. Aoki, T. Toyone, T. Furuya, M. Koda, K. Takahashi, and S. Ohtori, “Freeze-dried platelet-rich plasma accelerates bone union with adequate rigidity in posterolateral lumbar fusion surgery model in rats,” *Sci Rep.*, vol. 6, p. 36715, 2016.
- [98] F. Losasso, R. Fedkiw, and S. Osher, “Spatially adaptive techniques for level set methods and incompressible flow,” *Computers & Fluids*, vol. 35, no. 10, pp. 995 – 1010, 2006.
- [99] K. Y. Lervåg and Å. Ervik, *Curvature Calculations for the Level-Set Method*, pp. 209–217. Berlin, Heidelberg: Springer Berlin Heidelberg, 2013.
- [100] S. Shin, “Computation of the curvature field in numerical simulation of multiphase flow,” *Journal of Computational Physics*, vol. 222, no. 2, pp. 872 – 878, 2007.
- [101] M. Raessi, J. Mostaghimi, and M. Bussmann, “Advecting normal vectors: A new method for calculating interface normals and curvatures when modeling two-phase flows,” *Journal of Computational Physics*, vol. 226, no. 1, pp. 774 – 797, 2007.
- [102] M. Coquerelle and S. Glockner, “A fourth-order accurate curvature computation in a level set framework for two-phase flows subjected to surface tension forces,” *Journal of Computational Physics*, vol. 305, pp. 838 – 876, 2016.
- [103] P. Macklin and J. Lowengrub, “An improved geometry-aware curvature discretization for level set methods: Application to tumor growth,” *Journal of Computational Physics*, vol. 215, no. 2, pp. 392 – 401, 2006.
- [104] D. Salac and W. Lu, “A local semi-implicit level-set method for interface motion,” *Journal of Scientific Computing*, vol. 35, no. 2, pp. 330–349, 2008.
- [105] K. Yngve Lervåg, “Calculation of interface curvature with the level-set method,” *ArXiv e-prints*, July 2014.

- [106] A. Ervik, K. Y. Lervag, and S. T. Munkejord, “A robust method for calculating interface curvature and normal vectors using an extracted local level set,” *Journal of Computational Physics*, vol. 257, Part A, pp. 259 – 277, 2014.
- [107] J.-C. Nave, R. R. Rosales, and B. Seibold, “A gradient-augmented level set method with an optimally local, coherent advection scheme,” *Journal of Computational Physics*, vol. 229, no. 10, pp. 3802 – 3827, 2010.
- [108] B. Seibold, R. R. Rosales, and J.-C. Nave, “Jet schemes for advection problems,” *Discrete and Continuous Dynamical Systems - Series B*, vol. 17, no. 4, pp. 1229–1259, 2012.
- [109] C. J. Vogl, “A curvature-augmented, REA approach to the level set method,” *SIAM Journal on Scientific Computing*, vol. 38, no. 2, pp. A833–A855, 2016.
- [110] M. Sussman and E. G. Puckett, “A coupled level set and volume-of-fluid method for computing 3D and axisymmetric incompressible two-phase flows,” *Journal of Computational Physics*, vol. 162, no. 2, pp. 301 – 337, 2000.
- [111] D. Enright, R. Fedkiw, J. Ferziger, and I. Mitchell, “A hybrid particle level set method for improved interface capturing,” *Journal of Computational Physics*, vol. 183, no. 1, pp. 83 – 116, 2002.
- [112] H. L. Holtorf, N. Datta, J. A. Jansen, and A. G. Mikos, “Scaffold mesh size affects the osteoblastic differentiation of seeded marrow stromal cells cultured in a flow perfusion bioreactor,” *Journal of Biomedical Materials Research Part A*, vol. 74A, no. 2, pp. 171–180, 2005.
- [113] N. Datta, Q. P. Pham, U. Sharma, V. I. Sikavitsas, J. A. Jansen, and A. G. Mikos, “In vitro generated extracellular matrix and fluid shear stress synergistically enhance 3D osteoblastic differentiation,” *Proceedings of the National Academy of Sciences of the United States of America*, vol. 103, no. 8, pp. 2488–2493, 2006.
- [114] M. Batchelor, R. Burne, B. Henry, and S. Watt, “Deterministic kpz model for stromatolite laminae,” *Physica A: Statistical Mechanics and its Applications*, vol. 282, no. 1, pp. 123 – 136, 2000.
- [115] M. M. Nava, M. T. Raimondi, and R. Pietrabissa, “A multiphysics 3D model of tissue growth under interstitial perfusion in a tissue-engineering bioreactor,” *Biomechanics and Modeling in Mechanobiology*, vol. 12, pp. 1169–1179, Nov 2013.
- [116] S. Ehrig, J. Ferracci, R. Weinkamer, and J. W. C. Dunlop, “Curvature-controlled defect dynamics in active systems,” *Phys. Rev. E*, vol. 95, p. 062609, Jun 2017.

- [117] P. R. Buenzli, “Osteocytes as a record of bone formation dynamics: A mathematical model of osteocyte generation in bone matrix,” *Journal of Theoretical Biology*, vol. 364, pp. 418–427, 2015.
- [118] R. Martin, “The effects of geometric feedback in the development of osteoporosis,” *Journal of Biomechanics*, vol. 5, no. 5, pp. 447 – 455, 1972.
- [119] P. Christen and R. Müller, “In vivo visualisation and quantification of bone resorption and bone formation from time-lapse imaging,” *Current Osteoporosis Reports*, vol. 15, pp. 311–317, Aug 2017.
- [120] R. G. Erben, *Bone-Labeling Techniques*, pp. 99–117. Totowa, NJ: Humana Press, 2003.
- [121] F. A. Schulte, F. M. Lambers, G. Kuhn, and R. Müller, “In vivo micro-computed tomography allows direct three-dimensional quantification of both bone formation and bone resorption parameters using time-lapsed imaging,” *Bone*, vol. 48, no. 3, pp. 433 – 442, 2011.
- [122] F. M. Lambers, K. Koch, G. Kuhn, D. Ruffoni, C. Weigt, F. A. Schulte, and R. Müller, “Trabecular bone adapts to long-term cyclic loading by increasing stiffness and normalization of dynamic morphometric rates,” *Bone*, vol. 55, no. 2, pp. 325 – 334, 2013.
- [123] A. R. Altman, W.-J. Tseng, C. M. de Bakker, A. Chandra, S. Lan, B. K. Huh, S. Luo, M. B. Leonard, L. Qin, and X. S. Liu, “Quantification of skeletal growth, modeling, and remodeling by in vivo micro computed tomography,” *Bone*, vol. 81, pp. 370 – 379, 2015. Epigenetic Mechanisms Regulating Bone Biology and Pathology.
- [124] Z. Li, G. Kuhn, M. von Salis-Soglio, S. J. Cooke, M. Schirmer, R. Müller, and D. Ruffoni, “In vivo monitoring of bone architecture and remodeling after implant insertion: The different responses of cortical and trabecular bone,” *Bone*, vol. 81, no. Supplement C, pp. 468 – 477, 2015. Epigenetic Mechanisms Regulating Bone Biology and Pathology.
- [125] I. V. Pratt and D. M. L. Cooper, “A method for measuring the three-dimensional orientation of cortical canals with implications for comparative analysis of bone microstructure in vertebrates,” *Micron*, vol. 92, no. Supplement C, pp. 32 – 38, 2017.
- [126] F. A. Schulte, D. Ruffoni, F. M. Lambers, D. Christen, D. J. Webster, G. Kuhn, and R. Müller, “Local mechanical stimuli regulate bone formation and resorption in mice at the tissue level,” *PLoS One*, vol. 8, 04 2013.

- [127] P. Christen, K. Ito, R. Ellouz, S. Boutroy, E. Sornay-rendu, R. D. Chapurlat, and B. Van Rietbergen, “Bone remodelling in humans is load-driven but not lazy,” *Nature Communications*, vol. 5, p. 4855, 09 2014.
- [128] R. B. Martin, “Porosity and specific surface of bone,” *Crit Rev Biomed Eng*, vol. 10, no. 3, pp. 179–222, 1984.
- [129] C. Lerebours, C. Thomas, J. Clement, P. Buenzli, and P. Pivonka, “The relationship between porosity and specific surface in human cortical bone is subject specific,” *Bone*, vol. 72, pp. 109–117, 2015.
- [130] P. R. Buenzli., P. Pivonka, and D. Smith, “Bone refilling in cortical basic multicellular units: insights into tetracycline double labelling from a computational model,” *Biomechanics and Modeling in Mechanobiology [P]*, vol. 13, no. 1, pp. 185–203, 2014.
- [131] J. Lee, A. A. Abdeen, K. L. Wycislo, T. M. Fan, and K. A. Kilian, “Interfacial geometry dictates cancer cell tumorigenicity,” *Nature Materials*, vol. 15, pp. 856–862, 08 2016. Copyright - Copyright Nature Publishing Group Aug 2016; Document feature - ; Graphs; Photographs; Last updated - 2016-10-10.